Universidade da Coruña

Doctoral Thesis

Mathematical modeling and numerical simulation of tumor angiogenesis

Author:

Guillermo Vilanova Caicoya

Supervisors:

Dr. Héctor Gómez Díaz
Dr. Ignasi Colominas Ezponda

Programa de doctorado en Ingeniería Civil
2016

Abstract

Cancer is nowadays the second leading cause of death in the world. Cancer starts with a single cell that has accumulated several mutations usually over a long period of time. One of the main characteristics of this cell is its ability to replicate unbounded producing, in most occasions, a mass of densely packed daughter cells that form a solid tumor. Cancerous cells depend on nutrients and oxygen supplied by pre-existent blood vessels to proliferate. This supply is not enough to maintain the growth and most tumors remain small and benign due to this constraint. Occasionally, however, some cells develop the ability to promote the growth of new capillaries towards them. This process is called tumor-induced angiogenesis and through it tumors acquire a constant supply of nutrients and oxygen and access to the whole body through the circulatory system. Tumors that are able to trigger angiogenesis become malignant as they can grow unbounded and metastasize. Malignant tumors can grow large enough to damage the functionality of the host organ and, eventually, lead to death.

A few decades ago, scientists have proposed that blocking angiogenesis could be an effective treatment against cancer. This therapy, known as antiangiogenic therapy, has shown promising results in pre-clinical trials, but has not translated into the expected results in the clinic. A new emerging paradigm in Medicine, namely, Predictive Medicine, is expected to change the Oncology field and may be the tool to understand the problems with this therapy. Predictive Medicine is based on mathematical modeling and computation and has been so far successfully applied to several areas of Medicine. In the Oncology field it has only been started, but has already produced sound advances. In particular, in tumor-induced angiogenesis numerous researchers have proposed mathematical models to address the problem of antiangiogenic therapies, although there is still a need for improvement to attain this goal. Angiogenesis is a complex multiscale process that involves several key mechanisms, many of them not yet accounted for in the models. In addition, most

models are simulated in two-dimensional simple geometries, while angiogenesis is a three-dimensional process and occurs in tissues with non-trivial geometries.

In this thesis we develop mathematical models of tumor-induced angiogenesis that include key biological mechanisms and we simulate these models in relevant experimental setups and in three-dimensional, subject-specific geometries. To achieve our modeling and simulation goals, we develop adequate numerical algorithms. Every model in this thesis is hybrid and involves coupling averaged continuous theories and cellular-scale discrete agents. In addition, the models are grounded on the phase-field method which requires solving higher-order partial differential equations. To overcome these problems we developed a seamless coupling between the continuous variables and the discrete elements to permit an efficient numerical treatment of the coupled problem. For the resolution of the high-order partial differential equations involved in the formulation we used isogeometric analysis, which in addition provides accuracy, robustness, and the geometric flexibility that we require to perform simulations in real geometries.

This manuscript presents three new mathematical models for tumor-induced angiogenesis. In the first one we started with a previous model to which we added a conceptual model for haptotaxis, one of the main mechanisms that governs capillary growth. The extended model permitted us to assess the role of haptotaxis in tumor angiogenesis. Furthermore, we developed for the first time a simulation of one of the most widely used *in vivo* assays, the mouse corneal micropocket angiogenesis assay, using a three-dimensional, subject-specific geometry. The results are in agreement with the experiments and predict well-known vascular structures in three dimensions. In addition, they suggest that, for mathematical models to achieve the topological complexity observed in *in vivo* angiogenesis experiments, two-dimensional simulations may not be enough.

The second model focuses on the long-term dynamics of tumor-induced angiogenesis, that is, on the regression and regrowth events occurring after the first growth of blood vessels. The model was simulated both in a two-dimensional replication of the mouse corneal micropocket assay and in a reproduction of an *in vivo* experimental setup. Our simulations predict plasticity and dynamic evolution of angiogenesis at long time spans and are in quantitative agreement with experiments.

Finally, we developed a fully continuum theory for fluid flow at the tissue scale, which we coupled with our model for tumor angiogenesis. The model shows how fluid flow alters tumor-induced vascular patterns through convection, which has been overlooked in mathematical modeling. Our model predicts a substantial impact of convection in angiogenesis and an increased malignancy of small solid tumors.

Contents

List of Figures

List of Tables

List of Symbols

Abbreviations

ATP	Adenosine 5'-triphosphate
CAD	Computer-aided design
CAM	Chorioallantoic membrane
Dll-4	Delta-like ligand 4
ECM	Extracellular matrix
EMT	Epithelial-to-mesenchymal transition
FEA	Finite element analysis
FGF	Fibroblast growth factor
HYC	Hypoxic cell
IGA	Isogeometric analysis
MET	Mesenchymal-to-epithelial transition
MMP	Matrix metalloproteinases
MPI	Message passing interface

NURBS Non-uniform rational B-splines

SEC Stalk endothelial cell

SUPG Streamline upwind/Petrov–Galerkin method

TAF Tumor angiogenic factor

TEC Tip endothelial cell

VEGF Vascular endothelial growth factor

VMS Variational multiscale method

Main variables of the mathematical models

c Capillary order parameter

f Tumor angiogenic factor

p Fluid pressure

Main constants of the mathematical models

α Proliferative/apoptotic phenotype switch

β Proliferative/apoptotic phenotype switch

χ Chemotatic constant

δ Turning angle

δ_4 Dll-4 diffusion length

δ_{nox} Nutrient and oxygen diffusion length

λ Interface width

B_d TAF natural decay

B_p TAF proliferation rate

B_u TAF uptake rate

c_{act} Order parameter condition for de/activation

D	TAF diffusion
D_r	Rotational diffusivity
d_v	Turning coefficient
f_p	TAF condition for highest proliferation
f_{act}	TAF condition for de/activation
f_{HYC}	TAF production
G_{act}	TAF gradient condition for de/activation
G_{M}	TAF gradient for highest velocity
M	Mobility
R_{HYC}	HYC radius
R_{TEC}	TEC radius

Chapter 1

Introduction

1.1 Motivation and research objective

Motivation

Cancer facts Cancer is the second cause of death in the world, just behind cardiovascular diseases (see figure 1.1). According to the last estimation from the World Health Organization performed in 2012 (Ferlay *et al.*, 2012), approximately 8.2 million of people died from cancer, that is, 15% of all deaths worldwide. Furthermore, there have been 14.1 million estimated new cases that year. And, although 32.5 million people diagnosed with cancer from 2008 were alive at the end of 2012, an estimated 169,3 million years of healthy life were lost globally because of cancer in 2008. Despite the amount of funding and research in the field, these figures increase year after year, probably boosted by the growth and aging of the population.

The global fight against cancer is hindered by the different cancer burden and cancer types among regions, as highlighted by figures 1.1 and 1.2. Figure 1.1 shows how the number of people that die from cancer varies greatly between different income countries (using the World Bank income classification World Bank, 2014). Population aging and lifestyle —including smoking, diet, and physical activity— are among the main reasons of cancer deaths in the high and upper-middle income countries, while insufficient access to treatments and late diagnosis are the causes for high cancer mortality in lower-middle income countries. The high burden of

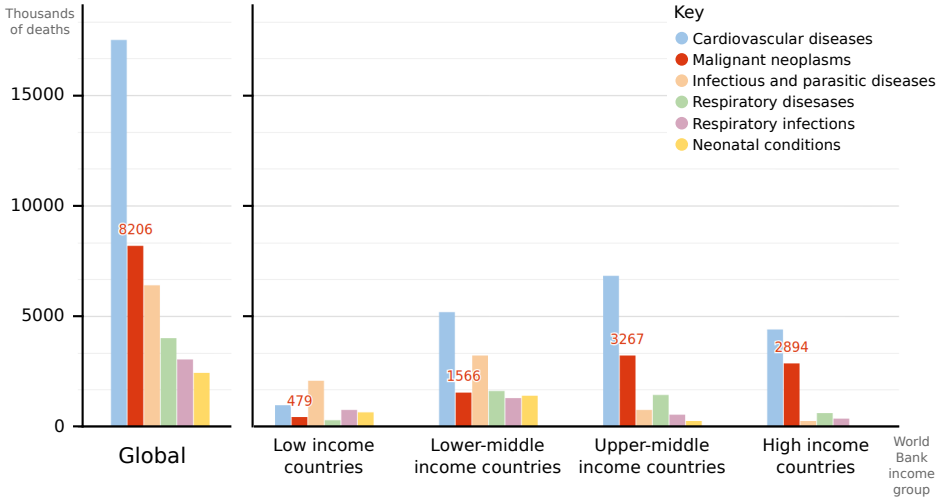

Figure 1.1. Leading cases of deaths by cause worldwide and by World Bank income group. *After heart diseases, cancer is the leading death cause globally and in the upper-middle and high income countries. (Data source: Latest estimates by the World Health Organization Ferlay* et al.*, 2012)*

infections and parasitic diseases in low income countries explain their lower cancer mortality. Figure 1.2 shows both the age-standardized cancer death rate per one thousand people and the top three cancer killers per region, separated by gender. This figure also highlights the non uniform distribution of cancer around the world, not only in its incidence by country, but also in the regional mortality of different cancer types. Among all cancer types, lung cancer, which is the most common cancer in men, causes most cancer deaths worldwide; almost a fifth. It is one of the top cancer killers in every region shown in figure 1.2, except in the Sub-Saharan Africa. Breast, colorectal, and prostate cancer are also among the most deadly ones.

All these facts highlight the importance of a community of interdisciplinary researchers coming from all the branches of Science equipped with all kind of tools to fight cancer. And among these tools, Knowledge has proven to be the more powerful. History has shown that the more we know about cancer, the better we are able to fight it.

Cancer through History Cancer is not a recent illness, but a disease affecting human beings since thousands of years ago. The first known description of cancer, which was in particular about breast cancer, comes from an Egyptian papyrus

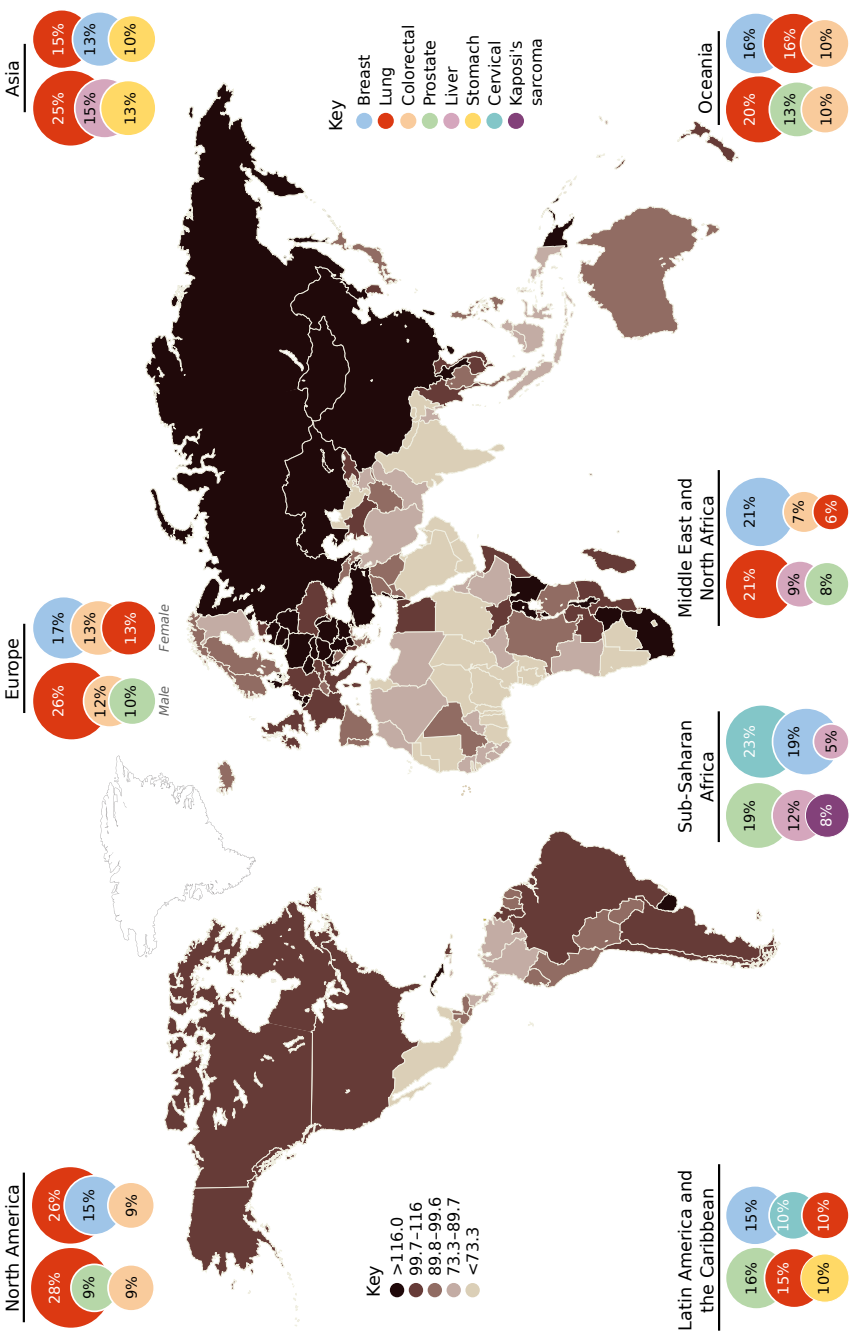

Figure 1.2. Cancer incidence. *Age-standardized cancer death rate per one thousand people by country (world map) and top three cancer killers in males and females per region (pie charts). (Adapted from May, 2014)*

which is a copy of an older book dating back to 3000 BC. This document explains how tumors were treated by cauterization with a tool called *fire drill*, although it is also written they knew there was no treatment for this disease. The Egyptian culture attributed the disease to gods will. The Greek civilization also knew about cancer. In fact the word we use now, *cancer*, is the Latin translation of the Greek *karkinos*, which means *crab* —because it resembled the shape of a crab—, and it is ascribed to Hippocrates. This physician, called the *Father of Medicine*, believed that the body was composed of four fluids: blood, phlegm, yellow bile, and black bile. He thought that an excess of black bile anywhere in the body caused cancer. And for more than 1400 years this was the general belief. It is not until the paradigm shift that came with the development of the Scientific Method in the Renaissance period that this theory was questioned again. Autopsies started to be performed and with them the study of cancer, Oncology, began. Now that bodies were analyzed looking for the causes of death, new theories began to replace the previous ones. In the Eighteenth century, John Hunter suggested surgery as a treatment for certain sorts of cancer: Those that had not yet invaded the neighboring tissues. Afterwards, the development of anesthesia involved advances in surgery that allowed improvements in the resection of certain tumors. The use of the modern microscope in the 19th century meant a big step in the study of cancer. For more detailed information about cancer History see (Olszewski, 2010; Sudhakar, 2009).

How cancer is understood nowadays At present, we understand cancer as a group of diseases —more than a hundred— that share common characteristics: The uncontrolled proliferation of cells and their ability to invade other tissues and continue there with their abnormal proliferation. Each cancer is different from the others in many aspects and they are usually named after the host tissue in which they develop at first, as in breast cancer, prostate cancer, or lung cancer.

Cancer is originated by a single abnormal cell (Weinberg, 1998) that acquires through mutations, that is changes in their DNA, malignant characteristics. This process, called *carcinogenesis*, is complex and may take years or decades to complete. In fact, there is not full knowledge of the reason for all mutations and that is why we usually refer to risk factors rather than mutations themselves when speaking about cancer causes. These factors may be divided into exogenous and endogenous. 75-80% of cancers develop due to the former and they can be either physical, chemical, or biological. As shown in figure 1.3, the exogenous factors with higher impact are tobacco use, obesity and overweight, and pathogen infections. Many authors estimate that 30% of cancer deaths could be prevented by reducing these factors through healthy life styles. On the other hand, the endogenous factors represent only 5-7% of the whole and are produced by hereditary

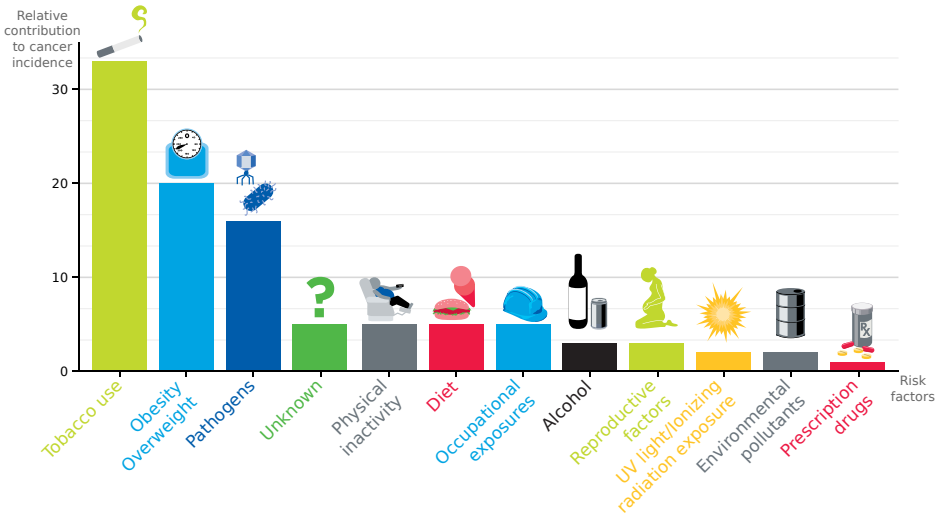

Figure 1.3. Exogenous cancer risk factors. *The two risk factors that most contribute to cancer incidence, tobacco and overweight, could be reduced to a minimum just with healthy habits. (Adapted from American Asociation for Cancer Research, 2015)*

alterations in the DNA sequence. The mechanisms by which cancer occurs in the remaining cases are not accurately known (Ames *et al.*, 1995). In addition, one of the most important factors is aging (Torre *et al.*, 2015), as explained latter in this document.

The consequence of carcinogenesis is usually the creation of solid masses or tumors, formed by cancerous cells that multiply rapidly, even ignoring the anti-growth signals sent by the own body. Tumors grow and develop going through a set of increasingly-malignant stages. Remarkably, tumors can gain the ability to invade nearby tissues or to colonize and create secondary tumors in distant organs using the vasculature as a means of transport. It is at this point, when the tumors are more malignant, that cancer is more lethal. However, there is not a single reason why cancer kills, but it depends on the type of cancer. One reason is the loss of function of a vital organ (or organs) due to the uncontrolled and abnormal growth of the tumor (or tumors). For instance, in lung cancer, eventually, there may be not enough healthy tissue to absorb oxygen or in colorectal cancer, the lumen of the digestive system may get blocked. Also, the fine tuned regulation of some chemical in the body may be unbalanced by a tumor located in the organ that produces them, for example, the liver. Or the amount of calcium in the blood may be risen by bone cancer causing unconsciousness and eventually death.

In most types of cancer, luckily, from carcinogenesis until cancer becomes a real thread to life, cancerous cells have to overcome several natural barriers that prevent tumor growth. Continuous research has deepened the knowledge in such barriers and, nowadays, they are understood as opportunities to treatments that delay or halt tumor growth. For example, tumors can not grow beyond a certain size until cancerous cells gain the ability to promote angiogenesis, that is, the creation of new blood vessels from the pre-existent ones.

The role of angiogenesis in cancer Certain types of cancer form solid tumors of aberrant, mutated cells. These cells, that proliferate in a high-rate manner, aggregate in solid masses that grow at the expense of the resources of the surroundings. At this stage of tumor growth (called the avascular stage), cancerous cells depend on diffusion mechanisms to obtain nutrients. However, when the tumor has grown up to a certain size, not larger than 2 mm radius in experiments (Folkman, 1971), its global growth stops. This occurs due to the scarceness of nourishment and oxygen that does not even cover the demands for maintaining the basic cell processes in the core of the mass. Tumors may stay dormant in this stage for years and only grow further if cancerous cells acquire the ability to induce angiogenesis. In order to promote vessel growth, tumor cells, and even malign-induced, non-cancerous cells from the tumor micro-environment, release chemical signals, called *tumor angiogenic factors* (TAFs), that alter the phenotype of the endothelial cells that line nearby capillaries. As a result, new capillaries grow towards the tumor and provide nourishment to cancerous cells. Thus, angiogenesis enables a boost in tumor development, the so-called *angiogenic switch* (see figure 1.4), moving the tumor to the vascular phase and endowing cancerous cells with nutrients and oxygen to grow without limits and with new ways of migration to other tissues or organs of the body.

The realization of the key role of angiogenesis has leaded to the development of antiangiogenic therapies. Although this will be explained later in the document, we advance here that these therapies have not achieved the expected results yet. Arguably, an emerging paradigm in Medicine called predictive medicine will change radically cancer investigation and may be the tool to unravel the problems with antiangiogenic therapy.

Predictive medicine Cancer is a disease with a high morbidity and mortality rate, thus it is hardly surprising that many people devote their efforts and work to deepen the knowledge we currently have on cancer, comprehending better the mechanisms involved and thereby being able to better diagnose and create new treatments. This research, as well as the clinical practice, is usually developed

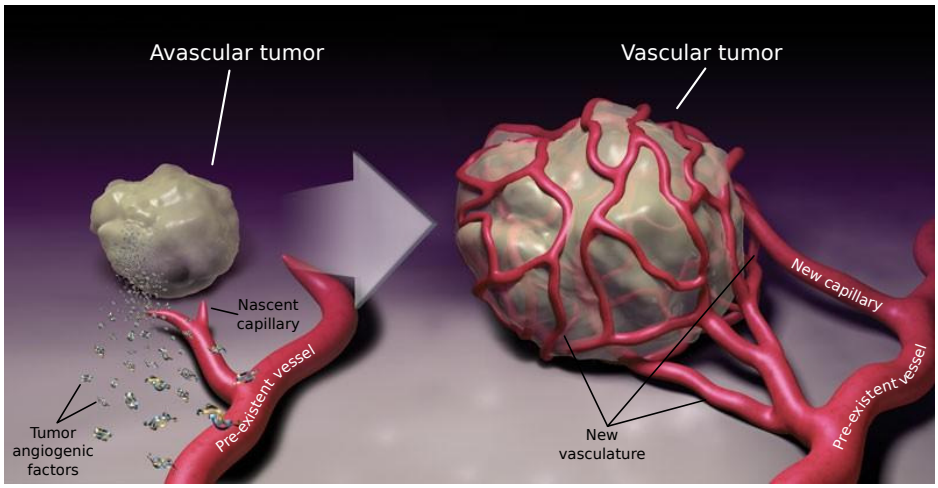

Figure 1.4. The angiogenesis switch. *Tumors are able promote angiogenesis, the growth of new vessels from pre-existing ones, through signaling. The nutrient from the new capillaries triggers a virtually unbounded tumor growth and the possibility to metastasize using the circulatory system.(Adapted from Bergers and Benjamin, 2003)*

by groups composed by physicians and biologists. They follow the diagnostic paradigm, which is heavily based on the experience of the physicians with previous patients and on statistical data of the effect of the treatments on large groups of individuals. In the last decades, however, a new paradigm has been proposed: predictive medicine. Its aim is to predict the emergence, development, and consequences of a disease, as well as to enhance current treatments and propose new ones. Predictive medicine is based on mathematical modeling and computation. This new approach has been successfully applied to cardiovascular diseases (Taylor and Figueroa, 2009) and orthopedics (Taylor and Prendergast, 2015), and it has recently started to be applied to Oncology (Chauviere *et al.*, 2010; Gatenby and Maini, 2003; Sanga *et al.*, 2007).

Objectives

This thesis continues the research developed by the Group of Numerical Methods in Engineering (GMNI) of the *Universidade da Coruña* in the field of computational mechanics, in particular, it is the first to explore the sub-field of computational biomechanics. It is also the first developed under the project *Modeling and Simulation of Cancer Growth* (MuSIC), whose objective is to introduce predictive models for cancer growth with the aim of shifting the traditional diagnostic paradigm of

cancer treatment towards a predictive, patient-specific one. In parallel with the MuSIC project, the objective of this thesis is to develop mathematical models of tumor-induced angiogenesis that include key biological mechanisms and to perform isogeometric-based numerical simulations in relevant experimental setups and three-dimensional, subject-specific geometries.

The objectives of this thesis may be divided into three categories:

- **Modeling**: The goal is to develop novel mathematical models of tumor-induced angiogenesis that include key biological mechanisms, namely, the migration of tip endothelial cells following different cues, the ability of capillaries to regress and regrow depending on exterior stimuli, and the role of interstitial fluid convection in pattern formation. These models involve continuous fields governed by high-order partial differential equations and discrete elements.

- **Simulation**: Most of the mathematical models found in the literature are simulated in simple, two-dimensional geometries. In fact, we also plan to perform *in silico* simulations of the above models in two dimensions that replicate relevant *in vivo* angiogenic configurations to facilitate the study of the model. However, angiogenesis is a three-dimensional process and occurs in tissues or organs with non-trivial geometries. Hence, the second objective of this thesis is to go one step beyond and perform three-dimensional simulations in real geometries that will permit the comparison with experiments. In particular, our goal is to develop a tumor-induced angiogenesis simulation of one of the most widely used *in vivo* assays, the mouse corneal micropocket angiogenesis assay, using a three-dimensional, subject-specific geometry. To the best knowledge of the author, this simulation will allow for the first time the comparison between a simulation and an experiment in a three-dimensional real geometry.

- **Computational**: The third objective is to develop numerical algorithms capable of performing the above simulations efficiently. First, we need to develop a mathematical framework that seamlessly integrates the discrete agents as part of one of the continuous fields. We also need to use a recently introduced technology, isogeometric analysis, able to handle the higher order terms of the partial differential equations in two- and three-dimensional complex geometries. Furthermore, the algorithms need to be robust, to overcome the stiffness in space and time that derives from the use of two scales, and to run efficiently in parallel.

1.2 Context

1.2.1 Biology background

The objectives of this thesis are deeply grounded on the biology of angiogenesis, the mathematical modeling of tumor angiogenesis, and the numerical methods to simulate the models. Therefore, this section is devoted to give a general context in these three aspects. It starts with a biology background to explain how cancer grows and spreads and how tumors promote angiogenesis; continues with the state of the art of mathematical modeling of tumor-induced angiogenesis; and finalizes with an explanation of the numerical method used to solve the models, namely, isogeometric analysis.

Cancer growth and spread

Carcinogenesis As said above, carcinogenesis, also called *tumorigenesis*, is the process whereby normal cells acquire the capabilities to become cancerous cells. These capabilities are usually gained through mutations, but also by non-mutational changes in mechanisms regulating gene expression —those exerting the transcriptional control; for example whether a gene should be transcribed or not or the transcription velocity needed under certain circumstances. However, in the rest of the document, we will refer to both of them just as *mutations* for the sake of clarity. There are many genes known to be involved in carcinogenesis and, surely, many more still unknown. These genes can be classified in oncogenes and tumor suppressor genes. The former ones refer to those whose upregulated expression trigger processes which lead to cancer development. On the other hand, tumor suppressor genes are those that must be removed from the genotype or downregulated to switch normal cells into malignant.

The first step towards cancer development starts when a cell undergoes a mutation in one of these genes and for any reason the machinery which was supposed to eliminate this cell through the apoptotic program fails in its function. This occurs because the mentioned machinery is not hundred percent efficient. Notwithstanding, this fact does not mean all cells that evade this natural barrier to defective cells lead to cancer formation. Most of the cells that elude the machinery either have minor or neuter changes in chromosomes —mutations in genes that do not jeopardize cell integrity[1]— or the alterations are so severe that the cell is not

[1] The mutated genes may be the target of future mutations. For example, one of these changes might be a replication of a gene. It would be a neuter mutation, but in the future, if mutated another time, it would not imply inviability for function loss, because its previous role would be maintained by the other gene (the copy).

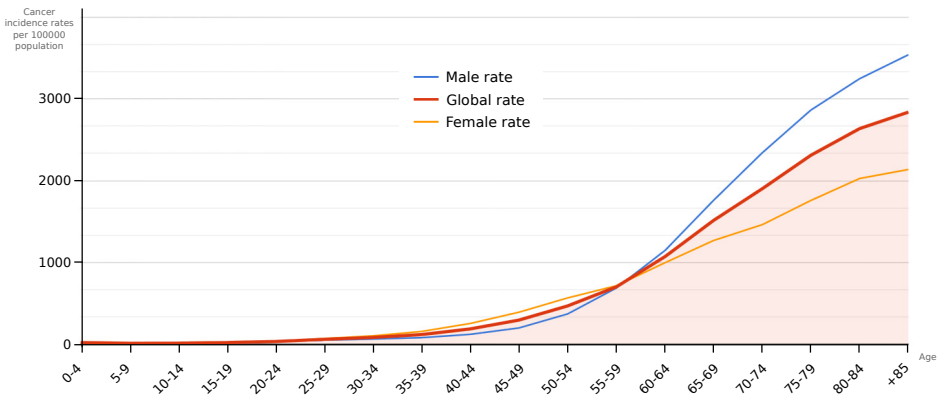

Figure 1.5. Cancer incidence as a function of age. *The incidence increases drastically with age, both in women and men, illustrating that many mutations accumulated along the years are necessary to develop cancer. (Data source: Cancer Research UK, 2015)*

viable and it is doomed to die. However, in the rare cases a mutation results in a viable cell with altered functions or characteristics it may suppose a step towards evolution or a step towards a disease like cancer.

The order of magnitude of the number of mutations that an individual may suffer through its lifespan is 10^{10} (Alberts *et al.*, 2007). The probability that one of these mutations affects the machinery that controls cell cycle is so high that, if only one mutation were required to develop cancer, we would be non-viable organisms. However, carcinogenesis is a multi-step process that usually takes a long time —years or decades— to be fully completed because normal cells only acquire a malignant phenotype through the accumulation of several mutations (Loeb *et al.*, 2003). For example, an individual who has been exposed to exogenous risk factors may develop clinically detectable cancer 20 years after[2]. In fact, many cancers never develop, because carcinogenesis starts late in the life of an individual, who may die first due to other reasons. It is remarkable that as life expectancy has elongated in the last centuries, cancer incidence has increased, demonstrating thus that aging is a cancer risk factor. Figure 1.5 evidences this fact.

For these reasons, Hanahan and Weinberg in the superb series of papers Hanahan and Weinberg (2000, 2011) highlighted that one of the main enabling characteristics to develop cancer is genome instability and mutation of cells. They also added to these characteristics the ability of tumors to promote inflammation and the aid from the recruited cells of the tumor micro-environment. The aim of these papers was to collect all the capabilities that cells must (at least) acquire through

[2]Cancers originated form endogenous factors usually take less time to develop.

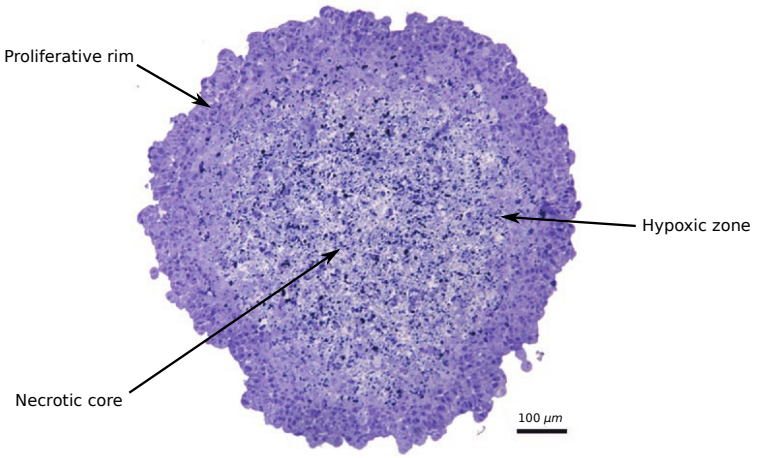

Figure 1.6. Section of an avascular tumor. *A non-invasive avascular tumor reaches a stable configuration with three main distinguished regions: The proliferative rim, the hypoxic zone, and the necrotic core. (Adapted from Yu* et al.*, 2004)*

mutations to become malignant. They called them *The Hallmarks of Cancer* and are the following: Sustaining proliferative signaling, evading growth suppressors, resisting cell death, enabling replicative immortality, inducing angiogenesis, activating invasion and metastasis, reprogramming of energy metabolism, and evading immune destruction. A brief description of them may be found in appendix B.

The stages of tumor growth As a result of carcinogenesis, there is a viable mutated cell, often called the *renegade cell* (Weinberg, 1998), which has acquired partially or totally one or more hallmarks. The cell and its daughters proliferate generating clonal expansions that inherit the hallmarks. The same process may be repeated triggered by carcinogenic agents leading to increased malignant subgroups of cells, each of them with different gathered traits. Thus, a heterogeneous mass of aberrant cells originates a tumor.

Tumor growth may be understood as a multistage process. For many tumors, the first of these stages is avascular growth. At this stage, the tumor relies on diffusion mechanisms to get nutrients and to remove the waste products of the cell activity through nearby blood and lymph vessels. However, as the tumor grows, diffusion mechanisms become insufficient to maintain the high proliferation rate of tumor cells. At this point, the tumor usually resembles a spheroid where those cells located far from the vessels, that is towards the center of the spheroid, enter non-proliferative hypoxic states or die from anoxia, starvation, or metabolic poisoning.

As a consequence, solid avascular tumors present a characteristic cell-layered configuration, as shown in figure 1.6. The outermost cells form a thin layer (2 to 3 cells wide), called the *proliferative rim*, where tumor cells have access to nutrient delivered by pre-existent, extratumoral capillaries. This layer envelops the so-called *hypoxic zone*, where the amount of nourishment is above a deadly threshold, but it is not enough for cell proliferation. Those cells in the hypoxic zone enter a quiescent state, only altered when the levels of nutrients vary. Finally, if the tumor is big enough, there is no means for the cells at its core to obtain nutrients. These cells necrose[3] and form a *necrotic core*. Contrary to apoptosis, necrosis generates toxic wastes and, because there is no means to remove the wastes, the toxicity promotes malignancy or necrosis in the surrounding cells. Hence, diffusion-limited growth imposes a threshold in the maximum diameter of an avascular tumor (usually between 1 and 2 mm), for which the cell subdivision rate at the proliferative rim is balanced with cell death rate at the necrotic core (Folkman, 1971). The tumor may be years or decades immersed in the avascular stage (Folkman and Kalluri, 1984) without causing any harm to the host tissue.

Eventually, a tumor cell may find a way to access nutrients and to eliminate wastes. One of these ways (first hypothesized by Folkman, 1971) is to create its own blood supply through a process called angiogenesis: the creation of new capillaries from pre-existing ones. The genomic instability of tumor cells may lead to daughter cells that have gained the ability to control the balance of angiogenic factors (one of the above-mentioned hallmarks), for example under hypoxic conditions. As a consequence, the tumor may overcome the size-limited avascular growth and enter the so-called vascular stage. This step, usually called the *angiogenesis switch* (Bergers and Benjamin, 2003; Folkman and Kalluri, 1984), is often related to a malignant state of the tumor, as cell proliferation is no longer limited and cells may enter the bloodstream and migrate to any part of the body, attaining the tumor invasive-metastatic stage. Due to this key role played by angiogenesis in tumor growth, we anticipate here that controlling angiogenesis is the aim of some cancer treatments: the antiangiogenic therapies. Another way through which tumors get access to nutrients is by co-opting the pre-existing vessels, that is, cancerous cells migrate towards vessels and proliferate around them. Usually, the high pressure that the cells exert produces the collapse of the vessel, returning thus the tumor to an avascular stage.

Invasion and metastasis is usually the last step of tumor growth and typically the cause of death. It is also the most complex one, as cancer cells must survive in alien environments from where they were originated and for long times in many cases. To achieve this stage, as shown in figure 1.7, cells undergo the so called

[3] Necrosis: It is the premature death of cells caused by external factors. In contrast to apoptosis, which is a naturally occurring cause of cellular death, necrosis is almost always detrimental.

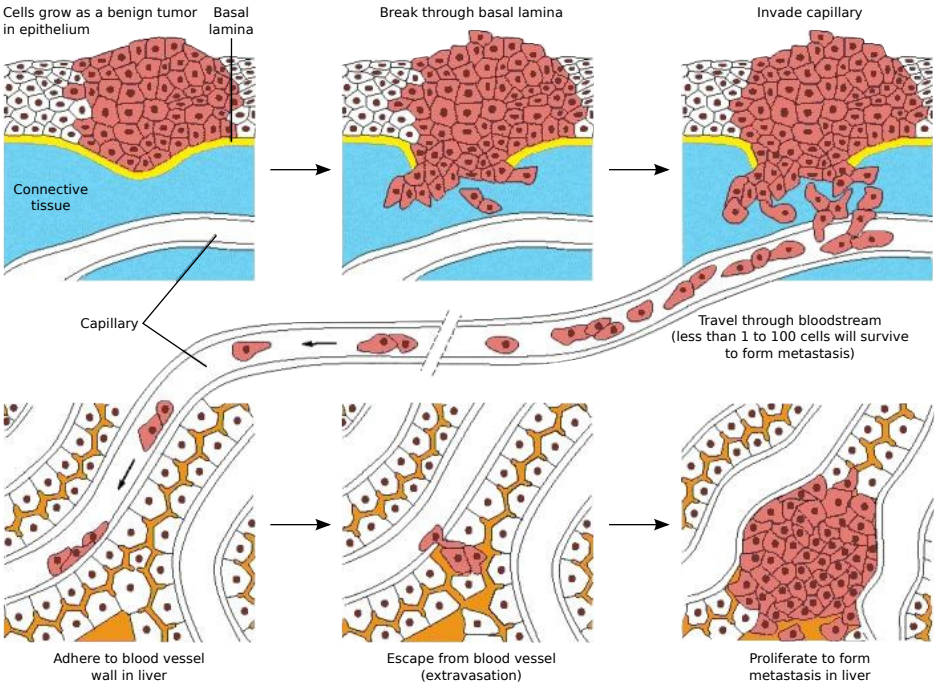

Figure 1.7. Invasion and metastasis. *Tumor cells may achieve the ability to break through the basal lamina that envelopes all the tissues and colonize the adjacent ones. They may also enter the blood flow and spread to distant tissues, generating secondary tumors or metastases. (Reproduced from Alberts* et al.*, 2007)*

invasion-metastasis cascade (Fidler, 2003; Talmadge and Fidler, 2010), which consists of the following steps:

- Intravasation: Cancer cells enter the blood and lymphatic vessels.
- Dissemination: The circulatory system transports cancer cells passively throughout the organism. Cancer cells may stay dormant in the blood stream for long times without producing any harm.
- Extravasation: Cancer cells escape from the vessels into the other distant tissues.
- Micro-metastasis: Once outside the vessels, cancer cells form small nodules.
- Colonization: Micro-metastasis can only grow further to form macroscopic tumors if they are able to survive and proliferate in their new emplacement. To do so they sequester or enslave the cells that form their new tumor

micro-environment.

Tumor stroma One of the changes in the way cancer is understood nowadays is to consider tumors composed, not just by the cancerous cells, but also by their micro-environments. If a tumor spreads beyond the vascular steady phase it is due to the recruitment of the neighboring cells which are present in the extracellular matrix (ECM). These cells are not malignant *per se*, but tumors use them for their own purposes, commonly attracting and controlling them through signaling. Generally, the tumor-recruited cells are referred to as *tumor stroma*, because they are part of the supporting normal tissues.

As shown in figure 1.8, the tumor stroma is composed, at least, by the following elements:

- Cancer cells: They do not form a homogeneous group, since every lineage is doted with different traits (the aforementioned hallmarks and characteristics). For example, figure 1.8 not only shows cancer cells, but also invasive and stem cancer cells.
- Cells associated to newly formed blood and lymph vessels: These are essentially the endothelial cells that line the vessels acting as the blood or lymph physical barrier and the coverage cells that enwrap the endothelial cells and provide structural support to the vessels. Both types of cells are recruited by tumors to satisfy their nutrient needs.
- Activated fibroblasts or cancer-associated fibroblasts: In this category, two types of fibroblasts are included, namely, reprogrammed variants of normal fibroblastic cells and myofibroblasts. It has been demonstrated that tumors use them to enhance proliferation, angiogenesis, invasion, and metastasis.
- Inflammatory infiltrates: They develop several roles in cancer, being the most prominent their labor in cleaning death cells and debris.

The realization of the key role played by the tumor stroma in cancer development has implied a big step in understanding this disease. What is more, the core of some new cancer therapies derived from the regulation of the cancer stroma. For example, as explained below, antiangiogenic therapy aims to control the development of vessels that form part of the malignant stroma. Also, some treatment fails may be attributed to the reductionist view of targeting only cancer cells or only a sub-type of them.

The main treatments Currently, there are several treatments, which can be grouped as follows:

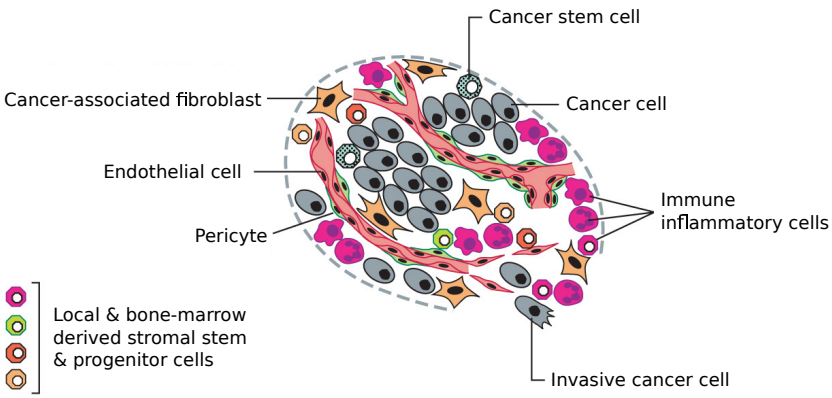

Figure 1.8. Tumor stroma. *Cancer cells recruit other cells from their micro-environment to form the tumor stroma. This stroma includes cancer cells, cells associated to newly formed vessels, activated fibroblasts, and inflammatory infiltrates. (Reproduced from Hanahan and Weinberg, 2011)*

- **Surgery**: It is the removal of the tumor (and some surrounding tissue) using surgical procedures. This treatment is used for small tumors and, despite its invasiveness, it has the advantage of being highly localized, minimizing side effects. However, as the contours of the tumor are not well defined, there can always remain cancerous cells in the tissue which are very likely to regrow.

- **Radiation therapy**: This treatment is based on the fact that many of the cancer cells have reduced their ability to repair DNA. Therefore, when exposed to radiation, the DNA is altered, cells cannot repair it, and they die. This treatment is relatively localized, but affects a significant number of healthy cells.

- **Chemotherapy**: It uses one of the features that distinguish cancer cells from normal cells: Their high proliferation rate. Chemotherapy usually interrupts one or more of the phases of the cell cycle or alters its external conditions, so that proliferating cells fail to reproduce and die. It is a non-localized treatment, thus it can affect any cell in the body, specially those that multiply rapidly as the cells of nails and hair.

- **Immunotherapy**: It consists of stimulating the immune system to recognize cancer cells, hence, letting the body itself be the one that removes them. The most common side effects are skin reactions caused by the injections, flu-like symptoms, or allergic reactions.

- **Targeted therapies**: Those therapies that focus on specific proteins by binding to the surface cell receptors, disrupting pathways, or interrupting somehow specific processes that occur especially or to a greater extent in cancer cells. The drugs for some targets are hard to develop and many of them can cause side effects. In addition, cancer cells can become resistant to such drugs.
- **Hormone therapy**: Slows or stops the growth of cancer that uses hormones to grow in some type of cancer, as prostate or breast cancer. The side effects of these therapies are related to the particular hormone that is blocked or interfered.
- **Antiangiogenic therapy**: They prevent the formation of new vessels required for tumor growth. The importance of angiogenesis in processes like wound healing, heart and kidney functions, fetal development, and reproduction lead to side effects that include problems when bleeding, clots in vessels, hypertension, and protein in the urine.
- **Other treatments**: Biological response modifiers, vaccines, stem cell transplant, and complementary and alternative medicines.

Usually these treatments are not used exclusively, but combined. For example, radiation as adjuvant therapy[4] to surgery to eliminate those cells that otherwise could be left by the surgeon; neo-adjuvant[5] chemotherapy before radiation to make cancer cells more sensitive to radiation; or concomitant radiation and chemotherapy, to ensure the elimination of all cancer cells. Further information about cancer treatments can be found in (Camidge and Jodrell, 2005; Fentiman, 2005; Jackson and Porte, 2005; Kiltie, 2005).

Despite all the effort made in research, all of these treatments are far from being definitive, but palliative in many cases, and some of them entail many side effects. Besides, the therapy chosen for an individual is based on the physicians experience with previous patients and on the mean treatment response in the clinical phases of the treatment, that is, the diagnostic paradigm. However, an individual may be highly responsive to a therapy rejected *a priori* according to those criteria, or *vice versa*. That is why a shift towards the new medical model patient-specific, predictive medicine is gaining momentum in the last decade. Its aim is to provide the physicians with another tool to help them assign a treatment to a patient, based on predictive mathematical models which are fed with data from the specific patient that will be treated. This model has been successfully applied to

[4] An adjuvant therapy is a therapy given in addition to the primary, main, or initial one to maximize its effectiveness.

[5] A neo-adjuvant therapy is the one given as a first step to shrink the tumor before the main treatment.

other medical disorders, as in cardiovascular disease, and it is only starting to be developed for cancer. As shown later in this chapter, the mathematical oncology community is doing a lot of effort to develop mathematical models for cancer growth and spread and, in particular, in blood vessel growth and angiogenesis to model the angiogenic switch and its consequences.

Blood vessel growth. Angiogenesis

The circulatory system One of the most important systems in the body is the circulatory system, since its main function is to deliver and collect the vast majority of molecules that sustain cell life. It serves as a means of oxygen and nutrient delivery, waste products' disposal from the cell cycle, long distance signaling transport, such as hormones and immune surveillance. In addition, it plays a central role in organogenesis. The circulatory system is often seen as composed by the cardiovascular system and the lymphatic system. The major components of the former are the blood, a fluid chiefly consisting of platelets, blood cells, and plasma; the heart, a muscle responsible for pumping blood; and the blood vessels, the ducts that span the body and through which blood flows. The lymphatic system is also formed by a fluid, the lymph, and by vessels, the lymphatic vessels. Its role is more related to the immune system.

All cells in our body, apart from rare exceptions such as corneal cells, rely on the circulatory system for survival. Thus, it is necessary for the system to span the whole body. This is only achieved through a strict double tree-like hierarchy (figure 1.9). Heart-pumped blood is transported through large-caliber, high-pressurized arteries to the main parts of the body. The blood is then distributed by progressively smaller vessels, namely, medium arteries and arterioles, until it reaches the capillary beds. There, the tree-like hierarchy is replaced by a lattice-like structure of capillaries, prioritizing thus delivery over transport. It is in the capillaries, the thinner tubes of the circulatory system, where most of the molecular and cellular exchange is performed. The molecules leak out (extravasate) and enter (intravasate) through the permeable walls of these vessels. Once a molecule is outside them, it reaches the cells mainly by diffusion (Alberts *et al.*, 2007). This process limits the molecules scope to 100 to 200 micrometers away from the extravasation point. Therefore, every cell should be at that maximum distance from a capillary; otherwise it would enter in a hypoxia state. Put in other words, the vessel network has to be dense enough to allow access to every single cell. The waste and other byproducts of these cells are collected by venules that start the second tree-like hierarchy (with the opposite direction to the former). Venules discharge into medium-caliber veins, that in turn flow into large veins. Note that a great proportion of the waste products as well as immune cells return through

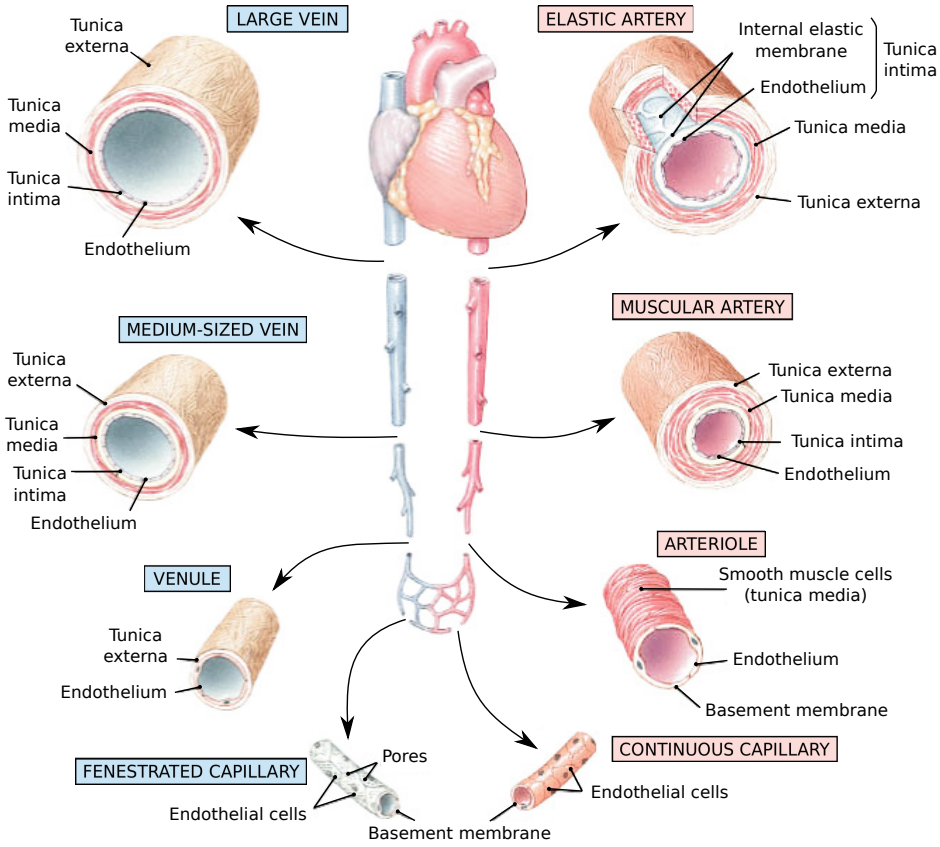

Figure 1.9. The circulatory system. *(Reproduced from Marieb, 2003)*

the lymphatic system.

The vessels of the circulatory system are formed by different layers, whose number and purpose varies with the caliber and function of the vessel (see figure 1.9). The innermost layer, the endothelium, is formed by the main component of the vascular system, as well as of the lymphatic system: the endothelial cells. These cells line the blood vessels forming a tube, the lumen, and are usually at a quiescent state. Blood vessels are enveloped by pericytes whose main function is to stabilize endothelial cells, but also collaborate in other activities such as regulating the permeability in certain organs (eg. blood-brain barrier). Pericytes and endothelial cells share a common basement membrane and the three of them (and occasionally smooth muscle cells) are the main components of capillaries. Greater vessels are formed

by increasing number of layers that provide them with support to accommodate the dynamic loads of the flowing blood.

Mechanisms of vessel growth Functions carried out by the circulatory system are essential to sustain life, therefore the generation and maintenance of such an intricate and complex system is vital. It is during embryogenesis when the blood and the blood vessel network develops. First, through a process known as vasculogenesis, endothelial cell precursors[6] migrate from the bone marrow towards the corresponding emplacement and differentiate into endothelial or blood cells, forming a plexus. Afterwards, the vascular bed is extended and remodeled via several mechanisms such as angiogenesis (Carmeliet, 2005) and intussusception or splitting angiogenesis (Kurz *et al.*, 2003). Then, in adult life, physiological vasculogenesis, angiogenesis, or intussusception appear at very specific, tightly regulated events and only for a short time span, usually days or weeks. Examples of such events are the female reproductive cycle or tissue repair, as in the wound healing process shown in figure 1.10. Due to the importance of the vascular system, it is not surprising that defective maintenance of blood vessels or deregulation of its growth are associated with a number of diseases. When there is an inadequate vessel maintenance or a downregulated growth, the absence of blood vessels may affect the tissue repairing program, as in ischemic chronic wounds in diseases such as stroke, obesity-associated disorders, or myocardial infarction. On the other hand, an abnormal remodeling or upregulated growth, may promote inflammatory diseases, age-related macular degeneration, or cancer, to name but a few. For a longer list of diseases related to blood vessel maintenance and formation, the reader is referred to Carmeliet and Jain (2000). In particular, in cancer, tumors gain access to the vasculature using several mechanisms (see figure 1.11):

- Using existing blood vessels:
  - **Vessel co-option**: Cancer cells engulf existing blood vessels (Leenders *et al.*, 2002).
  - **Vessel translocation**: Vessels are attracted towards the tumor location (Kilarski *et al.*, 2009).
- Creating new blood vessels:
  - **Angiogenesis**: It is the formation of new blood vessels from the preexisting ones.
  - **Postnatal vasculogenesis**: It is the formation of new blood vessels

[6] Endothelial precursor cells: They are one of the three types of stem cells to be found in bone marrow.

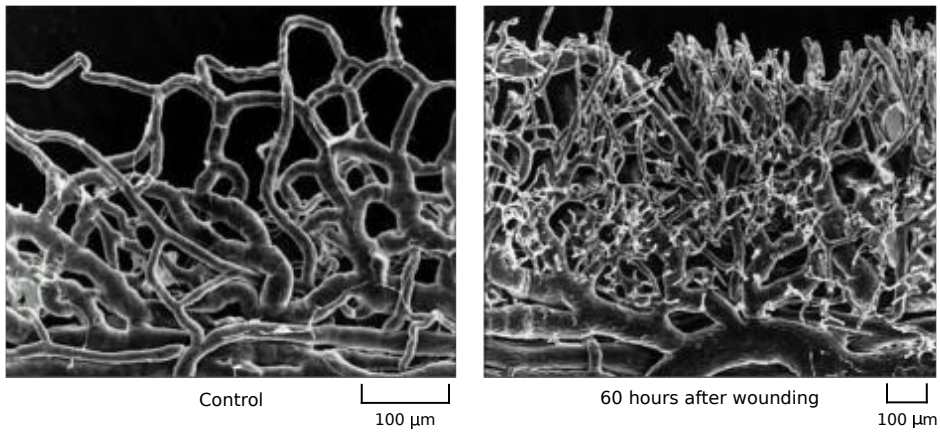

Figure 1.10. New capillary formation in response to wounding. *In the left panel an image of the control situation is shown. The right one illustrates the blood vessel configuration sixty hours after wounding.(Reproduced from Alberts* et al.*, 2007)*

through the migration from bone-marrow and differentiation of endothelial precursor cells.

- **Intussuception or splitting angiogenesis**: It is the splitting of one vessel into two through the formation of a transluminal pillar and its extension (Burri *et al.*, 2004; Kurz *et al.*, 2003).
- **Mosaic vessel formation**: It is the incorporation of cancer cells among the endothelial cells of the vessel walls.
- **Vasculogenic mimicry**: It is the transdifferentiation of cancer cells into endothelial cells.

As it might be expected, tumors may exploit several of these mechanisms along their growth, even at the same time. However, among all of them, angiogenesis is assumed to account for a substantial fraction of vessel growth and it will be the objective of study here. It is worth noting that there is not full agreement between these terms and some authors use *angiogenesis* as a general term which includes all these mechanisms of vessel creation and growth. Here, however, we will use it as the specific term defined above.

The process of tumor angiogenesis Endothelial cell quiescence is maintained by a tightly controlled balance between chemicals that promote angiogenesis (pro-angiogenic factors) and those that inhibit angiogenesis (anti-angiogenic factors).

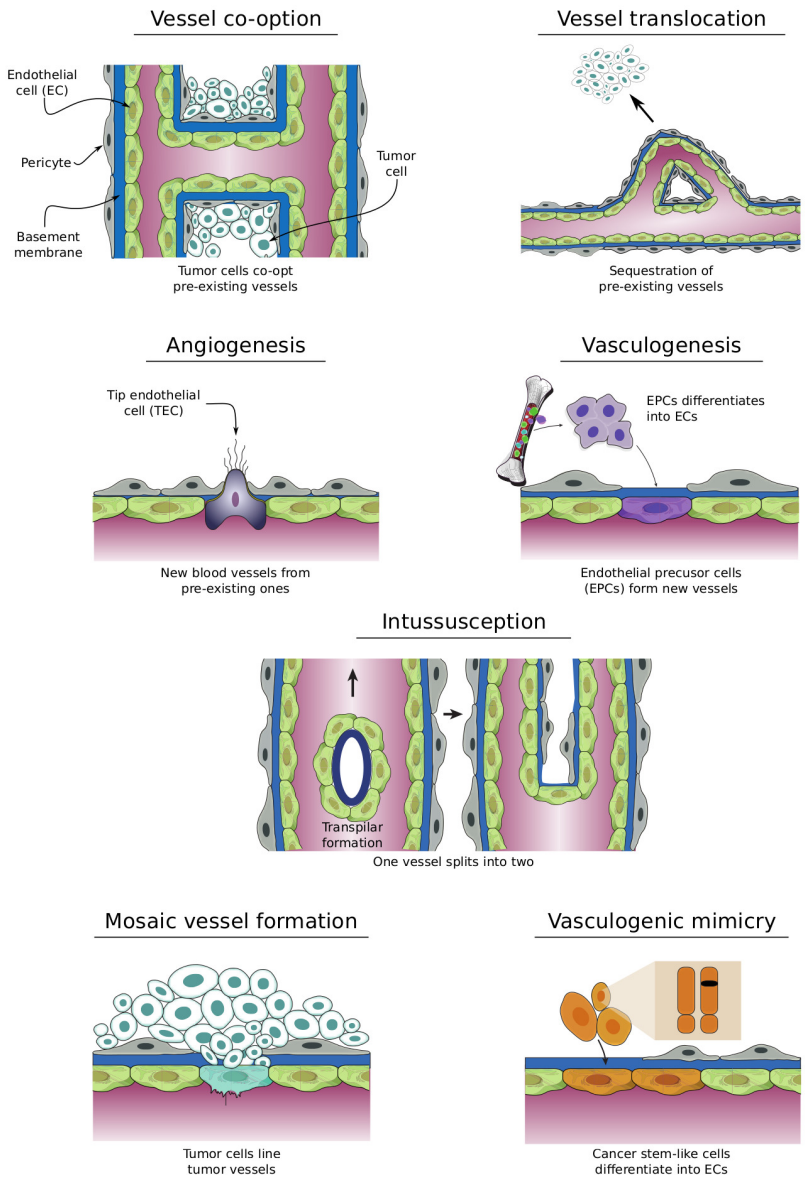

Figure 1.11. Mechanisms of tumor neovascularization. *Tumor cells may gain access to blood vessels using different mechanisms and usually through a combination of them. (Adapted from Carmeliet and Jain, 2011)*

Despite this tight control, tumors are able to trigger angiogenesis. Tumor angiogenesis is a complex phenomenon governed by intertwined molecular mechanisms whose main components are the so-called tumor angiogenic factors (TAFs). The latter are chiefly soluble molecules, released by hypoxic cancer cells and their malignant micro-environment, and membrane receptors in tumor stroma cells. There are more than twelve known of such molecules and many others still under research. In addition, there are complex interplays among them that are still being disentangled and started to be comprehended. More information on TAFs may be found by the interested reader on appendix C, where we detail the sources, receptors, and main functions of the best well-known TAFs.

Angiogenesis, as shown in figure 1.12, may be described as a multistage process composed of the following steps: activation, initiation of the sprout, growth of the capillary, and finalization of the process (Carmeliet and Jain, 2011; Figg and Folkman, 2011a; Potente *et al.*, 2011; Weis and Cheresh, 2011). As said above, the activation starts when the equilibrium of the pro- and anti-angiogenic factors is disturbed near the endothelial cells that line the blood vessels. The disequilibrium may be caused by the arrival of tumor pro-angiogenic factor molecules that diffuse from the hypoxic tumor cells and bind to the receptors of the endothelial cells. Well-known examples of these factors are vascular endothelial growth factor (VEGF), fibroblast growth factor (FGF), angiopoietin 2 (Ang-2), or chemokines. Those cells affected by these tumor angiogenic factors are activated to become the leading cells of the incipient sprout: the tip endothelial cells (TECs). However, there is a mechanism, called *lateral inhibition*, that prevents the formation of several sprouts in the same region (Hellström *et al.*, 2007): even though several neighboring endothelial cells may sense the disequilibrium of angiogenic factors, only one of them changes its phenotype from quiescent to a migratory one and becomes a TEC. The remaining cells, instead, change their phenotype to a proliferative one. The latter, referred to as stalk endothelial cells (SECs), will play a role in the elongation of the sprout, as explained below. The key molecular players of lateral inhibition are the Delta-like ligand 4 (Dll-4) and its receptor Notch-1. In brief, TAFs activate the expression of Dll-4 which binds to the membrane Notch-1 receptors of the adjacent cells. Those cells whose Notch-1 receptors get activated become SECs and only one, the first to express Dll-4, becomes a TEC. By the end of the activation phase, the endothelial cells have changed their phenotype and are prepared to create a new sprout. They are, however, still confined by the mural cells and the basement membrane.

The initiation of the sprouts starts with the liberation of endothelial cells. First, the pericytes that enwrap the vessels, by means of Ang-2, detach from the region of the incipient sprout. Then, tumor stromal cells release matrix metalloproteinases (MMPs) that produce a proteolytic breakdown of the basement membrane that

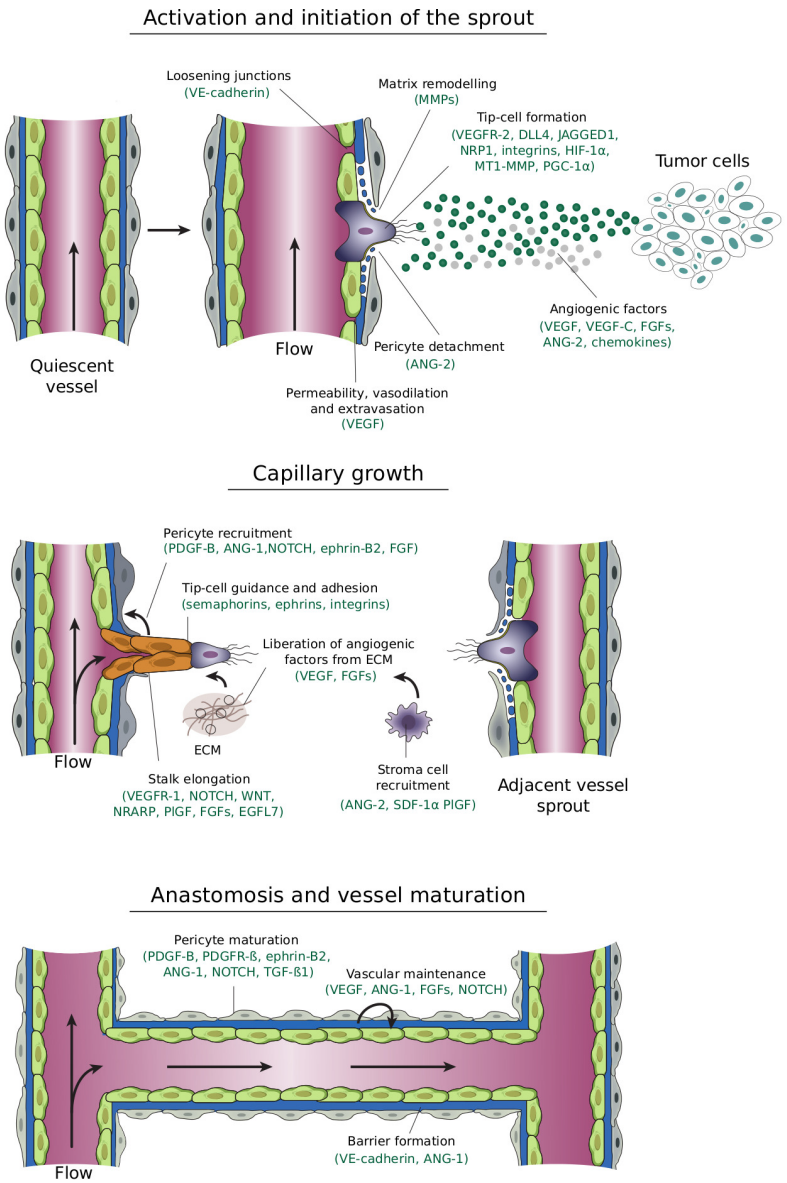

Figure 1.12. The angiogenic process. *Angiogenesis starts with the activation of tip endothelial cells by tumor angiogenic factors. The incipient sprout, once liberated from the capillary coverage, grows towards the source of tumor angiogenic factors. The capillary elongates by the proliferation of stalk endothelial cells. The growth continues until two capillaries anastomose. The new vessel maturates and blood flows though it irrigating the tissue.*

envelopes the endothelial cells. MMPs also liberate cleaved TAFs from the extracellular matrix. Once the basement membrane is degraded, the endothelial cells loosen their junctions (VE-Cadherin), the nascent vessel dilates, and a provisional ECM is laid out to facilitate migration. TECs develop slender cytoplasmic protrusions, called *filopodia*, rich in receptors that enhance the detection of the stimuli that guide the migration (Gerhardt *et al.*, 2003). The adjoining SECs follow the first movements of the TEC out of the capillary.

The growth of the capillary includes the guidance of the TECs and the elongation of the capillary. TECs are guided at least by three different mechanisms, namely, chemotaxis, haptotaxis, and mechanotaxis. The first refers to the movement towards a gradient of soluble molecules, in this case, TAFs such as VEGF or FGF. Haptotaxis and mechanotaxis also contribute to establish the growth direction through focal adhesion sites and the mechanical forces, respectively. Lately, it has been hypothesized that endothelial cells compete for the TEC position as the capillary grows (Jakobsson *et al.*, 2010). Behind the TEC, SECs are continuously dividing stimulated by angiogenic factors, promoting thus the elongation of the capillary. Meanwhile, the endothelial cells form a lumen, allowing the blood to flow through them. Furthermore, they attract smooth muscle cells and pericytes, that provide support to the capillary. This last process, called maturation, is usually defective in tumor-induced capillaries.

The growth continues until the lumina of two capillaries fuse forming a loop that allows blood to flow. This phenomenon is called *anastomosis*. When this happens, the endothelial cells revert their phenotype to a quiescent one (also called *phalanx* phenotype) and recruit more pericytes that help to maintain this phenotype through signaling. Also, both types of cells create a shared basement membrane and the endothelial cells reestablish their junctions. The growth may also be stopped if the driving stimuli end. In tumor angiogenesis, this point is reached when the hypoxic cancerous cells are supplied with enough nutrients and oxygen as to become normoxic. The capillaries promoted by tumors are usually slightly different from those created under normal circumstances, as explained below. Specifically, they become dependent on TAF presence, thus, when the stimuli are no longer present, the capillaries regress. In addition, the high pressure inside the tumor combined with the weakness of the vessels may make them collapse. Finally, the regrowth of the capillaries is common in tumor development and it is done at a faster speed aided by the scaffold of basal lamina left behind by the regression of the vessels (Mancuso *et al.*, 2006).

Characteristics of tumor vessels As a result of the angiogenesis switch, the once growth-stable avascular tumor has turned into an unstable, vascular, and malignant tumor pervaded with capillaries. However, as shown in figure 1.13, the

new capillaries are defective in several senses (Baluk *et al.*, 2005). Overexpression of pro-angiogenic factors and/or underexpression of anti-angiogenic factors lead to the formation of a new vasculature that is structurally abnormal. At the anatomical level, the precocious and disorganized capillary sprouting and endothelial cell proliferation, combined with localized events of regression and regrowth, plus the increased vascular shunting and collapse result in a marked loose of the strict hierarchy that characterizes the normal vasculature. In addition, capillaries present saccular regions with haphazard patterns of interconnections. At the cellular level, endothelial cells show an irregular and disorganized morphology, that even present long cytoplasmatic projections that transverse the capillary lumen. The association between endothelial cells is weak, leading to loose connections between cells. The perivascular cells that ensheathe normal vessels is loosely attached or even absent in tumor-induced vessels. The vascular membrane is unusually thick in some tumors or very thin or absent on others.

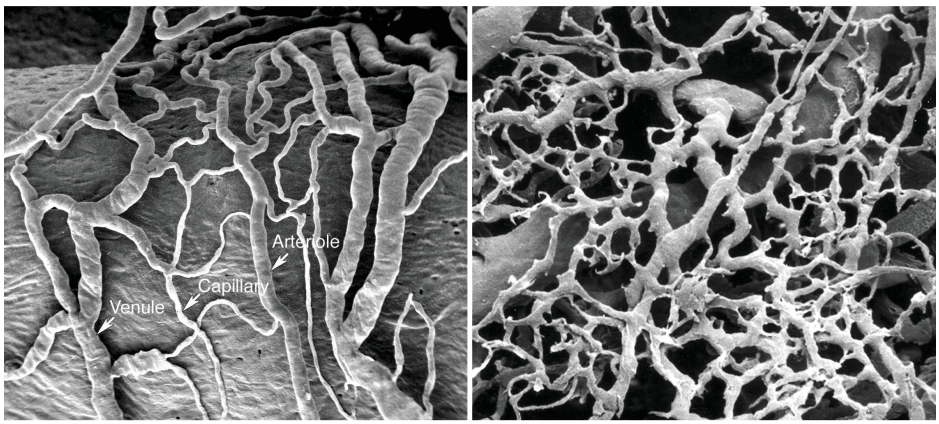

Figure 1.13. Physiological versus tumor vessels. *Unlike vessels created under physiological conditions (left panel), tumor vessels (right panel) show a clear loss of the vessel hierarchy and structure, a marked aberrant morphology, and disorganized and abundant sprouting. (Reproduced from McDonald and Choyke, 2003)*

These anatomical and cellular abnormalities have drastic influences at the functional levels of the new vasculature:

- **Heterogeneity in blood flow.** Structural defects promote spatial and temporal heterogeneity blood flow. Furthermore, the flow is often redundant in closed and blind loops.
- **High interstitial pressure.** Defects at the cellular levels confer leakiness to the vasculature. Thus, the intravascular fluids and plasma easily extravasate,

increasing the interstitial pressure. In addition, the absence of functional intratumoral lymphatic vessels results in impaired clearance of the fluid. The high interstitial pressure hinders the delivery of systemically administered therapies.

- **Regional hypoxia.** Tumors present local regions of hypoxia due to several factors such as vascular collapse, regression and regrowth events, regional poor perfusion, and high interstitial pressure. As cancer cells are more resistant to hypoxia than normal cells, hypoxia promotes their malignant phenotype, facilitating, for instance, their ability to form metastasis.
- **Acidosis.** It is caused by the byproducts of necrosis that cannot leave the tumor because of the faulty transport functionality of the vasculature. Acidosis compromises the cytotoxic functions of immune cells that infiltrate the tumor, enhancing the malignant phenotype.

Antiangiogenic treatments Since Folkman hypothesized the angiogenic switch, antiangiogenic therapy has been a promising treatment against cancer. In the last decades, different kinds of inhibitors of angiogenesis have been developed, being most of them VEGF blockers or multi-targeted tirosine-kinase receptor inhibitors (see appendix C). Some of them, as bevacizumav or sorafeniv, have even been approved for clinical use against specific types of cancer and usually in combination with chemotherapy.

However, despite their success in pre-clinical trials, the translation of most angiogenic inhibitors to antiangiogenic treatments in humans, that is, to clinical practice, has not resulted as expected: although in some cases the disease-free progression has increased, the overall survival did not. There are many hypotheses that try to explain this general failure. Most of these hypotheses are based on the differences between the pre-clinical and the clinical settings in terms of simplicity of the former compared to the latter, the unknowns in dose amount, or the dose timing. Also, some patients are refractory to the treatment and many others develop resistance to them. For example, Dvorak and colleagues (Nagy and Dvorak, 2012) have detected that anti-VEGF therapy is effective only at certain stage of vessel growth (see figure 1.14a), and is refractory otherwise. Recently, Jain and co-workers have hypothesized that the little efficacy of antiangiogenic therapies may be due to an excessive pruning of the vasculature (Goel *et al.*, 2011; Jain, 2001, 2005). High doses or treatments over long time spans prune the vasculature too much and promote hypoxia in the tumor, which in turn increases the malignancy of tumor cells and their resistance to radiotherapy and chemotherapy. Thus, excessively pruning leads to more aggressive forms of cancer. They propose that the aim of antiangiongenic therapy should be instead the normalization of

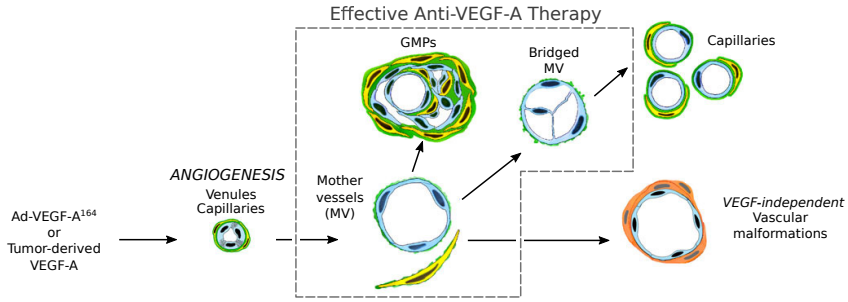

(a) *Antiangiogenic therapy may be only effective at certain stages of capillary growth. (Adapted from Nagy and Dvorak, 2012)*

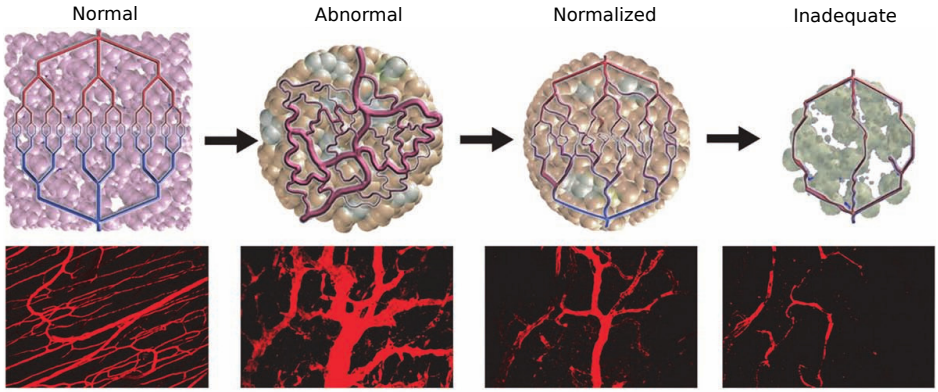

(b) *Normalizing the vasculature through antiangiogenic inhibitors, instead of excessive pruning, may lead to better vascularized tumors, which, in turn, may lead to better distribution of systemic therapies and to remove hypoxic regions that promote malignancy. (Adapted from Jain, 2005)*

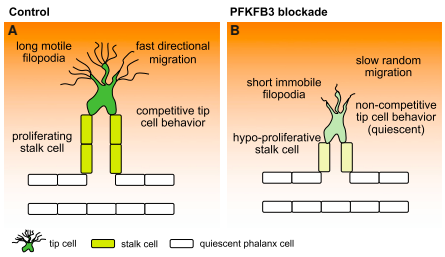

(c) *Targeting the metabolic differences of differentiated endothelial cells. (Reproduced from Bock* et al.*, 2013)*

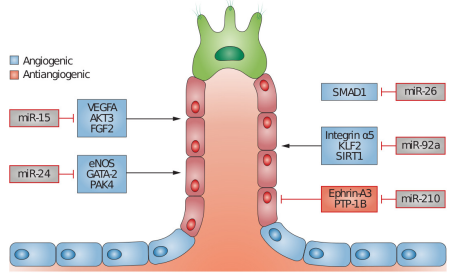

(d) *Targeting microRNAs as an alternative to VEGF inhibitors. (Reproduced from Boon and Dimmeler, 2015)*

Figure 1.14. New approaches to antiangiogenic therapies.

the vasculature, as shown in figure 1.14b, such that the adjuvant therapies that are administered systemically are not impaired by a defective vasculature. Finally, most antiangiogenic therapies focus on the inhibition of VEGF and, although the inhibition may be successful, cancer cells may get vascularized through other molecular pathways or even through other vascularization mechanisms, such as vasculogenesis. Several researchers are working on new molecular targets and principles to overcome this problem. For example, figure 1.14c shows how the different metabolisms of endothelial cells with respect the remaining cells of the body may be a new target to stop angiogenesis. Other examples include work with microRNAs (figure 1.14d) or immunotherapy combined with antiangiogenic treatments.

1.2.2 Mathematical models of tumor-induced angiogenesis

This section reviews the mathematical models that are setting the basis for predictive medicine in cancer. As there is a wide literature regarding tumor induced-angiogenesis modeling, only the most prominent models are shown here. Extensive reviews can be found in Araujo and McElwain (2004); Chaplain (1996); Chaplain and Anderson (2006); Logsdon *et al.* (2014); Lowengrub *et al.* (2010); Mantzaris *et al.* (2004); Moreira and Deutsch (2002); Oden *et al.* (2015); Qutub *et al.* (2009); Roose *et al.* (2007); Sanga *et al.* (2006); Scianna *et al.* (2013); Travasso *et al.* (2011a).

Classification of the Models

Prior to the review of the state of the art, we define some concepts that may help to classify the mathematical models. Cancer is a multiscale process, as it starts with a gene mutation and, in the last phases, may spread to other tissues. Handling every scale is a non-trivial problem for mathematical models and, in many cases, they are limited to one of the following:

- Subcellular scale: The characteristic order of magnitude for this scale is nanometers and it includes phenomena such as oncogene transcription, protein creation, signaling cascades, or mutational events.
- Cellular scale: The basic unit of this scale is the cell, that is, 10-20 μm. Examples of characteristic phenomena occurring in cancer at this scale are proliferation, apoptosis, cellular communication, and tip endothelial cell migration.

Table 1.1. Characteristics of discrete, continuous, and hybrid models.

	Continuous models	Discrete models	Hybrid models
Scale	Tissue	Cellular and subcellular	Cellular, subcellular, and tissue
Advantages	Allow to model tumor growth without spatial and temporal limits	Track cells Discrete event description	Combine the advantages of both methods
Disadvantages	Can not track individual cells Can not describe discrete events	Spatially and temporally limited	Greater complexity in the coupling

- Tissue scale: The order of magnitude of this scale is centimeters and it includes phenomena such as vascular tumor growth, angiogenesis, or adjacent tissue invasion.

In the subsequent review of the literature the models are classified, according to their mathematical abstraction of the biology, into continuous, discrete, and hybrid models. As shown in table 1.1, each type of model spans different scales. Continuous models are those that use averaged continuous fields (cell densities or volume fractions, for instance) governed by equations; generally, partial differential equations. These models are based on continuum mechanics. They are able to describe cancer from a tissue scale, but, in general, cannot track individual cells. Discrete models, on the contrary, are those which track individual cells. These models usually include cellular and subcellular scales, but are not capable of handling the tissue scale, since they are limited by computational power. There are several sub-types of discrete models. The simpler ones are *agent-based models*: Those composed by single units that represent cells which interact among them in a lattice-free space, subject to certain rules. When the space is subdivided with a lattice and each site can be only occupied by a single cell, the model sub-type is called *Cellular Automaton*. In this case the cellular shape is not taken into account and it allows the representation of a slightly larger scale. The last discrete sub-type model is the *Cellular Potts Model*, which can be thought as a generalization of the Cellular Automaton. In the Cellular Potts model each cell may be composed by several lattice locations or pixels whose states change to minimize a global energy. Finally, hybrid models benefit from the discrete and continuous models advantages, by using both of them. In particular, when there is a single description for each phase they are usually referred to as composite discrete-continuous models.

Review of the literature

Avascular tumor growth The first mathematical models for cancer, developed during the first half of the last century, focused in the avascular tumor stage and used a continuum description. These models were posed from a single macroscale point of view and modeled tumors as multicellular spheroids. They were cell population models whose objective was to study tumor growth dynamics. One of those models was posed by Mayneord (1932). There, using a continuous mathematical model, he showed that the linear growth dynamics of rat sarcomas observed in experiments (instead the theoretical exponential growth) could be explained assuming that not all cells of the tumor proliferated, but only those cells located in the exterior border of the tumor (the proliferative rim). These population models evolved to include diffusion processes. For example, Burton (1966) developed a model for solid tumor in which the growth dynamics were controlled by oxygen diffusion. As a result he derived a Gompertzian tumor growth law. Laird (1964) showed that this Gompertzian law fitted with a variety of transplanted tumors.

In the 1970's, the angiogenesis switch hypothesis by Folkman (1971) led to the development of avascular models that tried to explain why some tumors stay dormant. It also led to the study of angiogenesis alone and coupled with vascular tumors, as explained in next sections. Many authors proposed models based on growth inhibitors to explain the referred avascular dormant tumors. One of the most notable was posed by Greenspan in 1972 and 1974 (Greenspan, 1972, 1974). He proposed two alternative explanations for the origin of the agent that acted as growth inhibitor: Either it was produced by necrotic debris or by metabolic processes associated with the cellular growth. The most prominent models from the 1980's were from Adam and Maggelakis (Adam, 1986, 1987a,b; Adam and Maggelakis, 1989, 1990), in which they used a non-uniform growth inhibitor and obtained as a result a stable tumor with a necrotic core and a proliferating rim. In the 1990's there was an exponential growth of mathematical models for avascular tumors focused in explaining the observed features of multicellular tumor spheroids, in particular the differentiation between the necrotic core, the hypoxic zone, and the proliferative rim. Chaplain and Britton presented a predictive model to examine the steady-state profile of the growth inhibitory factor in spheroids (Chaplain and Britton, 1993), and Byrne and Chaplain studied the stability of steady, radially-symmetric solutions with respect to perturbations (Byrne, 1999; Byrne and Chaplain, 1997) by assuming the existence of the three distinct layers. However, detailed experimental investigations showed that the transitions between the three layers could be gradual, rather than sharp (Hystad and Rofstad, 1994). This led to mathematical models in which the layers were defined by continuum densities of proliferative, quiescent, and dead cells (Hinow *et al.*, 2009; Sherratt

and Chaplain, 2001). Some other models of avascular growth focus on reproducing different features, such as, for example growth saturation or cell movement (Pérez-García *et al.*, 2011; Thompson and Byrne, 1999; Ward and King, 1997, 1999). From a methodological point of view, the mixture theory has been a useful framework within the continuum modeling of avascular growth (Byrne *et al.*, 2003; Byrne and Preziosi, 2003; Preziosi and Tosin, 2009). More recently, a new approach based on the multiphase porous media mechanics theory, has also been proposed (Sciumè *et al.*, 2013a, 2014, 2013b). Another framework which has produced very relevant results is that provided by the phase-field method (Cristini *et al.*, 2009; Hawkins-Daarud *et al.*, 2013, 2012; Lima *et al.*, 2015; Oden *et al.*, 2010, 2013; Wise *et al.*, 2008). As explained later, the phase-field method is the key method of the mathematical theories developed in this thesis.

Although all the models presented until now were continuous, the literature is also rich on discrete models belonging to the class of cellular automata or agent-based methods that have tried to model avascular growth by considering cell-cell interactions, cell-matrix interactions, and the effect of the micro-environment (Boondirek *et al.*, 2010; Gerlee and Anderson, 2007; Moreira and Deutsch, 2002). Hybrid models have also been posed to study specific phenomena, such as cell adhesion (Anderson, 2005) or interactions between tumors and the immune system.

Tumor induced-angiogenesis Since the discovery of the critical role of angiogenesis in tumor progression, many researchers have tried to model angiogenesis under different assumptions. One of the most common is to consider the tumor just as a fixed source of TAF, that is, to model only the growth of capillaries without modeling the tumor. Here we review the most notable of these models, many of which were used afterwards with tumor growth models (as shown in next section).

One of the first models of angiogenesis as developed by Deakin in 1976 (Deakin, 1976). It was a continuous model consisting of two variables: The endothelial cell density and one chemical species that represented the TAF. Both variables were governed by convection-diffusion equations. Most continuous models coming later, although involving more variables and representing more phenomena, followed a similar structure. For example, in 1985, Balding and McElwain (Balding and McElwain, 1985) posed a similar continuum model which also considered one chemical species, but distinguished between tip endothelial cell concentration that migrated chemotactically following the gradient of TAF and stalk endothelial cell concentration that proliferated in the presence of TAF. Furthermore, the model included branching and anastomosis events. A decade later, Byrne and Chaplain (1995; 1996) extended Balding and McElwain's model by adding TAF consumption and secondary tip proliferation. In the same years, Chaplain and

Stuart (1993) developed a model that included many essential mechanisms of angiogenesis, which was subsequently simplified in Chaplain *et al.* (1995) to permit a deeper mathematical analysis. This analysis showed that both endothelial cell proliferation and migration were essential to angiogenesis. Figure 1.15a shows an example of a simulation of one of these first models, which were usually one dimensional.

The next step in continuum models of angiogenesis was the incorporation of haptotaxis. It came from Orme and Chaplain (1998; 1997) where, besides chemotactic migration, endothelial cells also migrate following a concentration gradient of fibronectin through the ECM (see figure 1.15b). This work studies the importance of haptotaxis versus chemotaxis and the role of fibronectin in haptotaxis. Furthermore, by altering the parameters of the model, they analyze different anti-angiogenic strategies. Anderson and Chaplain (1998b) developed a model to prove an experimental observation: If endothelial cells do not proliferate, angiogenesis does not reach the tumor and it fails to deliver the nourishment. It was a one-dimensional model including chemotaxis and haptotaxis, which was subsequently widespread to two dimensions in the first part of Anderson and Chaplain (1998a) and in Chaplain and Anderson (1999), and to more complex geometries in Valenciano and Chaplain (2004) and in Peterson *et al.* (2007), as shown in figure 1.15c. By 2000, several angiogenesis inhibitors were already discovered and quite well known. Anderson *et al.* (2000) modeled how secondary tumors remained in dormant states because already vascularized primary tumor released angiogenic inhibitors that prevented the vascularization of secondary tumors.

Continuous models keep evolving to include many other key mechanisms of angiogenesis. For example, Levine and collaborators (2001a; 2000; 2001b; 2002) developed models that included endothelial cell migration by chemotaxis (TAF) and haptotaxis (fibronectin), ECM degradation (protease enzyme), and angiogenesis inhibition (angiostatin). It required over sixty parameters to be calibrated. Plank *et al.* (2004), extended the previous models to include random walks into TEC migration. Some continuum models include mechanochemical interactions between endothelial cells and the extracellular matrix, due to the traction exerted by endothelial cells on ECM fibers when migrating, for instance Holmes and Sleeman (2000). Others even consider other mechanisms of tumor vascularization, as in Stamper *et al.* (2007), where they model vasculogenesis besides angiogenesis. One of the latest continuous models was developed by Santos-Oliveira *et al.* (2015), which is based in the phase-field method. In this work they model the traction forces exerted by tip endothelial cells and the cell-cell adhesion forces. They study how different responses of other endothelial cells to these forces alter the morphology of incipient sprouts.

Another question which appears when modeling angiogenesis with continuous

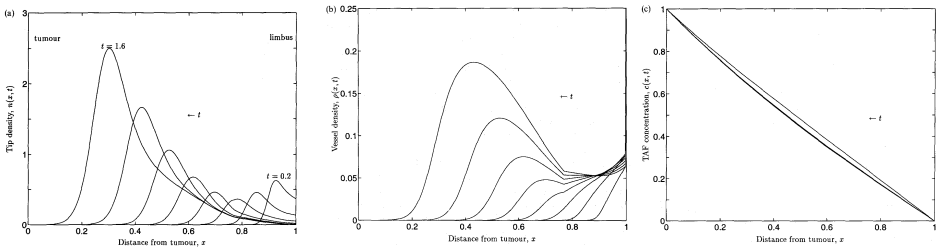

(a) *From left to right: Concentration of tip endothelial cells, endothelial cells, and tumor angiogenic factor. (Reproduced from Byrne and Chaplain, 1995)*

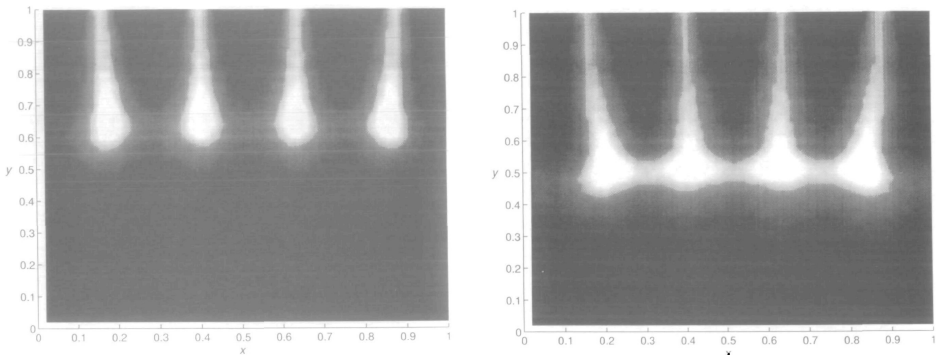

(b) *Concentration of endothelial cells forming four sprouts, before (left) and after (right) anastomoses takes place. Tip endothelial cells are guided by chemotaxis and haptotaxis. (Reproduced from Orme and Chaplain, 1997)*

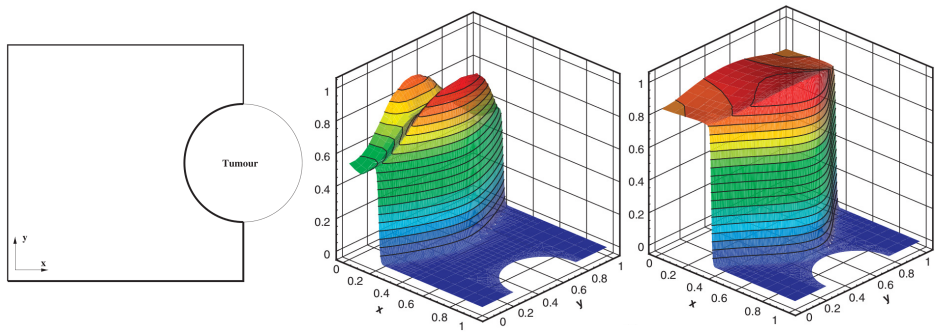

(c) *Definition of the geometry (left) and time evolution of the concentration of tip endothelial cells (middle and right) in a two dimensional model. (Reproduced from Peterson et al., 2007)*

Figure 1.15. Continuous models of tumor-induced angiogenesis.

models is the emplacement of the first endothelial cells, that is, where the activation of angiogenesis starts. In most models, this selection is imposed *a priori* by means of initial conditions. However, some authors endowed their models with different criteria to select those locations. Orme and Chaplain (1996a) solved this problem taking into account the local accumulation of endothelial cells as the origin of new sprouts. Levine *et al.* (2000) addressed the problem by selecting the tip endothelial cell through the interaction of endothelial cells, TAF's, proteases, fibronectin, angiostatin, pericytes, and macrophages. Addison-Smith *et al.* (2008) even developed a model to predict the origin and spacing between sprouts.

Discrete modeling has also produced quality models to study angiogenesis. Contrary to continuous ones, these models are able to predict the structure of the new vasculature, allowing comparison with *in vitro* or even *in vivo* experiments. Agent-based models, in general, track TECs which migrate under the influence of a continuum field, while SECs follow their path. One example is the model posed by Stokes and Lauffenburger (1991). It is a lattice-free, two-dimensional model in which every sprout is characterized by its TEC, whose velocity and position is governed by a differential equation (chemotaxis) altered by randomness and viscosity. Furthermore, they include branching ruled by a probability function and anastomosis whenever a tip is away from another endothelial cell a distance equivalent to a cell size. It is noteworthy that the model includes the influence of the redistribution of endothelial cells between the sprout and the parent vessel. Contrary to this detailed description of TEC, the TAF is assumed to be in a steady state. Sleeman and coworkers (Plank and Sleeman, 2003, 2004; Sleeman and Wallis, 2002) also developed an agent-based model by getting rid of the lattice of a cellular automata model. In their approach, they model TEC migration as a random walk, in particular, in Plank and Sleeman (2004), they used a biased circular random walk (Codling *et al.*, 2008), based on the work of Hill and Häder (1997) for the trajectories of micro-organisms. Sun *et al.* (Sun *et al.*, 2005) introduced the influence of the extracellular matrix in their agent-based model through an anisotropic directional field that affected tip endothelial cell migration. Milde and coworkers (Milde *et al.*, 2008) used a similar approach to model the interactions between the TEC and the ECM, as shown in figure 1.16a. Capasso *et al.* (Capasso and Morale, 2009) also included random walks in their model. Yet another example is the three-dimensional model developed by Das *et al.* (Das *et al.*, 2010) that includes cell-cell communication and migration as a stochastic process. The work by Bentley and coworkers (Bentley *et al.*, 2009) supposed a breakthrough in angiogenesis modeling. There, they studied lateral inhibition by means of a hierarchical agent-based model and showed how the feedback loop between VEGF-A and Dll-4 determined tip or stalk cell differentiation (see figure 1.16b).

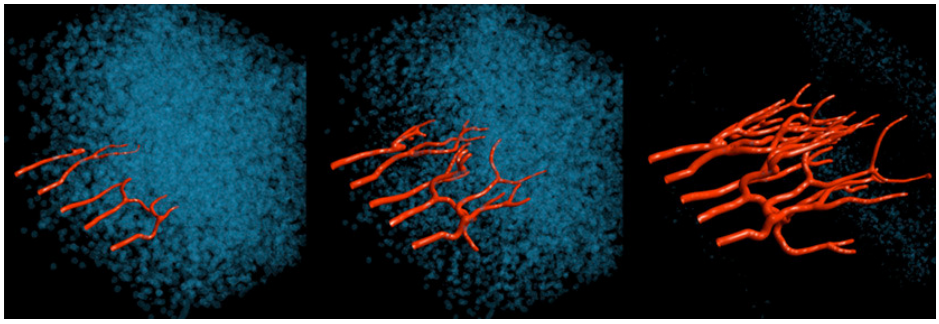

(a) *Three-dimensional discrete agent-based model that includes the iterations between the TECs and the ECM. (Reproduced from Milde* et al., *2008)*

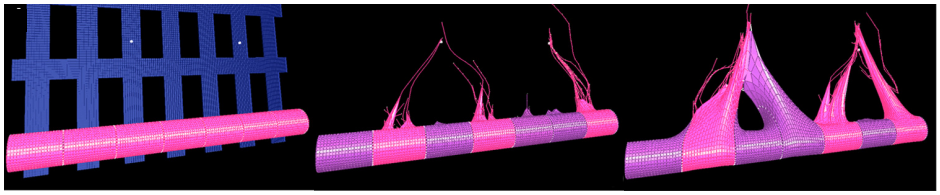

(b) *Discrete model of several endothelial cells that differentiate into TECs governed by lateral inhibition. (Reproduced from Bentley* et al., *2009)*

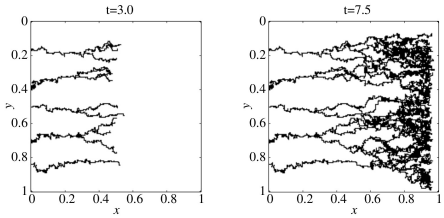

(c) *Discrete model obtained through the discretization of a continuous one. (Reproduced from Anderson and Chaplain, 1998a)*

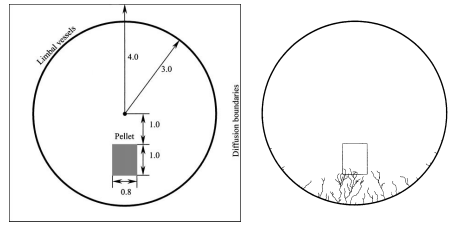

(d) *First simulation of the corneal micropocket assay in a squared domain. (Reproduced from Tong and Yuan, 2001)*

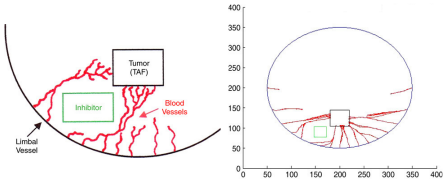

(e) *Mouse corneal micropocket assay including an angiogenesis inhibitor. (Reproduced from Harrington* et al., *2007)*

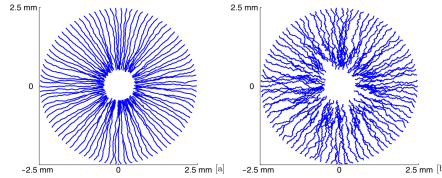

(f) *Influence of branching in angiogenesis in the corneal micropocket assay. (Reproduced from Jackson and Zheng, 2010)*

Figure 1.16. Discrete models of tumor-induced angiogenesis.

One of the most celebrated discrete model, shown in figure 1.16c, was developed by Anderson and Chaplain (Anderson and Chaplain, 1998a; Chaplain and Anderson, 1996). They discretized the equations of a continuous model to create a Cellular Automata model that governed the TECs. The probabilities for TEC movement in the Cellular Automata included diffusion, chemotaxis, and haptotaxis mechanisms, as in the continuous model. Notably, the results were compared with *in vivo* assays performed in the eye of a rabbit (Gimbrone Jr *et al.*, 1974) and in the cornea of a mouse (Muthukkaruppan *et al.*, 1982) giving successful similarities. This idea supposed a breakthrough to represent vascular structures and was further expanded to three-dimensions, to include different branching and anastomosis criteria, and to model blood flow (Chaplain, 2000; McDougall *et al.*, 2006, 2002, 2012; Stéphanou *et al.*, 2005, 2006). And, as shown in next section, many authors use modified versions of this model to simulate vascular tumor growth. In 2005, Kevrekidis and Whitaker (2005), using a similar idea, also presented a one-dimensional hybrid model (extended to two dimensions in Kevrekidis *et al.*, 2006) that included TAFs, ECM, proteases, and angiogenesis inhibitors. The Cellular Potts models introduced by Glazier and Graner (Graner and Glazier, 1992) were also used to model angiogenesis. Bauer *et al.* (2007) used such a model, where endothelial cells were able to migrate guided by chemotaxis and haptotaxis, the sprouts were able to branch and anastomose, and the extracellular matrix was modeled in detail. The authors extended further the model to study the influence of the ECM in TEC migration (Bauer *et al.*, 2009). Some other examples of Cellular Potts models include the work by Mahoney *et al.* (2008), where they added haptotaxis to TEC migration, and by Szabó and Czirók (2010); Szabó *et al.* (2008), where they studied the role of cell-cell adhesion.

Finally, discrete models were also used to replicate the corneal micropocket angiogenesis assay. The first one was developed by Tong and Yuan in 2001 (Tong and Yuan, 2001). It is a two-dimensional model with an initial circular capillary and a pellet that release TAF, both embedded in a square domain (see figure 1.16d). New TECs originate at the capillaries stochastically and migrate and anastomose according to discrete rules. This model was extended in Harrington *et al.* (2007) to include an angiogenesis inhibitor (see figure 1.16e). Furthermore, in Tong and Yuan (2008b) the authors improved the continuous equation that governs the dynamics of TAF. In 2011, Jackson and Zheng (Jackson and Zheng, 2010) proposed a different model for corneal angiogenesis (see figure 1.16f) that included a mechanical model for the elongation of the sprouts and angiopoietin-regulated phenotypes.

Although discrete models can capture the structure of the vascular network, in general, they only describe the migration of TECs and assume that SECs follow their path. In addition, discrete models become computationally unaffordable as

the number of cells increases. Some authors have developed hybrid models to circumvent these problems. The common approach in hybrid models for angiogenesis is to model TECs using a discrete description, while every other component of the model, such as SECs or TAFs, are modeled as continuum fields. Hence, these models are able to represent the vascular networks, while benefiting from the computational effectiveness of continuum modeling. The hybrid model proposed by Travasso *et al.* (2011b) and Dias Soares Quinas Guerra and Travasso (2012) fits into the latter type of theories. It couples cellular-scale discrete agents with an averaged continuous theory based on the phase field method. The model has shown significant potential predicting *in vivo* patterns of tumor-induced capillary growth (see figure 1.17). In opposition to the classical description of sharp interfaces, the phase-field model describes the interface between phases as diffuse. This permits avoiding the resolution of moving boundary problems, but requires solving a higher-order partial differential equation with diffuse interfaces evolving dynamically over the computational domain. In subsection 1.2.3, we present our methodology to treat these computational challenges.

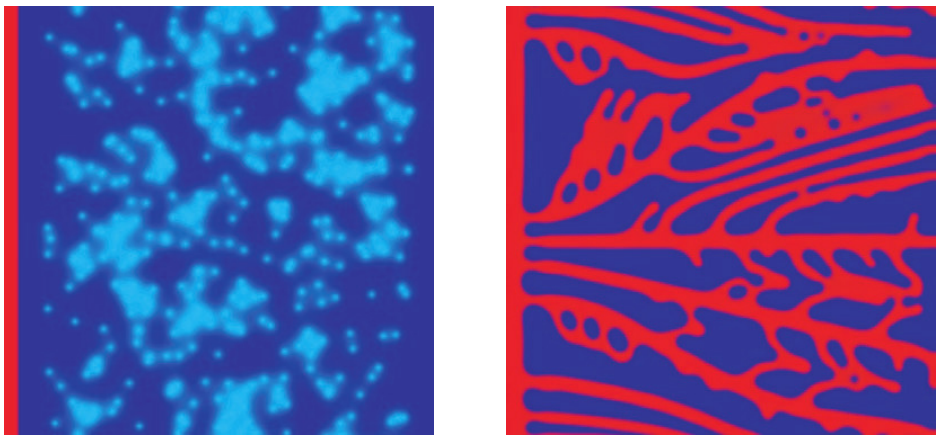

Figure 1.17. A hybrid model of tumor-induced angiogenesis. *Tumor angiogenic factor (light blue) promotes angiogenesis from an initial vessel (left). The model captures the formation of a new vascular network (right). (Reproduced from Travasso* et al.*, 2011b)*

Relevant angiogenesis models have also been developed for wound healing, as in Olsen *et al.* (1997); Valero *et al.* (2013, 2015a); Vermolen and Javierre (2012) (see Valero *et al.*, 2015b for a review), and for skeletal muscle, as in Carlier *et al.* (2012); Liu *et al.* (2011); Reina-Romo *et al.* (2013).

Vascular tumor growth Vascular growth modeling has attracted significant interest in the last few years. Prime examples include the work of Frieboes *et al.* (Frieboes *et al.*, 2010, 2007), which couples phase fields to describe tumor growth with discrete random walks to model angiogenesis. We also mention the ten-species model of Lima *et al.* (Lima *et al.*, 2014), which was recently proposed. Multiscale techniques have also proven important on the development of vascular growth theories, as shown in Alarcón *et al.* (2003). Significant examples within the Cellular Automata framework were given in Gevertz and Torquato (2006); Perfahl *et al.* (2011). Other important work includes Breward *et al.* (2004); Cristini *et al.* (2003); Hogea *et al.* (2006); Orme and Chaplain (1996b); Shirinifard *et al.* (2009); Zheng *et al.* (2005).

Fluid transport in the vicinity a tumor, and in particular blood flow through the newly created vessels, has received special attention in mathematical modeling for its important role in tumor growth. Baxter and Jain were among the first to model fluid flow. In the series of papers Baxter and Jain 1989, 1990, 1991a,b they studied transport of fluid and molecules in one- and two-dimensional settings and addressed the role of fluid pressure in tumor growth. Pries, Secomb, and collaborators worked on the role of blood flow in vascular network, including the adaptation of vessels to this flow (Pries *et al.*, 2001, 1996, 1998, 1990, 1994; Secomb and Pries, 2011). Most of the subsequent models that included blood flow used their theory. As an example, they recently developed a mathematical model (Secomb *et al.*, 2013) that coupled the discrete angiogenic model of Tong and Yuan (Tong and Yuan, 2001) with their models of blood flow and vascular adaptation. Rieger and coworkers developed a two-dimensional Cellular Automata model (Bartha and Rieger, 2006) (which was extended to three-dimensions in Lee *et al.*, 2006) that considered both tumor growth and angiogenesis and included vessel co-option, vessel collapse, and cell death. Notably, vessels collapse and regress due to absence of intravascular blood flow. In Welter *et al.* (2008) the authors incorporated details from the Cellular Automata model in Alarcón *et al.* (2003) and analyzed the distribution of a drug injected into the vasculature. Posterior developments of this model (Welter *et al.*, 2009; Welter and Rieger, 2010, 2013) included more realistic arterio-venous initial vascular networks and interstitial fluid pressure to study the influence in tumor growth. Phipps and Kohandel also studied interstitial fluid pressure within a continuous angiogenesis model (Phipps and Kohandel, 2011). In Wu *et al.* (2009, 2008), Wu and coworkers built intravascular and extravascular fluid pressure into an augmented version of the angiogenesis model developed in Anderson and Chaplain (1998a). They used the model in Pries *et al.* (1994) for the intravascular flow and the work in Baxter and Jain (1989) for the extravascular flow. Later, in Cai *et al.* (2011) they coupled this model with a tumor growth model based on the work in Anderson (2005). Wu *et al.* followed a similar approach in Wu *et al.* (2013), but they also incorporated

the effect of the lymphatic system.

1.2.3 Isogeometric analysis

The numerical approximation of the higher-order partial differential equation describing the vascular networks entails several difficulties, such as, for example, stiffness in space and time, resolution of diffuse interfaces that evolve dynamically, and discretization of higher-order differential operators. In the literature, we find that on simple geometries it is common to use the finite difference method (Frieboes *et al.*, 2007; Travasso *et al.*, 2011b; Wise *et al.*, 2008) or spectral methods (Ye and Cheng, 2005) to approximate higher-order derivatives. However, our goal is to undertake the discrete/continuous coupling using a global functional description adequate for finite element methods, which are geometrically flexible. Variational formulations of higher-order equations require the use of functions which are globally highly continuous. In particular, the fourth-order equation that we solve in this thesis requires globally $\mathcal{C}^1$-continuous functions. Although significant progress has been made, see for example (Stogner and Carey, 2007), the derivation of three-dimensional and geometrically flexible $\mathcal{C}^1$-continuous finite elements is to the best of our knowledge an open problem. Most existing approaches require the introduction of additional degrees of freedom or stabilization parameters. This has made that the vast majority of the finite element community continues to utilize mixed methods (Hawkins-Daarud *et al.*, 2012) that permit the use of $\mathcal{C}^0$-continuous elements at the cost of doubling the number of degrees of freedom. Alternative approaches outside the classical continuous finite element methods include, among others, the discontinuous Galerkin method (Xia *et al.*, 2007), the continuous/discontinuous Galerkin method (Engel *et al.*, 2002) or maximum entropy approximations (Arroyo and Ortiz, 2006; Cyron *et al.*, 2009; Rosolen *et al.*, 2013).

Recently, Hughes *et al.* (Hughes *et al.*, 2005) developed a new technology, isogeometric analysis (IGA), that naturally deals with high-order equations being at the same time geometrically flexible. IGA is a generalization of finite element analysis (FEA, Hughes, 1987) whose initial goal was to unify computer-aided design (CAD) and FEA. The main idea of this method is to replace the FEA traditional basis functions with those utilized in CAD, such as B-splines, non-uniform rational B-splines (NURBS) (Piegl and Tiller, 1997; Rogers, 2001), T-splines (Bazilevs *et al.*, 2010; Casquero *et al.*, 2015b), hierarchical B-splines (Schillinger *et al.*, 2012; Scott *et al.*, 2014), trimmed NURBS (Schmidt *et al.*, 2012), polynomial splines over hierarchical T-meshes (PHT-splines) (Nguyen-Thanh *et al.*, 2011), Powell-Sabin B-splines Speleers *et al.* (2012), or rational Triangular Bézier Splines Xia *et al.* (2015). IGA invokes the isoparametric concept, that is, the unknown variables

are represented in terms of the same basis functions which define the geometry. The coefficients of the basis functions are the degrees of freedom or control variables. IGA is a nascent technology compared with the long tradition behind FEA, and, consequently, it still presents some topics that are being addressed, such as optimized quadrature rules Auricchio *et al.* (2012); Hughes *et al.* (2010) or the creation of solid volumes from surfaces. The growing community behind IGA is currently dealing with these topics, which, in any case, are not directly related with this thesis.

Contrary to FEA, IGA uses basis functions capable of representing the exact geometry and imposes them on the solution mesh. As a result, this new technology has potential to overcome the long times dedicated to meshing and bridged the gap between CAD and FEA. In addition, because IGA uses the CAD description of the geometry it benefits from the naturally built-in geometric flexibility and the high-order continuity of the basis functions, which makes it an excellent numerical method to solve our model. Moreover, IGA also excels in its high-order accuracy, robustness, and compact support. For these reasons, IGA has been successfully used in several fields such as fluid mechanics (Akkerman *et al.*, 2011; Bazilevs *et al.*, 2007; Evans and Hughes, 2013), phase-field models (Bueno *et al.*, 2015, 2016; Dhote *et al.*, 2014, 2015; Gomez *et al.*, 2008; Liu *et al.*, 2013, 2015), structural vibrations (Cottrell *et al.*, 2006; Hughes *et al.*, 2008), shell modeling (Benson *et al.*, 2010; Kiendl *et al.*, 2010), contact problems (De Lorenzis *et al.*, 2011; Dimitri *et al.*, 2014a,b), fluid-structure interaction problems (Bazilevs *et al.*, 2008, 2006; Casquero *et al.*, 2015a), shape optimization (Wall *et al.*, 2008), electromagnetics (Buffa *et al.*, 2010), and biology applications (Auricchio *et al.*, 2015; Bazilevs *et al.*, 2006; Morganti *et al.*, 2015). Also, several groups have developed software for IGA, such as, PetIGA (Collier *et al.*, 2013), igatools (Pauletti *et al.*, 2015), or GeoPDEs (de Falco *et al.*, 2011).

NURBS-based isogeometric analysis and the Galerkin method

Here, we briefly describe the concept of B-splines and NURBS and we show a NURBS-based IGA example based on the Galerkin discretization. We show this method because it is the one we use in this thesis, but note, however, that IGA is not restricted to it and has been used with other discretizations such as the collocation method (Auricchio *et al.*, 2010; Casquero *et al.*, 2016; Reali and Gomez, 2015; Reali and Hughes, 2015) or the least-squares finite element method (Kadapa *et al.*, 2015), or in combination with the meshfree method (Rosolen and Arroyo, 2013; Valizadeh *et al.*, 2015).

B-splines and NURBS For the construction of a B-spline, we need to define a basis of B-splines and a knot vector, that is, a non-decreasing set of coordinates in the parameter space[7]. Let $\Xi = \{\xi_1, \xi_2, \ldots, \xi_{n+p+1}\}$ be the knot vector, where $\xi_i \in \mathbb{R}$ is the ith knot, i is the knot index, $i = 1, 2, \ldots, n + p + 1$, $n \in \mathbb{N}$ is the number of basis functions, and p the polynomial order or degree. A univariate B-spline basis, $N_{i,p}$, is defined recursively given some degree $p \in \mathbb{N}$ and a knot vector Ξ[8]. Starting with piece-wise constants ($p = 0$):

$$N_{i,0}(\xi) \begin{cases} 1 & \text{if } \xi_i \leq \xi < \xi_{i+1}, \\ 0 & \text{otherwise.} \end{cases} \tag{1.1}$$

For higher degrees $p = 1, 2, \ldots$ the basis is defined using the Cox-de Bor recursion formula:

$$N_{i,p}(\xi) = \frac{\xi - \xi_i}{\xi_{i+p} - \xi_i} N_{i,p-1}(\xi) + \frac{\xi_{i+p+1} - \xi}{\xi_{i+p+1} - \xi_{i+1}} N_{i+1,p-1}(\xi). \tag{1.2}$$

Figure 1.18a shows an example for $p = 2$. Note that the support of each basis function consists of a few number of elements.

B-spline curves $\mathbf{C}(\xi)$ in $\mathbb{R}^d$, where d is the number of spatial dimensions, are constructed by taking a linear combination of n B-spline basis as follows:

$$\mathbf{C}(\xi) = \sum_{i=1}^{n} \mathbf{B}_i N_{i,p}(\xi), \tag{1.3}$$

where $\mathbf{B}_i \in \mathbb{R}^d$ is a vector of coefficients referred to as control points. p-degree B-splines are $\mathcal{C}^{p-1-m}$-continuous across knot spans, where m is the multiplicity of the knot, and $\mathcal{C}^{\infty}$-continuous elsewhere. As an example, figure 1.18b shows a two-dimensional B-spline where $p = 2$ and $\Xi = [0, 0, 0, 1, 1, 3, 4, 5, 5, 5]$. Note that the fourth knot value is repeated twice, so the continuity there is $\mathcal{C}^0$.

Using the notion of tensor products, these concepts can be easily generalized to B-splines of multiple dimensions. Let d_p be the number of parametric directions; for each parametric direction $\ell = 1, \ldots, d_p$ we define a knot vector Ξ^ℓ, such that,

$$\Xi^\ell = \left\{\xi_1^\ell, \xi_2^\ell, \ldots, \xi_{n_\ell + p_\ell + 1}^\ell\right\}, \tag{1.4}$$

where p_ℓ and n_ℓ are the polynomial order and the number of basis functions for each parametric direction, respectively. We also define a multi-index $\mathbf{i} \in \mathbb{Z}$, the set

$$I = \left\{\mathbf{i} = \left\{i_1, \ldots, i_{d_p}\right\} \mid i_\ell \in \{1, \ldots, n_\ell\},\ \ell = 1, \ldots, d_p\right\}, \tag{1.5}$$

[7] Knots partition the parameter space into elements.

[8] The standard in CAD are open knot vectors, defined as those whose first and last knot values appear $p + 1$ times.

and a multi-index of polynomial orders $\mathbf{p} = \{p_1, p_2, \ldots, p_{d_p}\}$. Given a control net $\{\mathbf{B_i}\}$ a multivariate B-spline is defined by

$$\mathbf{V}(\boldsymbol{\xi}) = \sum_{i \in I} \mathbf{B_i} N_{\mathbf{i},\mathbf{p}}(\boldsymbol{\xi}), \tag{1.6}$$

where, using a tensor product structure, the multivariate basis function $N_{\mathbf{i},\mathbf{p}}(\boldsymbol{\xi})$ is defined as

$$N_{\mathbf{i},\mathbf{p}}(\boldsymbol{\xi}) = \prod_{\ell=1}^{d_p} N^{\ell}_{i_\ell,p_\ell}(\xi^\ell). \tag{1.7}$$

Non-uniform rational B-splines or NURBS are a generalization of B-splines. $\mathbb{R}^d$ NURBS are obtained from the projection of $\mathbb{R}^{d+1}$ B-splines and they allow the exact representation of several useful geometries, such as conics. Given $\mathbf{i}$ and $\mathbf{p}$, the basis of a B-spline can be projected to create a basis of NURBS in the following way:

$$R_{\mathbf{i},\mathbf{p}}(\boldsymbol{\xi}) = \frac{w_{\mathbf{i}} N_{\mathbf{i},\mathbf{p}}(\boldsymbol{\xi})}{\sum_{\mathbf{j} \in I} w_{\mathbf{j}} N_{\mathbf{j},\mathbf{p}}(\boldsymbol{\xi})}, \tag{1.8}$$

where $w_{\mathbf{i}}$ are positive constants referred to as weights. Similarly to B-spline, NURBS curves, surfaces, and volumes are created by the linear combination of a control mesh and their piece-wise basis functions as

$$\mathbf{V}(\boldsymbol{\xi}) = \sum_{i \in I} \mathbf{B_i} R_{\mathbf{i},\mathbf{p}}(\boldsymbol{\xi}). \tag{1.9}$$

Figure 1.18c shows the exact parametrization of a conic section, in particular a disk, and figure 1.18d shows a cone built with NURBS. More complex geometries are constructed using two or more NURBS patches, that is, the union of NURBS, as shown in figure 1.18e. We advance here that we exploit the concept of NURBS patches to build our parallel code (see subsection 2.3.3). NURBS and B-splines can also be refined using three different strategies: knot insertion (classical h-refinement), order elevation (classical p-refinement), and k-refinement, which increases smoothness in addition to order.

Galerkin discretization in isogeometric analysis Here we show a boundary value problem solved using isogeometric analysis and the Galerkin method. In particular, the model problem involves a fourth order partial differential equation, as that is the maximum order of the equations of the present thesis. However, as shown along the derivation of the method, isogeometric analysis provides a framework in which dealing with other orders is straightforward and just a matter of changing the smoothness of the basis functions. For more details about the

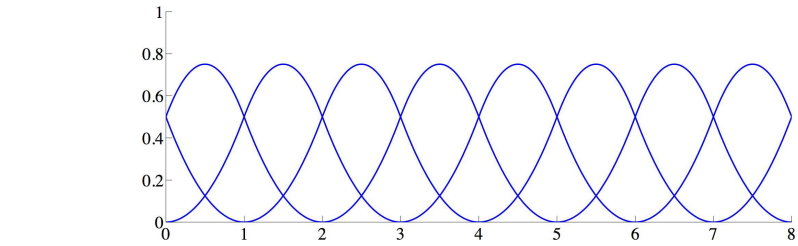

(a) *Basis functions.*

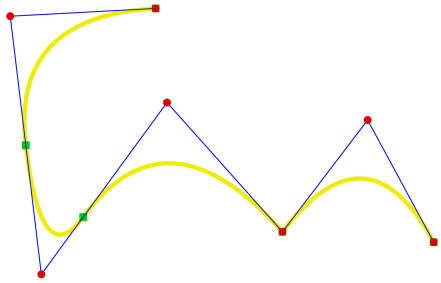

(b) *B-spline curve.*

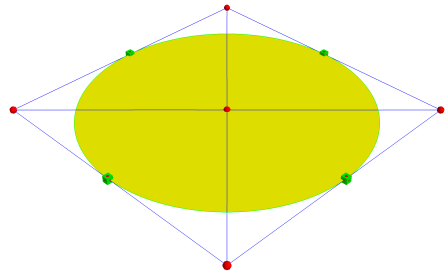

(c) *NURBS surface.*

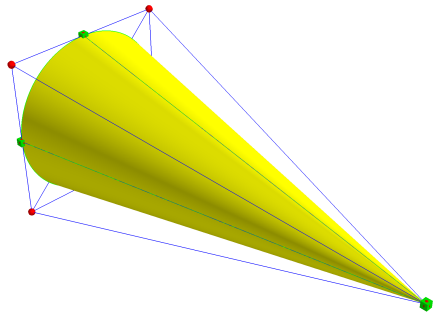

(d) *NURBS volume.*

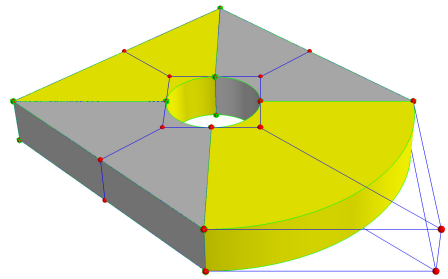

(e) *NURBS patch.*

Figure 1.18. Basis functions, B-splines, and NURBS. *Control points are drawn as red dots, knots as green squares, control nets as blue lines, and knot spans as green lines.*

resolution of higher-order partial differential equations using isogeometric analysis, the reader is referred to (Auricchio *et al.*, 2007; Fischer *et al.*, 2011; Gomez *et al.*, 2008, 2010; Gomez and Nogueira, 2012; Gomez and París, 2011).

Let $\Omega \subseteq \mathbb{R}^d$ be an open, connected d-dimensional domain and let $\partial\Omega = \Gamma$ be the Lipschitz boundary of this domain. We consider a linear fourth-order operator $\mathcal{A}$ and appropriate operators $\mathcal{B}_E$ and $\mathcal{B}_N$ so that they define essential and natural boundary conditions on Γ, respectively. The strong form of our model problem is as follows: Given the smooth functions $f : \Omega \mapsto \mathbb{R}$, $g_E : \Gamma \mapsto \mathbb{R}$, and $g_N : \Gamma \mapsto \mathbb{R}$, find $u : \overline{\Omega} \mapsto \mathbb{R}^d$ such that

$$\mathcal{A}(u) = f \quad \text{in} \quad \Omega \tag{1.10}$$

$$\mathcal{B}_E(u) = g_E \quad \text{on} \quad \Gamma \tag{1.11}$$

$$\mathcal{B}_N(u) = g_N \quad \text{on} \quad \Gamma. \tag{1.12}$$

Similarly to classical FEA, we derive now the weak form or variational formulation of the strong problem, by multiplying equation (1.10) with smooth test functions v, integrating over the domain, and integrating by parts twice. The strong form of the problem is equivalent under certain assumptions to the following variational formulation: Given the smooth functions $f : \Omega \mapsto \mathbb{R}$, $g_E : \Gamma \mapsto \mathbb{R}$, and $g_N : \Gamma \mapsto \mathbb{R}$, find $u \in \mathcal{U}$ such that $\forall v \in \mathcal{V}$:

$$a(u, v) = (f, v) + b\langle g_N, v\rangle, \tag{1.13}$$

where $a(\cdot,\cdot)$ and $b\langle\cdot,\cdot\rangle$ are bilinear forms defined over Ω and Γ respectively and $(\cdot,\cdot)$ denotes the $\mathcal{L}^2(\Omega)$ inner product. $b\langle\cdot,\cdot\rangle$ collects the boundary terms that enforce the natural boundary conditions. $\mathcal{U}$ denotes the trial solution space whose members satisfy the essential boundary conditions of the strong problem and $\mathcal{V}$ denotes the weighting function space whose members are identical to those of $\mathcal{U}$, but satisfy the homogeneous counterpart of the essential boundary conditions. The assumption here is that all the functions are sufficiently smooth, so that the solution of this weak formulation is a solution of the strong form and vice versa. In our model problem in particular, because the fourth-order terms of the strong form are reduced to second-order in the variational formulation, we need our trial and weighting functions to be at least $\mathcal{C}^1$-continuous. Thus, the spaces $\mathcal{U}$ and $\mathcal{V}$ are defined as subsets of $\mathcal{H}^2$, the Sobolev space of square integrable functions with square integrable first and second derivatives. If our strong problem only involved second order terms, for example, we could work with the less restrictive functional spaces $\mathcal{U}, \mathcal{V} \subset \mathcal{H}^1$.

Now, we need to derive a numerical approximation of the variational formulation. We perform it using the Galerkin method, which consists on defining discrete

spaces $\mathcal{U}^h \subset \mathcal{U}$ and $\mathcal{V}^h \subset \mathcal{V}$ in which the approximate solution u^h and weighting function v^h of our problem live. Thus, we approximate equation (1.13) by the following variational problem over the finite-dimensional space: find $u^h \in \mathcal{U}^h \subset \mathcal{U}$ such that $\forall v^h \in \mathcal{V}^h \subset \mathcal{V}$:

$$a\left(u^h, v^h\right) = \left(f, v^h\right) + b\left\langle g_N^h, v^h\right\rangle. \tag{1.14}$$

We need to make a choice on the particular finite-dimensional spaces or, equivalently, of their basis functions $\{N_i\}_{i=1}^{n_b}$, where n_b is the dimension of the discrete space. Here, making use of isogeometric analysis, u^h is defined as

$$u^h(\mathbf{x}, t) = \sum_{i=1}^{n_b} \hat{u}_i(t) N_i(\mathbf{x}), \tag{1.15}$$

where N_i are B-spline or NURBS basis functions and the coefficients $\hat{u}_i$ are the control points. The weighting function v^h is defined equivalently to equation (1.15). Furthermore, we assume that there exists a function $g_N^h \in \mathcal{V}^h$ such that $g_N^h\big|_\Gamma = g_N$. Note that in IGA the basis functions are defined by the geometry, as in equation (1.3), but they still need to fulfill some analysis requirements. In our model problem in particular, as we use a conforming discretization, N_i must be a subset of $\mathcal{H}^2$ so that the relation $\mathcal{V}^h \subset \mathcal{V}$ holds. As explained before, this requirement is guaranteed by a B-spline or NURBS of order $p \geq 2$ (provided that there are no repeated knot values) because its global continuity is $\mathcal{C}^1$. Occasionally, the simplest basis that represents the geometry may not be smooth enough. However, these problems can be easily solved using the powerful, yet simple, refinement techniques of IGA. For example, given our fourth order model problem and a square geometry parametrized by B-splines of order $p = 1$, the parametrization can be k-refined to obtain $p = 2$, so to increment the global continuity to $\mathcal{C}^1$.

Finally, making use of the choice of u^h and v^h, we can rewrite the problem as the following linear system:

$$\mathbf{A}\hat{\mathbf{u}} = \mathbf{F}, \tag{1.16}$$

where

$$\hat{\mathbf{u}} = (\hat{u}_i)_{i=1}^{n_b}, \tag{1.17}$$

$$\mathbf{A} = (a_{i,j})_{i,j=1}^{n_b}, \text{ with } \quad a_{i,j} = a(N_j, N_i), \text{ and} \tag{1.18}$$

$$\mathbf{F} = (F_i)_{i=1}^{n_b}, \text{ with } \quad F_i = (f, N_i) + b\left\langle g_N^h, N_i\right\rangle. \tag{1.19}$$

Due to the compact support of the basis functions, the non-zero elements of the stiffness matrix $\mathbf{A}$ are concentrated on a reduced-bandwidth diagonal, which reduces computational costs.

1.3 Thesis overview

Following this introduction, in chapter 2 we present a hybrid model for tumor-induced angiogenesis with chemotactically-guided tip endothelial cells. There, we put the model into a coherent mathematical and algorithmic framework and introduce a numerical method for the theory. In chapter 3 we propose a new model that accounts for chemotactic and haptotactic tip endothelial cell migration, coupling the previous theory with a discrete random walk. Using the same numerical method, we investigate the role of haptotaxis and chemotaxis in the mobility of tip endothelial cells and its influence in the final vascular patterns. In chapter 4 we show how the effectiveness of our method permitted us to perform large-scale three-dimensional simulations and to reproduce, also in three dimensions, one of the most widely used angiogenesis assays: the mouse corneal micropocket angiogenesis assay. In chapter 5, following a non-conserved phase-field methodology, we propose a model of tumor angiogenesis that incorporates not only growth of new capillaries, but their natural regression and regrowth. We also quantitatively compare the predictions of this model with an *in vivo* experiment. In chapter 6 we derive a theory that includes the influence of intravascular, transvascular, and interstitiicial flow in angiogenesis. There, we study the different vascular patterns altered by tumor angiogenic factor convection under different configurations and the effect of high intratumoral pressure in angiogenesis. Finally, in chapter 7 we present a summary and the conclusions of this thesis, as well as some recommendations for further developments.

At the end of this document, the reader may find a list of publications that resulted from the work in this thesis, the appendices, and the bibliography.

Chapter 2

A mathematical model of tumor-induced angiogenesis

In this chapter we present a hybrid mathematical model for tumor-induced angiogenesis and introduce a numerical method based on isogeometric analysis that naturally couples the discrete cellular-scale kinetics with the continuous description of the macroscale. We develop a mathematical framework that seamlessly integrates mobile, discrete agents, that represent tip endothelial cells, into the dynamics of the continuous variables. The latter combined with the high-order accuracy and the $\mathcal{C}^1$ continuity of isogeometric analysis leads to highly efficient algorithms for solving the mathematical model. The accuracy and versatility of the method allowed us to perform several simulations that provide insight into the dynamics of the governing equations and the underlying biological process.

2.1 Introduction

Our modeling strategy is based on the theory proposed by Travasso *et al.* in Travasso *et al.* (2011b), which is a multiscale, hybrid model that describes the vascular development caused by tumor angiogenesis factors released by hypoxic cells. In their work, both the TECs that lead the capillary growth and the hypoxic cells are modeled using discrete agents, while the TAF and the capillaries are modeled as continuous variables. The model accounts for multiple biological phenomena,

such as for example, the release of TAF by hypoxic cells; the activation of quiescent endothelial cells and their differentiation into SECs and TECs; and the capillary growth by chemotaxis. These biological processes are summarized in figure 2.1, where we also show in light gray fonts some other phenomena not accounted for in the theory. In Travasso *et al.* (2011b), the authors focus on the predictive capabilities of the model, showing that it reproduces *in vivo* patterns of newly formed vascular networks (see figure 1.17). Here, we emphasize the mathematical

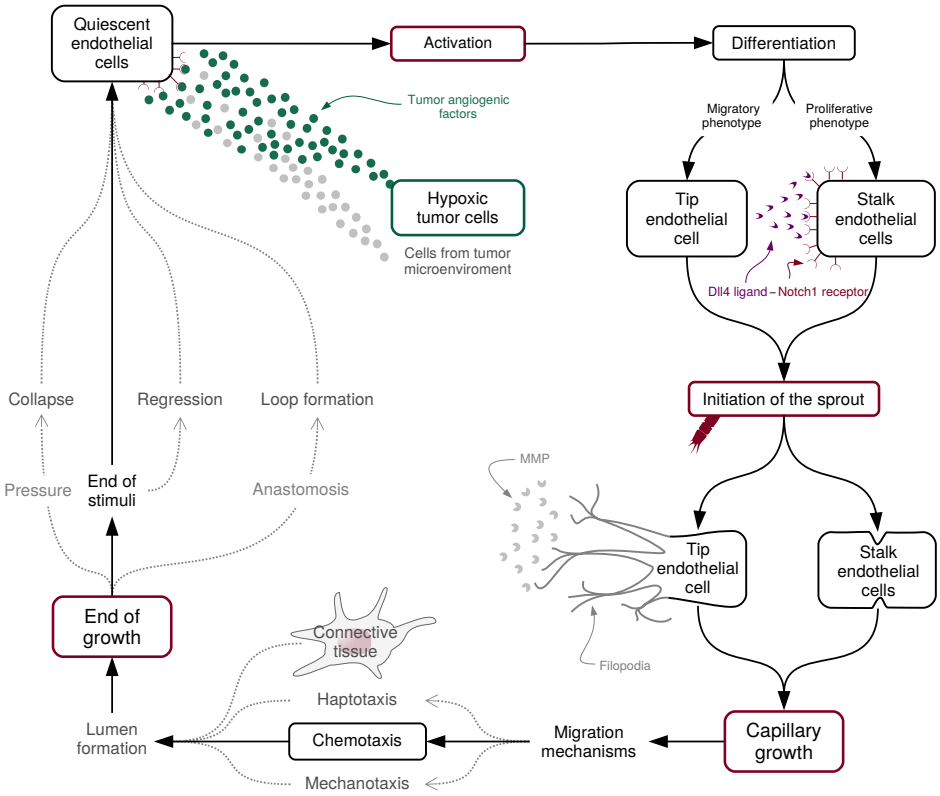

Figure 2.1. Conceptual scheme of the tumor angiogenesis process. *The process starts on the top-left corner of the plot, when the quiescent endothelial cells get activated by tumor angiogenic factors. Thereafter, a series of events lead to the formation of new capillaries: the differentiation of the endothelial cells by means of tumor angiogenic factors and lateral inhibition; the initiation of the sprout that breaks into the extracellular matrix; the capillary growth following different mechanisms; and the end of the growth. The mathematical model utilized in this chapter accounts for all the phenomena in this figure, except for those plotted with light gray fonts.*

and algorithmic aspects of the numerical approximation of the theory. Besides its predictive capabilities, we feel this model is appealing for several reasons: (1) the model can easily accommodate cellular-scale kinetics into the discrete part; (2) in spite of the complexity of the vasculature patterns, the continuous part is simply defined by a system of two partial differential equations on a fixed domain. This is due to the use of the phase field method to describe the capillary patterns. The phase-field method is a mathematical theory introduced to solve interfacial problems. Originally developed for microstructure evolution (Chen, 2002; Emmerich, 2003) and phase transition (Gomez *et al.*, 2008; Gomez and Hughes, 2011; Kobayashi, 1994), it has been successfully applied to a number of physical phenomena such as infiltration (Cueto-Felgueroso and Juanes, 2009), multicellular systems (Nonomura, 2012), or fluid vesicles (Campelo and Hernández-Machado, 2006). Even more relevant to this thesis is the recent application of the phase-field method to modeling cancer growth (Cristini *et al.*, 2009; Oden *et al.*, 2010).

The rest of the chapter is organized as follows: we describe the tumor angiogenesis model and develop a mathematical framework for it in section 2.2. Then, we propose a numerical method to solve the model in section 2.3. In section 2.4 we show the time evolution of a numerical example, a parametric study of the model, and several simulations under different initial conditions. We finalize with the conclusions in section 2.5.

2.2 The tumor angiogenesis model

In this section, we put the model into a coherent mathematical and algorithmic framework. We understand the model as a staggering scheme that alternatively uses the continuous and discrete descriptions. Therefore, before introducing the fundamental equations of the model, we need to discretize the time interval of interest, namely, $(0, T)$, into N sub-intervals $I_n = (t_n, t_{n+1})$, $n = 0, 1, \ldots, N-1$, where $0 = t_0 < t_1 < \cdots < t_N = T$. We will use the notation $\Delta t_n = t_{n+1} - t_n$. To advance the variables of interest, namely, the phase field describing the endothelial cells' location (c) and the TAF concentration (f), we need to solve first a discrete, agent-based model and subsequently a continuous boundary value problem. The discrete and continuous problems are defined on different spatial domains that we introduce in what follows. For a pictorial description of the spatial domains involved in the model, the reader is referred to figure 2.2.

2.2.1 The spatial domain of the continuous problem

Let $\Omega \subset \mathbb{R}^d$ be an open set, where $d = 2$ or 3, and let Γ be the boundary of the domain Ω. The boundary Γ is assumed to be sufficiently smooth (e.g., Lipschitz) and to have a well-defined unit outward normal denoted by $\mathbf{n}$. The set Ω represents a portion of tissue that remains fixed over the time interval $(0, T)$ and is associated to the continuous part of the model. In Ω, we will define the fields $c : \Omega \times (0, T) \mapsto [-1, 1]$ and $f : \Omega \times (0, T) \mapsto [0, f_{\text{HYC}}]$, which represent, respectively, the phase field describing the endothelial cells' location and the TAF concentration, where f_{HYC} is a positive constant.

2.2.2 The spatial domain of the discrete model

The discrete component of the model takes place on two subsets of Ω that may vary from one time step to the next. We call these subdomains the hypoxic cell subdomain Ω_{HYC} and the tip endothelial cell subdomain Ω_{TEC}.

The hypoxic cell subdomain

This subdomain is associated to hypoxic cell locations, where the TAFs are released. At the initial time stage, t_0, we define this set as $\Omega_{\text{HYC}}(t_0) = \bigcup_{i=1}^{N_{\text{HYC}}} \Omega^i_{\text{HYC}}(t_0)$, where N_{HYC} is the initial number of hypoxic cells and each of the $\Omega^i_{\text{HYC}}(t_0)$ is a circular-shaped (spherical-shaped if $d = 3$) subset of Ω with radius R_{HYC} and center $\mathbf{x}^i_{\text{HYC}}$. This can be considered as an initial condition, which determines the location of the hypoxic cells that release TAF, triggering the growth of new capillaries. This set may vary from one time step to the next, because some TAF sources may become inactive and stop releasing TAF. In particular, at each time step, the set $\Omega_{\text{HYC}}(t_{n+1})$ is obtained from $\Omega_{\text{HYC}}(t_n)$ using biologically motivated deterministic conditions to be defined in subsection 2.2.4. If at the time stage t_n, a particular subdomain indexed by j meets those conditions, then $\Omega^j_{\text{HYC}}(t_{n+1}) = \Omega^j_{\text{HYC}}(t_n)$. If those conditions fail to be satisfied, then $\Omega^j_{\text{HYC}}(t_{n+1}) = \varnothing$.

The tip endothelial cell subdomain

This subdomain is associated to TECs, which are mobile discrete agents in the model. At the initial time stage t_0, there are no active TECs, and, thus, $\Omega_{\text{TEC}}(t_0) = \varnothing$. As time evolves, some TECs will get activated, leading at the stage t_n, to a set $\Omega_{\text{TEC}}(t_n) = \bigcup_{i=1}^{N_{\text{TEC}}(t_n)} \Omega^i_{\text{TEC}}(t_n)$, where each of the $\Omega^i_{\text{TEC}}(t_n)$ is a circular-shaped (spherical-shaped if $d = 3$) subset of Ω with radius R_{TEC} and center $\mathbf{x}^i_{\text{TEC}}$. Note

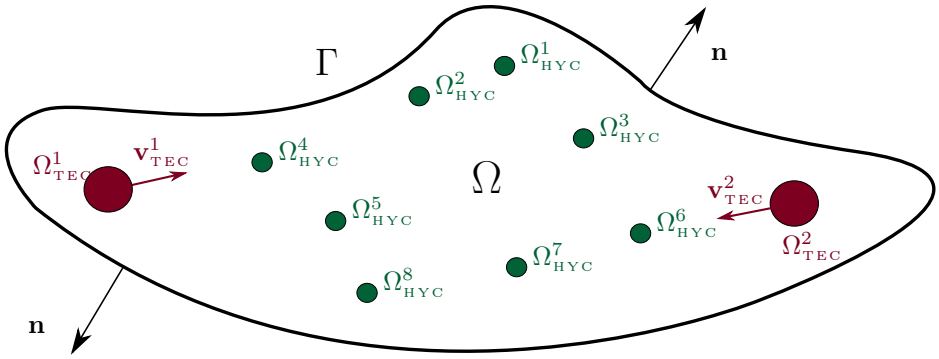

Figure 2.2. Two-dimensional representation of the different spatial domains involved in the model. *The boundary* Γ *of the domain* Ω *has natural boundary conditions. The unit normal outward to the boundary is denoted by* $\mathbf{n}$*. In addition, there are two types of circular subdomains in* Ω*, namely,* Ω^i_{TEC} *(red) that move with a velocity* $\mathbf{v}^i_{\text{TEC}}$*, where* $i = 1, 2$*, and* Ω^j_{HYC}*,* $j = 1, \ldots, 8$*, (green) with fixed positions.* Ω *simulates a tissue,* Ω_{TEC} *the tip endothelial cells, and* Ω_{HYC} *the hypoxic cells.*

that the number of subdomains $N_{\text{TEC}}(t)$ composing Ω_{TEC} may vary from one time step to the next, because new subdomains are created when new TECs become active. The biological conditions under which a new subdomain is created will be defined in subsection 2.2.4. Once a TEC subdomain is created, it needs to satisfy some conditions (also to be defined in subsection 2.2.4) to remain active. If an existing subdomain fails to satisfy those conditions at the time stage t_n, it will become the empty set at stage t_{n+1}. Each of the existing subdomains that still satisfy the conditions at the stage t_n gives rise to a new, but different, subdomain at the time stage t_{n+1}. Let us assume that $\Omega^k_{\text{TEC}}(t_n)$ is one of these subdomains. Its corresponding subdomain at time t_{n+1} is obtained by applying an affine transformation to $\Omega^k_{\text{TEC}}(t_n)$. The affine transformation, namely, φ^k_n, is defined by

$$\varphi^k_n(\mathbf{x}) = \mathbf{x} + \Delta t_n \mathbf{v}^k_{\text{TEC}} \ , \tag{2.1}$$

and the new subdomain is defined as $\Omega^k_{\text{TEC}}(t_{n+1}) = \varphi^k_n(\Omega^k_{\text{TEC}}(t_n))$. In equation (2.1), $\mathbf{v}^k_{\text{TEC}}$ represents the velocity of the TEC and is defined by

$$\mathbf{v}^k_{\text{TEC}} = \chi \nabla f(\mathbf{x}^k_{\text{TEC}}) \mathcal{L}\left(\|\nabla f(\mathbf{x}^k_{\text{TEC}})\|\right) \ , \tag{2.2}$$

where χ is a chemotactic constant, $\mathcal{L}$ is a limiting function to be defined in subsection 2.2.4, and the operator $\|\cdot\|$ denotes the Euclidean norm of a vector. Note that equations (2.1) and (2.2) treat the TECs as discrete mobile agents, assigning them an individual velocity that depends on the gradient of TAF (chemotactic velocity).

2.2.3 The coupled discrete/continuous model

Here we present the algorithmic rules to advance the fields of interest from one time step, say t_n, to the next. Given $c(\cdot, t_n)$, $f(\cdot, t_n)$, $\left\{\Omega^i_{\text{HYC}}(t_n)\right\}_{i=1,N_{\text{HYC}}}$, and $\left\{\Omega^i_{\text{TEC}}(t_n)\right\}_{i=1,N_{\text{TEC}}(t_n)}$, proceed as follows:

1. Find $\left\{\Omega^i_{\text{HYC}}(t_{n+1})\right\}_{i=1,N_{\text{HYC}}}$ and $\left\{\Omega^i_{\text{TEC}}(t_{n+1})\right\}_{i=1,N_{\text{TEC}}(t_{n+1})}$ following the steps indicated in subsections 2.2.2 and 2.2.2, and the conditions defined in subsection 2.2.4.

2. Set $f = f_{\text{HYC}}$ in $\Omega_{\text{HYC}}(t_{n+1})$, overwriting the values of $f(\cdot, t_n)$ in $\Omega_{\text{HYC}}(t_{n+1})$. Call the resulting field $\widetilde{f}(\cdot, t_n)$.

3. Set
$$c = c^i_{\text{TEC}} = \frac{\mathcal{B}_p\left(f\left(\mathbf{x}^i_{\text{TEC}}\right)\right)\pi R_{\text{TEC}}}{2\|\mathbf{v}^i_{\text{TEC}}\|} \tag{2.3}$$
in $\Omega^i_{\text{TEC}}(t_{n+1})$ for all $i = 1, \ldots, N_{\text{TEC}}(t_{n+1})$, overwriting the values of $c(\cdot, t_n)$ in $\Omega_{\text{TEC}}(t_{n+1})$. Call the resulting field $\widetilde{c}(\cdot, t_n)$.

4. Solve the boundary value problem

$$\frac{\partial f}{\partial t} = \nabla \cdot (D\nabla f) - B_u f c\mathcal{H}(c) \quad \text{in} \quad \Omega \times (t_n, t_{n+1}) \tag{2.4}$$
$$\frac{\partial c}{\partial t} = \nabla \cdot \left(M\nabla\left(\mu_c - \lambda^2\Delta c\right)\right) + \mathcal{B}_p(f)\, c\mathcal{H}(c) \quad \text{in} \quad \Omega \times (t_n, t_{n+1}) \tag{2.5}$$
$$D\nabla f \cdot \mathbf{n} = 0 \quad \text{on} \quad \Gamma \times (t_n, t_{n+1}) \tag{2.6}$$
$$M\nabla\left(\mu_c - \lambda^2\Delta c\right) \cdot \mathbf{n} = 0 \quad \text{on} \quad \Gamma \times (t_n, t_{n+1}) \tag{2.7}$$
$$M\lambda^2\Delta c = 0 \quad \text{on} \quad \Gamma \times (t_n, t_{n+1}) \tag{2.8}$$
$$f(\mathbf{x}, t_n) = \widetilde{f}(\mathbf{x}, t_n) \quad \text{in} \quad \Omega \tag{2.9}$$
$$c(\mathbf{x}, t_n) = \widetilde{c}(\mathbf{x}, t_n) \quad \text{in} \quad \Omega. \tag{2.10}$$

The notation in the boundary value problem is as follows: D is the diffusion constant; B_u is the uptake rate constant; $\mathcal{H}(\cdot)$ is the Heaviside function; M is the constant mobility; μ_c is the chemical potential; λ is a positive constant proportional to the width of the capillaries wall; and $\mathcal{B}_p(\cdot)$ is the proliferative rate function. In what follows, we describe in detail all the functions and algorithmic rules involved in the theory.

2.2.4 The discrete component

The discrete, agent-based component of the model includes the production of angiogenic factor by the hypoxic cells, the deactivation of the hypoxic cells, and the activation, migration, and deactivation of the tip endothelial cells.

Hypoxic cells

The tumor angiogenic factor is produced by randomly-distributed hypoxic cells with fixed positions denoted by $\mathbf{x}^i_{\text{HYC}}$. It is assumed that the hypoxic cells create a subdomain Ω^i_{HYC} around them in which the value of f remains constant and equal to f_{HYC} while the hypoxic cell is active. The hypoxic cells are only deactivated, ceasing their production, when a capillary, considered here as all those points in which $c \geq c_{\text{act}}$, is closer than a distance δ_{nox}. This distance represents the diffusion length of the nutrients and oxygen from the blood vessels.

Tip endothelial cells

Activation of tip endothelial cells When the tumor angiogenic factor reaches a capillary, a new tip endothelial cell is activated if the following conditions are met in a point $\mathbf{x}^* \in \Omega$:

1. $c \geq c_{\text{act}}$,
2. $f \geq f_{\text{act}}$,
3. $G \geq G_{\text{act}}$, and
4. $\|\mathbf{x}^* - \mathbf{x}^j_{\text{TEC}}\| \geq \delta_4$, $\forall j = 1, \ldots, N_{\text{TEC}}(t_n)$.

Condition 1 restricts the candidate points to tip endothelial cells to those satisfying $c \geq c_{\text{act}}$, i.e., those inside a capillary. The following two are lower limit conditions: the value of the factor f and the modulus of its gradient $G = \|\nabla f\|$ must be greater than certain thresholds defined by $f \geq f_{\text{act}}$ and $G \geq G_{\text{act}}$, respectively. Finally, condition 4 accounts for lateral inhibition, that is, the above-described differentiation phenomena driven by the Dll-4 ligand and the Notch receptor. In the model, no point can be activated as the position of the new tip endothelial cell if there is another closer than a certain distance δ_4. This distance represents the range of action of the ligand Dll-4.

If the four conditions are met in $\mathbf{x}^*$, then a new subdomain is created. Let us assign the index l to the new subdomain $\Omega^l_{\text{TEC}}(t_{n+1})$, which is centered at $\mathbf{x}^* = \mathbf{x}^l_{\text{TEC}}$

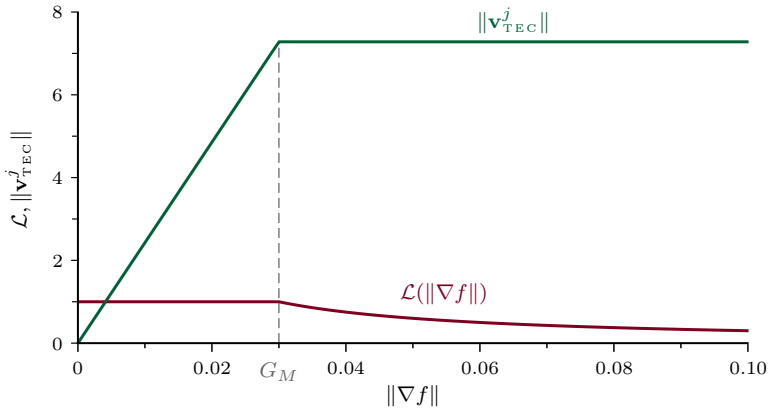

Figure 2.3. Limiting function and velocity modulus. *Limiting function* $\mathcal{L}(\cdot)$ *for the velocity of the tip endothelial cells plotted in red and velocity modulus* $\|\mathbf{v}^j_{\text{TEC}}\|$ *plotted in green. For this graph* $\chi = 242.67$ *and* $G_M = 0.03$.

and defined as

$$\Omega^l_{\text{TEC}}(t_{n+1}) = \left\{\mathbf{x} \in \Omega \,\middle|\, \|\mathbf{x} - \mathbf{x}^l_{\text{TEC}}\| \leq R_{\text{TEC}}\right\}, \tag{2.11}$$

If there are two or more points that satisfy the conditions, only one tip endothelial cell is created per time step. Inside the subdomain $\Omega^l_{\text{TEC}}(t_{n+1})$, the value of the concentration of endothelial cells is described by equation (2.3), merging thus the discrete component with the continuous description. This value is the ratio of the material produced in the subdomain by proliferation and the area swept in the movement of the tip endothelial cell, assuming that the problem is posed on a two-dimensional domain.

Migration of tip endothelial cells The subdomains $\{\Omega^j_{\text{TEC}}\}_{j=1,\ldots,N_{\text{TEC}}(t_n)}$ are updated using equation (2.1), which translates them into the direction of the gradient of angiogenic factor with a modulus proportional to this gradient through χ. In addition, the modulus of the velocity is affected by a function given by

$$\mathcal{L}\left(\|\nabla f\|\right) = 1 + \left(\frac{G_M}{\|\nabla f\|} - 1\right) \mathcal{H}\left(\|\nabla f\| - G_M\right) \tag{2.12}$$

where G_M is a constant. This function maintains the modulus of the velocity under a threshold, namely, $v_{\text{TEC,max}} = \chi G_M$. Both the function and its effect on the velocity are represented in figure 2.3.

Deactivation of tip endothelial cells The deactivation of tip endothelial cells is accomplished through two conditions. Whenever the value of the tumor angiogenic factor or its gradient is less than their activation thresholds, f_{act} and G_{act}, respectively, the corresponding TEC is deactivated, vanishing its associated subdomain.

2.2.5 The boundary value problem

The boundary value problem (2.4)–(2.10) determines the continuous part of the model. The tumor angiogenic factor diffuses throughout the domain Ω according to equation (2.4) and is consumed by the endothelial cells at a rate of B_u, as modeled by the reactive term in the equation. Free flux conditions are imposed on the boundary Γ through equation (2.6). The initial conditions for the tumor angiogenic factor at each time stage are described by equation (2.9). The dynamics of the endothelial cells are modeled by a phase-field equation (2.5), where c is the order parameter of the concentration of endothelial cells. If we assume that the reactive term $\mathcal{B}_p(f)\, c\mathcal{H}(c)$ is small, the evolution of c is such that it tends to adopt the configuration of minimum energy given by the energy functional:

$$\mathcal{E}(c) = \int_{\Omega} (\Psi_c + \Psi_s)\, d\mathbf{x}, \tag{2.13}$$

where Ψ_c is the chemical free energy and Ψ_s is the surface free energy. The chemical free energy, given by

$$\Psi_c = -\frac{c^2}{2} + \frac{c^4}{4}, \tag{2.14}$$

is a double-well, non-convex function with two local minima, each one representing a phase, as shown on the left-hand side of figure 2.4. One of the minima is at $c = 1$, where the concentration of endothelial cells is maximum, and the other is at $c = -1$, where there are no endothelial cells, but only host tissue cells. The local maximum in $c = 0$ corresponds to the capillary walls. The energy term Ψ_c leads to the separation of the phases. The chemical potential μ_c is given by $\mu_c = \Psi_c' = -c + c^3$, where Ψ_c' is the derivative of the chemical free energy with respect to c. The surface free energy is defined as

$$\Psi_s = \frac{1}{2}\lambda^2 \|\nabla c\|^2, \tag{2.15}$$

where λ is a length scale of the model. The surface term endows the capillary walls with an energy, penalizing the appearance of new sprouts. Equation (2.5)

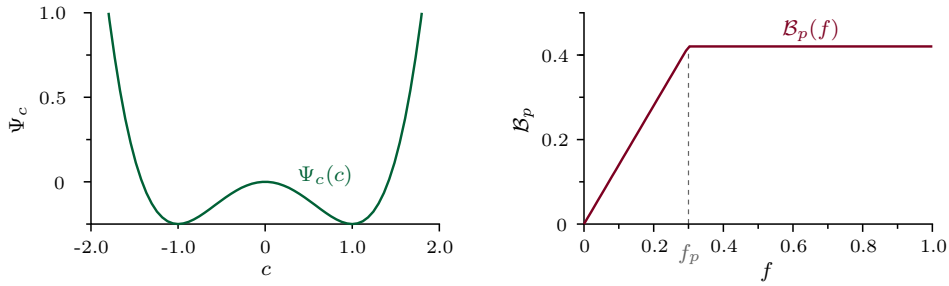

Figure 2.4. Energy functional and proliferation function. *Plot of the energy functional (left) that leads to phase separation and plot of the proliferation function (right) that controls the proliferation of the endothelial cells.*

also involves a reactive term that makes the theory non-conservative (Emmerich, 2008). This term is introduced to model the proliferation of endothelial cells in the presence of angiogenic factor (SECs). The proliferative rate function $\mathcal{B}_p(f)$, present in the reactive term, and given by

$$\mathcal{B}_p(f) = \begin{cases} B_p f & \text{if } f < f_p \\ B_p f_p & \text{if } f \geq f_p \end{cases}, \tag{2.16}$$

increases with the value of TAF until a threshold f_p. Above f_p the proliferation remains constant. The function is plotted on the right-hand side of figure 2.4. For the phase field equation, we also apply free flux boundary conditions on Γ, described by equations (2.7) and (2.8). At each time step, the initial condition for the phase field is defined by equation (2.10).

2.2.6 Parameters

Many of the parameters that characterize the equations of the model were obtained by Travasso *et al.* from observed values *in vivo* (see references in Travasso *et al.*, 2011b). On the contrary, those related with the tumor angiogenic factor quantity and the condition of the order parameter for TEC activation (c_{act}) are estimated for the simulation (we note that, in this context, the validation/calibration methodology for parameters presented in Hawkins-Daarud *et al.*, 2012 may be relevant). As the equations are written in dimensionless form, it is necessary to obtain the corresponding dimensionless parameters (referred to as the *in silico* value of the parameters) for those that come from *in vivo* observation. The length and time scales $L_0 = 1.25\,\mu\text{m}$ and $T_0 = 1560\,\text{s}$ allow retrieving physical values

from the simulation results. Table 2.1 presents all the parameters of the model, including the *in vivo* and *in silico* values.

2.3 Numerical method

In this section we propose a numerical method for solving the equations of the mathematical model. We consider separately the discrete component and the boundary value problem (2.4)–(2.10). We explain first the numerical method for the discrete component in subsection 2.3.1, where we describe how the discrete rules are considered and how the discrete component is merged with the continuous equations. Subsection 2.3.2 describes the algorithms utilized to discretize the continuous problem. Finally, we detail the implementation of the code in subsection 2.3.3. For the reader's convenience, we present a flowchart of the numerical method and the code in figure 2.6.

2.3.1 The discrete component

The numerical method for the discrete module of the theory is composed of two parts, namely, the update of the spatial domains Ω_{HYC} and Ω_{TEC} and the algorithm to overwrite the values of the fields f and c on Ω_{HYC} and Ω_{TEC}, respectively.

Update of the spatial domains of the discrete component

We define a sufficiently fine uniform grid of sample points (typically, twice as fine as that used for the continuous boundary value problem), where we calculate the values of the tumor angiogenic factor, its gradient, and the order parameter. With these evaluations we are able to determine whether the discrete rules for the activation and deactivation of the tip endothelial cells are satisfied. In addition, we calculate the value of the order parameter in those points which are closer than a distance δ_{nox} from the center of the subdomains $\{\Omega^i_{\text{HYC}}\}_{i=1,\dots,N_{\text{HYC}}}$ that permit us to deactivate the HYC according to the discrete rules. Finally, we evaluate the tumor angiogenic factor, its gradient, and the order parameter in the center of the subdomains $\{\Omega^i_{\text{TEC}}\}_{i=1,\dots,N_{\text{TEC}}(t_n)}$ to calculate the corresponding imposed order parameter c^j_{TEC} and velocity $\mathbf{v}^j_{\text{TEC}}$ necessary to move the subdomains using equation (2.1).

Table 2.1. In vivo *and* in silico *values of the parameters of the model. The* in vivo *parameters were obtained from experiments detailed in the references of Travasso* et al. *(2011b).*

Parameter	Symbol	*In vivo* value		*In silico* value
TEC radius	R_{TEC}	5	µm	4
HYC radius	R_{HYC}	5	µm	4
Nutrient and oxygen diffusion length	δ_{nox}	25	µm	20
Dll-4 range of action	δ_4	20	µm	16
Interface width	λ	1.25	µm	1
Diffusion constant	D	10^{-13}	$\mathrm{m^2\,s^{-1}}$	100
Constant mobility	M	10^{-15}	$\mathrm{m^2\,s^{-1}}$	1
Uptake rate constant	B_u	0.004	$\mathrm{s^{-1}}$	6.25
Proliferative rate	B_p			1.401
Chemotactic constant	χ			242.67
TAF production	f_{HYC}			1
TAF condition for highest proliferation	f_p			0.3
Order parameter condition for activation/deactivation	c_{act}			0.9
TAF condition for activation/deactivation	f_{act}			0.055
TAF gradient condition for activation/deactivation	G_{act}			0.01
TAF gradient for highest velocity	G_M			0.03

Impose the constraints on the fields $c^h(\mathbf{x}, t_n)$ and $f^h(\mathbf{x}, t_n)$

Since we will use isogeometric analysis to solve the boundary value problem (2.4)–(2.10), the phase field and the TAF field will be elements of a finite dimensional space. This is why we use the notation $c^h(\mathbf{x}, t_n)$ and $f^h(\mathbf{x}, t_n)$ with the superscript h. We have to impose f_{HYC} in $\{\Omega^i_{\text{HYC}}\}_{i=1,\dots,N_{\text{HYC}}}$ and c^j_{TEC} in Ω^j_{TEC}, $\forall j = 1, \dots N_{\text{TEC}}(t_n)$, according to equation (2.3). Let us illustrate how we overwrite the value of $c^h(\mathbf{x}, t_n)$ on a given subdomain $\Omega^j_{\text{TEC}}(t_n)$, where j is a fixed index that takes one of its admissible values, namely, $1, \dots, N_{\text{TEC}}(t_n)$. Let us define the template function $g^j_c : \Omega \mapsto [-1, 1]$ as

$$g^j_c(\mathbf{x}) = \left(\frac{c^j_{\text{TEC}} - 1}{2}\right) - \left(\frac{c^j_{\text{TEC}} + 1}{2}\right) \tanh\left(\frac{\|\mathbf{x} - \mathbf{x}^j_{\text{TEC}}\| - R_{\text{TEC}}}{2\epsilon}\right) \tag{2.17}$$

where $\epsilon = 0.1$. Note that g^j_c is a multidimensional generalization of an exact one-dimensional solution to the Cahn-Hilliard equation on an infinite domain. Thus, we overwrite the value of $c^h(\mathbf{x}, t_n)$, using a template function as close as possible to the fundamental solution of the partial differential equation (2.5). Figure 2.5 presents a one-dimensional illustration of g^j_c in which $\Omega^j_{\text{TEC}}(t_n) = (30, 40)$. Taking into account all of this, our goal is to find

$$\widetilde{c}^j(\mathbf{x}, t_n) = \begin{cases} g^j_c(\mathbf{x}) & \text{if } \mathbf{x} \in \Omega^j_{\text{TEC}}, \\ c(\mathbf{x}, t_n) & \text{otherwise.} \end{cases} \tag{2.18}$$

To undertake the coupling between the discrete and continuous parts of the algorithm, we need to find an approximation of $\widetilde{c}^j(\mathbf{x}, t_n)$ that lives in the finite dimensional space. Let us call Π the L^2 projection operator associated to the discrete space. We define $\widetilde{c}^{j,h}(\mathbf{x}, t_n) = \Pi\left(\widetilde{c}^j(\mathbf{x}, t_n)\right)$. This process can be repeated for all relevant j to obtain the overwritten field $\widetilde{c}^h(\mathbf{x}, t_n)$.

We proceed analogously to impose the constraints on the field $f^h(\mathbf{x}, t_n)$. This case is somewhat simpler because the imposed value f_{HYC} will always be greater than the value of the field $f^h(\mathbf{x}, t_n)$ due to the maximum principle satisfied by equation (2.4). Let us illustrate the process by imposing the restriction on $\Omega^i_{\text{HYC}}(t_n)$. We define the template function $g^i_f : \Omega \mapsto [0, f_{\text{HYC}}]$ as

$$g^i_f(\mathbf{x}) = \frac{1}{2} - \frac{1}{2}\tanh\left(\frac{\|\mathbf{x} - \mathbf{x}^i_{\text{HYC}}\| - R_{\text{HYC}}}{2\epsilon}\right). \tag{2.19}$$

Figure 2.5 shows a one-dimensional illustration of the template function. Since g^i_f will be greater than $f^h(\mathbf{x}, t_n)$ in $\Omega^i_{\text{HYC}}(t_n)$, we can define $\widetilde{f}^i(\mathbf{x}, t_n)$ as

$$\widetilde{f}^i(\mathbf{x}, t_n) = \max\left(f^h(\mathbf{x}, t_n), g^i_f(\mathbf{x})\right). \tag{2.20}$$

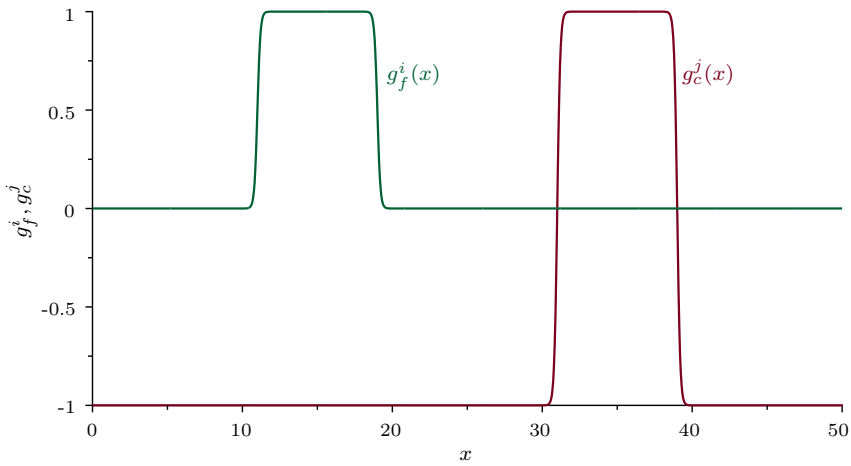

Figure 2.5. Template functions. *One-dimensional examples of the template functions used to merge the discrete component with the continuous variables. In green is plotted $g_f^i(x)$ and in red $g_c^j(x)$, where $\Omega^i_{\text{HYC}}(t_n) = (10, 20)$, $\Omega^j_{\text{TEC}}(t_n) = (30, 40)$, and $c^j_{\text{TEC}} = 1$.*

The process is finalized projecting $\widetilde{f^i}$ onto the discrete space as $\widetilde{f^{i,h}}(\mathbf{x}, t_n) = \Pi\left(\widetilde{f^i}(\mathbf{x}, t_n)\right)$, and repeating for all relevant i.

Remark:

1. Only when the value of c^j_{TEC} is greater than $c(\mathbf{x}^j_{\text{TEC}}, t_n)$, equation (2.18) reduces to
$$\widetilde{c^j}(\mathbf{x}, t_n) = \max\left(c^h(\mathbf{x}, t_n), g_c^j(\mathbf{x})\right). \tag{2.21}$$
However, in the opposite case, $c^j_{\text{TEC}} \leq c(\mathbf{x}^j_{\text{TEC}}, t_n)$, we also use the latter equation. We have verified that using this simplification rather than equation (2.18) does not lead to significant changes in the solutions.

2.3.2 The continuous equations

We begin by considering a weak form of equations (2.4) and (2.5). Let $\mathcal{V}$ denote the trial and weighting function spaces, which are assumed to be identical. The space $\mathcal{V}$ is a subset of $\mathcal{H}^2$, the Sobolev space of square integrable functions with square integrable first and second derivatives. The weak form of the problem is obtained by multiplying equations (2.4) and (2.5) with smooth functions, integrating over the domain, and applying integration by parts repeatedly under the assumption

of free flux boundary conditions. The problem may be stated as follows: find $f, c \in \mathcal{V}$ such that $\forall w, q \in \mathcal{V}$:

$$\left.\begin{aligned} &\left(w, \frac{\partial f}{\partial t}\right)_\Omega + (\nabla w, D\nabla f)_\Omega + (w, B_u f c\mathcal{H}(c))_\Omega = 0 \\ &\left(q, \frac{\partial c}{\partial t}\right)_\Omega + (\nabla q, M\nabla\mu_c)_\Omega \\ &\qquad + \left(\Delta q, M\lambda^2\Delta c\right)_\Omega \\ &\qquad - (q, \mathcal{B}_p(f)\, c\mathcal{H}(c))_\Omega = 0 \end{aligned}\right\}, \tag{2.22}$$

where $(\cdot,\cdot)_\Omega$ is the $\mathcal{L}^2$ inner product with respect to the domain Ω. We make use of the Galerkin method to obtain the spatial discretization of the previous weak formulation. We approximate equation (2.22) by the following variational problem over the finite dimensional spaces: find $f^h, c^h \in \mathcal{V}^h \subset \mathcal{V}$ such that $\forall w^h, q^h \in \mathcal{V}^h \subset \mathcal{V}$:

$$\left.\begin{aligned} &\left(w^h, \frac{\partial f^h}{\partial t}\right)_\Omega + \left(\nabla w^h, D\nabla f^h\right)_\Omega \\ &\qquad + \left(w^h, B_u f^h c^h \mathcal{H}\left(c^h\right)\right)_\Omega = 0 \\ &\left(q^h, \frac{\partial c^h}{\partial t}\right)_\Omega + \left(\nabla q^h, M\nabla\mu\left(c^h\right)\right)_\Omega \\ &\qquad + \left(\Delta q^h, M\lambda^2\Delta c^h\right)_\Omega \\ &\qquad - \left(q^h, \mathcal{B}_p\left(f^h\right) c^h \mathcal{H}\left(c^h\right)\right)_\Omega = 0 \end{aligned}\right\}. \tag{2.23}$$

Here f^h is defined as

$$f^h(\mathbf{x}, t) = \sum_{A=1}^{n_b} f_A(t)\, N_A(\mathbf{x}), \tag{2.24}$$

where n_b is the dimension of the discrete space $\mathcal{V}^h$ and f_A are the so-called control variables, which act as coefficients of the basis functions N_A. The functions c^h, w^h, and q^h, which also live in the space $\mathcal{V}^h$, are defined analogously. Since we will use a conforming discretization, the relation $\mathcal{V}^h \subset \mathcal{V}$ holds and the discrete functions are required to be in $\mathcal{H}^2$. This condition is satisfied by the globally $\mathcal{C}^1$-continuous basis functions that we consider in this thesis, by means of isogeometric analysis, as explained in subsection 1.2.3. In particular, as we will only deal with two-dimensional squared geometries in this chapter, we use B-splines of order $p = 2$.

We integrate in time using the generalized-α method (Chung and Hulbert, 1993; Jansen *et al.*, 2000). The generalized-α method is a second-order accurate, unconditionally A-stable method with controllable high-frequency dissipation that

can be easily implemented within an adaptive time step framework. All these features make it a good choice for highly nonlinear problems (Bazilevs *et al.*, 2006, 2010; Gomez *et al.*, 2013) such as that addressed in this thesis (for time integrators specifically designed for phase-field models, the reader is referred to Gomez and Hughes, 2011; Liu *et al.*, 2013). In addition, we use a time-step size selection algorithm that considerably reduces the computational time. This algorithm was first proposed for reaction-diffusion equations and was then utilized for other mathematical models, such as in Gomez *et al.* (2008). After space and time discretization, we obtain a non-linear system which is solved using a predictor multi-corrector algorithm based on the Newton-Raphson method.

We use the notation $\dot{f}_n^h, f_n^h, \dot{c}_n^h, c_n^h$ for the fully discrete solutions of the tumor angiogenic factor time derivative, the tumor angiogenic factor, the phase-field time derivative, and the phase-field, respectively. The problem can be stated as: given $\dot{f}_n^h, f_n^h, \dot{c}_n^h, c_n^h$, and $\Delta t_n = t_{n+1} - t_n$, find $\dot{f}_{n+1}^h, f_{n+1}^h, \dot{c}_{n+1}^h, c_{n+1}^h$ such that:

$$\left.\begin{aligned} &\left(w^h, \dot{f}^h_{n+\alpha_m}\right)_\Omega + \left(\nabla w^h, D\nabla f^h_{n+\alpha_f}\right)_\Omega \\ &\qquad + \left(w^h, B_u f^h_{n+\alpha_f} c^h_{n+\alpha_f} \mathcal{H}\left(c^h_{n+\alpha_f}\right)\right)_\Omega = 0 \\ &\left(q^h, \dot{c}^h_{n+\alpha_m}\right)_\Omega + \left(\nabla q^h, M\nabla\mu\left(c^h_{n+\alpha_f}\right)\right)_\Omega \\ &\qquad + \left(\Delta q^h, M\lambda^2 \Delta c^h_{n+\alpha_f}\right)_\Omega \\ &\qquad - \left(q^h, \mathcal{B}_p\left(f^h_{n+\alpha_f}\right) c^h_{n+\alpha_f} \mathcal{H}\left(c^h_{n+\alpha_f}\right)\right)_\Omega = 0 \end{aligned}\right\}, \tag{2.25}$$

where

$$\dot{f}^h_{n+\alpha_m} = \dot{f}^h_n + \alpha_m\left(\dot{f}^h_{n+1} - \dot{f}^h_n\right), \tag{2.26}$$

$$f^h_{n+\alpha_f} = f^h_n + \alpha_f\left(f^h_{n+1} - f^h_n\right), \tag{2.27}$$

$$f^h_{n+1} = f^h_n + \Delta t_n \dot{f}^h_n + \gamma\Delta t_n\left(\dot{f}^h_{n+1} - \dot{f}^h_n\right), \tag{2.28}$$

$$\dot{c}^h_{n+\alpha_m} = \dot{c}^h_n + \alpha_m\left(\dot{c}^h_{n+1} - \dot{c}^h_n\right), \tag{2.29}$$

$$c^h_{n+\alpha_f} = c^h_n + \alpha_f\left(c^h_{n+1} - c^h_n\right), \tag{2.30}$$

$$c^h_{n+1} = c^h_n + \Delta t_n \dot{c}^h_n + \gamma\Delta t_n\left(\dot{c}^h_{n+1} - \dot{c}^h_n\right), \tag{2.31}$$

$$\gamma = \frac{1}{2} + \alpha_m - \alpha_f, \tag{2.32}$$

$$\alpha_m = \frac{1}{2}\left(\frac{3-\rho_\infty}{1+\rho_\infty}\right), \tag{2.33}$$

$$\alpha_f = \frac{1}{1+\rho_\infty}, \tag{2.34}$$

and ρ_∞ is the spectral radius of the amplification of the matrix as $\Delta t \to \infty$. We obtain second-order accuracy if $\gamma = \frac{1}{2} + \alpha_m - \alpha_f$ is satisfied and unconditional stability (for a linear problem) provided that $\alpha_m \geq \alpha_f \geq \frac{1}{2}$.

Now, let $\dot{\mathbf{F}}^n$, $\mathbf{F}^n$, $\dot{\mathbf{C}}^n$, and $\mathbf{C}^n$ be the vector of degrees of freedom of $\dot{f}_n^h$, f_n^h, $\dot{c}_n^h$, and c_n^h, respectively, and $\mathbf{S}^n = \{\mathbf{F}^n, \mathbf{C}^n\}^T$ be a vector of all the degrees of freedom. The time stepping scheme may be implemented as follows: given $\dot{\mathbf{S}}^n$, $\mathbf{S}^n$, and Δt_n, find $\dot{\mathbf{S}}^{n+1}$ and $\mathbf{S}^{n+1}$ such that $\mathbf{R} = 0$ where

$$\mathbf{R} = \begin{Bmatrix} R_A^f \\ R_A^c \end{Bmatrix}, \tag{2.35}$$

$$\left.\begin{aligned} R_A^f &= \left(N_A, \dot{f}^h_{n+\alpha_m}\right)_\Omega + \left(\nabla N_A, D\nabla f^h_{n+\alpha_f}\right)_\Omega \\ &\qquad + \left(N_A, B_u f^h_{n+\alpha_f} c^h_{n+\alpha_f} \mathcal{H}\left(c^h_{n+\alpha_f}\right)\right)_\Omega \\ R_A^c &= \left(N_A, \dot{c}^h_{n+\alpha_m}\right)_\Omega + \left(\nabla N_A, M\nabla\mu\left(c^h_{n+\alpha_f}\right)\right)_\Omega \\ &\qquad + \left(\Delta N_A, M\lambda^2 \Delta c^h_{n+\alpha_f}\right)_\Omega \\ &\qquad - \left(N_A, \mathcal{B}_p\left(f^h_{n+\alpha_f}\right) c^h_{n+\alpha_f} \mathcal{H}\left(c^h_{n+\alpha_f}\right)\right)_\Omega \end{aligned}\right\}. \tag{2.36}$$

Equating the residual to zero, we define a non-linear system of algebraic equations. We use the Newton-Raphson method to solve the system, which leads to a two-stage predictor-corrector algorithm:

1. *Predictor stage*: Set

$$\dot{\mathbf{S}}^{n+1,(0)} = \frac{\gamma - 1}{\gamma} \dot{\mathbf{S}}^n, \tag{2.37}$$

$$\mathbf{S}^{n+1,(0)} = \mathbf{S}^n. \tag{2.38}$$

2. *Multi-corrector stage*: Repeat the following steps for $i = 1, 2, \ldots, i_{max}$ or until $\|\mathbf{R}_f^{n+1,(i)}\| / \|\mathbf{R}_f^{n+1,(0)}\| \leq \Upsilon_{\text{N-R}}$ and $\|\mathbf{R}_c^{n+1,(i)}\| / \|\mathbf{R}_c^{n+1,(0)}\| \leq \Upsilon_{\text{N-R}}$, where $\Upsilon_{\text{N-R}}$ is a given tolerance.

   (a) Evaluate the iterates at the α-levels:

$$\dot{\mathbf{S}}^{n+\alpha_m,(i)} = \dot{\mathbf{S}}^n + \alpha_m \left(\dot{\mathbf{S}}^{n+1,(i-1)} - \dot{\mathbf{S}}^n\right), \tag{2.39}$$

$$\mathbf{S}^{n+\alpha_f,(i)} = \mathbf{S}^n + \alpha_f \left(\mathbf{S}^{n+1,(i-1)} - \mathbf{S}^n\right). \tag{2.40}$$

(b) Assemble the residual vector and tangent matrix:

$$\mathbf{R}^{n+1,(i)}; \qquad \mathbf{K}^{n+1,(i)} = \nabla_{\dot{\mathbf{S}}^{n+1,(i)}} \mathbf{R}^{n+1,(i)}, \tag{2.41}$$

where

$$\nabla_{\dot{\mathbf{S}}^{n+1,(i)}}(\cdot) = \left\{ \begin{array}{c} \frac{\partial(\cdot)}{\partial \dot{\mathbf{F}}^{n+1,(i)}} \\ \frac{\partial(\cdot)}{\partial \dot{\mathbf{C}}^{n+1,(i)}} \end{array} \right\}. \tag{2.42}$$

(c) Solve the following linear system using the GMRES algorithm:

$$\mathbf{K}^{n+1,(i)} \Delta \dot{\mathbf{S}}^{n+1,(i)} = -\mathbf{R}^{n+1,(i)}. \tag{2.43}$$

(d) Use $\Delta \dot{\mathbf{S}}^{n+1,i}$ to update the iterates:

$$\dot{\mathbf{S}}^{n+1,(i)} = \dot{\mathbf{S}}^{n+1,(i-1)} + \Delta \dot{\mathbf{S}}^{n+1,(i)}, \tag{2.44}$$

$$\mathbf{S}^{n+1,(i)} = \mathbf{S}^{n+1,(i-1)} + \gamma \Delta t_n \Delta \dot{\mathbf{S}}^{n+1,(i)}. \tag{2.45}$$

The implementation of an adaptive time step reduces the computation time of the numerical simulations more than an order of magnitude compared with maintaining a constant time step. Further, it permits us to analyze the accuracy of the method, regarding the time integration. To define an adaptive time step, we make use of the fact that the generalized-α method transforms into the backward Euler method by setting $\gamma = \alpha_m = \alpha_f = 1$. Comparing the results from both methods we are able to evaluate an error estimate e and to update the time-step size using the formula

$$F(e, \Delta t) = \rho \left(\frac{\Upsilon_{\Delta t}}{e} \right)^{\frac{1}{2}} \Delta t, \tag{2.46}$$

where, according to the values suggested in Lang (1995), the safety coefficient ρ is set to 0.9 and the tolerance of the method $\Upsilon_{\Delta t}$ is set to 10^{-3}. Thus, for a certain time-step n, we can implement a time-step size adaptive algorithm as follows:

Algorithm 1 Adaptive time-step size

Given: $\dot{\mathbf{S}}^n$, $\mathbf{S}^n$, and Δt_n,

1: Compute $\mathbf{S}_{\text{BE}}^{n+1}$ using backward Euler and Δt_n
2: Compute $\mathbf{S}_{\alpha}^{n+1}$ using generalized-α and Δt_n
3: Calculate $e_{n+1} = \frac{\|\mathbf{S}_{\text{BE}}^{n+1} - \mathbf{S}_{\alpha}^{n+1}\|}{\|\mathbf{S}_{\alpha}^{n+1}\|}$
4: **if** $e_{n+1} > \Upsilon_{\Delta t}$ **then**
5: Recalculate time-step size $\Delta t_n \leftarrow F(e_{n-1}, \Delta t_n)$
6: **goto** 1
7: **else**
8: Update time-step size $\Delta t_{n+1} = F(e_{n+1}, \Delta t_n)$
9: **continue**
10: **end if**

2.3.3 Code development and implementation

Open or free source isogeometric codes such as PetIGA, igatools, or GeoPDEs focus on the resolution of partial differential equations. As we want to solve a hybrid model that involves discrete agent-based elements besides the partial differential equations, we have developed a home-made code based on the above-explained numerical method[1]. The most prominent features of this code are: (1) It is capable of handling both discrete agents and partial differential equations; (2) it runs efficiently sequentially and in parallel (the code has been tested with up to 512 processors); (3) it can perform simulations both in two- and three-dimensions with any NURBS geometry of arbitrary degree; (4) it uses the generalized-α method and an adaptive time-step for the time iterations, the Newton-Raphson method for nonlinear system, and GMRES as linear parallel solver; (5) it finds efficiently parametric coordinates of a physical point in parallel.

The flow of the code is as follows (see figure 2.6). The code starts by initializing all the appropriate variables and by reading the input files. The most important of these input files is the one that contains the mesh, which was previously generated with our own meshing algorithm. If the mesh contains several patches (as it is the case for parallel simulations), this file is accompanied by connectivity files that particularize the connections and continuity restrictions among contiguous patches. Then, the code enters a time loop with a preset time step (typically 10^{-4}). Note that this time step will automatically adapt to the requirements of the model, so the initial value is just a first approximation. Each time iteration the code goes through three subroutines or modules. The first one is the HYC module that

[1] In addition, by the time this thesis started, these codes were just not available.

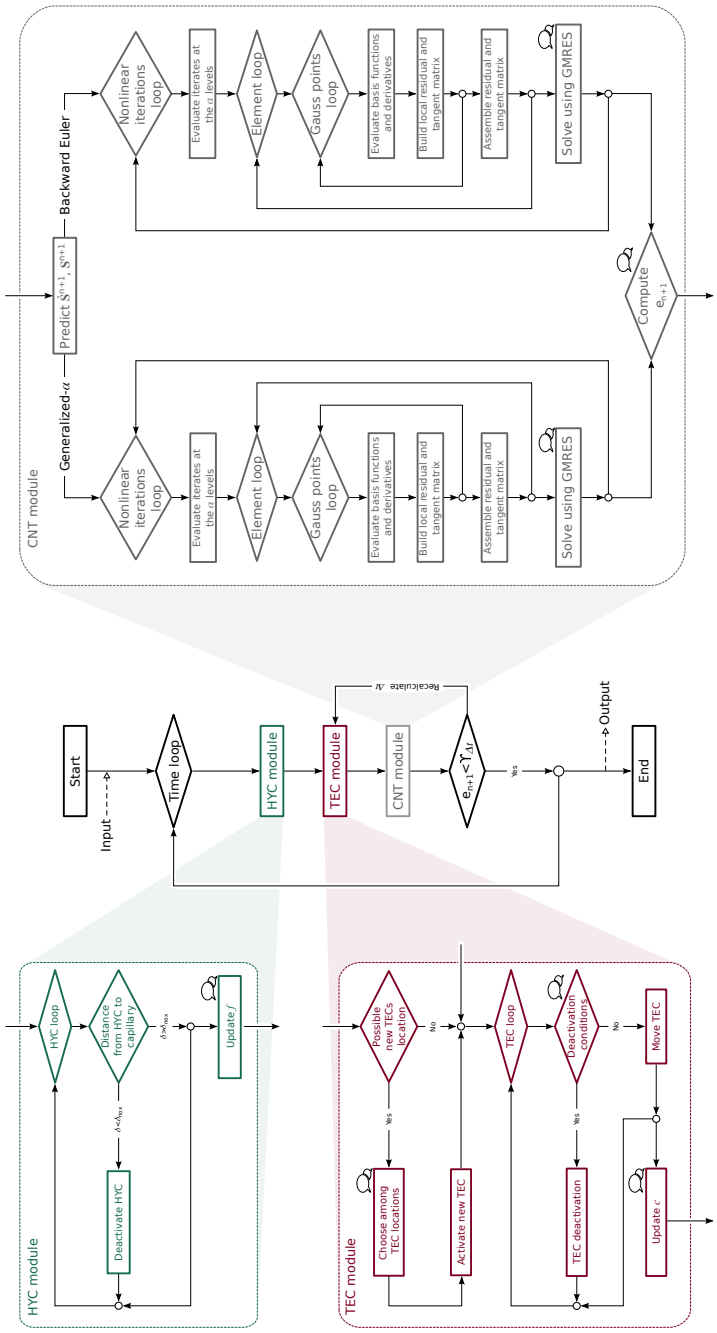

Figure 2.6. Flowchart of the numerical method. *This flowchart highlights the two discrete parts (HYC and TEC modules, on the left-hand side) and the continuous solver (*CNT *module, on the right-hand side). In addition, as the code can run in parallel, we detailed with a bubble symbol those points in the code where there is communication among processors.*

handles the HYC discrete agents. It loops through all HYC deactivating those which are located closer than a distance δ_{nox} to a capillary and updates the TAF field f using equation (2.20). The second module, namely the TEC module, deals with tip endothelial cells. It checks whether any point in the sample point grid fulfills the activation conditions specified in subsection 2.2.4 and activates a new TEC if appropriate. Then, it loops through all TECs, deactivating those that fail to meet the deactivation conditions detailed in subsection 2.2.4 and moving those that remain active following equation (2.2). Finally, using equation (2.21), the phase-field c is updated. Following these two modules for the discrete components of the model comes the CNT module that solves the updated continuous fields c and f. This module encodes the first three steps of algorithm 1: It computes the solution of the continuous model using both backward Euler and generalized-α methods and then calculates the relative error e_{n+1} with respect to the generalized-α solution of the time step. For computing the solution of the continuous model, the code uses the two-stage, predictor-corrector algorithm described in the previous subsection 2.3.2, as shown in figure 2.6. After the modules, the flow of the code returns to the main thread, where the relative error is compared with a given tolerance $\Upsilon_{\Delta t}$, as in algorithm 1. If the error is greater than the tolerance, the time-step size is recomputed using equation (2.46). Note that the code does not return to the beginning of the time step, but to the TEC loop instead, because the previous calculations remain equal. Contrarily, if the relative error is below the tolerance, the time-step size is updated (also with equation (2.46)) and time iteration ends. The simulation continues until there are no HYCs, neither TECs, and all TAF is consumed. Finally, prior to termination, the code outputs the necessary information to post-process the results (post-processing is also done with a home-made code and visualization with Paraview Ahrens *et al.*, 2005).

As mentioned above, this code can run in parallel using message passing interface (MPI) protocol. Note that in figure 2.6 at certain points of the flowchart appears a bubble symbol. It is only at those points that the processors share information with each other. Great care has been taken to reduce these communications to a minimum in order to improve the efficiency of the code. The paralelization of the code is done by dividing the mesh into rectangular (in the parametric space) patches, so that each processor takes care of one patch. In order to generate these patches, our mesh generator code first generates a single-patch geometry and then divides it in multiple patches by inserting knots at those knot lines selected as processor division lines until the local continuity of the mesh reduces to $\mathcal{C}^0$[2]. This strategy provides each processor with its own mesh (one patch) so that it can perform calculations independently from other processors during a great part of

[2]Knot insertion does not change the NURBS mesh geometrically or parametrically, thus the patches match.

the simulations. However, the original continuity ($\mathcal{C}^1$ for our fourth order problem) must be enforced at certain stages of the code, namely, in the linear solver and in the c and f updates in the discrete modules (as shown in figure 2.6 by the above-mentioned symbols). To do it, the code uses the continuity constraints created by the mesh generator which are added to the global linear system. In our particular case, $\mathcal{C}^1$ is maintained across processors by enforcing the two last control points of one processor to be aligned with the two first control points of the next processor in one direction.

One of the major challenges in the implementation of this hybrid mathematical model is to evaluate efficiently the continuous fields at physical points to assess the discrete rules. The challenge stems from two facts. First, the discrete agents may be located at any point in the physical domain: HYCs are initialized at random positions and TECs, although they get activated at known points (the sample grid), they can move to any point within the physical domain. Therefore, to compute the continuous fields at the evaluation points we first have to invert the mapping to retrieve the parametric coordinates each time step and for each evaluation point[3]. This would not suppose a major computational cost if it were not for the second fact: the code must be able to deal with complex, three-dimensional geometries and with multiple patches that live in different processors. Hence, for each evaluation point and each time step, the code must solve a nonlinear system (because the mapping is nonlinear for complex geometries) for each patch or processor. Furthermore, to assess a discrete rule of a discrete agent located in one processor, we need to evaluate the continuous fields at points that may or may not lie in the same processors. This increases the communication among processors, which, if not addressed in an efficient way, results in unmanageable computational times.

2.4 Results and discussion

In this section we present some numerical results of our numerical method for the tumor angiogenesis model. We begin with the description of the development of a vascular network through a numerical example. We also show the effect of the time-step size adaptivity. Next, we present the influence of relevant parameters of the model in a parametric study. Finally, we conclude the section with an analysis of different examples with variations in the initial conditions.

[3] If, on the contrary, the evaluation points were restricted to a set of *a priori* fixed points, we could invert the mapping just once at the initialization of the code.

2.4.1 Numerical example

We perform this numerical example on a square domain $\overline{\Omega} = [0, 300]^2$ which represents a tissue of 375 µm × 375 µm. We define a mesh composed by 256^2 quadratic elements that spans all the domain. The simulation implements the numerical method described in section 2.3, including the adaptive time stepping scheme presented in algorithm 1.

We establish the following initial conditions for this numerical example: The value of the order parameter is set to minus one, $c = -1$, in all the domain, except for a stripe of constant width at the bottom of the domain, where we set $c = 1$. This stripe represents a pre-existent 37.5 µm wide blood vessel (note that at the scale considered in this example, the average capillary width varies from 5 µm to 10 µm Shiu *et al.*, 2005). At the beginning of the simulation $\Omega_{\text{TEC}}(t_0) = \varnothing$ and $\Omega_{\text{HYC}}(t_0) = \bigcup_{j=1}^{200} \Omega^j_{\text{HYC}}(t_0)$, where the $\mathbf{x}^j_{\text{HYC}}$, $j = 1, \ldots, 200$, are randomly distributed in Ω. We employ periodic boundary conditions in the horizontal direction and free flux conditions in the vertical direction. The above-described initial configuration, shown in figure 2.7, simulates an avascular tumor and its environment in a tissue. The tissue is square, although the implementation of the periodic boundary conditions allows the vasculature and the tumor angiogenic factor to spread horizontally without reaching the end of the domain in this direction. The tumor is modeled as 200 hypoxic cells, Ω_{HYC}, and the environment

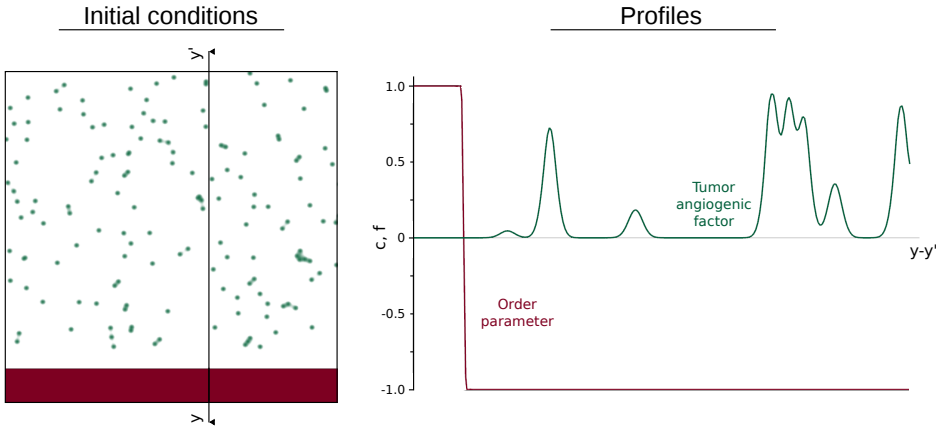

Figure 2.7. Initial conditions. *Initial conditions of the numerical examples of figures 2.8 and 2.10. On the left-hand side is plotted a square domain ($\overline{\Omega} = [0, 300]^2$) that represents a tissue with an initial capillary at the bottom (red) and 200 randomly-distributed hypoxic cells (green). The profiles of the order parameter and the tumor angiogenic factor along $y - y'$ are plotted on the right-hand side.*

is composed by host cells, $c = -1$, and endothelial cells forming a capillary, $c = 1$.

Figure 2.8 shows snapshots of the numerical example at different times (the interested can find the full simulation in video S2.1 in the supporting information). The tumor angiogenic factor produced by the hypoxic cells diffuses from them throughout the domain, filling it. As the diffusible factor reaches the endothelial cells, they consume it. For a time lapse there is a pseudo-equilibrium situation, in which all the domain is filled with tumor angiogenic factor and the TAF produced is consumed by the endothelial cells. This situation is maintained, until the factor pervades the capillary in a point with enough quantity to activate a tip endothelial cell. Figure 2.8b presents a snapshot several time steps after the pseudo-equilibrium is broken. The incipient capillary starts to take shape starting by a single cell followed by proliferative cells in the stalk of the sprout. The proliferation entails a consumption of the tumor angiogenic factor that becomes more evident in figure 2.8c. The capillary continues growing and new sprouts appear forming branches (figures 2.8d and 2.8e). During the simulation the tip endothelial cells find other endothelial cells in their growing direction. In these cases (see details in figures 2.8f and 2.8g) they merge one with another originating anastomoses. The growth and branching proceeds (figure 2.8h) until all the hypoxic cells become normoxic. This process creates a vascular pattern characteristic of tumor angiogenesis, shown in figure 2.8i.

Figure 2.9 shows the evolution of the time step size, Δt, with respect to time, t. At the beginning of the simulation, the Δt is set to 10^{-4}. Then it follows an increasing trajectory, along which the time step becomes larger. During this period, the dominating phenomenon is the diffusion of the tumor angiogenic factor. Also several new capillaries appear at the end of ascending slope, characterized by little descends in the time-step size. The time step size acquires its maximum value in the vicinity of $t = 19$. From this point, the time-step curve presents a global descending trend with several fluctuations. This implies a deceleration of the numerical method related with the increment in complexity of the vascular network. The local minima of the fluctuations correspond to the creation of new sprouts.

2.4.2 Parametric study of the model

Here we present a study of two of the most biologically relevant parameters of the model: B_p, that controls the proliferation, and χ, that alters the chemotactic velocity. The characteristics of the domain size, mesh, and initial and boundary conditions are the same as those used for the numerical example in subsection 2.4.1. All the parameters of the model, except those object of the study, maintain the

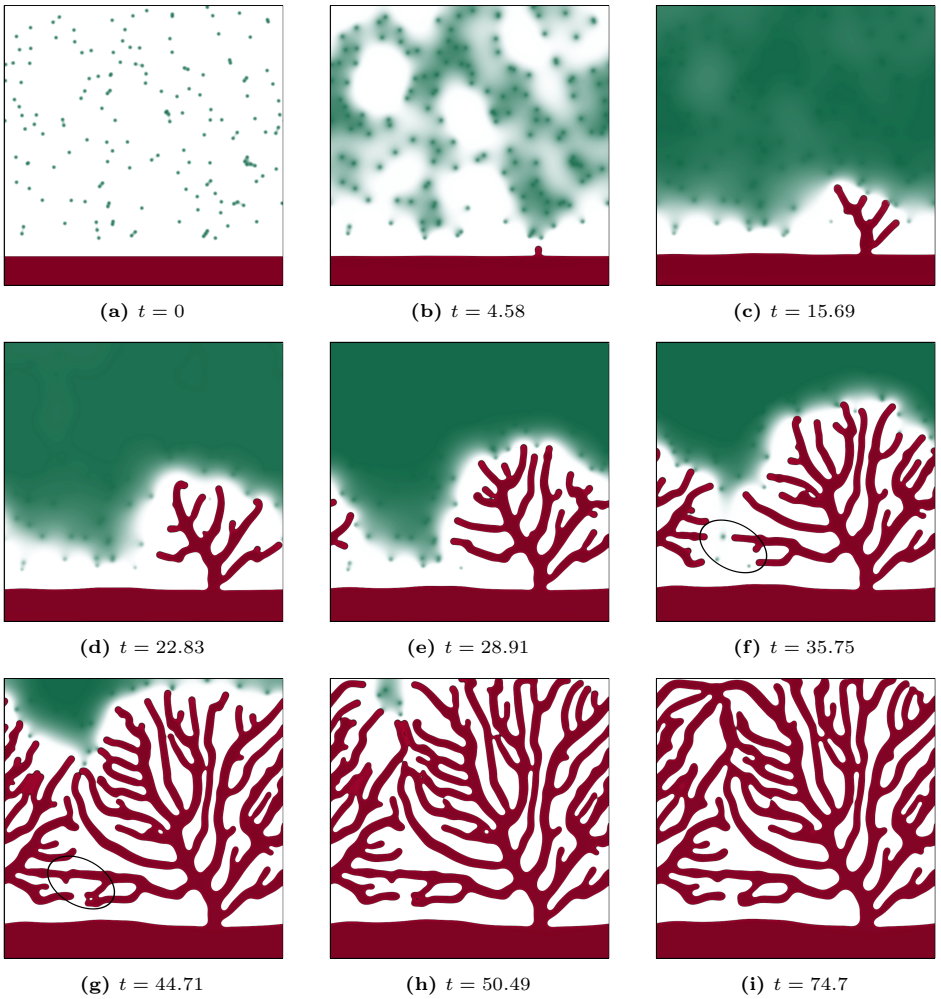

(a) $t = 0$ **(b)** $t = 4.58$ **(c)** $t = 15.69$

(d) $t = 22.83$ **(e)** $t = 28.91$ **(f)** $t = 35.75$

(g) $t = 44.71$ **(h)** $t = 50.49$ **(i)** $t = 74.7$

Figure 2.8. Snapshots of the formation of a vascular pattern at different times. *The parameters used for this numerical example are those presented in table 2.1 and the domain is* $\overline{\Omega} = [0, 300]^2$. *The tumor angiogenic factor (green) is produced by randomly-distributed hypoxic cells and promotes the growth of new capillaries (red) from the initial one situated at the bottom of the domain. In their growth, the capillaries fuse one with another (anastomosis) as shown in the highlighted areas. The final pattern shows the disorganized sprouting and tortuous capillaries characteristic of tumor angiogenesis.*

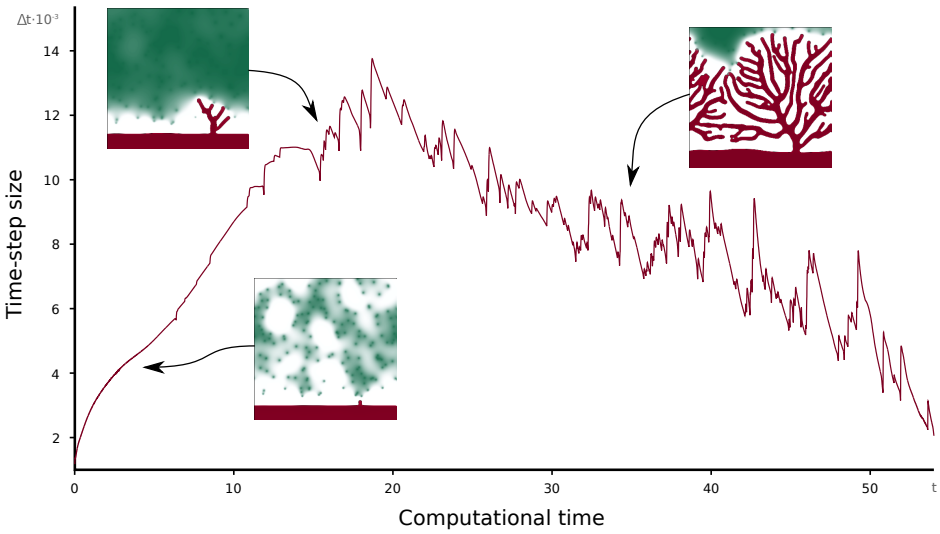

Figure 2.9. Time-step size. *Evolution of the time-step size (Δt) with respect to time (t) of the numerical example of figure 2.8 using the adaptive time-step algorithm 1. The snapshots show captures of the evolution of the capillary growth at different instants. The time-step size increases at the beginning when there are few new capillaries until a maximum around $t = 19$. From this point the evolution of the time step is characterized by a decrease in its size due to an increment in the complexity in the capillaries pattern.*

values given in table 2.1.

We used our numerical method to perform nine simulations (figure 2.10) in which the parameters take the following values: 50, 100, and 130 % of B_p (as given in table 2.1) and 16, 100, and 200 % of χ (as given in table 2.1). The disposition of the simulations is such that the one with lower proliferation and chemotactic velocity is in the bottom-left corner and the one with the highest parameter values is in the opposite corner. In the center of the grid is shown the final pattern of the numerical example of subsection 2.4.1, which we take as reference point for comparison purposes.

The resulting vascular networks present different characteristic patterns. If we compare the simulations within the same row, we observe a decrease in the capillary width as the chemotactic velocity increases. This behavior is produced by the fact that the stalk endothelial cells are provided with less time to proliferate. An analysis of the second column, shows a variation in the capillary width driven by the proliferative parameter. As B_p increases, so does the width of the capillaries. Furthermore, these simulations show sparser patterns when the proliferation is

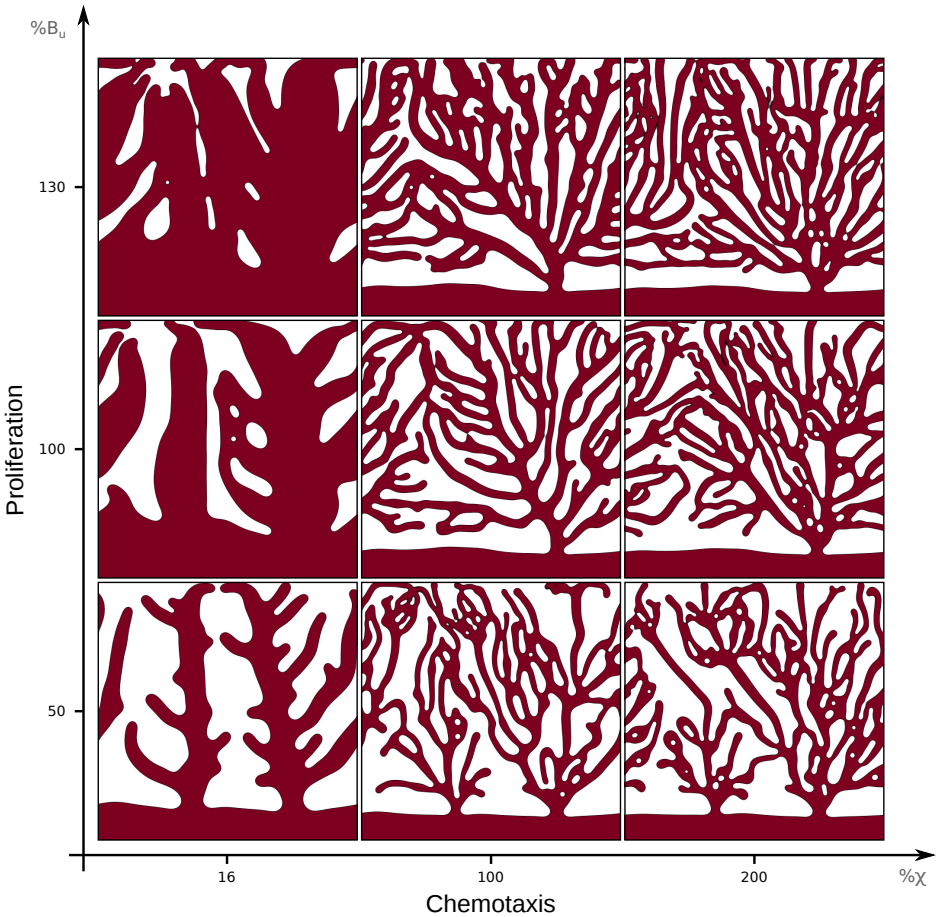

Figure 2.10. Parametric study of the model. *Comparison of nine stationary patterns resulting from different parameter combinations. The value of the parameters is shown in the axis as a percentage of the proliferation (B_u) and chemotaxis (χ) from table 2.1. The nine patterns evolved from the same initial conditions defined in figure 2.7.*

low. It is remarkable the difference in the patterns of the first column and the rest. The low value of the chemotactic velocity, 16 % of χ, gives rise to very wide capillaries. In addition, within this column we can easily appreciate the influence of the proliferation rate. When it is low, the capillaries are over-dimensioned, but with well-defined boundaries. Conversely, they become a mass of endothelial cells that spans almost all the domain when the proliferation is high as shown in the snapshot in the top-left corner.

2.4.3 Influence of the hypoxic cell distribution and initial capillaries

We study the influence of HYCs distribution and initial capillaries by performing several simulations on the domain $\overline{\Omega} = [0, 700]^2$, which represents a tissue of 875 µm × 875 µm. Note that the surface of the domain is approximately 5.4 times larger than that of the previous examples. However, we use the same mesh composed by 256^2 quadratic elements. We implement our numerical method and the adaptive time step scheme given in algorithm 1. As initial conditions, we set diverse capillary configurations, maintaining the width of the vessels to 37.5 µm. The location of the initial hypoxic cells is random and different between the numerical examples. The tumor angiogenic factor is initially zero in $\Omega \backslash \Omega_{\text{HYC}}(t_0)$, and there are no TECs at the beginning of the simulations, therefore, $\Omega_{\text{TEC}}(t_0) = \varnothing$.

We present in figure 2.11 the results of four different numerical examples with an initial capillary at the bottom of each domain. We also present the full evolution of the top-left simulation in video S2.2 in the supporting information. Each simulation has a different random distribution of 200 hypoxic cells according to a uniform density function. The objective of these simulations is double. On the one hand, these simulations serve as proof for the accuracy of the method. Although we use here the same mesh as in subsection 2.4.1 for a domain with a surface approximately 5.4 times larger, the numerical method is still able to capture the more complex vascular pattern with accuracy. On the other hand, these simulations allow us to perform an analysis of the different patterns formed under the influence of diverse initial hypoxic cells. From figure 2.11 we may conclude that the final patterns hold similar characteristics, regarding the width of capillaries, the number of branches, and the density of the pattern. Note that, because the model does not include haptotaxis, the number of anastomosis events in all simulations is low and most of them are mainly located at the position of hypoxic cells. In addition, as highlighted in the left-hand side plots of the figure, TECs get deactivated even in the proximity of other capillaries. This phenomenon is an artifact result of the mathematical model because TECs are only guided by chemotaxis. In this particular case, TECs should have anastomosed

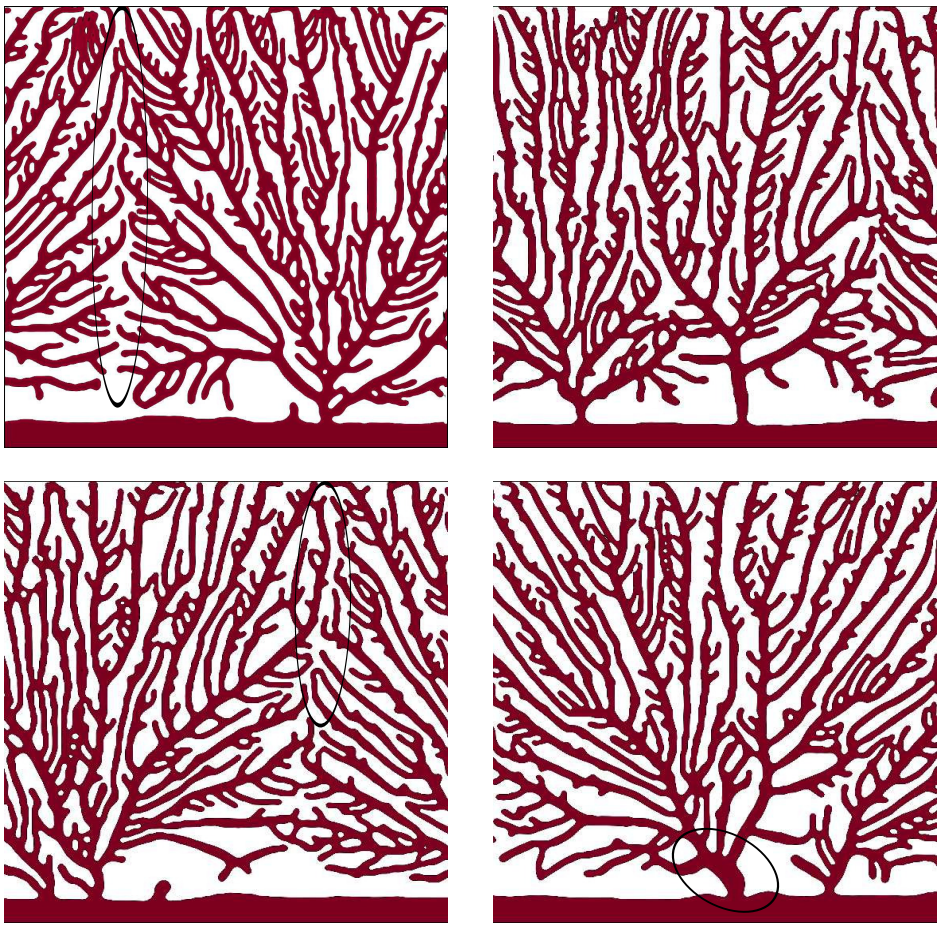

Figure 2.11. Numerical examples of the model with different randomly distributed hypoxic cells on the domain $\overline{\Omega} = [0, 700]^2$. *The patterns present similar characteristics in all four simulations regarding the width and number of capillaries and the density of the network.*

and formed vessel loops with nearby capillaries following mechanotactic cues. If haptotaxis and mechanotaxis were included in the model, anastomosis events would be more frequent and not determined by HYC locations. We also observe differences in the distance between the sprouts that grow from the main initial capillary. Usually, the growth from the initial capillary occurs when the pseudo-equilibrium situation mentioned in subsection 2.4.1 is broken. Thereafter, the

few capillaries that originate from the initial one get soon deactivated due to the scarcity of TAF in the region. One remarkable difference in the patterns is the wide capillary highlighted in the bottom-right plot. This situation is caused by the initial conditions of that particular simulation: Several initial HYCs gathered in a small region and surrounded by an empty zone produce great amounts of TAF promoting high SEC proliferation. Finally, as the model does not include the characteristic capillary regression observed in tumor-induced angiogenesis, the final pattern is full of short, useless vessels that do not allow blood flow.

Finally, figure 2.12 shows three numerical examples (see also videos S2.3 to S2.5 in the supporting information). We performed each of the simulations with different initial conditions for the hypoxic cell distribution and the initial capillaries. We show these initial configurations on the left-hand side snapshots of figure 2.12, while the correspondent final results are shown on the right-hand side snapshots. For the simulation in the first row, we choose a circular initial capillary surrounding two hundred hypoxic cells randomly distributed in the domain according to a uniform density function. This configuration could be interpreted as a two-dimensional approach of an *in vivo* assay of angiogenesis in a cornea (Kenyon *et al.*, 1996; Muthukkaruppan *et al.*, 1982), at a different scale. The circular capillary would be equivalent to the corneal limbus and the space inside with the hypoxic cells would be the avascular cornea with cancerous cells. Additionally, the configuration could also be compared to the vascular growth of a tumor implanted in the dorsal skin of a mouse and observed trough intravital microscopy (Jain *et al.*, 2002) with no previous capillaries in the observed domain. The final network of this configuration is formed by three main capillaries grown from the circular one that branch as they get closer to the hypoxic cells. In the second row of figure 2.12 we present a simulation in which the two hundred hypoxic cells are the same as in the previous row, but the initial capillaries are different. Instead of geometric shapes, we create a more likely approach to an initial vascular network in a real tissue. The resulting pattern covers the positions of the hypoxic cells. Finally, we present in the last row of figure 2.12 a configuration with four initial capillaries, each of them in one boundary of the domain. In addition, we choose a distribution of hypoxic cells based on four normal density functions. Thus, the initial conditions of this simulation mimic a multifocal tumor in a tissue. This result shows how the model is able to create vascular patterns for each of the foci.

2.5 Conclusions

The dynamics of tumor angiogenesis and its impact on cancer growth remain as fundamental open problems in cancer biology. In this chapter, we derive an

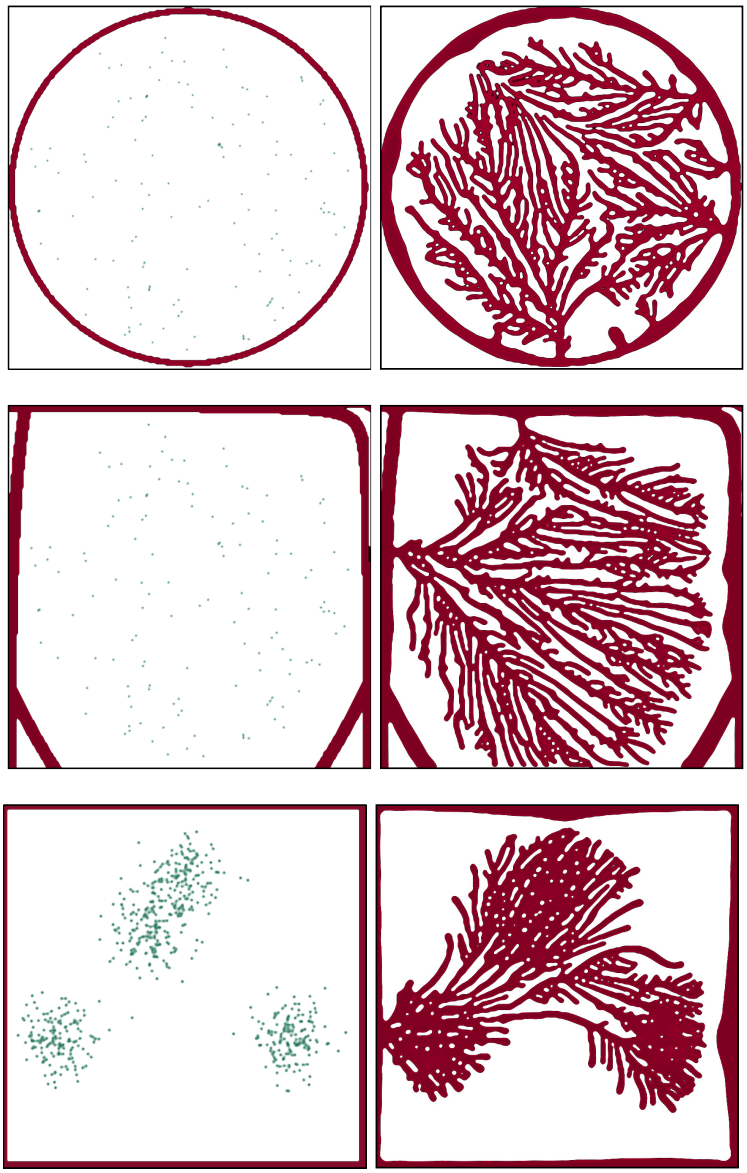

Figure 2.12. Numerical simulations with different initial conditions. *Initial conditions (left) and final patterns (right) of three simulations. The first row presents a circular initial capillary, the second represents a more real configuration of several capillaries in a tissue, and the third shows a multifocal distribution of hypoxic cells. The three simulations were performed on the domain* $\overline{\Omega} = [0, 700]^2$.

algorithmic framework for a hybrid model that couples cellular-scale kinetics and an averaged phase field description at the macroscale. We formulate the discrete cellular kinetics into a functional framework that seamlessly integrates with the continuous description and permits an efficient numerical treatment of the coupled problem. We perform several numerical simulations using our algorithms. The examples show the accuracy and efficiency of the method in a number of physically relevant situations. Our simulations provide insight into the dynamics of the governing equations and the underlying biological process behind them. They also highlight the lack of some key mechanisms of angiogenesis in the model, like haptotaxis, mechanotaxis, or vessel regression.

Both the developed mathematical framework and the multidimensional parallel code serve as a starting point for the remaining mathematical models of this thesis. In addition, by using IGA we paved the way for numerical simulations in three-dimensional, complex geometries.

2.6 Supporting information

Supporting information includes the following four videos that can be found online at http://caminos.udc.es/gmni/gente/gvilanovac/thesis/:

Video S2.1. Formation of the capillary network of figure 2.8. Two hundred randomly distributed hypoxic cells on a domain $\overline{\Omega} = [0, 300]^2$ promote the growth of the vasculature by means of the TAF.

Video S2.2. Formation of a capillary network whose final pattern is presented in the top-left plot of figure 2.11. The domain of this simulation is $\overline{\Omega} = [0, 700]^2$, approximately 5.4 times the size of the domain in figure 2.8.

Video S2.3. Formation of the capillary network from an initial circular capillary on a $[0, 700]^2$ domain. This video corresponds to the simulation shown in the first row of figure 2.12.

Video S2.4. Formation of the capillary network of the simulation presented in the second row of figure 2.12. The initial setup of the parent capillaries try to replicate a realistic configuration.

Video S2.5. Formation of the capillary network of the simulation presented in the third row of figure 2.12. Angiogenesis is triggered by four groups of hypoxic cells as in a multifocal tumor.

Chapter 3

Tip endothelial cells guided by chemotatic and haptotactic cues

In this chapter, we couple the previous hybrid deterministic model with a circular random walk model biased in the direction of chemotactic migration. We believe that the stochastic component may represent a simple mathematical conceptualization of haptotaxis, a biological phenomenon whose underlying physics takes place at a significantly smaller spatial scale. We use our model and simulations to investigate the role of haptotaxis and chemotaxis in the mobility of tip endothelial cells and its influence in the final vascular patterns. Furthermore, we developed an automated numerical method that allow us to study the patterns using quantitative indicators, complementing the usual qualitative observations.

3.1 Haptotaxis

As explained in subsection 1.2.1 the migration of tip endothelial cells is thought to be driven by several coordinated mechanisms. One of them is chemotaxis, defined as the movement following a gradient of concentration of a certain soluble chemical, in this case the soluble fraction of angiogenic factor. This mechanism was implemented in the model of the previous chapter. A second one is haptotaxis, which is the motion driven by gradients of non-soluble chemoattractants bounded to the substrate of the extracellular matrix (in angiogenesis the fraction

of angiogenic factor bounded to the extracellular matrix) or driven by gradients of focal adhesion sites (see figure figure 3.1). Both the non-soluble chemoattractants and the focal adhesion sites depend on the spatial distribution of the fibers of the extracellular matrix. As the characteristic length scale of the fiber distribution is significantly smaller than that of the global motion of the tip endothelial cells, haptotaxis may be understood as variations in the direction of cells movement.

In this chapter, we extend the model to account for haptotaxis cues during the migration of the tip endothelial cells. The original model treats this type of cells as discrete agents and assumes their movement to be deterministic and driven by chemotaxis. Thus, the velocity of tip endothelial cells is proportional to the gradient of the tumor angiogenic factor. We introduce a new definition for the velocity based on the random walk framework, specifically on the work in Plank and Sleeman (2004). The new model considers the migration of the tip endothelial cells as an stochastic process and defines it as a biased circular random walk. The biasing direction of the random walk represents chemotaxis, whereas the directional randomness is understood as haptotaxis, which acts at a smaller spatial scale. In addition, we detail the formulation of the model for three-dimensional settings, so that, after its analysis in the current chapter, we can use it to perform subject-specific, three-dimensional simulations in chapter 4.

Remark:

1. Tip endothelial cells also migrate by mechanotaxis, that is, the movement stimulated by mechanical forces. It is not implemented in the model, al-

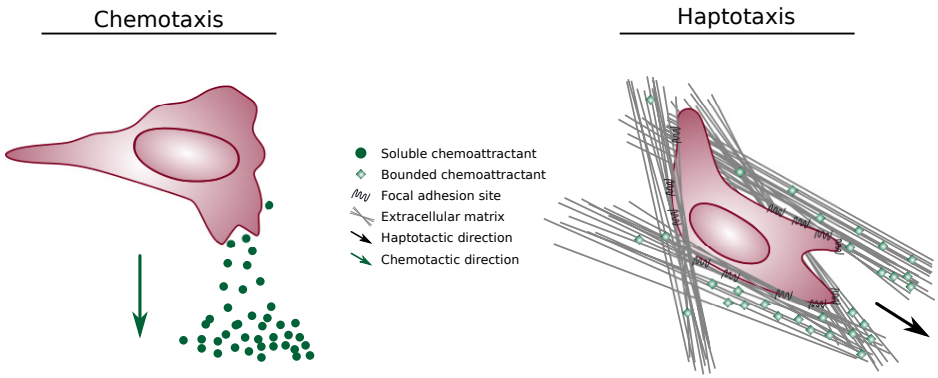

Figure 3.1. Chemotaxis and haptotaxis. *Chemotaxis is the movement following gradients of soluble chemoattractants, while haptotaxis is the motility up a gradient of matrix-bounded chemoattractants or focal adhesion sites. (Adapted from Friedl and Weigelin, 2008)*

though we plan to include it in the future (see chapter 7).

3.2 The mathematical model

In the following, we summarize the new model, detailing the definition of the velocity of the tip endothelial cells. First, we describe the continuous equations for the tumor angiogenic factor and the quiescent and stalk endothelial cells. Afterwards, we explain the discrete agents, both for the hypoxic cells and for the tip endothelial cells. At this point, we introduce the biased circular random walk for the tip cells. Then, we proceed describing how the discrete agents at the cellular level are coupled with the macro-scale, continuous equations.

3.2.1 The continuous problem

The model considers two continuous variables defined in the spatial domain $\Omega \subset \mathbb{R}^d$, where $d = 2, 3$. The first one, f, represents a balance of tumor angiogenic factors released by hypoxic cells that promote the activation of tip endothelial cells and the proliferation of the stalk cells. The second continuous variable, c, is a phase field defining the location of the capillaries in the extracellular matrix. The equation that governs the dynamics of c favors two homogeneous states ($c = 1$ and $c = -1$) that can co-exist stably. The region where $c \geq 0$ represents the capillaries, while $c < 0$ defines the area of the extracellular matrix without capillaries.

The dynamics of the tumor angiogenic factor concentration is governed by the following reaction-diffusion equation

$$\frac{\partial f}{\partial t} = \nabla \cdot (D \nabla f) - B_u f c \mathcal{H}(c), \tag{3.1}$$

where D is the diffusion constant, B_u is the uptake rate constant, and $\mathcal{H}(\cdot)$ is the Heaviside function. The first term on the right-hand side of the equation models the diffusion of the tumor angiogenic factor from the hypoxic cells to the remaining part of the extracellular matrix. The second term accounts for the consumption of the factor by the endothelial cells.

The dynamics of the quiescent and stalk endothelial cells is described by the phase-field equation

$$\frac{\partial c}{\partial t} = \nabla \cdot \left(M \nabla \left(\mu_c - \lambda^2 \Delta c \right) \right) + \mathcal{B}_p(f)\, c \mathcal{H}(c), \tag{3.2}$$

where M is the constant mobility, $\mu_c(c) = -c + c^3$ is the chemical potential, and λ is a positive constant proportional to the width of the capillary wall. $\mathcal{B}_p(\cdot)$ is the proliferative rate function, given by

$$\mathcal{B}_p(f) = \begin{cases} B_p f & \text{if } f < f_p \\ B_p f_p & \text{if } f \geq f_p \end{cases}, \tag{3.3}$$

where B_p is the proliferative rate constant and f_p is the tumor angiogenic factor condition for highest proliferation.

The dynamics of equation (3.2) may be understood in the context of phase-field methods. The chemical potential μ_c is the derivative of a double-well potential that energetically favors two homogeneous states separated by a smooth interface. The separation force can be interpreted from a biological standpoint as the driving force that maintains endothelial cells together exerted by the cells themselves. In addition, the second term on the right-hand side accounts for the proliferation of stalk cells in presence of tumor angiogenic factor.

Remarks:

1. In equation (3.2) the value of λ defines the length scale of the problem. As $\lambda \to 0$ the model tends to a sharp interface model (Kobayashi, 1994). The lower this value, the more accurate is the description of the capillary walls, at the expense of a higher computational cost.
2. The proliferative rate is defined as a piecewise linear function with a plateau that imposes a maximum threshold for proliferation. Hence, this function accounts for the saturation of the tumor angiogenic factor receptors of the surface of the endothelial cells.

3.2.2 The discrete agents

The model accounts for two types of discrete agents, which represent, respectively, hypoxic and tip endothelial cells. These cells are supposed to be spherical with radii R_{HYC} and R_{TEC}, respectively.

Hypoxic cells

A hypoxic cell is assumed to be a static agent centered at a fixed point that we call generically $\mathbf{x}_{\text{HYC}}$. The agents associated to hypoxic cells have two states: active and inactive. Initially, all the hypoxic cells are distributed in the hypoxic regions

of the tissue and are active. While they are active, they produce a fixed amount of angiogenic factor f_{HYC}. Whenever a hypoxic cell becomes normoxic, its associated agent becomes inactive. The model assumes that this situation happens when a capillary is closer than a certain distance, δ_{nox}, which represents the oxygen characteristic diffusion length. An inactive agent does not produce angiogenic factor.

Tip endothelial cells

These agents may be created at any point of the domain or removed according to several criteria. A new agent is created at a point, provided that the following conditions are met: (1) the point is inside a capillary ($c \geq c_{\text{act}}$); (2) the tumor angiogenic factor concentration is high enough to stimulate the differentiation of an endothelial cell ($f \geq f_{\text{act}}$); (3) the chemotactic signal is strong ($G = \|\nabla f\| \geq G_{\text{act}}$); and (4) there is no other tip endothelial cell nearby releasing Dll-4 to prevent its differentiation. The characteristic range of action of the Dll-4 is denoted here by δ_4. If at some point a tip endothelial cell fails to meet these conditions, its associated agent is removed, assuming that the cell changed its phenotype to a non-migratory one.

In contrast to hypoxic cells, tip endothelial cells are mobile. We define the movement of a tip endothelial cell as a biased circular random walk. Let us discretize the time interval of interest, namely $(0, T)$, into N sub-intervals $I_n = (t_{n-1}, t_n)$; $n = 1, \ldots, N$, where $0 = t_0 < t_1 < \cdots < t_N = T$. We call $\Delta t_n = t_n - t_{n-1}$. Given a tip endothelial cell defined by its center, $\mathbf{x}^n_{\text{TEC}} = (x^n_{\text{TEC}}, y^n_{\text{TEC}}, z^n_{\text{TEC}})$, at time t_n, we define its trajectory by the set of equations

$$\left.\begin{aligned} x^n_{\text{TEC}} &= x^{n-1}_{\text{TEC}} + \rho\cos(\theta_n)\sin(\varphi_n)\Delta t_n \\ y^n_{\text{TEC}} &= y^{n-1}_{\text{TEC}} + \rho\sin(\theta_n)\sin(\varphi_n)\Delta t_n \\ z^n_{\text{TEC}} &= z^{n-1}_{\text{TEC}} + \rho\cos(\varphi_n)\Delta t_n \end{aligned}\right\} , \tag{3.4}$$

where ρ, the velocity magnitude, is a deterministic function of the model parameters and the magnitude of the gradient of tumor angiogenic factor concentration. θ_n and φ_n are realizations of the discrete stochastic variables Θ_n and Φ_n which denote, respectively, the azimuthal and the polar (zenith) angles of the spherical system of coordinates. We will assume that Θ_n and Φ_n are independent for all $n > 0$. The range of Θ_n, namely R_{Θ_n}, is defined as

$$R_{\Theta_n} = \{\theta_{n-1} + \delta, \theta_{n-1}, \theta_{n-1} - \delta\} \ , \tag{3.5}$$

while the range of Φ_n is

$$R_{\Phi_n} = \{\varphi_{n-1} + \delta, \varphi_{n-1}, \varphi_{n-1} - \delta\} . \tag{3.6}$$

Equations (3.5) and (3.6) can be straightforwardly applied to the case $n > 1$. When $n = 1$, θ_0 and φ_0 should be understood as deterministic values given by the gradient of the angiogenic factor at the initial time. We denote the azimuthal component of the gradient by θ_0^{ch} and the polar component by φ_0^{ch}, where the superscript indicates that this is the direction of chemotactic migration. Note that $\{\Theta_n\}_{n>0}$ and $\{\Phi_n\}_{n>0}$ define two Markov chains, as follows from equations (3.5) and (3.6), and the independence of Θ_n and Φ_n for all $n > 0$. Equations (3.5) and (3.6) show that, from one time step to the next and for each angular direction, the tip endothelial cell may turn clockwise or anticlockwise an angle δ or remain advancing in the same direction. The probabilities of these events are given by the probability functions of Θ_n and Φ_n defined as

$$P\left[\Theta_n = \theta_{n-1} + \delta\right] = \hat{\tau}^{+}_{\theta_n^{\mathrm{ch}}} \Delta t_n \ , \tag{3.7}$$

$$P\left[\Theta_n = \theta_{n-1} - \delta\right] = \hat{\tau}^{-}_{\theta_n^{\mathrm{ch}}} \Delta t_n \ , \tag{3.8}$$

$$P\left[\Theta_n = \theta_{n-1}\right] = \left(1 - \hat{\tau}^{+}_{\theta_n^{\mathrm{ch}}} \Delta t_n - \hat{\tau}^{-}_{\theta_n^{\mathrm{ch}}} \Delta t_n\right) \ , \tag{3.9}$$

$$P\left[\Phi_n = \varphi_{n-1} + \delta\right] = \hat{\tau}^{+}_{\varphi_n^{\mathrm{ch}}} \Delta t_n \ , \tag{3.10}$$

$$P\left[\Phi_n = \varphi_{n-1} - \delta\right] = \hat{\tau}^{-}_{\varphi_n^{\mathrm{ch}}} \Delta t_n \ , \tag{3.11}$$

$$P\left[\Phi_n = \varphi_{n-1}\right] = \left(1 - \hat{\tau}^{+}_{\varphi_n^{\mathrm{ch}}} \Delta t_n - \hat{\tau}^{-}_{\varphi_n^{\mathrm{ch}}} \Delta t_n\right) \ , \tag{3.12}$$

where $\hat{\tau}^{+}_{\theta_n^{\mathrm{ch}}}$, $\hat{\tau}^{-}_{\theta_n^{\mathrm{ch}}}$, $\hat{\tau}^{+}_{\varphi_n^{\mathrm{ch}}}$, and $\hat{\tau}^{-}_{\varphi_n^{\mathrm{ch}}}$ are the so-called transition rates and θ_n^{ch} and φ_n^{ch} are the azimuthal and polar directions given by the positive gradient of the tumor angiogenic factor at time t_n. The transition rates are given by

$$\hat{\tau}^{\pm}_{\theta_n^{\mathrm{ch}}} = 2\nu \frac{\tau_{\theta_n^{\mathrm{ch}}}\left(\left(n \pm \frac{1}{2}\right)\delta\right)}{\tau_{\theta_n^{\mathrm{ch}}}\left(\left(n + \frac{1}{2}\right)\delta\right) + \tau_{\theta_n^{\mathrm{ch}}}\left(\left(n - \frac{1}{2}\right)\delta\right)} \ , \tag{3.13}$$

$$\hat{\tau}^{\pm}_{\varphi_n^{\mathrm{ch}}} = 2\nu \frac{\tau_{\varphi_n^{\mathrm{ch}}}\left(\left(n \pm \frac{1}{2}\right)\delta\right)}{\tau_{\varphi_n^{\mathrm{ch}}}\left(\left(n + \frac{1}{2}\right)\delta\right) + \tau_{\varphi_n^{\mathrm{ch}}}\left(\left(n - \frac{1}{2}\right)\delta\right)} \ , \tag{3.14}$$

where $\nu = \frac{D_r}{\delta^2}$ and D_r is the so-called rotational diffusivity. The derivation of the transition rates can be found at Othmer and Stevens (1997). The transition probabilities $\tau_{\theta_n^{\mathrm{ch}}}$ and $\tau_{\varphi_n^{\mathrm{ch}}}$ used in equations (3.13) and (3.14) are von Mises probability density functions given by

$$\tau_{\theta_n^{\mathrm{ch}}}(\alpha) = \frac{1}{2\pi I_0(\frac{d_v}{D_r})} \exp\left(\frac{d_v}{D_r}\cos(\alpha - \theta_n^{\mathrm{ch}})\right) \ , \tag{3.15}$$

$$\tau_{\varphi_n^{\mathrm{ch}}}(\alpha) = \frac{1}{2\pi I_0(\frac{d_v}{D_r})} \exp\left(\frac{d_v}{D_r}\cos(\alpha - \varphi_n^{\mathrm{ch}})\right) \ , \tag{3.16}$$

where $I_0(\cdot)$ is the modified Bessel function of the first kind and zeroth order and d_v is the turning coefficient. Figure 3.2 shows the evolution of the probability function of turning clockwise for 200 time steps and for various values of the turning coefficient.

Following Travasso *et al.* (2011b), the velocity magnitude of the tip endothelial cell is a function of the norm of the gradient of the tumor angiogenic factor evaluated at the center of the tip endothelial cell, such that

$$\rho = \chi \left\| \nabla f \left(\mathbf{x}_{\mathrm{TEC}} \right) \right\| \mathcal{L} \left(\left\| \nabla f (\mathbf{x}_{\mathrm{TEC}}) \right\| \right) \ , \tag{3.17}$$

where χ is a chemotactic constant, the operator $\| \cdot \|$ denotes the Euclidean norm

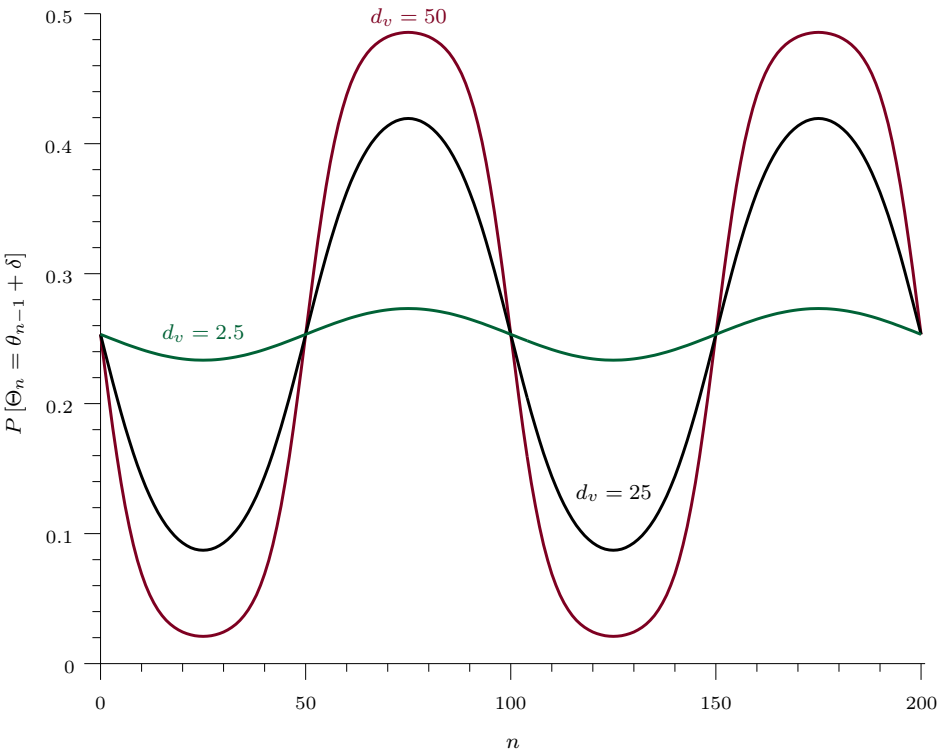

Figure 3.2. Turning probability function. *Probability function of turning clockwise through an angle* $\delta = \frac{\pi}{50}$ *for 200 time steps. We plot three probability functions, each for a different value of the turning rate* d_v*. The rotational diffusivity is* $D_r = 1$*, the biased direction is* $\theta_0 = 0$*, and the time step size is* $\Delta t_n = 0.001$*.*

of a vector, and $\mathcal{L}$ is a limiting function defined as

$$\mathcal{L}\left(\|\nabla f\|\right) = 1 + \left(\frac{G_M}{\|\nabla f\|} - 1\right)\mathcal{H}\left(\|\nabla f\| - G_M\right) \ , \tag{3.18}$$

where G_M is a constant.

3.2.3 The continuum/discrete coupling

Both the discrete hypoxic cells and tip endothelial cells must be coupled with the continuous equations of the model. First, as said above, hypoxic cells are responsible for the introduction of the tumor angiogenic factor in the system. Hence, these discrete components are coupled with equation (3.1). In the regions occupied by active hypoxic cells the value of the tumor angiogenic factor is constant and equal to f_{HYC}. Second, as discrete tip endothelial cells move, they produce, by proliferation, an excess in the concentration of endothelial cells. Consequently, they are coupled with equation (3.2). The ratio of the material produced in the tip cell to the volume swept as the cell migrates, gives us the value of the order parameter inside the tip endothelial cell. Thus, in the region of the domain occupied by a tip endothelial cell, the order parameter is given by

$$c_{\text{TEC}} = \frac{4\mathcal{B}_p\left(f\left(\mathbf{x}_{\text{TEC}}\right)\right)R_{\text{TEC}}}{3\rho}. \tag{3.19}$$

3.2.4 Parameters

As the equations of the mathematical model are written in dimensionless form, we detail the value of all the corresponding dimensionless parameters. The model presented here shares some parameters with the one presented in the previous chapter. These parameters are kept equal, as many of them were matched to or obtained from experiments *in vivo* (see Travasso *et al.*, 2011b and the references therein). For the convenience of the reader we repeat their value here. The physical values of these parameters may be retrieved using the length and time scales $L_0 = 1.25\,\mu\text{m}$ and $T_0 = 1560\,\text{s}$.

In table 3.1 we show the dimensionless parameters of the continuous equations (3.1) and (3.2) in the same order as in the text. The remaining parameters come from the discrete agent description. The radii of the discrete agents, namely R_{HYC} and R_{TEC} are assumed to be equal. Travasso *et al.* (2011b), in agreement with Gebb and Stevens (2004), fixed the radius of the tip endothelial cells in $5\,\mu\text{m}$, which is 4 in the dimensionless formulation of the model. The mean nutrient and

Table 3.1. *Dimensionless parameters of the continuous equations* (3.1) *and* (3.2).

Parameter	Value
Diffusion constant	$D = 100$
Uptake rate constant	$B_u = 6.25$
Constant mobility	$M = 1$
Interface width	$\lambda = 1$
Proliferative rate	$B_p = 1.401$
TAF condition for highest proliferation	$f_p = 0.3$

oxygen diffusion length, δ_{nox}, is 25 µm (20 in dimensionless quantities) as in Grote (1989). The production of tumor angiogenic factor per time step is $f_{\text{HYC}} = 1$. The parameters that determine the activation or deactivation of tip endothelial cells are:

1. Order parameter condition for activation or deactivation $c_{\text{act}} = 0.9$.
2. Tumor angiogenic factor condition for activation or deactivation $f_{\text{act}} = 0.055$.
3. Tumor angiogenic factor gradient condition for activation or deactivation $G_{\text{act}} = 0.01$.
4. Dll-4 range of action $\delta_4 = 16$. The value of this parameter *in vivo* is 20 µm.

Finally, in table 3.2 we show the dimensionless parameters related to the movement of tip endothelial cells. The value of the rotational diffusivity and the turning coefficient were obtained through a parametric study of the model. The value of the turning angle δ was maintained equal to that proposed in Plank and Sleeman (2004).

3.3 Numerical method

In this section we present a numerical method to solve the mathematical model. As in the model, we naturally divide the algorithm in three blocks: the method for the discrete agents, the method for coupling the discrete and the continuous variables,

Table 3.2. *Parameters related to the movement of the tip endothelial cells.*

Parameter	Value
Chemotactic constant	$\chi = 242.67$
TAF gradient for highest velocity	$G_M = 0.03$
Rotational diffusivity	$D_r = 0.05$
Turning coefficient	$d_v = 25$
Turning angle	$\delta = \frac{\pi}{50}$

and the algorithm for solving the continuous equations. In the method for the discrete agents, we first evaluate the discrete rules that determine the activation and deactivation of the agents. This process is simple, so we omit the details of the related algorithms. Therefore, we start this section explaining the method to compute the displacement of the tip endothelial cells following the biased circular random walk. Then, we outline how we solve the coupling between the discrete components and the continuous equations. We close the section explaining the method for solving the continuous equations, which is essentially the one used in the previous chapter.

3.3.1 The tip endothelial cell motion

After activation/deactivation of the discrete agents in time step t_n, we move each active tip endothelial cell according to equation (3.4). The velocity magnitude ρ is a deterministic function given by equation (3.17) which we evaluate at the center of the tip endothelial cells. The angles that determine the direction, on the contrary, are given by the realizations θ_n and φ_n of the random variables Θ_n and Φ_n, respectively.

We follow the technique used in Plank and Sleeman (2004); Sleeman and Wallis (2002) to obtain the value of the realizations. For the direction Θ we generate a random number r with uniform distribution over the interval [0,1] and divide the unit interval in three sub-intervals. If the random number falls into the first sub-interval, $[0, \hat{\tau}_n^+ \Delta t_n)$, then $\theta_n = \theta_{n-1} + \delta$ and the tip endothelial cell turns clockwise through an angle δ; if it falls into the second sub-interval, $[\hat{\tau}_n^+ \Delta t_n, 2\nu\Delta t_n)$, then $\theta_n = \theta_{n-1} - \delta$ and the cell turns anticlockwise through an angle δ; and if the random number falls into the last sub-interval, $(2\nu\Delta t_n, 1]$, then $\theta_n = \theta_{n-1}$ and

the tip endothelial cell continues in its current direction. The realization φ_n is obtained analogously.

Remark:

1. Note that equations (3.7) to (3.12) impose an upper bound on the time step Δt_n, because all probabilities should remain below one. We think of this restriction as an stability condition for the time-stepping scheme.

3.3.2 The coupling methodology

We start by giving some definitions for the domains of the discrete agents, following the ideas of the mathematical framework of this model developed in the previous section. Recalling that for any time step, each hypoxic cell is characterized by its center and its constant radius, R_{HYC}, we can define Ω^i_{HYC} as the domain occupied by the i-th hypoxic cell, which in three dimensions is a sphere centered at $\mathbf{x}^i_{\mathrm{HYC}}$. Furthermore, we can define the domain of all the active hypoxic cells for a given time step, say t_n, as

$$\Omega_{\mathrm{HYC}}(t_n) = \bigcup_{k \in A_{\mathrm{HYC}}(t_n)} \Omega^k_{\mathrm{HYC}} \tag{3.20}$$

where $A_{\mathrm{HYC}}(t_n)$ is the set of indices of the active hypoxic cells at time t_n.

Similarly, for the same time step we define the domain $\Omega^j_{\mathrm{TEC}}(t_n)$ as the spherical domain occupied by the j-th tip endothelial cell, with radius R_{TEC} and center $\mathbf{x}^j_{\mathrm{TEC}}$. Notice the time dependency of the domain of each tip cell due to its movement, opposed to the hypoxic-cell domains which are time-independent and only the set of indices depends on time, indicating which agents are active. The domain of tip endothelial cells is given by

$$\Omega_{\mathrm{TEC}}(t_n) = \bigcup_{l \in A_{\mathrm{TEC}}(t_n)} \Omega^l_{\mathrm{TEC}}(t_n) \tag{3.21}$$

where $A_{\mathrm{TEC}}(t_n)$ is the set of indices of tip endothelial cells at time t_n. All of the above-defined domains are subsets of Ω.

These definitions facilitate the coupling between the discrete components and the continuum variables. Therefore, we can now overwrite the value of the tumor angiogenic factor, $f(t_{n-1})$, and the value of the order parameter, $c(t_{n-1})$, in the subdomains $\Omega_{\mathrm{HYC}}(t_n)$ and $\Omega_{\mathrm{TEC}}(t_n)$, with f_{HYC} and c_{TEC}, respectively. Consequently, we would introduce discontinuities in the fields f and c. However, we try to avoid the artificial inclusion of sharp transitions in the continuous variables,

for it goes against the philosophy of the phase-field equation. For this purpose we define template functions for f_{HYC} and c_{TEC} that are multidimensional generalizations of the analytical solution to the one-dimensional Cahn-Hilliard equation, a simplified version of equation (3.2). The template functions are continuous and introduce smooth transitions between the fields and the imposed values inside the subdomains of the discrete agents. As shown below, the discrete counterparts of the continuous variables f and c live in the finite dimensional space $\mathcal{V}^h$. For this reason, the template functions must be projected onto the same finite dimensional space $\mathcal{V}^h$ before overwriting the discretized fields.

3.3.3 The continuous equations

We begin by considering a weak form of equations (3.1) and (3.2). Let $\mathcal{V}$ denote the trial solution and the weighting function spaces, which are assumed to be the same. At this point we assume free-flux boundary conditions. Equations (3.1) and (3.2) may be recast in variational form by multiplying them with smooth functions, integrating over the domain, and applying integration by parts repeatedly. The problem may be stated as follows: find $f, c \in \mathcal{V}$ such that $\forall w, q \in \mathcal{V}$:

$$\begin{aligned}\int_\Omega w\frac{\partial f}{\partial t}d\Omega + \int_\Omega \nabla w D \nabla f d\Omega + \int_\Omega w B_u f c \mathcal{H}\left(c\right) d\Omega \\ + \int_\Omega q\frac{\partial c}{\partial t}d\Omega + \int_\Omega \nabla q M \nabla \mu_c \, d\Omega + \int_\Omega \Delta q M \lambda^2 \Delta c \, d\Omega \\ - \int_\Omega q\mathcal{B}_p\left(f\right) c\mathcal{H}\left(c\right) d\Omega = 0 \end{aligned} \quad (3.22)$$

The space $\mathcal{V}$ is a subset of $\mathcal{H}^2$, the Sobolev space of square integrable functions with square integrable first and second derivatives. To perform the spatial discretization of the previous weak formulation we make use of the Galerkin method. Let us define the discrete space $\mathcal{V}^h$, which is a subset of $\mathcal{V}$. We approximate equation (3.22) by the following variational problem over the finite dimensional space: find $f^h, c^h \in \mathcal{V}^h \subset \mathcal{V}$ such that $\forall w^h, q^h \in \mathcal{V}^h \subset \mathcal{V}$:

$$\begin{aligned}\int_\Omega w^h\frac{\partial f^h}{\partial t}d\Omega + \int_\Omega \nabla w^h D \nabla f^h d\Omega \\ + \int_\Omega w^h B_u f^h c^h \mathcal{H}\left(c^h\right) d\Omega + \int_\Omega q^h\frac{\partial c^h}{\partial t}d\Omega\end{aligned}$$

$$+\int_{\Omega}\nabla q^h M\nabla\mu(c^h)d\Omega+\int_{\Omega}\Delta q^h M\lambda^2\Delta c^h d\Omega$$
$$-\int_{\Omega}q^h\mathcal{B}_p\left(f^h\right)c^h\mathcal{H}\left(c^h\right)d\Omega=0 \quad (3.23)$$

Here f^h is defined as

$$f^h\left(\mathbf{x},t\right)=\sum_{A=1}^{n_b}f_A\left(t\right)N_A\left(\mathbf{x}\right) \quad (3.24)$$

where n_b is the dimension of the discrete space $\mathcal{V}^h$ and N_A are the basis functions. The rest of the variables of equation (3.23), namely c^h, w^h, and q^h, are defined analogously to f^h. Since we will use a conforming discretization, the relation $\mathcal{V}^h\subset\mathcal{V}$ holds and the discrete functions are required to be in $\mathcal{H}^2$. This condition is satisfied by the globally $\mathcal{C}^1$-continuous basis functions that we consider in this thesis, by means of isogeometric analysis.

As in chapter 2, we integrate in time using the generalized-α method (Chung and Hulbert, 1993; Jansen *et al.*, 2000). In addition, we use a time-step size selection algorithm that considerably reduces the computational time. After space and time discretization, we obtain a non-linear system which is solved using a predictor multi-corrector algorithm based on the Newton-Raphson method.

3.4 Results and discussion

In this section we analyze the proposed tumor angiogenesis model. Although the theory is prepared for three-dimensional simulations, this analysis is performed in two dimensions, as the visualization of the patterns created during angiogenesis is easier in this simplified setting. Then, in the next chapter, we will use the results of this study to perform three-dimensional simulations. Here, we show in figure 3.3 various snapshots that capture the time evolution of the vascular network. In this simulation we analyze the directionality of the tip endothelial cells, from the initiation of angiogenesis until the complete oxygenation of the tissue. Then, we compare the final patterns of the vasculature of this simulation with an identical one that does not include haptotaxis. The comparison is done qualitatively, but also quantitatively by transforming the vasculatures into distance-weighted graphs through skeletonization (see figure 3.4). Lastly, we present the final patterns of four two-dimensional simulations in figures 3.5a and 3.5b. One of the two parameters that determine the biased circular random walk, namely the rotational diffusivity

(D_r) and the turning coefficient (d_v), is changed for each pair of simulations. This enables us to study how the frequency and the amplitude of the turnings influence the development of the network.

The simulations that we present are performed on the square domain $\overline{\Omega} = [0, 300]^2$. This domain represents a tissue of 375 µm × 375 µm, although the periodic condition imposed in the horizontal direction, allows the vasculature to spread further than in a tissue of the mentioned size. We have used a regular mesh defined by 128^2 knot spans and quadratic basis functions with $\mathcal{C}^1$-continuity across element boundaries. In order to facilitate the comparison among the two-dimensional simulations, all the initial conditions are the same: a blood vessel at the bottom of the domain and 200 hypoxic cells randomly scattered on the extracellular matrix according to a uniform distribution. Note that this distribution is the same one as that used in the first simulation of chapter 2 (figure 2.8) to facilitate comparison. The radius of the initial vessel is set to 37.5 µm. The first snapshot of figure 3.3 shows these initial conditions, where we maintained the color code of the previous chapter (and will be maintained throughout the figures and videos of this document): red color for capillaries and green color for tumor angiogenic factor.

Figure 3.3 and video S3.1 shows the initiation and evolution of a new vascular network promoted by an avascular tumor, represented here by its hypoxic region. The simulation uses the parameters of the model presented in subsection 3.2.4. At the beginning of the simulation, the 200 hypoxic cells start to release tumor angiogenic factor, which diffuses throughout the domain. The angiogenesis process is initiated when the factor reaches the initial vessel at the bottom of the domain, with enough quantity to activate a tip endothelial cell. Thus, in the second snapshot of figure 3.3 we observe that one tip endothelial cell has become active and has started its migration. At this moment, there is only one of these cells, because the cell itself prevents the differentiation of the surrounding cells into the tip endothelial cell phenotype by means of the lateral inhibition mechanisms. The other cells stimulated by the tumor angiogenic factor, instead, attain a proliferative phenotype, generating the capillary behind the tip endothelial cell. However, as the leading cell moves away, new tip endothelial cells get activated, for the delta-like ligand 4 released by the first tip endothelial cell does not affect them anymore. Hence, more sprouts are created and the vascular network spreads. As the network grows, it consumes tumor angiogenic factor and returns the hypoxic cells into their normoxic condition, as shown in the remaining snapshots.

In this simulation we can study the movement of tip endothelial cells. Although the global migration of the leading cells is governed by the gradient of the tumor angiogenic factor, we observe how tip endothelial cells turn and reorient towards this gradient. This phenomenon, introduced by the biased circular random walk in the mathematical model, represents our conceptualization of haptotaxis. The

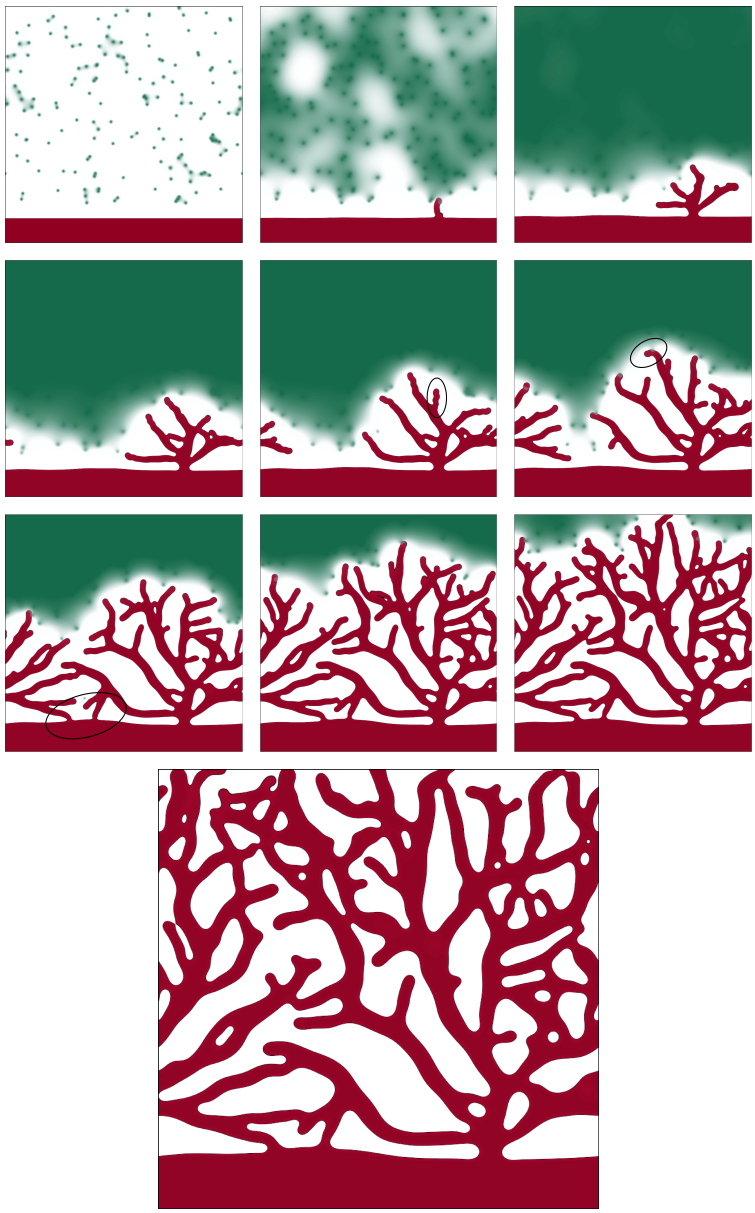

Figure 3.3. Formation of a vascular network driven by tumor induced angiogenesis. *200 hypoxic cells produce tumor angiogenic factor (green) that promotes the initiation and growth of new sprouts (red). The simulation is performed on the domain* $\overline{\Omega} = [0, 300]^2$ *using the parameters presented in subsection 3.2.4.*

variation of gradients of non-soluble molecules bounded to the extracellular matrix hinders the movement towards hypoxic cells. Tip endothelial cells find their chemotaxis-driven migration obstructed by a scarcity of non-soluble molecules, so they eventually alter their direction of migration. Additionally, the turns allow the cells to better detect the changes in their micro-environment, as they explore a broader area when they turn. In figure 3.3, several of these turning events are highlighted. For example, in the fifth snapshot (third row, first column) we distinguish a zigzag movement of various tip endothelial cells. This kind of short-angled, high-frequent turns only affect the direction of the capillary growth and do not create zigzag final patterns, for the undulating morphology is afterwards eliminated by the local remodeling of the phase-field equation. When the direction is maintained for a large time because the gradient of non-soluble molecules of the extracellular matrix favors one direction, tip cells do not reorient and the capillaries deviate from their supposed objective (the hypoxic cells). In these cases, the final pattern of the vasculature is significantly altered, as in the sixth snapshot where the highlighted tip endothelial cell turns leftward although a hypoxic cell is just above it. The previous set of examples shows, as observed in experiments, the relevant role of haptotaxis in the patterns of the vasculature after an angiogenesis event.

The influence of haptotaxis is more apparent in figure 3.4, where we compare the final pattern of this simulation (in red) with exactly the same simulation (identical initial conditions, boundary conditions, and parameters) without haptotaxis (in gray). The reader is also referred to the interactive figure S3.2 in the supporting information to compare both final patterns. Note that the simulation without haptotaxis is the final pattern of the numerical example in subsection 2.4.1. When the two final patterns defined by the phase-field are qualitatively compared, as in figure 3.4a, it is clear that, although both vasculatures span the domain and oxygenate the tissue, they are different. The superimposed images on the right-hand side of this figure show that the only characteristic shared by the patterns is that both were initiated from the same point in the parent vessel. This was predictable, as the criteria for the activation are equal. Besides this point (and the beginning of the branch that starts there), both vasculatures differ; there is not a single branch that follows the same path in both simulations.

In order to make a quantitative comparison we developed a numerical method to extract the graphs of both vascular networks. This numerical method is divided into two parts. The first one is to transform a discretized binary image of the phase-field that represents the capillaries into an skeleton, that is, a one-point-wide, body-centered curve topologically equivalent to the vascular network (see figure 3.4b). To obtain the skeleton, we use a two-fold-iteration parallel thinning algorithm based on Zhang and Suen (1984). As this algorithm does not ensure the

(a) *Comparison of the phase fields. The superimposed image on the right-hand side shows that haptotaxis completely alters the vascular patterns.*

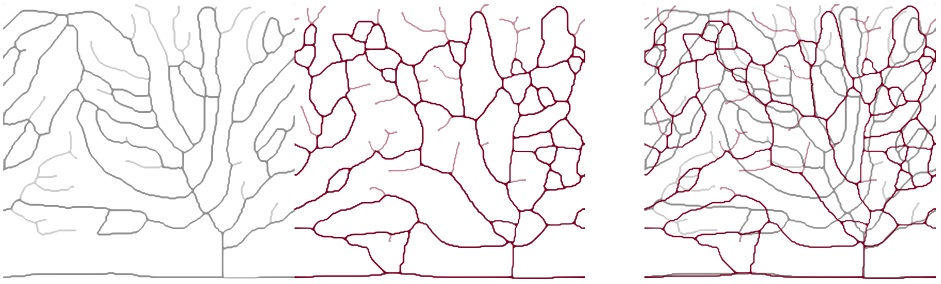

(b) *Skeletonization of the phase fields. The increased anastomosis in the simulation with haptotaxis changes the skeleton to lattice-like structure.*

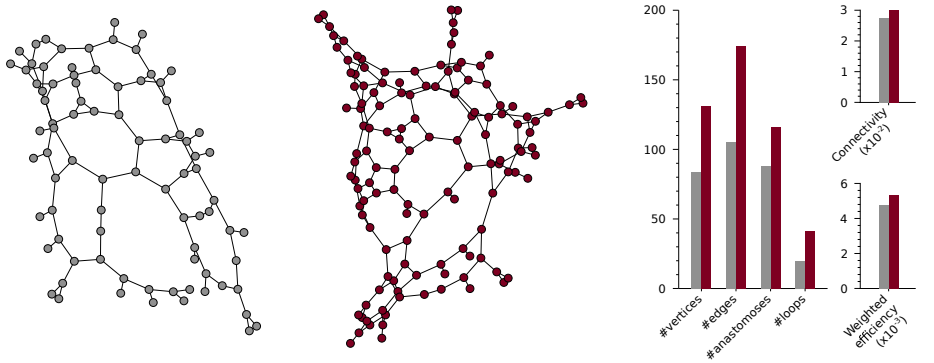

(c) *Skeletons are transformed into distance-weighted graphs to quantify the vascular networks. Note the increased connectivity and efficiency when haptotaxis is present.*

Figure 3.4. Comparison of two simulations without and with haptotaxis. *The simulation without haptotaxis (in gray) is that of figure 2.8i and the simulation with haptotaxis (in red) is final pattern of the previous example in figure 3.3. The parameters, initial conditions, and boundary conditions were kept equal in both simulations.*

skeleton to be one-point wide, we designed a sequential thinning algorithm that we apply to the previous skeleton to guarantee this property. The second part of the method is to define a distance-weighted simple graph from the skeleton. This is done by means of an algorithm that identifies the vertices and edges in the skeleton and assigns a distance to the edges (used as weights). From the resulting weighted graph (figure 3.4c) we can define and study quantities of interest to compare the vasculatures generated by both models.

The first remarkable observation is the representation of the skeletons in figure 3.4b already reveals distinguishing characteristics of the networks that were not clear in the phase-field representation. The skeleton of the simulation that includes haptotaxis shoes a lattice-like structure compared to the tree-like structure of the purely chemotatic simulation. This fact is even more apparent when we prune the branches of the skeleton that do not form loops (represented in light gray and red). These branches are those capillaries that do not allow blood flow because they do not form loops, so they barely contribute to tissue oxygenation. In addition, we observe that the reason for the lattice-like structure is that the branches of the skeleton do not run parallel to each other due to the haptotaxis conceptualization incorporated in this model. The quantitative measurements of the extracted graphs shown in figure 3.4c backup all these observations and add useful indices to compare the vasculatures. The graph of the model with haptotaxis presents a higher number of vertices and edges, that, is the model promotes more branching and anastomosis events. Furthermore, the average edge length is lower (10.31 versus 16.19 for the purely chemotactic) and the algebraic connectivity (Fiedler, 1973) is higher, distinctive of a more lattice-like network. And, as such, the graph of the haptotactic model has more than twice number of loops than the other (41 versus 20). We also analyzed the distance-weighted efficiency of the network, defined as

$$E = \frac{1}{n\,(n-1)} \sum_{i,j\in[1,n],i\neq j} \frac{1}{d\,(i,j)}\ , \tag{3.25}$$

where n is the number of vertices and $d\,(i,j)$ is the distance of the shortest path between vertices i and j. The efficiency measures the traffic capacity of the network and reflects its parallel transfer ability (Criado *et al.*, 2006). In our case, it represents the ability of the network to transport oxygen and nutrients to the tissue. It is the graph from the haptotactic model the one with higher efficiency.

In this mathematical model, anastomosis events can occur for two reasons. The first one, also considered in the model without the biased circular random walk, is the distribution of hypoxic cells. In this case, tip cells migrate towards the gradient of angiogenic factor and they mainly anastomose at the location of the hypoxic cells. The second cause of anastomosis is the new physics that we added to the model: haptotactic migration. Anastomosis events occur more frequently

in our model because tip endothelial cells alter their direction of migration and come across another endothelial cell. One example is in the highlighted area of the seventh snapshot where two capillaries turn towards the initial vessel producing anastomosis, although the hypoxic cell is in the other direction. We can see there that anastomosis events are not only determined by the location of hypoxic cells, but also depend on haptotaxis. In addition, as shown in figure 3.4c, there are more anastomoses than in the identical simulation of the model without haptotaxis.

Figures 3.5a and 3.5b allow us to further investigate how endothelial cells migrate under different values of two of the parameters that define the biased random walk, namely the rotational diffusivity D_r and the turning coefficient d_v. We maintain the remaining parameters and initial conditions equal to those in the simulation of figure 3.3, for the sake of an easier comparison. Thus, for the two simulations in figure 3.5a we alter the value of the rotational diffusivity. In the simulation on the left-hand side the value of the parameter is 1000 % of D_r and in that of the right-hand side, it is 10 % of D_r. The final patterns of both simulations are drastically different. In the first one, since the rotational diffusivity is increased, the frequency at which the turns occur is too high for tip endothelial cells to lead the capillaries towards the hypoxic cells following a smooth curve. This may be interpreted as a vascular network developing within an extracellular matrix with very low concentration of non-soluble molecules or focal adhesion sites. The tip endothelial cells in this situation wander in small regions, trying to find a migration path. In contrast, in the second simulation, the low value of the rotational diffusivity almost impedes the tip endothelial cells to deviate from its original trajectory. In this case, the distribution of the non-soluble chemoattractants or of the focal adhesion sites may be thought of as strongly biased in some preferential directions. The resulting capillaries are highly tortuous in the first simulation and too straight in the second.

In figure 3.5b, in the simulation on the left-hand side, the value of the turning coefficient is 200 % of d_v and in that of the right-hand side, it is 10 % of d_v. When the value of the turning coefficient is high, the ability of tip endothelial cells to reorient towards the preferred direction at each turn is increased, while when it is low, for the same value of the rotational diffusivity, the reorientation is hindered. We observe in the figure that the tip endothelial cells on the left-hand-side simulation tend to go rapidly towards the hypoxic cells, compared to the simulation on the right-hand side. The reason is that the bias of the random walk is increased on the left-hand-side simulation, so the chemotatic direction is highly favored. In addition, the higher the value of the turning coefficient the lower the number of anastomoses that are not promoted by the distribution of the hypoxic cells.

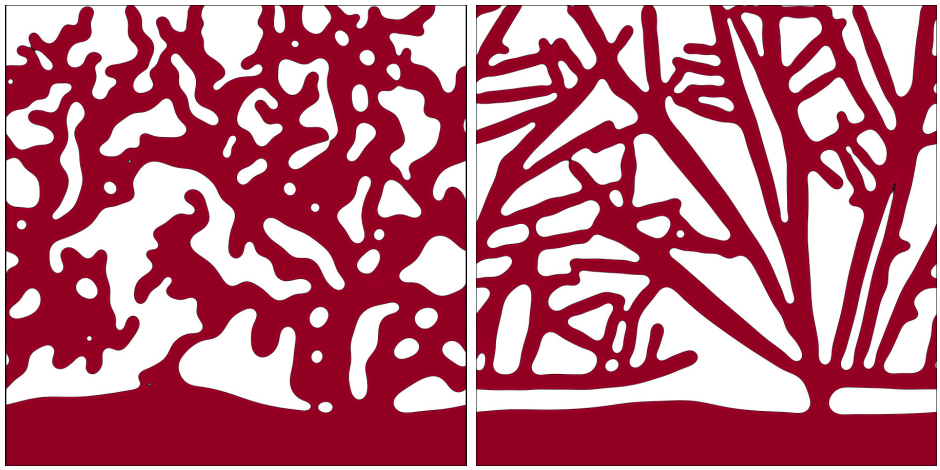

(a) *Comparison of the final patterns of two simulations for different values of the rotational diffusivity: 1000 % (left) and 10 % (right) of D_r. The remaining parameters and conditions of the simulations are the same as those in figure 3.3. Tip endothelial cells constantly change their direction for high values of the rotational diffusivity and do not change it for low values.*

(b) *Comparison of the final patterns of two simulations for different values of the turning coefficient: 200 % (left) and 10 % (right) of d_v. The remaining parameters and conditions of the simulations are the same as those in figure 3.3. The higher the values of d_v the better tip endothelial cells reorient towards hypoxic cells.*

Figure 3.5. Study of rotational diffusivity and turning coefficient values.

3.5 Conclusions

Tumor-induced angiogenesis is a complex biological phenomenon and our understanding of it is still limited. However, it is widely accepted that the migration of tip endothelial cells during the growth of new capillaries is driven by three migration mechanisms: chemotaxis, haptotaxis, and mechanotaxis. In this chapter, we coupled an existing continuum theory with a random walk model, to develop a generalized mathematical model that accounts for chemotaxis and a simple modelization of haptotaxis. We also proposed accurate and efficient algorithms to approximate the solution to the model.

Our model and algorithms provide a framework to study the role of haptotaxis and its interaction with chemotaxis in angiogenesis. Our results indicate that haptotaxis may have a significant impact in the final pattern achieved by capillary networks. We also prepared the formulation of the model and the numerical method to perform *in silico* three-dimensional assays, which are presented in the next chapter.

We believe that the quantitative method we employed to compare the vasculatures may serve as a basis for a future development of a robust and automated quantitative method which is needed both for the analysis of mathematical models of angiogenesis and for model validation. We also plan to extend the model to include mechanotaxis.

3.6 Supporting information

Supporting information includes the following video and interactive image that can be found online at `http://caminos.udc.es/gmni/gente/gvilanovac/thesis/`:

Video S3.1. Evolution of the vascular network of figure 3.3.

Figure S3.2. Comparison of two simulations without and with haptotaxis. This interactive figure shows both the phase-field and the skeleton of the vascular networks presented in figure 3.4.

Chapter 4

Mouse corneal micropocket angiogenesis assay

Among the variety of *in vivo* assays developed to study angiogenesis, the mouse corneal micropocket assay is one of the most widely used. As explained below, the main reasons for its success are the simplicity in the observation and quantification of the new vessels and the immunologically privileged conditions of the cornea. However, the assay is technically demanding, traumatic, and ethically questionable. Motivated by these reasons, in this chapter we develop three-dimensional numerical simulations of tumor-induced angiogenesis in setups that resemble that of the mouse corneal micropocket angiogenesis assay. This *in silico* assay may be regarded as a way to palliate the disadvantages of the experiment. In order to achieve this objective, first we study the experiment in section 4.1, perform three-dimensional simulations in a simple geometry (a cube) in section 4.2, and develop a computational mesh for a subject-specific (c57BL/6 mouse strain) cornea in section 4.3. With all these ingredients we are able to perform the *in silico* mouse corneal micropocket angiogenesis assay (section 4.4). Furthermore, we compare the neovasculature of the simulations with the *in vivo* experiment.

4.1 The assay

There is a wide variety of angiogenesis assays, both *in vitro* and *in vivo*, as shown in appendix D. While the former are undoubtedly useful and have produced essential breakthroughs in the field, they lack the completeness of the latter. *In vivo* angiogenesis assays are generally more informative as they show the overall effects of the experiment in the whole organism (Norrby, 2006). Among all of them, the corneal micropocket assay is considered one of the best *in vivo* assays (Figg and Folkman, 2011b). It was first developed for rabbits, but nowadays is mostly used in mice, as they are more economical, there are more reagents and tumor lines for mice, and there is a wider variety of transgenic or knockout mouse models than other animals.

The reason for the widespread use of the mouse corneal angiogenesis assay derives from the own characteristics of the cornea, which is a multilayer tissue that covers the anterior chamber, the iris, and the lens (see figure 4.1). It has five layers: epithelium, Bowman's layer, stroma, Descement's membrane, and endothelium, being the stroma approximately 90 percent of the corneal thickness (Staton *et al.*, 2007a). The function of the cornea is to provide fixed focus power to the eye by refracting the light that comes from the exterior. The light can only go through the cornea because it is a transparent tissue. In order to maintain transparency, the layers of the cornea are organized so that the light con transverse them. Furthermore, a whole machinery of biological mechanisms provides the cornea with what is called the *angiogenic privilege* (Ellenberg *et al.*, 2010), that is, they maintain the cornea as an avascular tissue[1]. Corneal cells get nutrients and oxygen from the anterior chamber and from the vasculature that surrounds the cornea, located at the limbus (see figure 4.1). Hence, the avascularity and transparency of the cornea makes it a privileged site for an angiogenesis assay, as there is no previous vasculature, new capillaries can only start from a known location (the limbus), and their growth can be easily monitored during the whole assay without interfering in their evolution.

There are several ways to perform the corneal assay and all of them share the same idea: To promote angiogenesis by releasing tumor pro-angiogenic factors to disturb the angiogenic privilege of the cornea. The assays differ, however, in the means of producing tumor angiogenic factor. Some examples are (Staton *et al.*, 2007a): Chemical cauterization or thermal injury, intrastromal injection, intrastromal tumor implantation, mechanical debridement or denudation, intracorneal suture,

[1] Some pathological situations cause the loss of this transparency through corneal neovascularization, such as viral or bacterial infections, parasite infestation, immune mediated keratitis, and chemical or mechanical injuries. These pathologies up-regulate pro-angiogenic factors or down-regulate anti-angiogenic factors, promoting the growth of capillaries from the limbal region.

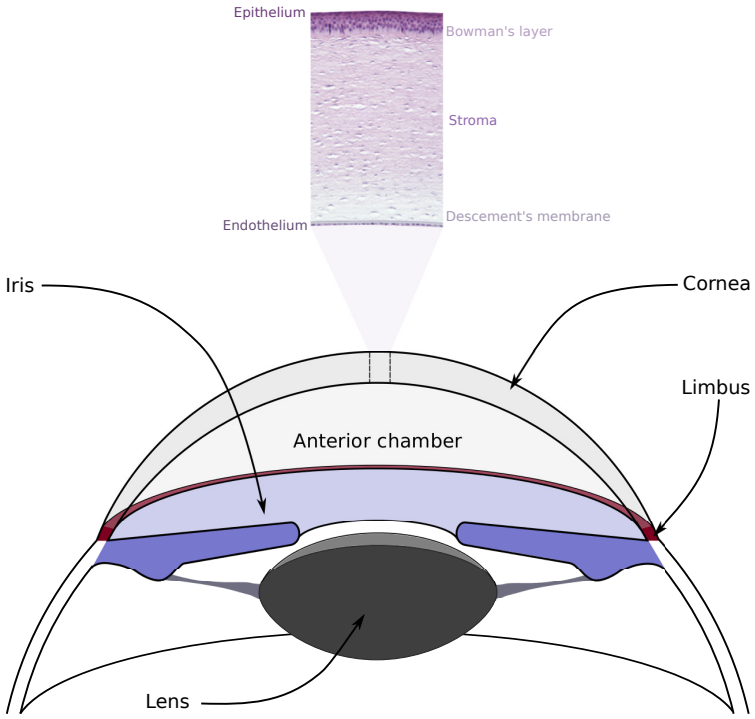

Figure 4.1. Characterization of the cornea. *The cornea is a multilayer, transparent tissue of the eye that covers the anterior chamber, the iris, and the lens. Its function is to refract light, providing focus power to the eye. In order to be transparent, the cornea needs to be avascular, being vessels located only at the limbus. (Histopathological corneal slice adapted from UCDavis, 2016)*

surgical grafts, and implantation of a slow-release polymer pellet in a micropocket. The last one is the most frequent because pellets permit a fair enough control over the released factors, which is not possible by other means. Thus, in this chapter we focus on the mouse corneal assay using this method (i.e. the mouse corneal micropocket angiogenesis assay) which we briefly describe in the following.

The first step in the elaboration of the mouse corneal micropocket angiogenesis assay is to produce the pellets. They are composed by four substances, namely a carrier-free agent, a slow-release polymer, sucralfate, and absolute ethanol (see figure 4.2). The carrier-free agent is a tumor angiogenic factor which can be used in different concentrations, for instance, 160 ng of VEGF per pellet (Rogers *et al.*, 2007), 180ng of VEGF per pellet (Kenyon *et al.*, 1996), or 80 ng of bFGF per pellet (Rogers *et al.*, 2007). Two polymers are commonly used: Elvax (poly ethylene-

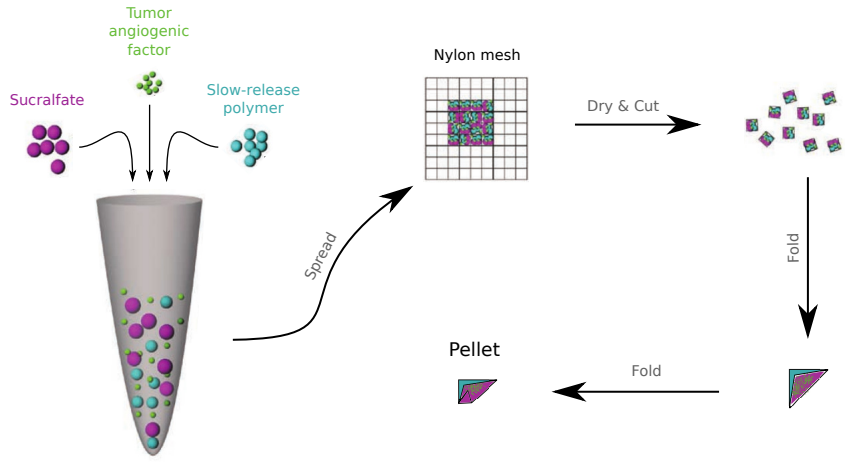

Figure 4.2. Pellet preparation. *The components of the pellet, that is the tumor angiogenic factor, the sucralfate, and the slow-release polymer, are mixed in with absolute ethanol. The product is spread on a nylon mesh. Once dried, even pellets are cut from the mesh and folded to the desired size. (Adapted from Cao* et al.*, 2011)*

vinylacetate) and Hydron (polyhydroxyethylmethacrylate). The combination of the polymer and the sucralfate provide stability to the pellet and sustained slow-rate release of the carrier-free agent. In the preparation of the pellet, the carrier-free, the polymer, and the sucralfate are mixed together with the absolute ethanol and spread into a nylon mesh. After drying, the mesh is cut apart into pellets that are suitable for the assay using a rat model. For mice, the pellet is folded to obtain a smaller one.

Once the pellets are ready, the mouse corneal micropocket assay proceeds as follows (see the graphical description in figure 4.3). First, mice are anesthetized and one eye[2] is treated with a topical anesthetic. Then, a small incision is made approximately one millimeter away from the limbus (figures 4.3a and 4.3b). This distance may vary depending on the carrier-free agent of the pellet (the weaker the agent angiogenic stimulation, the closer to the limbus). The incision is enlarged with a special tool (Graef knife) towards the limbus to create a micropocket under the epithelial layer and parallel to the layers (figure 4.3c), where the pellet is carefully introduced (figures 4.3d and 4.3e). Finally, the eye is treated with a topical ophtalmologic antibiotic ointment to prevent non-wanted inflammation responses. New vessels appear approximately one day after the implantation and they peak seven days after (figure 4.3f). Figure 4.4 shows several examples of

[2]The other eye is usually used as control.

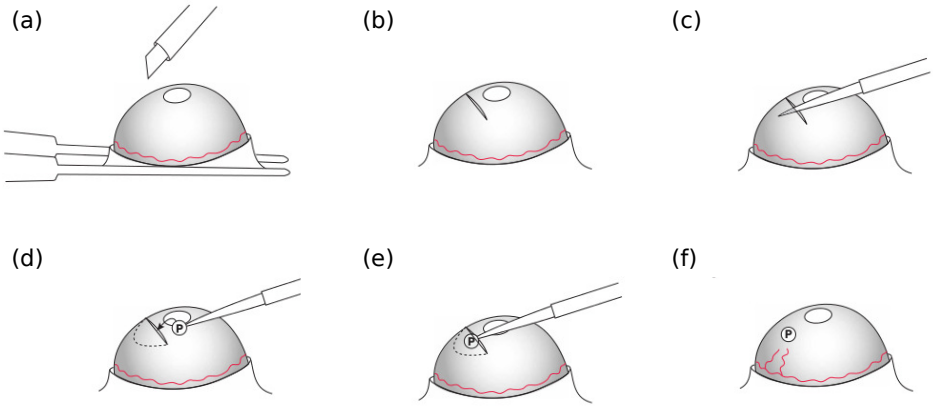

Figure 4.3. Protocol of the mouse corneal micropocket angiogenesis assay. *Using surgical procedures (a) a micropocket is done in the cornea (b). The pocket is enlarged (c) so that a pellet, P, can be inserted into it (d, e). The angiogenic factors released by the pellet promote angiogenesis (f). (Adapted from Rogers* et al.*, 2007)*

the resulting neovascularization promoted by a variety of tumor angiogenic factor concentrations. For a detailed description of the protocol of the mouse corneal micropocket angiogenesis assay the reader is referred to Rogers *et al.* (2007); Tang *et al.* (2011) and the references therein.

As said above, the evolution of the vasculature can be easily monitored during the assay using, for example, slit lamp microscopy as shown in Birsner *et al.* (2014). This method is very fast and does not require killing the animal. Another way to monitor the assay is through optical-resolution photoacustic microscopy (Liu *et al.*, 2014). Besides, at the end of the experiment, the corneas can be dissected and mounted, allowing thus further studies of the neovasculature using fluorescein angiography or a colloidal carbon-perfusion (Anijeet *et al.*, 2012). Through all these imaging techniques, the results of the experiment can be characterized using different approaches. It can be done qualitatively by assigning positive or negative results based on certain criteria (Polverini *et al.*, 1991). Some authors also use semi-quantitative scorings; for example, in Conrad *et al.* (1994) the authors use a scale from 0 to 6^+ according to the distances from the limbus to the end points of new vessels. Notably, the corneal micropocket angiongenesis assay can be also characterized quantitatively (Kirwan *et al.*, 2012; Staton *et al.*, 2007b; **?**). Different measures are used, like the vascularized area (expressed either as square mm or as percentage over the whole cornea surface), the limbus circumference length from which new vessels originate (usually in clock hours), various vessel lengths

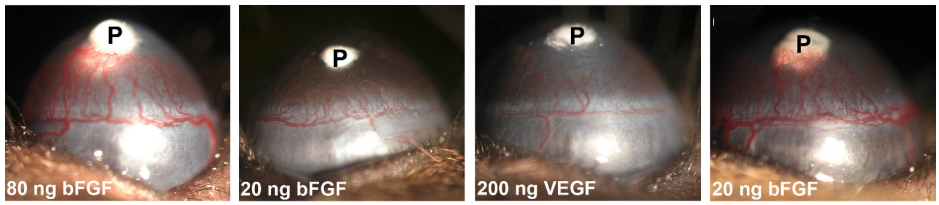

Figure 4.4. Examples of the mouse corneal micropocket angiogenesis assay. *The resulting vascular pattern varies with the distance of the pellet to the limbus and the concentration of tumor angiogenic factor. (Adapted from Birsner* et al.*, 2014)*

(total, maximum, minimum, average), vascular density, and even detailed vascular measures, such as capillary diameter or number of vessel sprouts.

4.2 Three-dimensional angiogenesis

In this section we perform large-scale simulations that show three-dimensional angiogenesis at a significant level of detail, using the mathematical model and the numerical algorithms developed in chapter 3 (recall that, although we only showed two-dimensional simulations, everything was prepared for three-dimensional ones). The objective of these simulations is to study the model in three dimensions in a simple geometry, prior to its application to the real and bigger geometry required to replicate the mouse corneal angiogenesis assay. By using a simple geometry, we are able to study the mathematical model in three dimensions without the inherent constraints and difficulties of a complex mesh. Hence, every simulation in this section is performed on the computational domain $\overline{\Omega} = [0, 300]^3$, which represents a cube with side length 375 µm. We use quadratic basis functions and a uniform mesh defined by the tensor product of open knot vectors, each composed by 72 knots. The boundary conditions are no-flux conditions in all directions, except in the direction parallel to the axis of the initial capillaries, where the domain is periodic. Therefore, as in the two-dimensional simulations of the previous chapters, we allow the capillaries to spread in the mentioned direction forming more connected patterns.

4.2.1 Angiogenesis triggered by a cluster of hypoxic cells

Here, we analyze two simulations (figures 4.5 and 4.6 and videos S4.1 and S4.2), showing four snapshots of the dynamic evolution of the vasculature. The first snapshot of each simulation represents the initial conditions, while the rest are

snapshots of relevant situations during the development of the vasculature. The simulations differ from each other in the initial conditions, while all the parameters are kept constant and equal to those described in chapters 2 and 3. For both simulations, we set two initial capillaries, rectilinear and parallel, which traverse the domain from one face of the cube to the opposite, being the axis of the capillaries perpendicular to both faces. This configuration allows angiogenesis to be initiated in both capillaries and increases the number of anastomoses. The initial diameter of the capillaries is constant and equal to 12.5 µm, in accordance with the data from the literature (Shiu *et al.*, 2005). The difference in the initial conditions comes from the distribution and number of hypoxic cells. In the first simulation (figure 4.5), we set 200 hypoxic cells with locations that follow a normal distribution and mimic a tumor centered in the domain. In the second example (figure 4.6), we set 300 hypoxic cells that aim to represent a three-focus tumor.

In figures 4.5 and 4.6, we observe the initiation and development of two vascular networks driven by the presence of hypoxic cells disposed in tumor-like structures. In both simulations, the tumor angiogenic factor, represented by green isosurfaces, diffuses from hypoxic cells until it reaches the initial capillaries. At that moment, new capillaries are initiated in the regions where hypoxic cells are closer to the initial capillaries. In the first simulation (figure 4.5), new sprouts appear first in the upper capillary and they grow forming a network while they consume the tumor angiogenic factor. Meanwhile, the factor reaches the other capillary and several tip endothelial cells become active and start its migration. Both networks continue growing, turning hypoxic cells into normoxic on their way. Towards the end of the simulation, both networks get connected through various anastomoses, allowing the blood to flow between the two main capillaries. The virtual tumor at the center of the domain is now completely pervaded by tortuous capillaries that may trigger the uncontrolled growth of the tumor.

In the second simulation (figure 4.6), the tumor angiogenic factor activates tip endothelial cells in three regions of the initial capillaries in a short time span, as shown in the second snapshot of the simulation. Thus, the three groups of new sprouts grow at a similar rate and almost at the same time. The third snapshot of the simulation shows a plain example of the effect of the biased circular random walk. In the set of sprouts that grow from the upper initial capillary, there are three of them which are led by tip endothelial cells that instead of migrating towards the hypoxic tumor regions grow towards the observer. As shown in chapter 3, in two-dimensional settings this migration driven by haptotaxis usually leads to anastomosis events. However, in three dimensions the probability of a tip endothelial cell coming across a capillary is significantly smaller. As shown in the last snapshot, in this specific case, the three sprouts just stop their growth when there is no more angiogenic factor before anastomosing. Furthermore, for

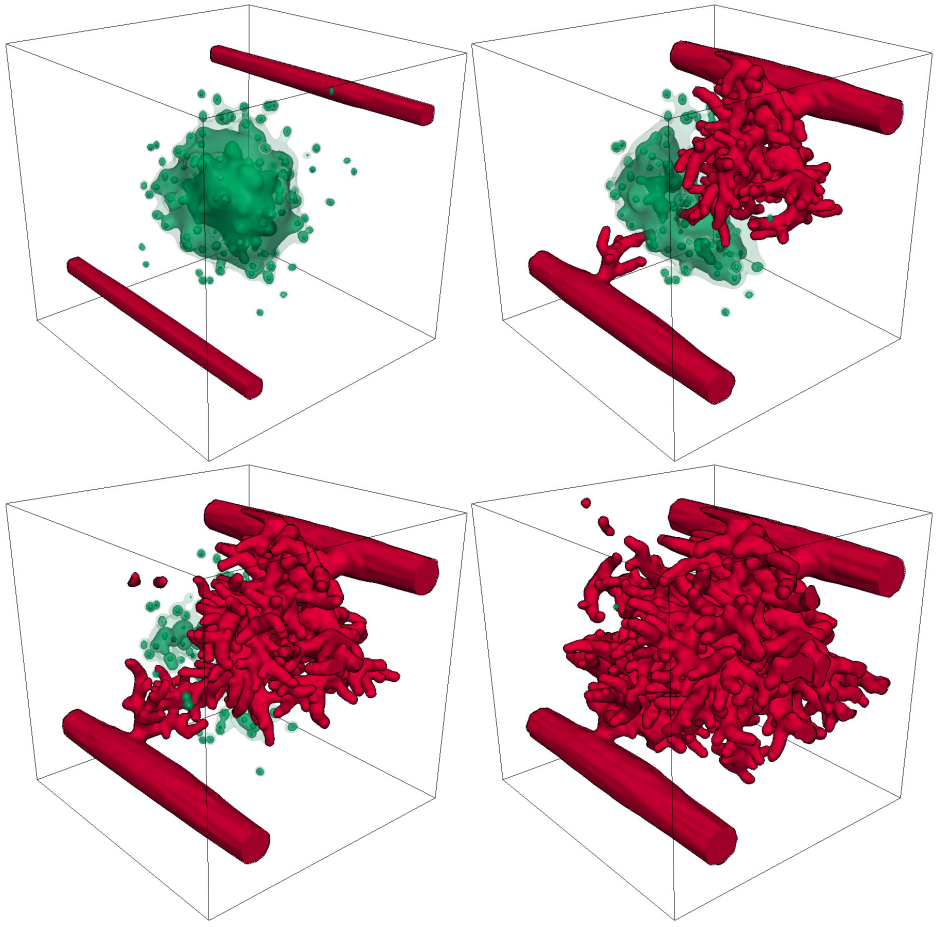

Figure 4.5. Three-dimensional angiogenesis from two parent capillaries. *A new vascular network develops from two parent capillaries. The new sprouts are initiated by the tumor angiogenic factor (green isosurfaces) released from hypoxic cells disposed forming a tumor-like structure. The tip endothelial cells that lead the growth of the sprouts migrate by chemotaxis and haptotaxis. At the end of the simulations the vasculature pervades the tumor, leaving no cells under hypoxic conditions. Many anastomosis events create loops in the new vasculature and connect the parent capillaries. The simulation is performed on the domain* $\overline{\Omega} = [0, 300]^3$ *using the parameters presented in chapters 2 and 3.*

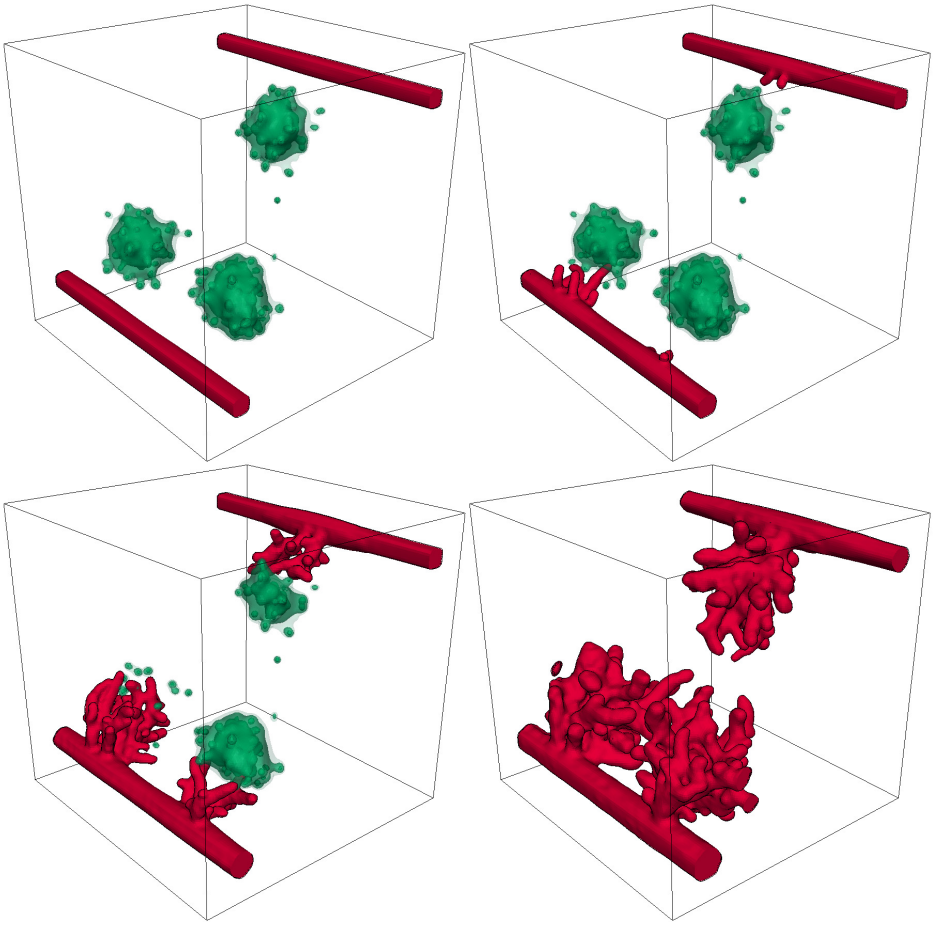

Figure 4.6. Evolution of a vascular network promoted by hypoxic cells mimicking a multifocal tumor. *Three sets of sprouts grow from the initial capillaries until there are not hypoxic cells. The simulation is performed on the domain* $\overline{\Omega} = [0, 300]^3$ *using the parameters presented in chapters 2 and 3.*

the same reason the two parent capillaries, unlike the previous simulation, do not get connected by the neovasculature.

In all the examples the simulation ends when there is no more tumor angiogenic factor, i.e. no more hypoxic regions are present in the domain. This model does not account either for the vascular shutdown produced by the high interstitial pressure inside the tumor, or for the characteristic capillary regression and regrowth (vascular remodeling) after the shutdown events. We think that this is the reason why when both simulations are compared to *in vivo* tumor images one may observe differences in the patterns (see figure 1 in Kaanders *et al.*, 2004 where some tumors present hypoxic regions).

4.2.2 Angiogenesis triggered by randomly distributed hypoxic cells

In figures 4.7a and 4.7b and videos S4.3 and S4.4, we present two simulations whereby we can analyze the influence of the number of hypoxic cells when they are randomly distributed in the cubic domain. The location of the initial capillaries is identical to that of the previous examples. On the snapshots of the initial conditions (left-hand side of figures 4.7a and 4.7b) the position and number of hypoxic cells is revealed by the isosurfaces of the tumor angiogenic factor: 200 for the first simulation (figure 4.7a) and 100 for the second (figure 4.7b). As shown on the remaining snapshots, the difference in the number of hypoxic cells promotes the creation of vascular patterns with distinguishing characteristics. There are three main differences, noticeable by simple observation: the thickness, local density, and number of capillaries. The three differences are intimately related. For example, in the first simulation, more hypoxic cells initiate more capillaries which, because they are densely packed, consume the tumor angiogenic factor in a high-rate manner. They leave less tumor angiogenic factor per branch for the proliferation of the stalk endothelial cells, and, consequently, the capillaries are thinner. On the contrary, in the second simulation, as fewer and more separated sprouts appear, each branch has more angiogenic factor and more stalk cells proliferate, enlarging the capillaries. Another difference is in the time of initiation of new branches, being shorter for the first simulation. In the second, the branching is delayed due to a lower number of hypoxic cells, which in turn, leads to a lower concentration of angiogenic factor, and delays the initiation of new sprouts at the beginning. As the network evolves, initiation events occur more and more frequently because the tumor angiogenic factor has enough time to diffuse throughout the extracellular matrix.

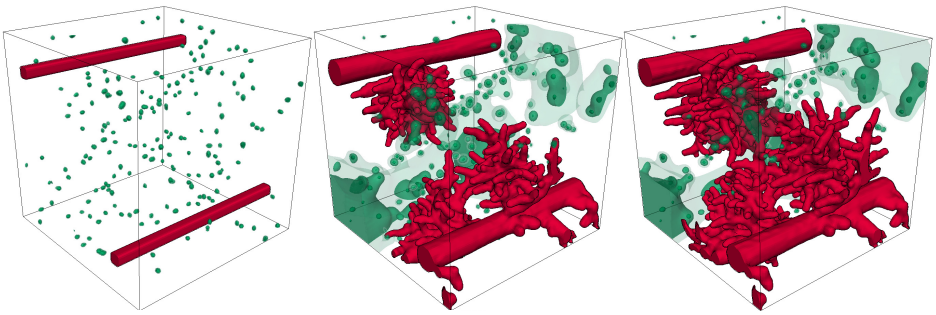

(a) *Vascular network promoted by 200 hypoxic cells.*

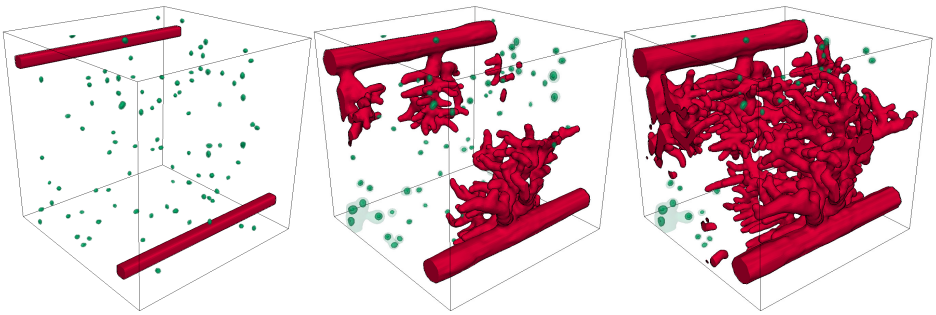

(b) *Vascular network promoted by 100 hypoxic cells.*

Figure 4.7. Three-dimensional angiogenesis promoted by different number of hypoxic cells. *A higher number of hypoxic cells promote the growth of more but thinner capillaries.*

4.2.3 Importance of haptotaxis

In figure 4.8 we present four pairs of numerical simulations at an advanced time stage of the network development, each pair corresponding to one of the rows of the figure. In the snapshots on the left-hand side we present the same numerical simulations we described in this section (figures 4.5, 4.6, 4.7a, and 4.7b) and in the same order. Each of these simulations has an associated simulation presented on the right-hand side of the figure, which represents exactly the same setting and conditions that its left-hand-side counterpart, but considering no haptotactic migration, that is, as the model in chapter 2. In the figure, we omitted the representation of the tumor angiogenic factor, in order to focus on the different vascular morphologies generated by both models.

We observe that the growth patterns are dissimilar in various aspects. The most prominent difference is the tortuosity of the sprouts. Thus, in the simulations of the

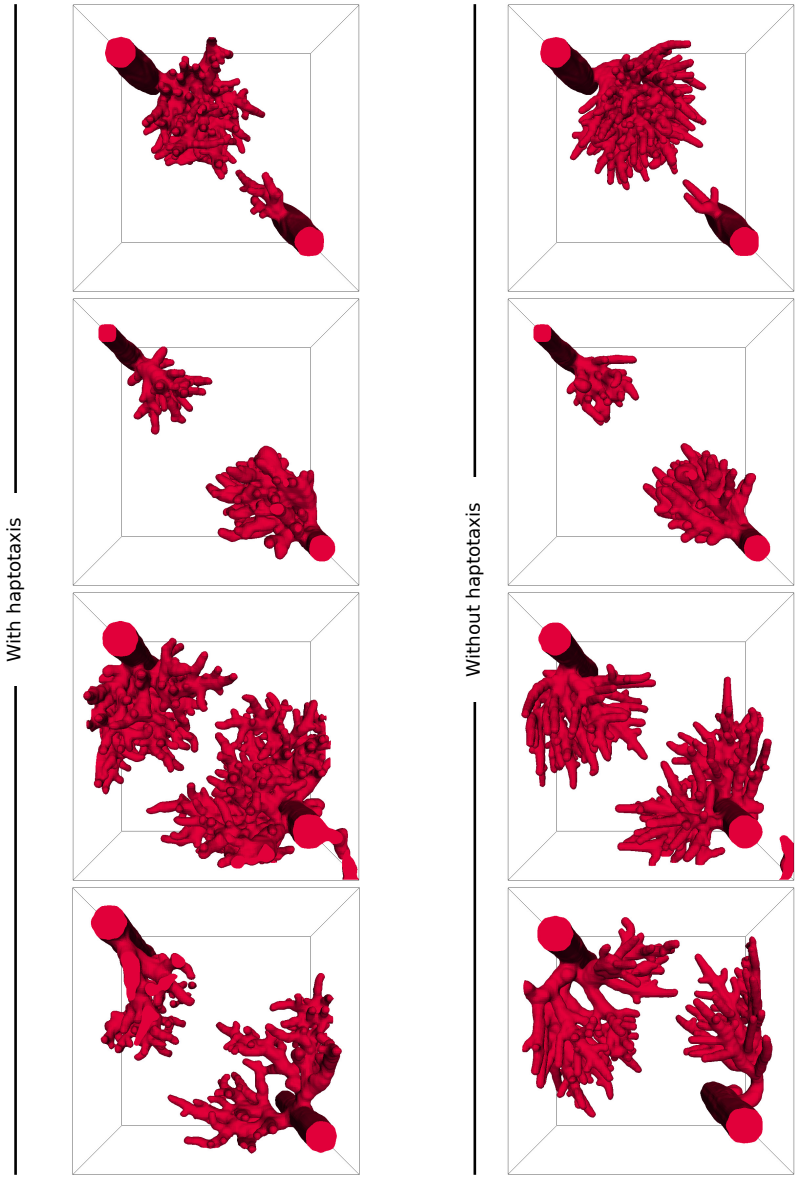

Figure 4.8. Influence of haptotaxis in angiogenesis. *Left column: Final pattern of four simulations (corresponding to figures 4.5, 4.6, 4.7a, and 4.7b). Right column: The same four simulations (identical parameters and initial conditions), but assuming no haptotactic migration. The patterns of the vasculature differ in tortuosity, number of anastomosis events (connectivity), and length of the capillaries.*

extended model, tip endothelial cells randomly deviate from the path marked by the gradient of angiogenic factor and create more tortuous capillaries. In contrast, in the simulations on the right-hand side, the tip endothelial cells go directly towards the hypoxic cells resulting in straighter capillaries. The second observable difference is that the number of anastomoses is higher in our model, leading to more connected vasculatures. This leads to a third fundamental difference between the morphology of the networks of both models: the capillaries are shorter in the proposed model because their growth is stopped by anastomosis. Note that these dissimilarities between the models are clearer in the three-dimensional settings than in the two-dimensional ones of chapter 3.

4.2.4 Discussion

The three-dimensional computations presented in this section serve us to investigate the mathematical model in simple, three-dimensional setups. By altering the initial conditions, we simulated several possible capillary and tumor arrangements and obtained, as a result, a variety of final vascular patterns richer than those presented in previous sections. The simulations suggest that, for mathematical models to achieve the topological complexity observed in *in vivo* angiogenesis experiments, two-dimensional simulations may not be enough. We also believe that the accurate modeling of anastomosis, a crucial process in tumor angiogenesis, may require full-scale three-dimensional simulation. The computations are also useful to test the numerical algorithms in three dimensions using a linear parametric-to-physical mapping, before using them with non-linear mappings (as required in the following sections for complex geometries).

4.3 Subject-specific computational mesh

In this section we describe the generation of a computational mesh for a mouse cornea. Its geometry is taken from data from the literature and we build the subject-specific mesh taking special care to construct analysis-suitable NURBS.

4.3.1 The geometry

There are many types of available laboratory mice that are commonly used for the corneal micropocket angiogenesis assay. Among them we found that the most widely used strain is the c57BL/6, hence we decided to use the same strain for our *in silico* experiments.

As said in the introduction, the main function of the cornea is to provide (fixed) optical power to the eye. To do it the cornea has an specific geometry which is defined by two spherical caps with different curvature. In particular, the radius of curvature of the posterior cornea surface (the interior) is greater than that of the anterior in mice[3]. In order to construct this geometry we take data from *in vivo* measures available in the literature (Henriksson *et al.*, 2009; Schmucker and Schaeffel, 2004). Figure 4.9 shows this geometry, where the red-highlighted measures are the *in vivo* data, while the rest are derived from them.

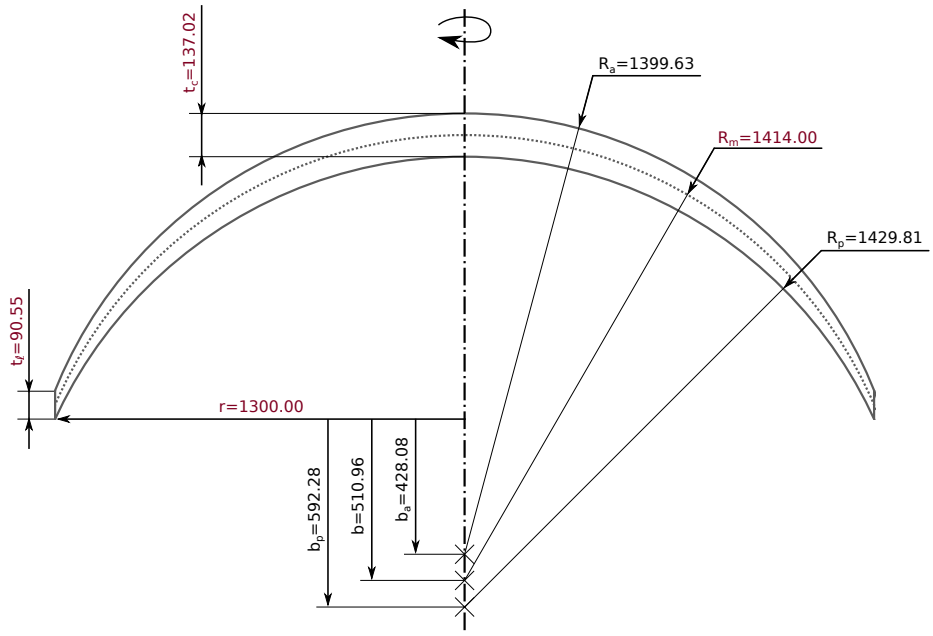

Figure 4.9. Geometry of the cornea of a c57BL/6 mouse. *Data drawn in red are taken from* in vivo *measures and data drawn in black are derived from the former. Measures are given in µm.*

4.3.2 The mesh

Our strategy to design the computational mesh for the specific geometry of figure 4.9 is as follows (see figure 4.10 and video S4.5). The first step is to define a disk of radius $r = 1.3$ mm, using an appropriate NURBS parametrization. The

[3] On the contrary, in humans, the radius of curvature of the posterior cornea surface is smaller than that of the anterior.

complication here is that every parametrization of the disk is singular, that is, it involves at least one basis function that does not fulfill the required regularity properties for integration. In our case, for the second order equations we require all basis functions to live in the Sobolev space of square integrable functions with square integrable first and second derivatives $\mathcal{H}^2$. Our approach to this problem is to study the existent parametrizations and choose the one in which the problematic basis function(s) are located at the boundary, so that we can remove them from the discrete space imposing Diriclet boundary conditions.

We present in figure 4.10a three possible parametrizations of the unit disk. There, we show both a coarse mesh in the top row and a refined mesh in the bottom row for each parametrization. The coarse meshes highlight control points, emphasizing those that share a common location, and control nets, that show how control points are connected. On the other hand, the refined meshes show knot span lines, patch lines, and only those control points associated to basis functions that are not in $\mathcal{H}^2$. We start the study with one of the most used parametrizations of the disk, which is built as a revolution surface rotating a segment 360 degrees around one of its ends (figure 4.10a, left). As a result, there is a singularity at the center of the disk due to the nine collapsing control points. The basis functions associated to these control points are not in $\mathcal{H}^1$. As suggested in Takacs and Jüttler (2011), one can replace these nine basis functions with a linear combination of them, so that the new one is in $\mathcal{H}^1$. The new basis functions and those associated to the control points adjacent to the central one are still in $\mathcal{H}^2$. The same authors, however, proposed in Takacs and Jüttler (2012) yet another linear combination to replace this functions with new ones that satisfies our regularity conditions. The counter part of these solutions is the increased code complexity and a reduced number of degrees of freedom in a region where we need full resolution, as the pellet is located nearby. In order to move the singular point away from the center of the domain, a second option is to build the disk using five patches (figure 4.10a, center): a square one centered in the domain and surrounded by 4 identical patches. This parametrization has 4 extraordinary points, one in each corner of the square patch, and $\mathcal{C}^{-1}$-continuity lines at the interface between patches. Although there are some ways to enforce the appropriate regularity in the related basis functions, we still loose degrees of freedom inside our computational domain. Furthermore, Collin and coworkers have recently shown in Collin *et al.* (2015) that this particular parametrization for $p = 2$ present convergence problems (what they call $\mathcal{C}^1$ *locking*) for the desired regularity. Yet, another option is to parametrize the domain as in the right-hand side of figure 4.10a. We will refer to this parametrization as *inflated*, because it can be generated by deforming a regular parametrization of a square inscribed in a disk until all the disk is filled, as if the square was a balloon that we had inflated inside a circle (see video S4.5 in the supporting information). The inflated parametrization has four (symmetric) groups of 5 control points, each

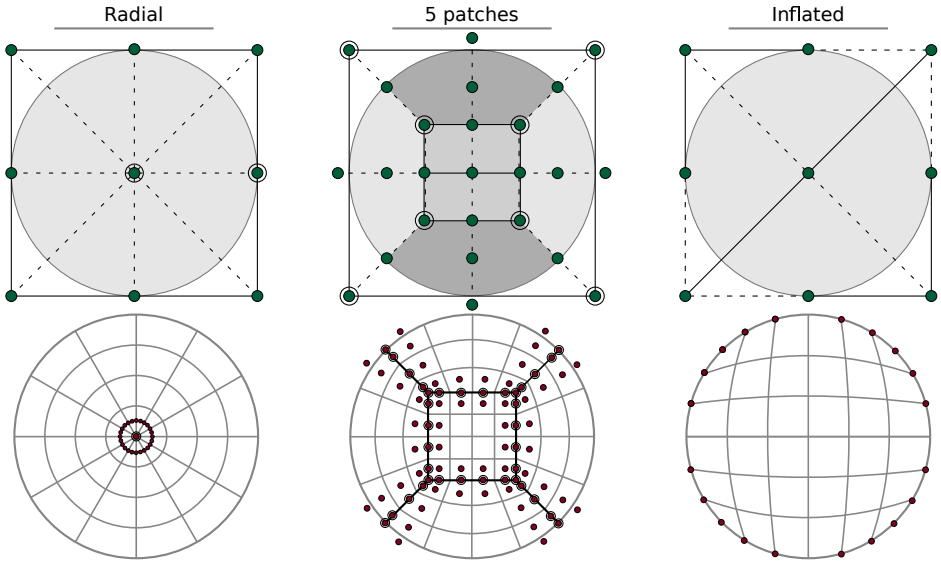

(a) *Common NURBS parametrizations of the disk. Top row: Coarsest parametrizations. Bottom row: Refined parametrizations. Black lines represent the control net (solid and dashed represent directions), gray lines the knot span lines, green disks control points, and red disks control points whose associated basis function is not in* $\mathcal{H}^2$*. Repeated control points are marked with a circle.*

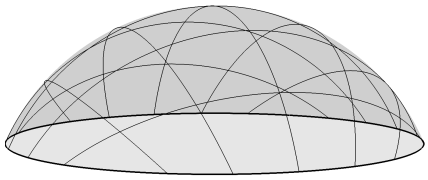

(b) *Posterior corneal surface built with the inflated parametrization of the disk.*

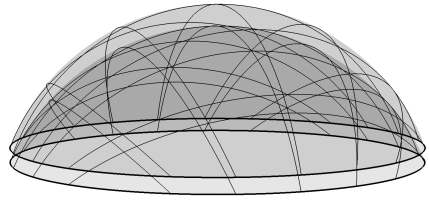

(c) *Posterior and anterior corneal surfaces in their final location.*

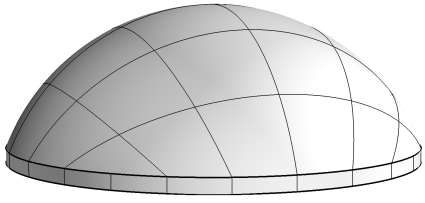

(d) *The volumetric mesh is built joining the posterior and anterior corneal surfaces.*

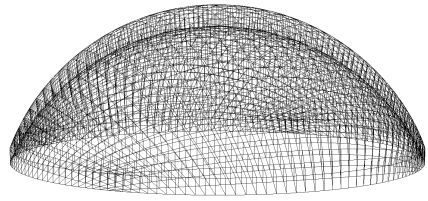

(e) *Example of an* h*-refined computational mesh of the geometry of a c57BL/6 mouse.*

Figure 4.10. Construction of the subject-specific computational mesh.

located at the boundary of the domain, whose associated control points are not in $\mathcal{H}^2$. Once again, Takacs and Jüttler (2012) have proposed a modification to the basis functions to recover the required regularity at the expense of loosing two degrees of freedom per quintuple. Alternatively, we avoid the integration in those elements spanned by the non sufficiently regular basis functions associated with this singular points by imposing Dirichlet boundary conditions for the phase-field equation in them.

Once we have chosen and appropriate parametrization of the disk we continue constructing the geometry. We transform this disk into a spherical cap with radius R_p to build the posterior cornea surface (see figure 4.10b). As in Piegl (1986), starting with the coarsest inflated parametrization of the disk (see figure 1.18c), we change the weight and the z coordinate of the control point at the center of the disk to $z = d$ and $w = 1 - c$, respectively, where

$$c = \frac{\left(2+\sqrt{2}\right) g^2}{r^2+g^2}, \quad d = \sqrt{\frac{cr^2\left(2-c\left(2-\sqrt{2}\right)\right)}{\left(2-\sqrt{2}\right)(1-c)^2}}, \quad g = R_p - b_p.$$

Then, we proceed similarly with the anterior cornea surface, but using $g = R_a - b_a + t_\ell$, and vertically translate the latter until its boundary circle is at a distance of t_ℓ with respect to the boundary circle of the first surface (see figure 4.10c). The next step is to create a volume by joining the two spherical caps using linear elements and order-elevate to also achieve $\mathcal{C}^1$-continuity in the vertical direction (figure 4.10d). Finally, we can h-refine the mesh as desired. In particular, our computational mesh is composed of 14489496 knot spans. Figure 4.10e shows an example of a refined mesh, although, for the sake of plot clarity, this mesh is coarser than the one we used. Note that the obtained computational mesh is geometrically exact and not an approximation to that in figure 4.9.

4.4 Angiogenesis in the mouse cornea

As mentioned in the review of the literature (page 36), there are few models that replicate the corneal micropocket angiogenesis assay, namely, Harrington *et al.* (2007); Jackson and Zheng (2010); Tong and Yuan (2001, 2008b), and all of them are two-dimensional. We showed in section 4.2 that three-dimensional simulations show a topological complexity more in agreement with *in vivo* vascular patterns which is not captured in two dimensions. Hence, in this section we reproduce for the first time the mouse corneal micropocket angiogenesis assay in three dimensions and in a real geometry with the aim of predicting the complex three-dimensional vascular patterns observed in the experiment.

The simulations shown here use the same mathematical model and numerical algorithms developed in chapter 2, which have proven to be robust and efficient in three dimensions and simple geometries in the previous chapter. Note, however, that in order to reproduce the mouse corneal micropocket angiogenesis assay our computational domain needs to be almost seven times greater than any one used until now in this thesis: while the side of the cube was 375 µm, the diameter of the cornea is 2600 µm. As the mathematical model was not conceived for such large-scale simulations, some parameters of the model which were not obtained from *in vivo* or *in vitro* data[4] need to be re-calibrated. Thus, we start this section with an study of appropriate parameters in subsection 4.4.1 through numerical tests and then proceed to simulate the assay and discuss the results in subsection 4.4.2.

4.4.1 Numerical tests

We perform the numerical tests in three different computational meshes, being each one reduced-size versions of the geometry of the cornea of figure 4.9. Our approach here is to study the behavior of the model in domains of increasing size. In particular, we start with numerical tests (figure 4.11) in a geometry whose size is one third of the real one, that is, in a fictitious cornea with radius $r = 433.37\,\mu\text{m}$. Note that, although smaller than a real cornea, this geometry is still more than twice the size of the geometry of the simulations in a cube. The first numerical test (figure 4.12a(i)) is performed using a relatively coarse computational mesh composed by $128 \times 128 \times 16$ knot spans and using the parameters of section 4.2. As shown on the left-hand side of that figure, the entire cornea is initially avascular except for its edge, where we locate a parent capillary that mimics the capillaries of the limbal region. We also include a pellet using the concept of fixed hypoxic cells developed in the mathematical model: It is modeled as one hypoxic cell with $R_{\text{HYC}} = 50\,\mu\text{m}$ and located 240 µm away from the edge of the cornea in the horizontal plane. The right-hand side snapshot of figure 4.12a(i) shows the vascular pattern at the end of the simulation. This simulation reveals that the developed numerical algorithm also works in a complex geometry with non-linear mappings. However, is also evinces two problems. The first one is that the mesh is too coarse to simulate such thin capillaries. Note that their surface is not smooth and that at the end of the capillaries the elements can be visually appreciated[5]. The second problem is that the final pattern is too dense compared to those generated in *in vivo* assays. Our conjecture is that the model misses some important biological mechanisms such as filopodia environment survey, migration by mechanotaxis,

[4] These parameters were estimated in the original model.

[5] Due to the phase-field dynamics, the base or beginning of the capillaries has already been smoothed out and the elements are no longer discernible.

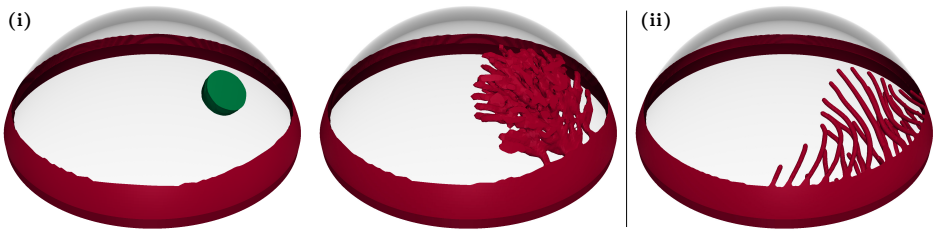

(a) *Initial conditions and final patterns of two numerical tests before (i) and after (ii) the first parameter re-calibration.*

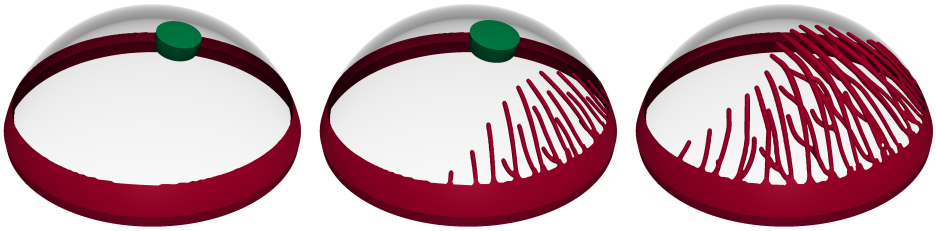

(b) *Evolution of the vascular pattern in a numerical test in which the pellet is farther from the limbus. The value of f_{act} needs to be reduced to get TEC activation.*

Figure 4.11. Numerical tests using a thrice smaller cornea geometry.

and regression and regrowth of capillaries, which have to be incorporated in it. With these new insights of the model we perform a second simulation on the same geometry and maintaining the initial conditions, whose final pattern is shown in figure 4.12a(ii). We h-refine the computational mesh in the horizontal directions (the vertical was already fine enough) to get a mesh composed by $256\times256\times16$ knot spans. Furthermore, in an attempt to include the missing biological mechanisms we increase the range of action of the Delta-Notch mechanisms fourfold and we (temporarily) remove haptotaxis to easily observe its effect. As a result, we obtain smoother capillaries that form a sparser final vascular pattern comparable with *in vivo* assays and, hence, we maintain the new parameter value for the Delta-Notch.

One of the major differences in the setup of the mouse corneal angiogenesis assay with respect to previous simulations is the distance between the hypoxic cells and the initial capillary. In the assay, the pellet can be located up to 1 mm away from the limbus, while in previous simulations, the minimum distance from the hypoxic cells to the initial capillaries was 40 µm. Hence, the next numerical tests in this reduced geometry investigate changes in the initial conditions, in particular, we study the behavior of the mathematical model as we move the pellet away from the parent capillary. We perform several numerical tests (results not shown) starting

with the same pellet location as in figure 4.11a and gradually moving the pellet towards the center of the cornea. When the pellet is located 300 µm away from the edge of the cornea in the horizontal plane (as in the left-hand side of figure 4.11b) the mathematical model reaches a stationary state in which no TEC gets activated (results not shown). This is a consequence of the parameter calibration of the TAF diffusion equation which was originally estimated for smaller domains. In order to get TEC activation, we opt to change their sensitivity to TAF. In particular, by setting $f_{\text{act}} = 0.001$ and $G_{\text{act}} = 0$, we recover TEC activation that creates the vascular pattern shown in figure 4.11b. Note how, even at this reduced-size geometry and without the haptotactic conceptualization, the capillaries cross one over another (without touching) forming a three-dimensional pattern.

Our next step in this numerical study is to increase the size of the geometry to two thirds of the real one. We also increase the number of knot spans of the computational mesh to $512 \times 512 \times 32$, accordingly. The initial conditions are similar to the previous numerical tests, as shown on the left-hand side of figure 4.13. However, as this geometry is larger, the pellet is located further away from the limbus, at 600 µm from it. As before, we need to increase the sensitivity of TECs, so that they detect the few amounts of TAF that reaches them. The result of this test is the final pattern shown on the right-hand side of figure 4.13 using a tenfold smaller value of f_{act}. Although we achieved TEC activation, we detect a problem which we show in the inset of the figure: capillaries break at their base by the time the neovasculature reaches the pellet. Our hypothesis is that the lower

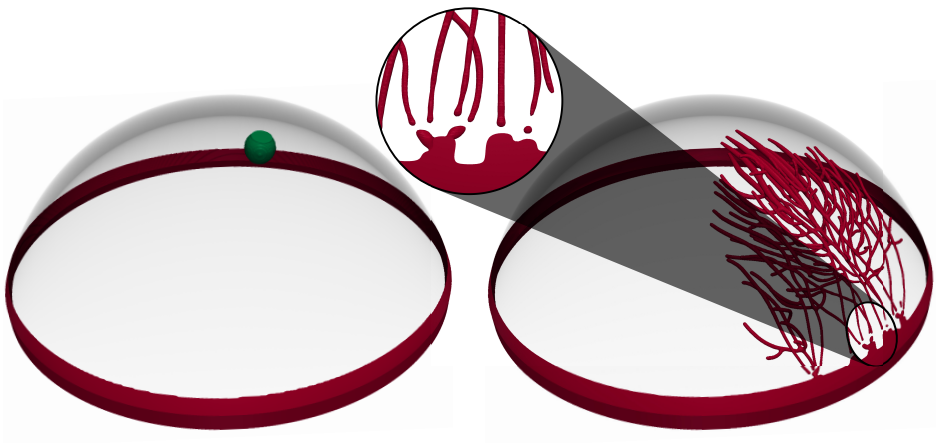

Figure 4.13. Numerical test using the cornea geometry reduced by a factor of 2/3**.** *The phase-field dynamics brake several capillaries at their base due to the reduced stalk cell proliferation at low TAF levels.*

Table 4.1. *Parameter re-calibration based on numerical tests to adapt the mathematical model to the bigger geometry of the mouse corneal micropocket angiogenesis assay.*

Parameter	Value in small-domain simulations	Value in the mouse corneal micropocket angiogenesis assay
δ_4	20 µm	80 µm
f_{act}	0.055	0.0001
G_{act}	0.01	0.0
R_{TEC}	5 µm	6.25 µm
δ	0.063	0.314

amounts of TAF towards limbal region favors the long-term phase-field dynamics that tend to nucleate the capillary field. This effect could not be appreciated in smaller-domain simulations as it was balanced by the proliferation of capillaries that tend to enlarge them in the presence of higher amounts TAF. One way to fix this problem is to increase the proliferative rate of stalk cell, that is, the value of B_p. Yet, a simpler way is to increase the radius of TECs within its biological range to $R_{\text{TEC}} = 6.25\,\mu\text{m}$. We opt for the latter, as it is easier to calibrate.

Finally, we perform a numerical test in the actual geometry of the cornea (results not shown). As in the previous tests the sensitivity of TECs needs to be increased so that they get activated by TAF released from a further away pellet. Table 4.1 summarizes the final values of the re-calibrated parameters that adapt the mathematical model developed for relatively small scales to the big scales spanned in the mouse corneal micropocket angiogenesis assay.

4.4.2 Numerical simulations of the mouse corneal micropocket angiogenesis assay

Here we present and discuss simulations of the mouse corneal micropocket angiogenesis assay using the mathematical model presented in chapter 3 with the parameter re-calibration for large scales shown in table 4.1. The simulations are performed in a computational mesh composed by $777 \times 777 \times 24$ knot spans which is an exact parametrization of the geometry of a c57BL/6 mouse defined in figure 4.9. Note that the mesh is more than three times finer than those used in numerical tests on three times smaller corneas (figure 4.11), so that the resolution

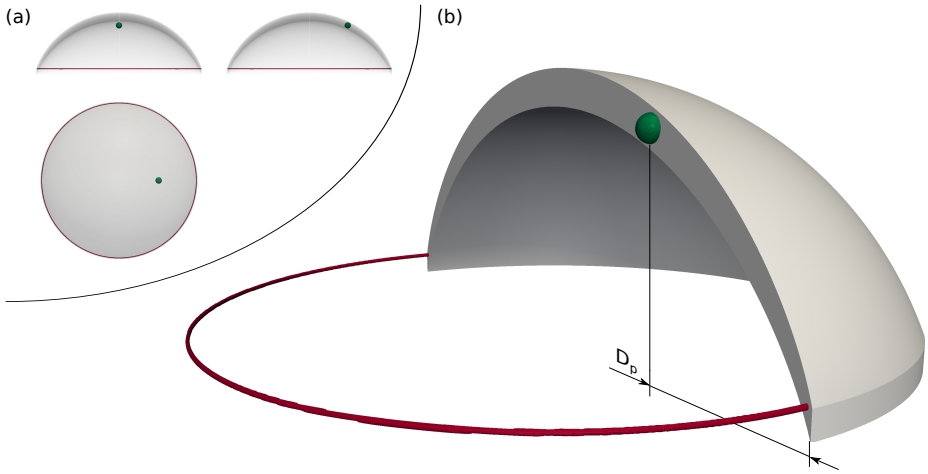

Figure 4.14. Initial conditions of the mouse corneal micropocket angiogenesis assay. *(a) Plan and elevations of the initial conditions. (b) Perspective view showing the initial capillary, the pellet, and half of the computational domain. The distance D_p varies among simulations.*

of the mesh is enough to capture the phase-field interfaces.

Figure 4.14 shows the initial conditions of the simulations. The initial capillary is a polished version of the one used for the numerical tests. Now, it is a thinner capillary with an approximate radius of 7 µm with a toroidal shape located all along the limbal region. The pellet is modeled as a spherical hypoxic cell of radius 62.5 µm whose center is placed at a distance D_p from the edge of the cornea. As explained in the introduction, this distance varies from experiment to experiment, although the protocol recommends to perform the initial incision to place the pellet at 1 mm from the limbus. Hence, D_p will be different among simulations to mimic different experimental setups.

In figure 4.15 and video S4.6 we show the time evolution of an *in silico* mouse corneal micropocket angiogenesis assay. In this particular simulation the pellet is located at $D_p = 1.06$ mm, following the protocol recommendation. Figure 4.15a shows a snapshot some time after the TAF has reached the initial capillary activating several TECs that start their migration following TAF gradients. This image evidences the important role of the lateral inhibition mechanism, whereby the nascent spouts are initially separated forming a salt-and-pepper pattern. As the capillaries grow towards the pellet (figure 4.15b), this regular pattern is lost, partially due to the alteration of the TAF regular front by capillary consumption and partially due to the activation of new TECs from the growing capillaries. Note that as they approach the pellet, the pattern starts to present the characteristic

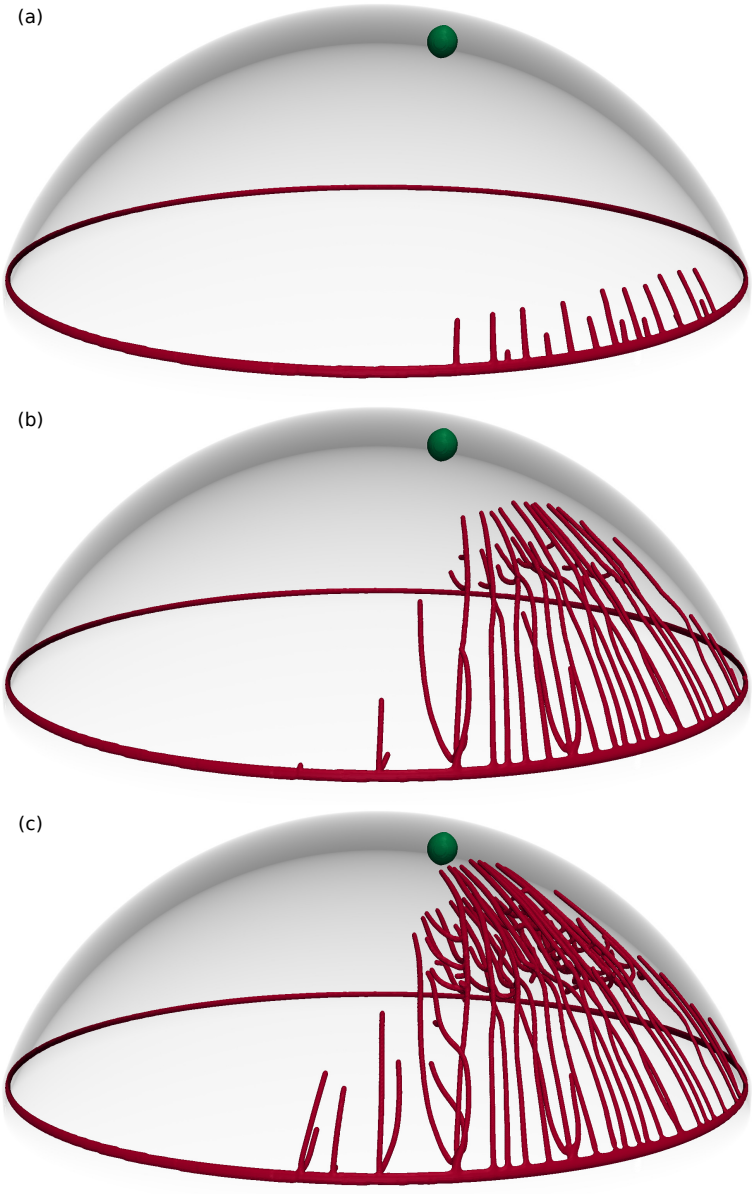

Figure 4.15. Simulation of the mouse corneal micropocket angiogenesis assay in the absence of haptotaxis. *The vascular network shows the brush-border effect as it approaches the pellet, located at* $D_p = 1.06\,mm$.

brush-border effect shown in the experiments (figure 4.16). In figure 4.15c we show the vascular pattern just before the capillaries reach the pellet. At that moment the *brush-border effect* has developed further and the leading capillaries get progressively closer one to each other driven by TAF gradients. Several new TECs (23 specifically) were activated in the parent capillary since the beginning of the simulation; however, comparison between figures 4.15a and 4.15c reveals that this activation reduces with time, as little TAF reaches the parent capillary along the simulation. Furthermore, the distance between TECs activated from the initial capillary increases, meaning that the limiting mechanism for TEC activation is no longer lateral inhibition, but the amount of available TAF.

We compare *in vivo* assays from Cao *et al.* (2003) with our simulations in figure 4.16. The *in vivo* assays differ one from the other both in the carrier-free agent and in the location of the pellet. While in figure 4.16a the pellet is composed by PDGF and located close to the limbus, in figure 4.16b it is composed by VEGF and located almost at the center of the cornea. We replicate these experiments by altering D_p in our simulations, setting $D_p = 1.06\,\text{mm}$ in the first one (figure 4.16c) and $D_p = 1.21\,\text{mm}$ in the second one (figure 4.16d). Although we are not able to change the carrier-free agent of the virtual pellet, we still obtain patterns that resemble those presented in the experiments. Thus, when the pellet is closer to the limbus the number of capillaries that start from the parent capillary is less than when it is further from the limbus as in figures 4.16a and 4.16b. As a consequence, the volume spanned by the neovasculature in the former is smaller than that in the latter. Finally, we want to emphasize here that the results of our simulations are three-dimensional vascular patterns that, as shown in the figure, resemble more closely the experiments than previous two-dimensional simulations.

The comparison in figure 4.16 reveals that although the main distribution of the neovasculature within in the cornea is captured in the simulations, the path followed by the capillaries *in silico* is not as tortuous as that *in vivo*. Recall, however, that we removed the conceptualization of haptotaxis to re-calibrate the model and to better study the results at full scale, as in figure 4.15. We recover now this conceptualization to show in figure 4.17 and video S4.7 the results of the same simulation of figure 4.15, but with haptotaxis. As occurred before, the parameters of the circular biased random walk presented in chapter 3 were not prepared for such big domain and, consequently, the turning angle δ has been increased five fold (see table 4.1).

From the very first moment, as shown in figure 4.17a, haptotaxis has a severe effect in the tortuosity of the capillaries. TECs that before leaded the capillaries straight towards the pellet (figures 4.16c and 4.16d), now wander around the domain influenced by the ECM through haptotaxis. The first consequence of this wandering is that capillaries no longer grow parallel to each other; instead, they

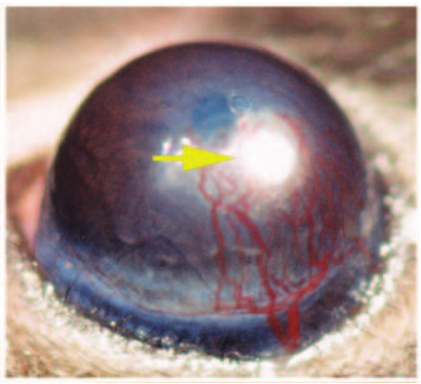

(a) *A pellet with a PDGF carrier-free agent is located closer to the limbus.*

(b) *VEGF used as carrier-free agent is located almost at the center of the cornea.*

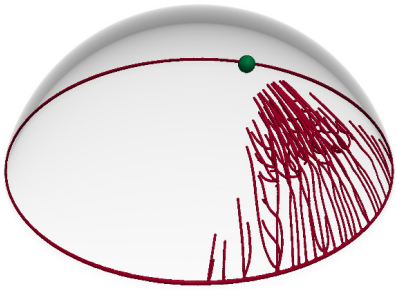

(c) *When* $D_p = 1.06\,mm$ *the neo-vasculature grows from a short delimited section of the limbus.*

(d) *Moving the pellet to* $D_p = 1.21\,mm$ *increases the limbus section from which new capillaries grow.*

Figure 4.16. ***In vivo*** **and** ***in silico*** **mouse corneal micropocket angiogenesis assays.** *These assays show the influence of pellet location (yellow arrows* in vivo*, green spheres* in silico*) on the pattern of the neovasculature. (*In vivo *assays reproduced from Cao* et al.*, 2003)*

have a more realistic, curved shape. What is more, TECs' trajectory does not so frequently lie on the middle plane of the cornea as before, so that as they move, they generate a more three-dimensional vascular pattern (figures 4.17b to 4.17d). In addition, this movement increases the likelihood of anastomosis events, even in the absence of an explicit model of TEC filopodia which are believed to be ultimately responsible for anastomosis. Thus, the neovasculature connectivity is highly increased compared to the previous simulation from the very beginning (figure 4.17b) and results in a more looped pattern (figure 4.17e). Another consequence of haptotaxis is that the role of the lateral inhibition mechanism, although still relevant, is not so marked in this simulation. As shown in figure 4.15c the

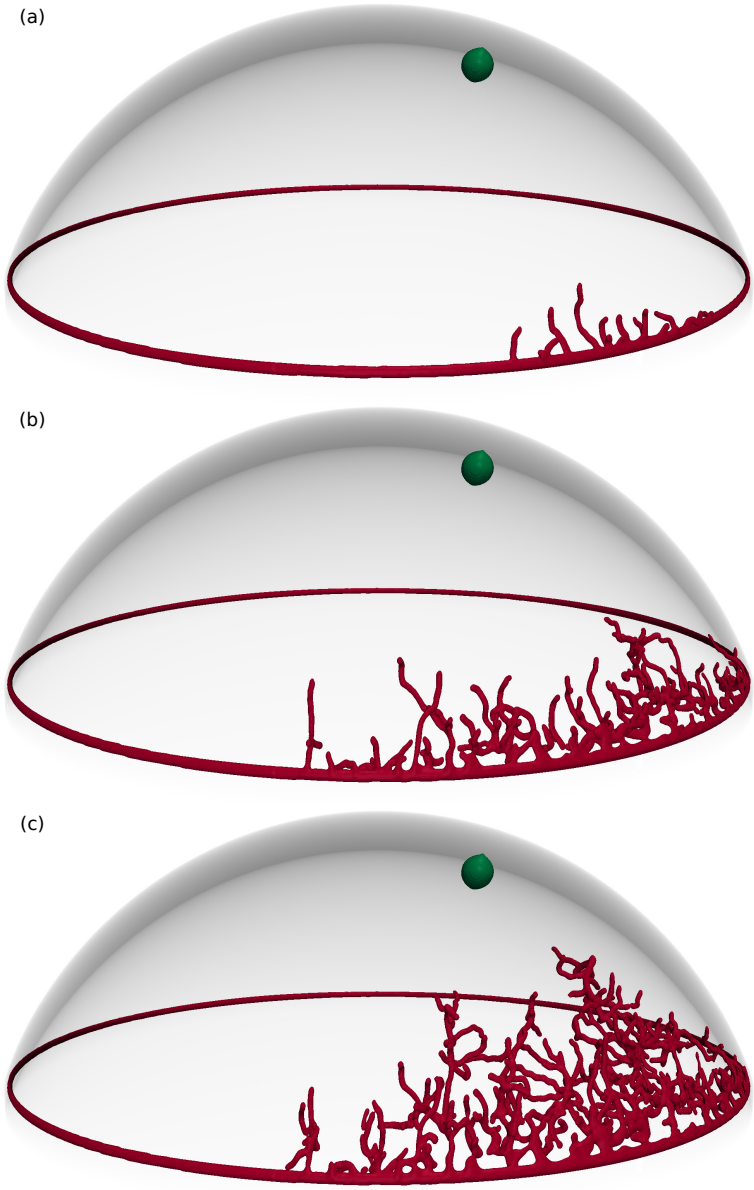

Figure 4.17. Time evolution of a simulation of the mouse corneal micropocket angiogenesis assay. *Haptotaxis augments the connectivity of the network by increasing the number of anastomosis. The pellet is located at* $D_p = 1.06\,mm$.

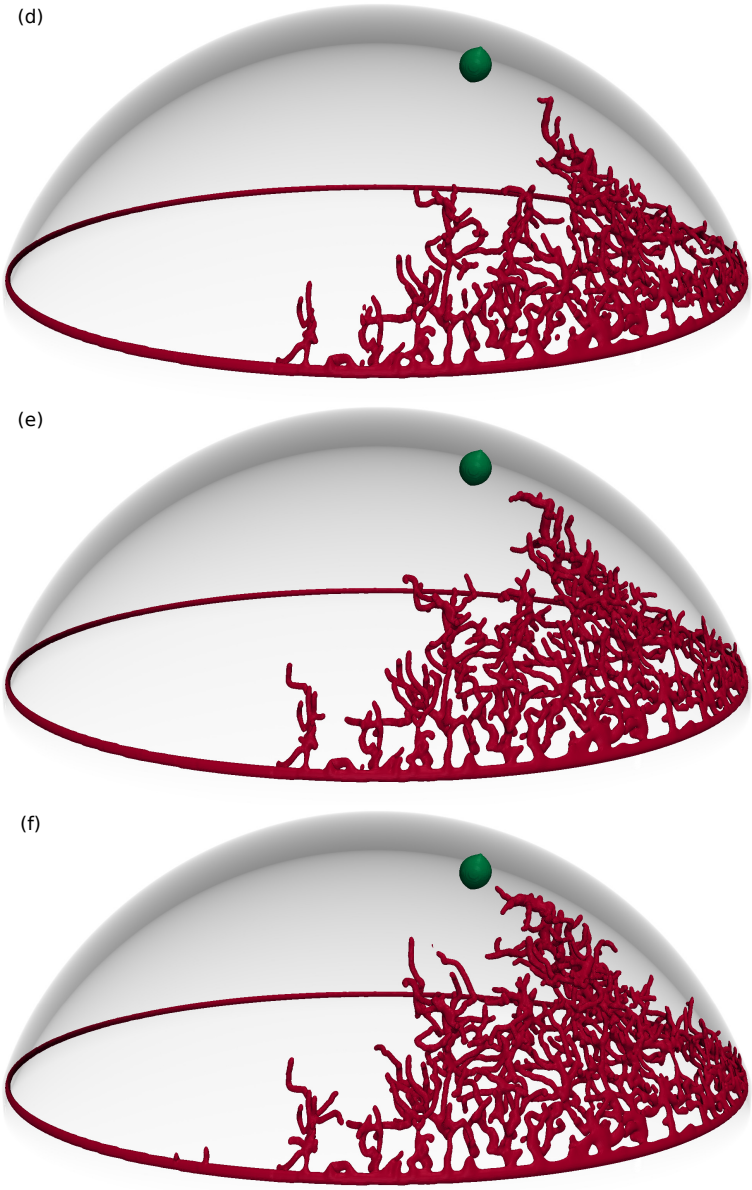

Figure 4.17. Time evolution of a simulation of the mouse corneal micropocket angiogenesis assay. *Continued.*

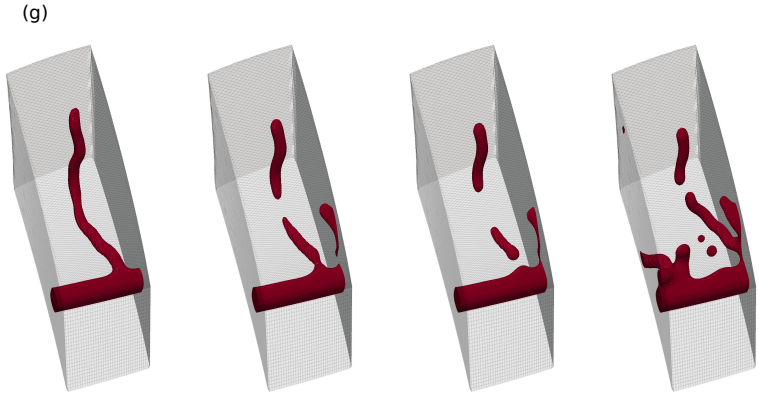

Figure 4.17. Time evolution of a simulation of the mouse corneal micropocket angiogenesis assay. *Continued.*

salt-and-pepper pattern of capillaries starting from the initial capillary is now lost.

Perhaps the most surprising consequence of haptotaxis in this simulation is the emergence regression, a new phenomenon not observed until now in any previous simulation and not explicitly built in the model. We show in the insets of figure 4.17c one of these events as an example. There, a capillary grows following TAF gradients, but its TEC eventually gets deactivated long before reaching the pellet due to the end of the stimuli ($f < f_{\text{act}}$). This situation by itself was rarely observable in previous simulations where most TECs either remained active until the end of the simulation when all TAF was consumed or (less frequently without haptotaxis) anastomosed. Here, however, several circumstances coalesce: The amount of TAF is lower, there are more capillaries that consume TAF, haptotaxis can drive TECs towards low-TAF regions, and the chances of anastomosis events, although higher than without haptotaxis, are lower than in two-dimensional simulations. After the deactivation, it is only the phase-field dynamics that govern the behavior of the capillary and, in particular, because there is no proliferation, only the first term on the right hand side of equation (3.2). This dynamics tend to minimize the area of the capillary which is particularly high due to its slender shape. Consequently, most of the capillary slowly regresses towards its parent capillary. Perhaps because it is a slow process, in the few TEC deactivation events in previous simulations, because the domain was smaller and the capillaries rapidly spanned the domain, there was no observable regression. Finally there are two aspects of this regression that we think must be highlighted. The first one is that, as shown in figure 4.17c, not the entire capillary regresses into its parent capillary,

but part of it is transformed into a spherical-like mass (phase-field nucleation) which eventually disappears. The second one, connected to the first, is that in the absence of proliferation the phase-field equation conserves mass, which translated to biological terms means that the endothelial cells in our simulation are not killed by apoptosis (contrary to reality); instead they join the surrounding vessels.

4.5 Conclusions

In this chapter we have simulated one of the most common angiogenesis assays in three dimensions using a subject-specific geometry and extracted the following conclusions:

- The mouse corneal micropocket angiogenesis assay is a widely used assay which provides a means to study angiogenesis *in vivo* in an avascular tissue, to control the location of the pellet, to know the release rate of the desired tumor angiogenic factor, and, what is more, to observe the whole angiogenic process from beginning to end in a non-invasive way. These characteristics fit with our model, as we have an avascular tissue and one tumor angiogenic factor released from a known location and at a desired rate and our simulations can be compared with the assay.

- The model and algorithms developed in chapters 2 and 3 provide a framework to perform the *in silico* version of this assay in three-dimensional simulations in complex geometries, which has not been previously done.

- The three-dimensional computations in simple geometries presented in this chapter suggest that, for mathematical models to achieve the topological complexity observed in *in vivo* angiogenesis experiments, two-dimensional simulations may not be enough. In particular, we found denser patterns with a higher number of anastomoses.

- Our results also indicate that haptotaxis may have a significant impact in the final pattern achieved by capillary networks in three-dimensions. In contrast with simulations of the model without haptotaxis, our results reveal increased vascular pattern complexity, more tortuous TEC trajectories, higher number of anastomosis events, and shorter capillaries.

- Our computational domain is the exact geometry of the cornea of a c57BL/6-strain mouse as defined in the literature. The analysis of several parametrizations of the disk using NURBS suggested the inflated parametrization as the more appropriate for this geometry.

- Numerical tests in scaled versions of the final geometry gave us insights of the behavior of the model in big scales. These tests reveal the need to re-calibrate five parameters for the model to produce results comparable with the assay. These re-calibrations stems from the fact that the model was calibrated for tumor angiogenesis occurring at small scales. The numerical tests were also used to assess the number of knot spans needed to accurately solve the problem, leading to a mesh composed by 14489496 knot spans.

- We performed several *in silico* mouse corneal micropocket angiogenesis assay, which to the best knowledge of the author, were done for the first time. They revealed that three-dimensional simulations are necessary to capture angiogenesis, as this phenomenon is essentially three dimensional.

- These simulations, even in the absence of the haptotaxis conceptualization, showed the well-known brush-border effect in three dimensions.

- Changes in the location of the pellet lead to different vascular patterns. In particular, the shorter the distance between the pellet and the limbus, the less number of capillaries that grow from the initial vessel and the less area filled by the neovasculature. These patterns are in agreement with *in vivo* assays through qualitative comparison.

- The simulations on the cornea uncovered a new phenomenon not explicitly built into the model. The dimensions of the cornea lead to longer capillaries, which required more time to develop. Under this longer time scales, the phase-field dynamics came to the forefront where the levels of tumor angiogenic factors were low. As result, the capillaries slip back into their parent vessels, as their slender shape is not energetically stable in terms of the phase-field dynamics. These behavior can be interpreted as capillary regression, which is investigated in the following chapter.

4.6 Supporting information

Supporting information includes the following videos that can be found online at `http://caminos.udc.es/gmni/gente/gvilanovac/thesis/`:

Video S4.1. Three-dimensional angiogenesis from two parent capillaries. This video is related to figure 4.5.

Video S4.2. Evolution of a vascular network promoted by hypoxic cells mimicking a multifocal tumor. Related to figure 4.6.

Video S4.3. Three-dimensional angiogenesis promoted by 200 hypoxic cells. Related to figure 4.7a.

Video S4.4. Three-dimensional angiogenesis promoted by 100 hypoxic cells. Related to figure 4.7b.

Video S4.5. Construction of the subject-specific computational mesh using the inflated parametrization presented in figure 4.10.

Video S4.6. Time evolution of a simulation of the mouse corneal micropocket angiogenesis assay using the model without haptotaxis, as shown in figure 4.15.

Video S4.7. Time evolution of a simulation of the mouse corneal micropocket angiogenesis assay, as shown in figure 4.17.

Chapter 5

Growth, regression, and regrowth

One of the most salient features of tumor-induced vascular networks is their instability: they are stimulus-dependent and may undergo alternating stages of growth, regression, and regrowth. Thus, tumor angiogenesis is a highly dynamic phenomenon in which the new vasculature is a sequence of patterns that are continuously shaping to tumor angiogenic factor distribution to better nourish and oxygenate the cells. Previous efforts to model tumor angiogenesis, including those presented in this thesis thus far, have chiefly focused on the initial growth of blood vessels, often using models which are fundamentally unable to predict the natural regression and regrowth observed in experiments. In this chapter, following a phase-field methodology, we propose a new model of tumor angiogenesis that reproduces the aforementioned features and highlights the importance of vascular regression and regrowth. The model also includes a conceptualization of tip endothelial cell filopodia (the cellular protrusions that aid TECs in their migration) that plays a key role in regrowth and loop formation. The predictions of our model are in quantitative agreement with *in vivo* experiments and may prove useful for the design of antiangiogenic therapies.

5.1 Stimuli dependency of tumor-induced vasculature

Tumors give rise to dense, tortuous, and defective capillary networks (see figures 1.13 and 5.1a), which are significantly different from those formed in physiological conditions (Carmeliet and Jain, 2000). Arguably, the most characteristic feature of tumor-induced capillaries is that they are TAF-dependent, as suggested by the experiments in Baffert *et al.* (2006); Falcon *et al.* (2011); Inai *et al.* (2004); Mancuso *et al.* (2006). Specifically, in Mancuso *et al.* (2006), the authors performed *in vivo* experiments where newly-formed capillaries regressed after chemically inhibiting VEFG receptor signaling of endothelial cells for a time span of 7 days (figure 5.1b). Perhaps more importantly, the experiment showed that tumor-induced capillaries regrew when VEGF receptors were made functional again (figures 5.1c and 5.1d). Due to this evidence, it is currently believed that vascular regression can also happen locally and spontaneously in areas which are temporarily well oxygenated. After local regression, nearby tumor cells become hypoxic again, activating back the angiogenesis cascade.

Mancuso et al. also observed in their work that regressing capillaries leave (temporarily) behind the vascular membrane that enveloped them. When new capillaries regrew afterwards, these vascular membranes were used by TECs as an scaffold that facilitated their migration (figure in supp material): By going through these empty sleeves of basement membrane TECs avoid or at least minimize the effort of degrading the ECM. As a consequence, the authors also observed that the regrowth was faster than the normal growth. Notably, the role of detecting the basement membranes relies on filopodia. As explained in the introduction of this thesis, filopodia are receptor-rich, slender cytoplasmatic protrusions that TECs extend to enhance their sensitivity (see figure 5.2). They can be thought as highly-dynamic probes sent forward by TECs to investigate their microenvironment and respond to it. In particular, as shown in figure 7c of Mancuso *et al.* (2006), when the filopodia sense the remnants of basement membrane, TEC alter their direction towards them to use them as the path of minimum resistance in their migration.

There is an emerging view that regression and regrowth may play a significant role in the long-term dynamics of tumor angiogenesis and cancer development (Goel *et al.*, 2011; Potente *et al.*, 2011). Numerous investigations have shed light on the intricate growth of capillaries through mathematical models as shown in subsection 1.2.2, but the dynamics of regression and regrowth has received little attention (Logsdon *et al.*, 2014). In this chapter, we present a model for tumor angiogenesis that includes not only growth of new capillaries, but their natural regression and regrowth. Due to the key role of filopodia in regrowth, we also

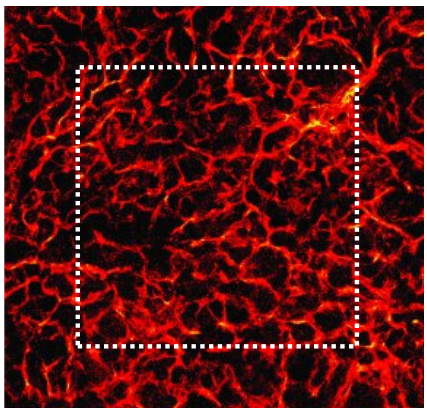

(a) *Growth of capillaries promoted by an untreated Rip-Tag2 tumor.*

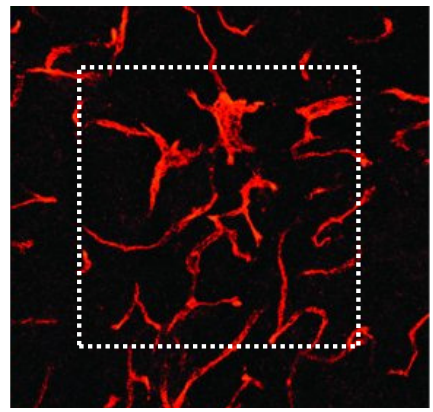

(b) *Regressed capillaries after a 7-day inhibition of VEGF receptors.*

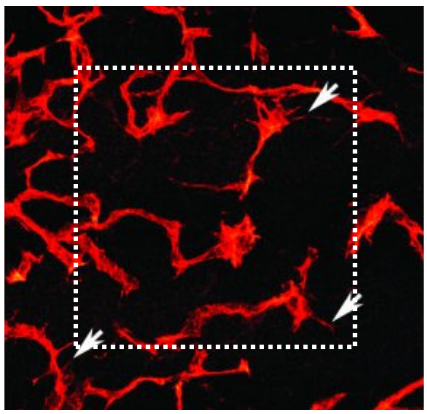

(c) *Rapid regrowth of first sprouts (arrows) 2 days after inhibition removal.*

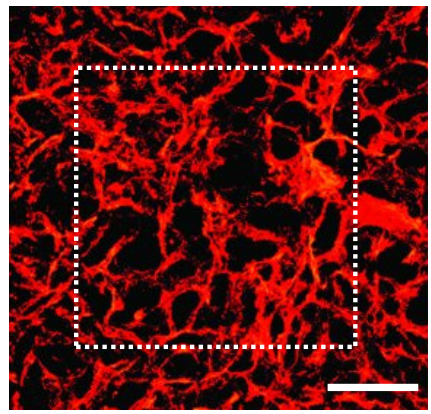

(d) *Regrown capillaries 7 days after inhibition removal showing pathological structure.*

Figure 5.1. Growth, regression, and regrowth *in vivo*. *Confocal micrographs of the tumor-induced vasculature in a RIP-Tag2–transgenic mice before, during, and after a treatment that inhibits VEGF receptors. Scale bar (applies to all images):* 115 μm. *(Adapted from Mancuso et al., 2006).*

incorporate a conceptualization of filopodia in our theory. Our results achieve good agreement with *in vivo* experiments and suggest that our model could be a useful tool for the design of antiangiogenic therapies, which are emerging as a promising treatment for cancer (Maxwell and Ashcroft, 2009).

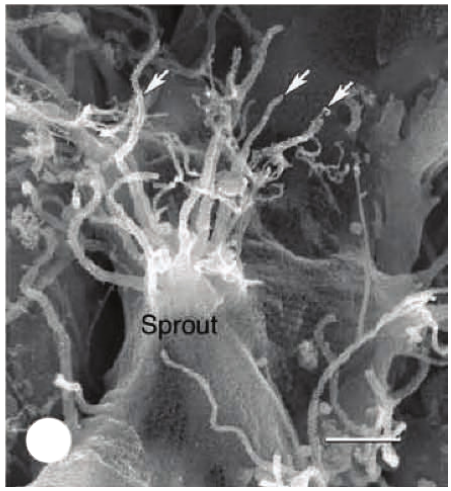

(a) *Scanning electron microscope image of an endothelial cell extending filopodia (white arrows). Scale bar: 2 µm. Reproduced from Figg and Folkman, 2011a.*

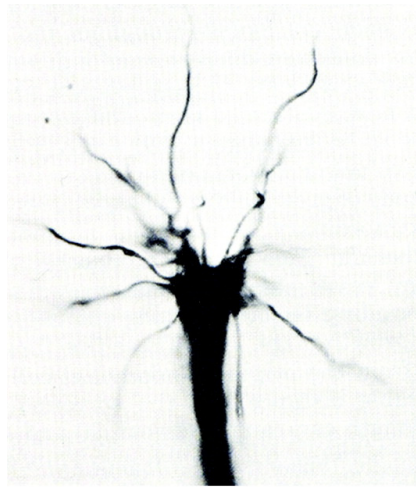

(b) *Electron microscope snapshot of embryonic tip endothelial cell showing filopodia extensions. Reproduced from Marin-Padilla, 1985.*

Figure 5.2. Filopodia. *Tip endothelial cells are characterized by the forward extension of filopodia that aid them to guide the growth of new sprouts during angiogenesis.*

5.2 The mathematical model

Our formulation accounts for three essential ingredients of angiogenesis, namely, TAF, capillaries, and TECs, as shown in figure 5.3. In our theory, TAF is interpreted as one general and potent angiogenic factor, for instance VEGF (as shown in appendix C the incomplete knowledge and wide variety of functions of TAFs makes it effectively impossible to account for everyone). We model TAF as a normalized continuous variable $f \in [0, 1]$ representing the concentration of the factor. Capillaries are modeled using an order parameter $c \in [-1, 1]$, such that the areas where $c \geq 0$ are identified with the endothelial cells that form capillaries and those where $c < 0$ represent the extravascular tissue. Furthermore, as capillaries are enveloped by a basement membrane and occasionally by a thin cell coverage (pericytes and smooth muscle cells), we extend the definition of c to include them: The extravascular tissue ($c < 0$) is compartmentalized into the capillary coverage, $-0.9 < c < 0$, and the extracellular matrix, $c < -0.9$. Finally, TECs are modeled as discrete agents which follow chemical cues and sense trhough filopodia nearby capillaries or empty basement membranes left by regressed capillaries.

Tumor angiogenic factor TAF is produced by tumor cells when they enter a hypoxic state. Tumor cells are located at fixed points and are assumed to be hypoxic when they do not have a capillary closer than the nutrient and oxygen diffusion length, δ_{nox}, as shown in figure 5.3. TAF diffuses from the hypoxic cells and throughout the tissue, decays naturally, is consumed by endothelial cells, and eventually triggers angiogenesis. Its dynamics is supposed to be governed by the reaction-diffusion equation

$$\frac{\partial f}{\partial t} = \nabla \cdot (D \nabla f) + \mathcal{P}(d)\,(f_{\text{HYC}} - f) - \mathcal{U}(c)\, f, \tag{5.1}$$

where D is the diffusion constant and f_{HYC} is the maximum TAF produced in a HYC. $\mathcal{P}$ and $\mathcal{U}$ are, respectively, production and uptake functions defined as

$$\mathcal{P}(d) = \begin{cases} P & \text{if } d < R_{\text{HYC}} \\ 0 & \text{if } d \geq R_{\text{HYC}} \end{cases}, \quad \mathcal{U}(c) = \begin{cases} B_u c & \text{if } c \geq 0 \\ -B_d c & \text{if } c < 0 \end{cases}. \tag{5.2}$$

Here, P is the production rate, d is the distance to the closest hypoxic tumor cell, R_{HYC} is an average cell radius, B_u is the endothelial cell uptake rate, and B_d is the TAF natural decay rate and the uptake rate by other cells.

Capillaries Endothelial cells receptors stimulated by TAF activate molecular pathways that change the cell phenotype either to a migratory (TECs, modeled separately) or to a proliferative one. In the absence of stimuli, endothelial cells lining immature, tumor-induced capillaries become apoptotic, which eventually leads to vascular regression (Potente *et al.*, 2011). The key idea to successfully model this phenotype switch is to make use of non-conserved phase-field dynamics rather than previously used conserved models (chapters 2 to 4). Thus, our phase-field equation is

$$\frac{\partial c}{\partial t} = M\left(\lambda^2 \Delta c - \mu(c, f)\right). \tag{5.3}$$

Here, $M > 0$ is a parameter, λ is a constant proportional to the width of the capillary wall, and

$$\mu(c, f) = \frac{1}{4}\left(c^2 - 1\right)\left(c - 3\alpha\gamma(f)\right) \tag{5.4}$$

is the derivative with respect to c of the double-well potential (see figure 5.4)

$$\Psi(c, f) = \frac{1}{16}(c+1)^2(c-1)^2 - \frac{1}{4}\alpha\gamma(f)\,(c+1)^2\,(c-2). \tag{5.5}$$

In equations (5.4) and (5.5), α is a parameter and the function

$$\gamma(f) = \exp\left[-\exp(\beta(f - f_{\text{act}}))\right] - \exp(-1), \tag{5.6}$$

where β is a constant, tilts the double well in such a way that capillary growth (proliferative phenotypes) is favored when $f > f_{\text{act}}$, as shown by the triangle-labeled curve in figure 5.4, and capillary regression (apoptotic phenotypes) is promoted otherwise, as shown by the square-labeled curve in figure 5.4.

Remarks:

1. The parameter α guaranties that the energy potential Ψ has two minimums provided that $-0.52733 < \alpha < 0.52733$.

2. The reader is referred to Karma and Rappel (1998); Kim *et al.* (1999); Kobayashi (1993); Provatas *et al.* (1998) for detailed descriptions of this kind of phase-field models often used in dendritic solidification, but also in biological problems (Ziebert *et al.*, 2012).

Tip endothelial cells When capillaries receive TAF signals, some privileged endothelial cells (TECs) acquire a migratory phenotype and lead the growth of new sprouts (De Smet *et al.*, 2009). This phenotype was not included in equations (5.3) to (5.6). When an endothelial cell becomes a TEC, it expresses Delta-like ligand 4 (Dll-4). Dll-4 binds to Notch receptors of nearby endothelial cells preventing them from becoming also TECs (Hellström *et al.*, 2007; Thurston and Kitajewski, 2008). TECs migrate following cues that guide the new capillaries towards nutrient-demanding cells. These cues may be, for example, chemical or mechanical. TECs are especially sensitive to such cues because they extend highly-dynamic, receptor-rich protrusions called filopodia (Gerhardt *et al.*, 2003) towards the angiogenic stimuli, as shown in figure 5.2 and in the top panel of figure 5.3. As filopodia probe the cell's microenvironment, they may detect nearby endothelial cells. In this event, the TEC anastomoses with the identified endothelial cell forming a loop between the growing sprout and the detected capillary. Note that this mechanism increases the vascular network connectivity. Perhaps more surprisingly, filopodia may even sense basement membranes left behind by regressed capillaries and use them to improve their migratory capacity (see Murakami *et al.* (2006) and the supporting information therein for examples of *in vitro* experiments).

As said above, the continuous field c represents the ECM, the basement membrane (and the thin cell coverage), and the endothelial cells. However, the phase-field equation that governs the dynamics of c was missing the migratory endothelial cell phenotype, that is, TECs. The reason is that as no other cell will become migratory in the vicinity of a TEC, they are ideally suited for a discrete description. Thus, TECs are discrete agents in our formulation (see bottom panel of figure 5.3), which are coupled with the continuous field c to close the model. They are modeled

using ideas from the literature (Travasso *et al.*, 2011b), but further extended to include filopodia, to detect nearby capillaries, and to migrate not only following chemotactic cues (figure 5.3, green arrows), but also using the empty sleeves of basement membrane left in the extracellular matrix (figure 5.3, black arrow) by regressed capillaries.

The discrete agents are characterized by their center and their radius R_{TEC}. TEC

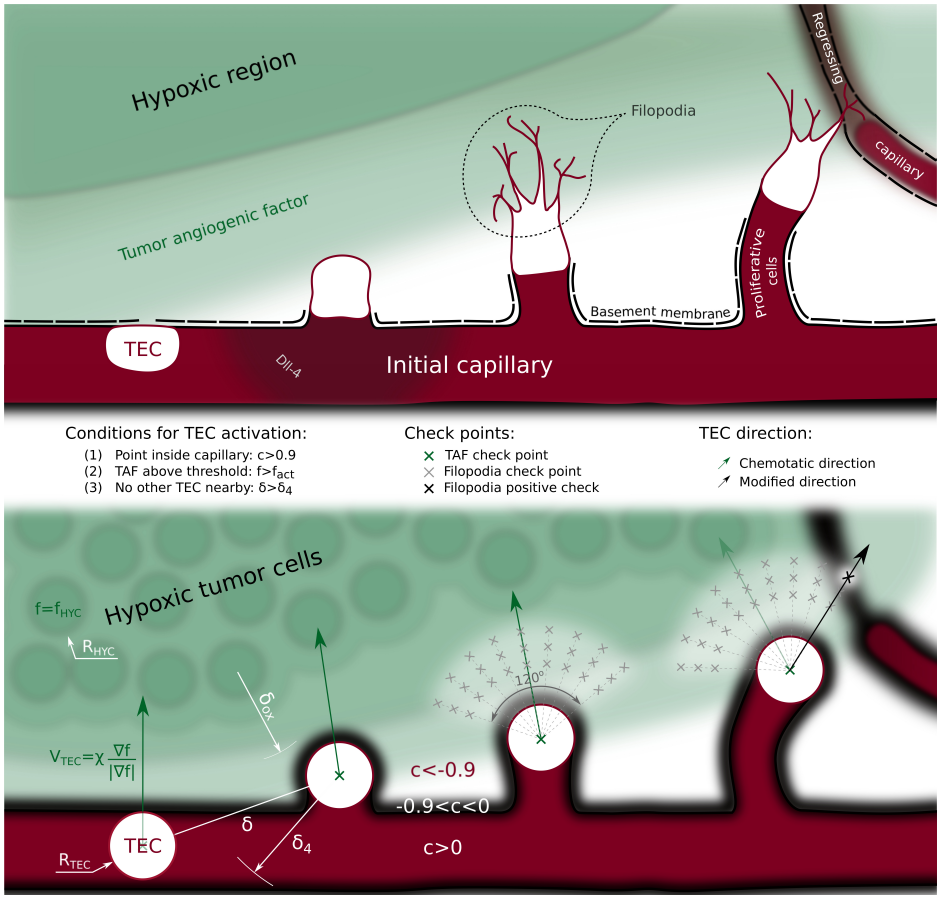

Figure 5.3. Conceptualization of tip endothelial cells. *(Top) Tumor angiogenic factor activates tip endothelial cells that extend filopodia to survey their environment. (Bottom) In the model, discrete circular agents are activated and migrate following TAF gradients (chemotaxis). Each agent evaluates conditions at filopodia check points. A positive check ($c > -0.9$) alters the (otherwise chemotactic) migration direction.*

activation, that is, the phenotype switch from quiescent or proliferative to migratory, is performed according to the following deterministic rules: A point of the domain is the center of a new TEC if

1. it is deep inside a capillary ($c > c_{\text{act}}$), to guarantee that it is an endothelial cell;
2. the tumor angiogenic factor is greater than a threshold ($f > f_{\text{act}}$), to assure that the stimuli is potent; and
3. there is no other TEC is in the vicinity (distance to every TEC greater than δ_4), to account for the lateral inhibition.

Activated cells, unless they detect a nearby basement membrane or a capillary, migrate following chemotactic cues with a velocity proportional to the TAF gradient, given by

$$\mathbf{v}_{\text{TEC}} = \chi \frac{\nabla f}{|\nabla f|}, \tag{5.7}$$

where χ is the chemotactic constant and $|\cdot|$, as in previous chapters, denotes the Euclidean norm. They also develop filopodia, which we model as a set of check points that mimic their high concentration of receptors (figure 5.3, gray crosses). Because tumor angiogenic factors polarize TECs such that they spread filopodia towards their front (De Smet *et al.*, 2009), we evenly place the check points into an annulus sector of angle $2\pi/3$ centered around the chemotactic direction, as shown in the bottom panel of figure 5.3. The internal and external radius of the annulus sector are set to $2R_{\text{TEC}}$ and $4R_{\text{TEC}}$, respectively. Filopodia do not develop immediately after TEC activation, thus, in the model, the check points are not tested until the sprout has been initiated, that is, until the TEC has migrated a diameter from its activation point and it is outside its parent vessel. A positive check (figure 5.3, black cross), defined as $c > -0.9$, means that the TEC has detected a basement membrane or a capillary through the filopodia. Under this circumstance, the direction of migration is altered towards the check point and the velocity module is doubled. In the event of several positive checks, the check point where the value of c is higher is selected.

There are two ways by which a TEC can be deactivated, that is, the endothelial cell looses its migratory phenotype. The first one occurs when the TEC anastomoses with another TEC or capillary. Anastomosis is modeled in a similar way to filopodia: TECs test the value of c in an $2\pi/3$-radians arc with radius R_{TEC} centered around the direction of migration. If any of these values is greater that 0.9, that is, the TEC is already touching the capillary, then there is an anastomosis event and the TEC gets deactivated. The second deactivating circumstance happens when the stimuli ceases (failure to meet condition 2). In both cases the discrete agent is removed.

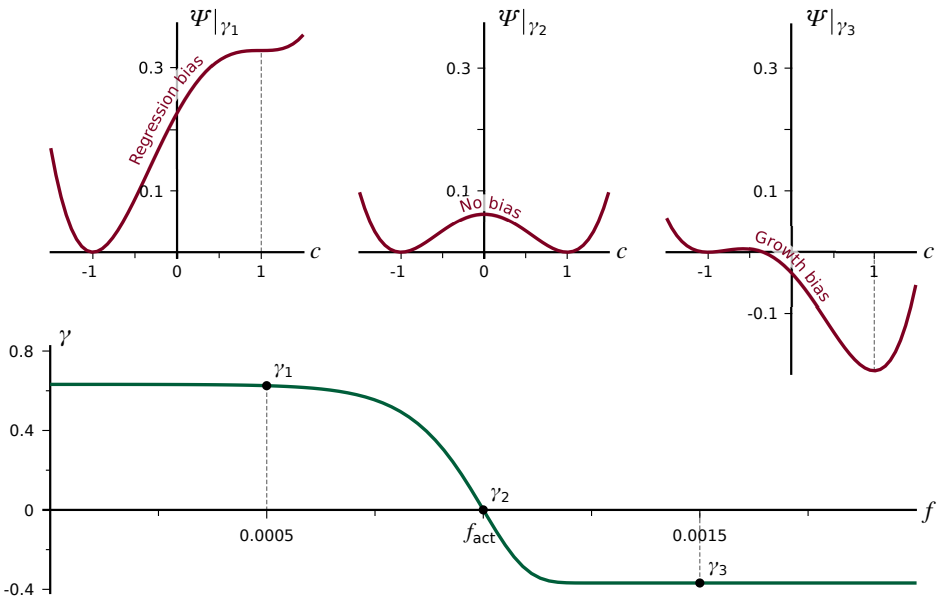

Figure 5.4. Chemical energy and tilting function. *The chemical free energy (in red), is a double-well potential tilted by the tumor angiogenic factor value through the function $\gamma(f)$ (in green). Low values of tumor angiogenic factor bias the evolution of c towards regression (top-left graph), while high values of tumor angiogenic factor promote the growth of the phase $c = 1$.*

Finally, to close the model, TECs need to be included in the phase-field description of endothelial cells, as they are also endothelial cells. This coupling between the discrete agents and the continuous variable is performed by updating c to $c = 1$ in those regions of the computational domain occupied by TECs.

5.3 Numerical methods

Our theory is composed by two continuum variables and a set of discrete agents. Thus, we need numerical methods for the partial differential equations, for the discrete agents, and for coupling both of them. As these methods were already developed in previous chapters, here we just give a brief description of them. First, we derive the weak form of the continuous partial differential equations (5.1) and (5.3) and we discretize them in space and time using the Galerkin method and the generalized-α method (Chung and Hulbert, 1993), respectively. Isogeometric Analysis (Cottrell *et al.*, 2009; Hughes *et al.*, 2005) permitted us to use globally

Table 5.1. *Parameters of the model in dimensionless units.*

Description	Symbol	Value
Equation (5.1) – Diffusion	D	100.0
Equation (5.1) – Maximum TAF production	f_{HYC}	1.0
Equation (5.2) – Production	P	100.0
Equation (5.2) – Natural decay	B_d	0.1
Equation (5.2) – Endothelial cell uptake	B_u	6.25
Equation (5.3) – Mobility	M	0.025
Equation (5.3) – Interface width	λ	1.0
Equation (5.4) – Phenotype switch	α	0.525
Equation (5.6) – Phenotype switch	β	10^4
Equation (5.7) – Chemotatic constant	χ	7.28
Condition 1 for TEC activation	c_{act}	0.9
Condition 2 for TEC activation	f_{act}	0.001
Condition 3 Dll-4 radius of action	δ_4	32.0
Nutrient and oxygen diffusion length	δ_{nox}	20.0
TEC radius	R_{TEC}	4.0
HYC radius	R_{HYC}	4.0

smooth functions on the domain and a means of accurately solve the equations. Additionally we implemented a time-step correction algorithm similar to those in (Gomez *et al.*, 2008, 2013; Gomez and Hughes, 2011). Then, we develop an algorithm that handles TEC activation, migration, filopodia probing, and deactivation. Note that the migration of TECs is meshless meaning that it is independent of the spatial discretization of the continuum variables. This fact hindered the coupling between the discrete agents and the continuum variables, which we performed by updating the value of the order parameter c at the locations of tip endothelial cells every time step using the templates defined in chapter 2.

The parameter values used in the computations are summarized in table 5.1. Some of them are taken from *in vivo* observations, while others have been used in previous models of tumor angiogenesis (Travasso *et al.*, 2011b). The physical quantities of these parameters may be retrieved by using the length and time scales $L_0 = 1.25$ µm and $T_0 = 5460$ s, respectively

5.4 Results and discussion

We open this section with a simple simulation whose aim is to give insight and study the proposed mathematical model. Then, we show how the theory is able to capture the growth patterns of the previously shown models, in particular in a two-dimensional simulation of the mouse corneal micropocket angiogenesis assay. Finally, we present the full potential of this new theory in a simulation that replicates the experiment shown in figure 5.1.

5.4.1 Intuition of the model

In order to give an intuition and to study how the model works, we perform a quite simple simulation on a square domain (figure 5.5 and video S5.1). The simulation has the same size and uses the same mesh as those of figures 2.8 and 3.3 of previous chapters, that is, a 375 µm × 375 µm domain and a mesh composed by 256^2 quadratic elements; a configuration that has already proven to be enough to capture the phase-field interface (see figure 5.5a). Figures 5.5c to 5.5k show the time evolution of this simple simulation by means of zoomed snapshots. We say it is simple because, contrary to the next simulation in this chapter, it only has an initial straight capillary and one HYC located close to it – approximately 60 µm away (see figure 5.5b). Furthermore, for the sake of simplicity, we have set f_{HYC} to 0.1 so as to reduce the potential number of new capillaries.

The simulation starts with the TAF being produced at the HYC which diffuses throughout the domain. The first activation of a TEC (red circumferences in figure 5.5) occurs when enough TAF infiltrates the initial capillary, that is, when the amount of TAF is greater than f_{act} (green lines in figure 5.5) inside the capillary. Several time steps afterwards, two other TECs get activated on both sides of the first one. Note that all TECs are separated from each other as dictated by the lateral inhibition mechanism. As shown in figure 5.5c, the three TECs initially migrate following the chemotactic direction, marked with green arrows. Figure 5.5d reveals, however, that the chemotactic direction may be altered. There, the filopodia of the rightmost TEC detect the presence of a capillary located on its left-hand side. Consequently, the chemotactic direction is overridden and, even though the green arrow points to the top-right corner, the TEC moves towards the detected capillary, anastomoses with it, and gets immediately deactivated. Meanwhile, the two other TECs, that have already promoted the deactivation of the HYC, continue their migration trough the ECM still following the chemotactic cues and the proliferating cells keep widening the capillaries. And, as shown in figure 5.5e, the growth process evolves unaltered until all TAF gets consumed.

At this point, in the absence of TAF, the endothelial cells of the tumor-induced vasculature, which are highly TAF-dependent, change their phenotype to an apoptotic one and regression starts. Figures 5.5f to 5.5h show how this process, although slower than the initial growth (note the time steps of the captions and its duration in the video), promotes the gradual disappearance of the capillaries. The vascular basement membrane that was enveloping the capillaries, however, remains after the capillaries have regressed forming the already mentioned empty sleeves, through which future TECs can migrate easily[1]. And, indeed, after the HYC gets activated again the new TECs that orchestrate the regrowth, aided by their filopodia, use these remnants of basement membrane to direct the formation of new capillaries (figures 5.5i to 5.5k). As shown in figure 5.5k, the regrowth and the growth pattern are not equal, even in this simple setup. The source of this difference is that TECs migrate faster through the empty sleeves than through the ECM, thus, their velocity is faster with respect to TAF consumption. In particular, in the regrowth process shown in that figure a new TEC gets activated soon after the anastomosis event between the rightmost TEC and the middle capillary, creating a new capillary that grows towards the top-right corner.

5.4.2 Vascular growth

As a first illustration of the capabilities of our model in an experimental-like setup, we show in figure 5.6 and video S5.2 computations in a configuration that resembles the mouse cornea micropocket angiogenesis assay (Rogers *et al.*, 2007, chapter 4). The cornea is an avascular tissue surrounded by a region called limbus formed by capillaries. Tumor cells in the cornea may promote the creation of new capillaries from the limbus. Thus, in our simulation, all the system is initially avascular (figure 5.6a), except for a circular capillary (red) that mimics the limbal vessels. We include a cluster of hypoxic tumor cells that release a generic tumor angiogenic factor (green) that triggers angiogenesis. Figure 5.6b shows a snapshot of the growing capillaries that are pervading the cornea and forming a new vessel network. As this network grows, endothelial cells consume angiogenic factor and tumor cells that are close to capillaries become normoxic and stop releasing TAF. Capillaries grow led by tip endothelial cells. TECs follow gradients of tumor angiogenic factor (triangle-labeled discrete agent of the inset), unless they sense nearby capillaries through filopodia (star-labeled agent of the same inset), until they reach the surrounding vasculature, producing anastomoses. The pattern obtained in this numerical simulation immediately after capillary growth has ceased (figure 5.6c) is similar to those observed *in vivo* (Kenyon *et al.*, 1996; Rogers *et al.*, 2007; Tong and Yuan, 2008a) and *in silico* (Harrington

[1] Given enough time without TAF, the basement membranes would eventually regress.

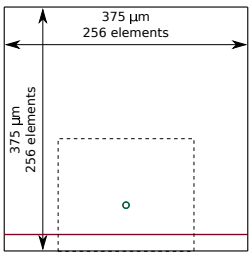

(a) *Initial conditions.*

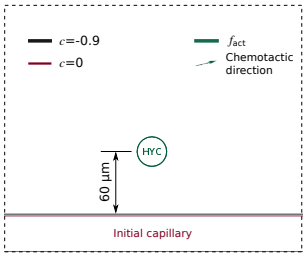

(b) *Initial conditions.*

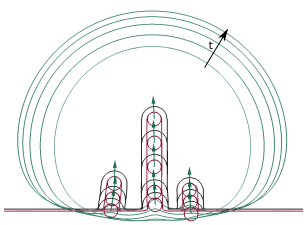

(c) *Growth (t =1.60, 2.23, 2.86, 3.49, 4.12).*

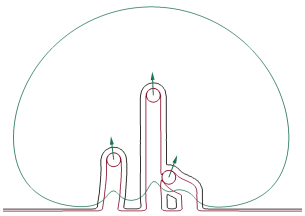

(d) *Growth (t =* 4.76*).*

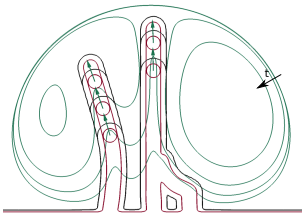

(e) *Growth (t =5.39, 6.02, 6.65, 7.28).*

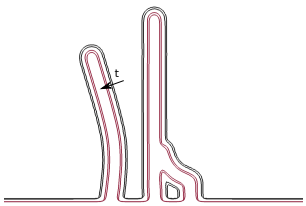

(f) *Regression (t =9.18, 12.95).*

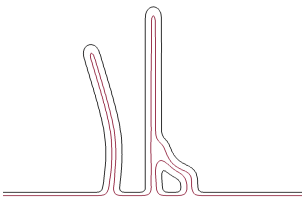

(g) *Regression (t =* 16.85*).*

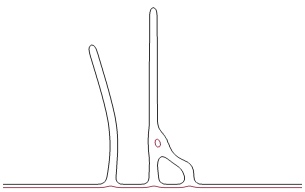

(h) *Regression (t =* 20.55*).*

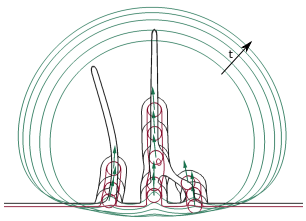

(i) *Regrowth (t = 22.45, 23.06, 23.72, 24.33, 24.95).*

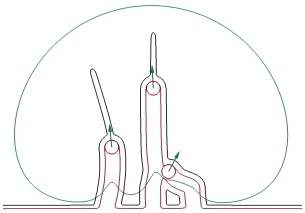

(j) *Regrowth (t =* 25.60*).*

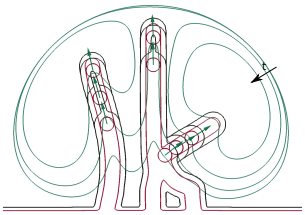

(k) *Regrowth (t = 26.23, 26.85, 27.48, 28.36).*

Figure 5.5. Intuition of the model. *Simulation of the mathematical model in a simplistic setup (a) that shows the process of growth (b-d), regression (e-f), and regrowth (g-i).*

et al., 2007; Tong and Yuan, 2001, 2008b). We performed a quantification of the neovasculature over time (figure 5.6d). The vasculature starts as a tree-like network (no loops) driven by an increasing number of TECs that create branches or bifurcations. However, as their filopodia detect nearby capillaries, the number of anastomosis events grows rapidly. Consequently, the tree-like network gradually evolves to a mesh-like one with loops that facilitate blood flow. By the end of the simulation approximately 30 anastomoses have shaped the vasculature into a highly-interconnected network with more than 20 loops. The pace at which the vasculature penetrates the cornea (measured as the distance from the limbus to the innermost TEC using the shortest path) is linear, as reported in Kenyon *et al.* (1996); Tong and Yuan (2008b). We also measured the maximum and average capillary length (distance between bifurcations) and observed that anastomoses reduce the maximum length compared to the penetration distance and, more surprisingly, maintain the average length almost constant.

5.4.3 Regression and regrowth

The result in figure 5.6 illustrates the capabilities of the model to predict vascular growth patterns, but a major goal of this work was to develop a model that naturally leads to regression and regrowth. We study this phenomenon motivated by the *in vivo* experiment shown in figure 5.1. To replicate the experiment, we need first to simulate the growth process. To this end, we chose as our computational domain the area enclosed by the dotted lines in figure 5.1. In the simulation, the system is initially avascular, except for a capillary placed on the boundary which serves as a precursor to the neo-vasculature (figure 5.7a). Randomly distributed hypoxic cells (that resemble the Rip-Tag2 tumor in the experiment) release angiogenic factor that activates tip endothelial cells. Initially, capillaries grow inwards, forming new vasculature. Then, the vasculature regresses due to the absence of TAF (figure 5.7c) and the system enters a transient behavior with local regressions and regrowths (see video S5.3 in the supporting information) similar to those observed in experiments. Figures 5.7d to 5.7h show snapshots of different patterns that highlight the dynamism and adaptation of the vasculature when regression and regrowth are considered. Note that in figure 5.7h the initial capillary has completely regressed. We assume that this configuration (figure 5.7h) is analogous to the starting point of the experiment (figure 5.1a).

The experimental procedure of Mancuso et al. is continued by chemically inhibiting the VEGF receptors of endothelial cells, so that capillaries are unable to detect the presence of TAF and eventually regress (figure 5.1b). The receptors are kept blocked for 7 days and the capillaries regrow afterwards (figures 5.1c and 5.1d). Our simulation proceeds along the same lines. We model the receptor inhibition

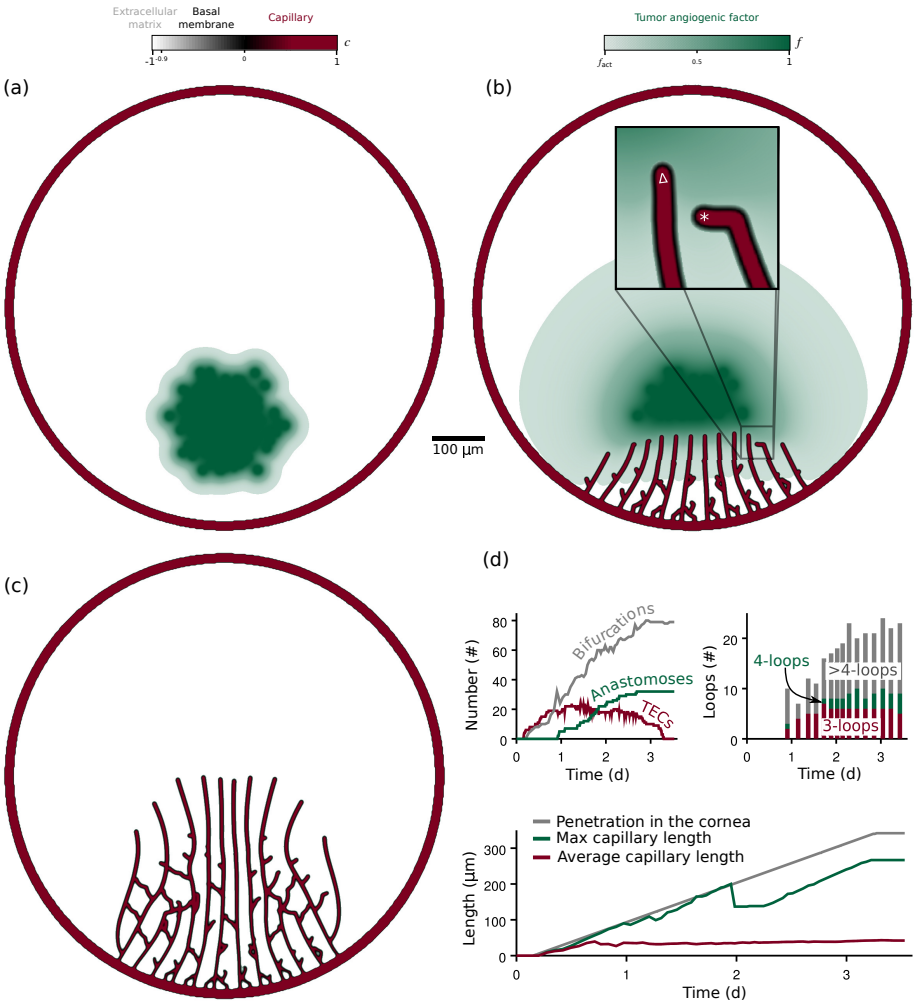

Figure 5.6. Corneal neovascularization. *(a) Circular initial capillary (red) and cluster of tumor cells that release tumor angiogenic factor (green). (b) Tip endothelial cells (TECs) lead the growth of the new capillaries. (c) Vascular pattern after growth. (d) Neovasculature quantification.*

by blocking the activation of new tip endothelial cells. Those that were active will eventually get deactivated in the absence of tumor angiogenic factor. During the inhibition, most capillaries regress, as shown in figures 5.7i to 5.7l. Note that regressed capillaries leave behind a trail (grayish colors representing low values of c in figure 5.7) which we identify with the basement membrane. If the treatment were prolonged, all the capillaries and basement membranes will eventually disappear. However, as in the experiment, we remove the inhibition after approximately 7 days (figure 5.7m) and the regrowth process starts (figures 5.7n to 5.7t). The high availability of TAF due to the treatment promotes an almost instant activation of TEC after its removal. New tip endothelial cells get rapidly activated. They migrate attracted by TAF, but also extend filopodia that detects the old basement membrane and guides capillaries to grow aided by the scaffold left behind after regression. Eventually, the vascular density returns to a state similar to that before the inhibition.

Visual inspection shows that the *in vivo* experiment and the numerical simulation compare well. In both cases the network is composed of tortuous, highly interconnected vessels that oxygenate the tissue unevenly. Also, as the new vasculature is particularly dependent on tumor angiogenic factor, the inhibition acts successfully, leaving in both cases few, barely functional capillaries in the region. The dependency on tumor angiogenic factor also implies that the vasculature recovers rapidly after the treatment, a finding that may be useful in the design of antiangiogenic therapies. Figure 5.8 shows a quantitative comparison between the simulation and the experiment. Vascular density suffers a drastic drop due to the inhibition. Then, the regrowth process starts and the vascular density eventually recovers its original value. After the regrowth, our model predicts mild oscillations of the vascular density due to spontaneous local regressions and regrowths. To some extent, this can also be inferred in the experiment, but there is insufficient data to be conclusive. Although precise agreement with *in vivo* experiments is a daunting task, the simulation clearly captures the trend of the experiment.

5.5 Conclusions

In conclusion, our model reinforces the view that tumors need to be analyzed as a complex system which interacts dynamically with its microenvironment. In this context, our study highlights the importance of regression and regrowth of tumor vasculature. The proposed model may be a useful tool not only to predict capillary growth patterns, but also for the design of antiangiogenic therapies, which are currently considered the fourth pillar of cancer treatment after surgery, chemotherapy, and radiation.

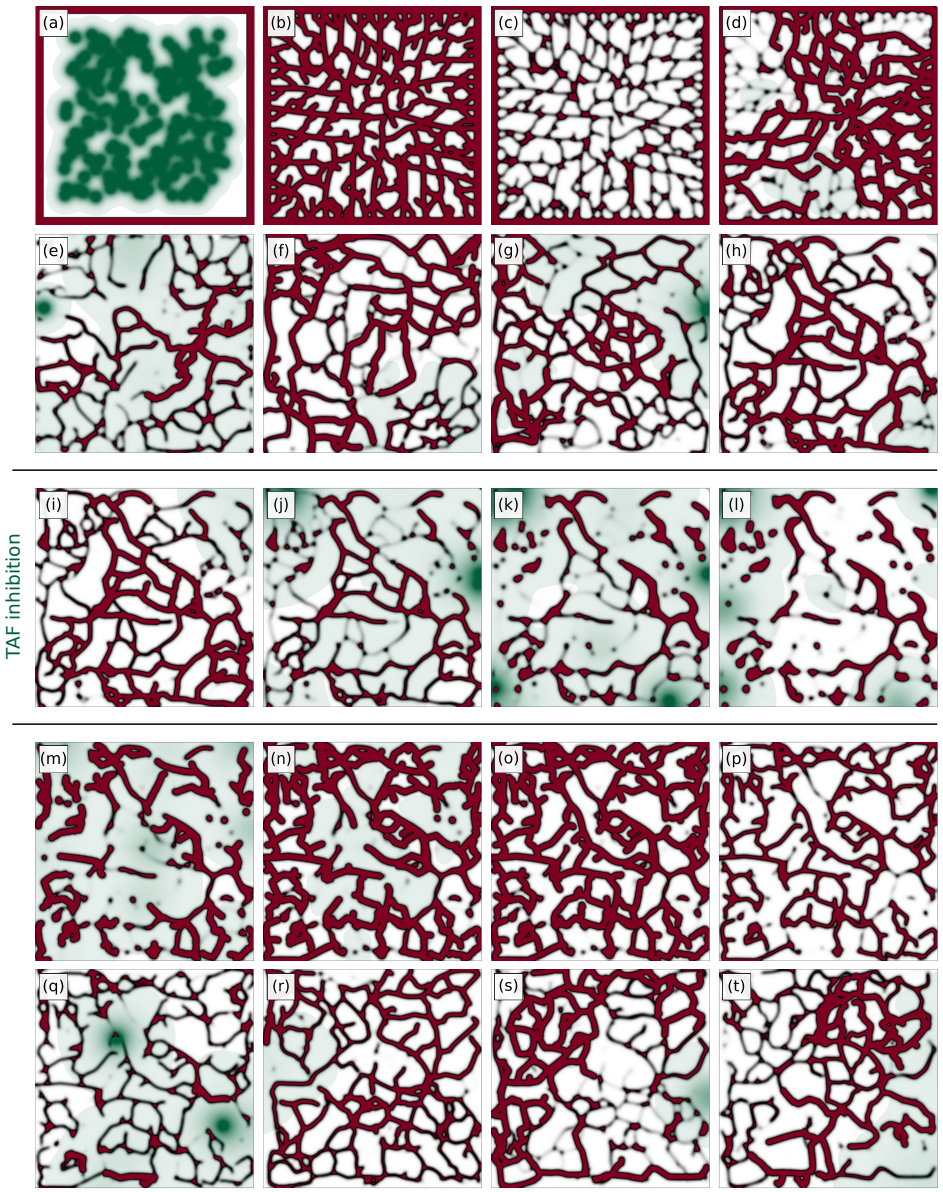

Figure 5.7. Tumor angiogenesis simulation: growth, regression, and regrowth. *This simulation replicates the experiment of figure 5.1 and both are compared in figure 5.8. The color scales are equal to those in figure 5.6.*

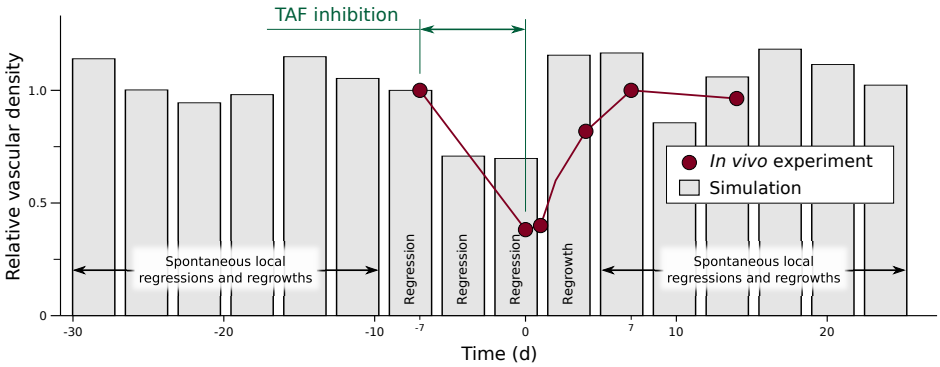

Figure 5.8. *Evolution of the relative vascular density (current vascular density over a reference vascular density). Both the experiment (red, Fig. 5.1) and the simulation (gray, Fig. 5.7) show regression promoted by TAF inhibition, followed by regrowth after the inhibition is over.*

5.6 Supporting information

Supporting information includes the following videos that can be found online at `http://caminos.udc.es/gmni/gente/gvilanovac/thesis/`:

Video S5.1. Simulation of the mathematical model in a simplistic setup, as shown in figure 5.5.

Video S5.2. Two-dimensional replication of the mouse corneal micropocket angiogenesis assay. This video is related to figure 5.6.

Video S5.3. Time evolution of a TAF-dependent vascular network featuring capillary growth, regression, and regrowth. This simulation, shown in figure 5.7, replicates the experiment of figure 5.1.

Chapter 6

Convection-driven vascular patterns

In this chapter, we investigate the role of convection in tumor-induced angiogenesis. The blood that circulates in the capillaries leaks through the vascular wall and reaches the cells, generating in the process an extravascular fluid flow. This flow not only transports oxygen and nutrients towards the cells, but also the wastes and signaling factors released by cells. In particular, in tumor angiogenesis, the extravascular fluid flow convects tumor angiogenic factors (altering the otherwise purely diffusive distribution), which, ultimately affects the creation of new vasculature. Here, we develop a continuum theory for intravascular, transvascular, and extravascular fluid flow based on a non-homogeneous Darcy's law. We couple the velocity of the fluid with the tumor-induced angiogenesis model through a convective term in the tumor angiogenic factor equation. We also develop efficient numerical methods which permit us to study the influence of fluid flow on vascular patterning under different hypothesis and configurations and to investigate the effect of high intratumoral pressure in angiogenesis.

6.1 Blood flow in the micro-circulatory system

Cells obtain the building blocks that sustain their activities from blood, which is transported by arteries, distributed within the micro-circulatory system (arteri-

oles, capillaries, and venules), and returned through veins. The heart pumps the blood through the circulatory system exerting a non-constant pressure gradient, which generates an intravascular flow. This gradient, however, is progressively damped as it travels from large-caliber arteries to the thinner micro-circulatory vessels, where it is usually assumed to be constant. Once in the micro-circulatory system, the blood exchanges material with the surrounding cells through the vascular wall. Most of this material (oxygen, nutrients, wastes from the cellular activity, or signaling factors) is dissolved in the fluid (water) and, consequently, extravassates with it through the thin openings between the endothelial cells[1]. The transvascular fluid flow is driven by the different pressures inside and outside the capillaries (figure 6.1). In particular, the intravascular hydrostatic pressure in the arterial side of the micro-circulatory system is approximately 32 mmHg higher than the extravascular hydrostatic pressure in the interstitium. In the venous side, due to the wider caliber of the vessels and the frictional effects the difference in the hydrostatic pressures drops to approximately 15 mmHg. If this were the only mechanism that orchestrated the transvascular transport, the water and those substances dissolved in it would exclusively extravassate the capillaries. There is, however, another mechanism involved, which is driven by the colloidal osmotic pressure. The blood transports large proteins which, due to their size, are not able go through the vascular wall, being their concentration higher in the intravascular than in the extravascular region. This creates an osmotic pressure difference between the blood and the interstitial fluid of about -22 mmHg which conveys the fluid into the vasculature. Summing up both mechanisms, the fluid is driven out of the capillaries in the arterial side by a net pressure of 10 mmHg and into the capillaries in the venous side by a net pressure of -7 mmHg. In the extravascular region, the substances reach the cells not only by diffusion, but the interstitial fluid flow convects them from the vessels to the cells. Likewise, the waste products from the cell cycle and other soluble substances (as signaling factors) reach the capillaries which collect them using both diffusion and convection mechanisms. Arguably, fluid flow has an influence in vascular patterning through convection, as soluble substances like tumor angiogenic factors or systemically-delivered antiangiogenic drugs are affected by convection.

As detailed in the review of the literature of this thesis (subsection 1.2.2) several authors have developed mathematical models for tumor angiogenesis that include fluid flow. All the works cited there that explicitly considered the vasculature base their modeling for fluid flow on a similar approach, which is to divide flow into different models: one for intravascular flow and one for extravascular flow, both coupled with a model for transvascular flow. The intravascular flow is modeled by

[1] The greater and more frequent openings in tumor-induced capillaries facilitates the extravassation of these substances and often creates high intratumoral pressures.

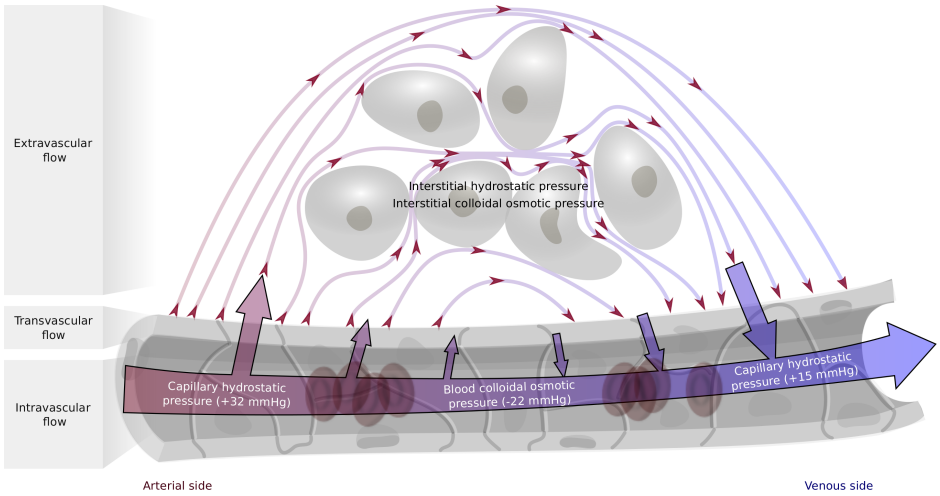

Figure 6.1. Transvascular fluid flow. *In the micro-circulatory system, fluid flows through thin gaps in the capillary walls driven by the differences in hydrostatic and osmotic pressures.*

a one-dimensional discrete method using Pries *et al.* (1990) or further augmented versions like Pries *et al.* (2001, 1998). For the extravascular flow, on the contrary, they use Darcy's law which is a continuous theory. Finally, the transvascular flow is modeled by Starling's law (Starling, 1896) and couples the two previous ones. Independently of the methods, the main goals of the referred works related to this topic are to measure interstitial fluid flow and pressure inside the tumor and to study drug delivery considering fluid convection, while tumor angiogenic factor convection was not considered.

In this chapter we present a hybrid mathematical model for tumor angiogenesis to study the influence of fluid flow in neovascular patterning through tumor angiogenic factor convection. The novelty of this theory is that we model intra-, trans-, and extra-vascular fluid flow at once using a continuous pressure variable, rather than using three different models. Our theory is deeply grounded in the smooth interfaces generated by the phase-field approach and on Darcy's law with highly non-linear hydraulic conductivity.

6.2 The mathematical model

Our model can be divided into a model for fluid flow and a model for angiogenesis. Under the assumptions explained below, the former is a continuous model for

fluid flow through porous media that uses Darcy's law for its formulation. The main variables of this model are the fluid velocity $\mathbf{u}$ and the pressure p. The latter model, as in previous chapters, is a hybrid theory with two continuous partial differential equations (a convection-diffusion equation for the tumor angiogenic factor f and a phase-field equation for the endothelial cell density c) and a set of discrete agents TECs for the tip endothelial cells. Both the fluid flow and the angiogenesis model are fully coupled: the fluid convects tumor angiogenic factor, which modifies the endothelial cell density field (both through endothelial cell proliferation and through the creation of TECs), which, in turn, affects the flow of the fluid through the variation of the hydraulic conductivity. In the rest of the section we detail the models separately.

6.2.1 The fluid flow model

The tumor stroma is formed by several types of cells, such as cancerous and host cells, and leaky tumor-induced capillaries, all embedded in the extracellular matrix. From a macroscopic point of view, the stroma may be understood as a continuous porous medium with a non-constant porous size through which blood and interstitial fluid flow. Thus, considering that blood plasma and the interstitial fluid have the same properties, we can model the fluid within the stroma using Darcy's law. Furthermore, under the assumptions of an incompressible, stationary, creeping flow, the mass balance and the Navier-Stokes equations for the fluid flow reduce, respectively, to

$$\nabla \cdot \mathbf{u} = 0, \tag{6.1}$$

$$\mathbf{u} = -\mathcal{K}\nabla p, \tag{6.2}$$

where $\mathcal{K}$ is the conductivity function. As the porous size of the medium is different throughout the tumor stroma, this function varies accordingly. Arguably, the major differences in the porous size are those between the intravascular, the transvascular, and the extravascular regions (see the remarks at the end of the section). Making use of the smooth interfaces between the intravascular and extravascular regions resulting from the phase field c, we define the following non-linear hydraulic conductivity function

$$\mathcal{K}\left(c, \|\nabla c\|\right) = \kappa^e \vartheta\left(c\right) \mathcal{T}\left(\|\nabla c\|\right), \tag{6.3}$$

where κ^e is the extravascular conductivity. Figure 6.2 illustrates the non-linearity of $\mathcal{K}$ based on the one-dimensional solution of the phase-field equation in an infinite domain. In equation (6.3), ϑ is a function of the phase field while $\mathcal{T}$ depends on the gradient of the phase field. The former accounts for the different

conductivities between the intra- and the extravascular region and is given by

$$\vartheta(c) = 1 + \frac{\bar{\kappa}^i - 1}{2}(\tanh(3c) + 1), \tag{6.4}$$

where $\bar{\kappa}^i = \kappa^i/\kappa^e$ is the normalized intravascular conductivity and κ^i is the intravascular conductivity. The second factor of equation (6.3), $\mathcal{T}$, can be understood as a weighting function that modifies ϑ in the transvascular region and is defined as

$$\mathcal{T}(\|\nabla c\|) = \frac{1+\bar{\kappa}^t}{2} - \frac{1-\bar{\kappa}^t}{2}\tanh\left(10\lambda\left(\|\nabla c\| - \frac{1}{2\sqrt{2}\lambda}\right)\right), \tag{6.5}$$

where $\bar{\kappa}^t = \kappa^t/\kappa^e$ is the normalized transvascular conductivity and κ^t is the transvascular conductivity. $\mathcal{T}$ depends on the gradient of the phase-field in such a way that only affects $\mathcal{K}$ in the transvascular region, that is, when the gradient is high. The term $1/(2\sqrt{2}\lambda)$ and the factor 10λ control the width and slope of this region.

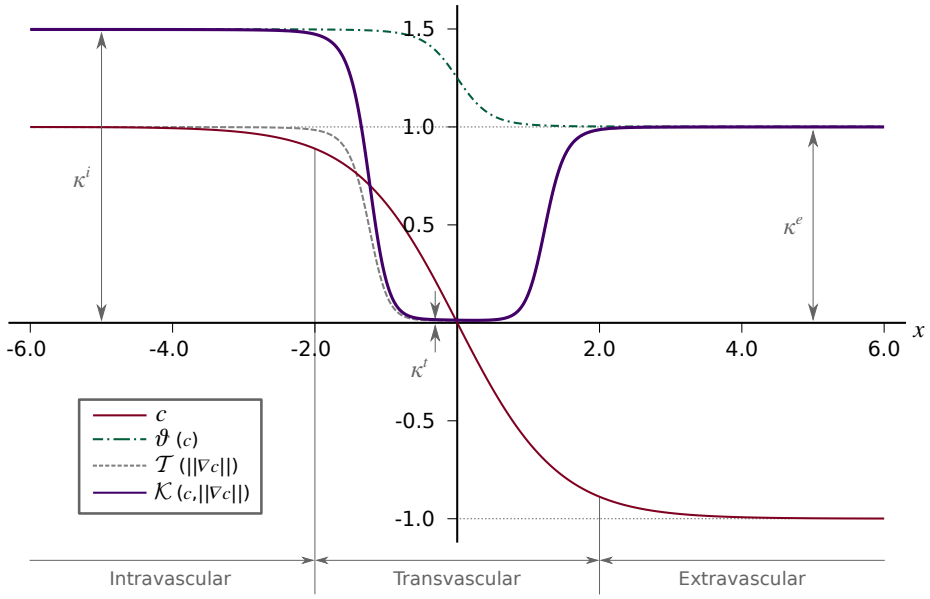

Figure 6.2. Hydraulic conductivity. *This figure plots the hydraulic conductivity $\mathcal{K}$ (and their factors ϑ and $\mathcal{T}$) as a function $c = tanh(-x/(\sqrt{2}\lambda))$, that is, the 1D solution to the phase-field equation in an infinite domain. The phase-field creates smooth interfaces that permit the differentiation of intravascular, transvascular, and extravascular regions. Accordingly, the hydraulic conductivity displays three plateaus, one per region, connected by smooth transitions. In this plot $\kappa^e = 1$, $\bar{\kappa}^i = 1.5$, $\bar{\kappa}^t = 0.01$, and $\lambda = 1$.*

As a result of the product of the smoothed, step-like functions ϑ and $\mathcal{T}$, the hydraulic conductivity $\mathcal{K}$ is a three-plateau function connected by smooth transitions. Each plateau has a value that correlates with the conductivity of a region of interest in such a way that the fluid flows easier inside the capillaries than outside them and extravassates with difficulty.

Remarks:

1. Tumor cells are densely packed compared to host cells, and consequently the hydraulic conductivity is lower in the intratumoral region. This fact is not explicitly considered in equation (6.3) as the tumor cell density is not considered in this model. We know, however, the location of the tumor through the hypoxic region and we use it in the examples to (weakly) impose higher pressure inside the tumor.
2. Several tumor angiogenic factors are known to increase the patency of capillaries (see appendix C). This mechanism may be built into the model by transforming the parameter κ^t into a function that depends on the concentration of that particular tumor angiogenic factor.
3. Several other choices are possible for the hydraulic conductivity $\mathcal{K}$, such as Heaviside functions; we opted, however, for a smooth continuous function, which benefits the numerical resolution of the equations. Note also that our definition of $\mathcal{K}$ preserves its properties through changes on the thickness of the phase-field interface.

6.2.2 The angiogenesis model

In this chapter we use a model for tumor angiogenesis similar to those used in other sections. For this reason, we describe it briefly, giving all its details, but focusing only on the new tumor angiogenic factor convection term.

The continuous variables (f and c) The tumor angiogenic factor f and the concentration of endothelial cells (or capillaries) c, that configure the continuous part of the model, are governed, respectively, by equations

$$\frac{\partial f}{\partial t} = \nabla \cdot (D \nabla f) - \nabla \cdot (\mathbf{u} f) + \mathcal{P}(d)\,(f_{\text{HYC}} - f) - \mathcal{U}(c)\, f, \tag{6.6}$$

$$\frac{\partial c}{\partial t} = \nabla \cdot \left(M \nabla \left(\mu(c) - \lambda^2 \Delta c \right) \right) + \mathcal{B}_p(f)\, c \mathcal{H}(c), \tag{6.7}$$

where D is the diffusion constant, f_{HYC} is the maximum TAF produced in a hypoxic region, M is the mobility, λ is a positive constant proportional to the width of the interface, and $\mathcal{H}$ is the Heaviside function. The remaining functions $\mathcal{P}$, $\mathcal{U}$, μ, and $\mathcal{B}_p$ are, respectively, the TAF production, the TAF uptake by capillaries, the chemical potential, and the endothelial cell proliferation, which are defined as

$$\mathcal{P}(d) = \begin{cases} P & \text{if } d < R_{\text{HYC}} \\ 0 & \text{if } d \geq R_{\text{HYC}} \end{cases}, \quad \mathcal{U}(c) = \begin{cases} B_u c & \text{if } c \geq 0 \\ -B_d c & \text{if } c < 0 \end{cases}, \tag{6.8}$$

$$\mu(c) = -c + c^3, \quad \mathcal{B}_p(f) = \begin{cases} B_p f & \text{if } f < f_p \\ B_p f_p & \text{if } f \geq f_p \end{cases}. \tag{6.9}$$

Here, P is the production rate, d is the distance to the closest hypoxic region, R_{HYC} is an average cell radius, B_u is the endothelial cell uptake rate, B_d is the TAF natural decay rate and the uptake rate by other cells, B_p is the proliferative rate constant, and f_p is the tumor angiogenic factor condition for highest proliferation. In addition, we take $P = 0$ if the concentration of endothelial cells is high in the vicinity of a hypoxic region, that is, if $c > 0.9$ within a radius δ_{nox} (nutrients and oxygen diffusion length) from the edge of the hypoxic cell.

Equation (6.6) is a convection-diffusion equation for the tumor angiogenic factor with two reaction terms, a source and a sink. As in previous models presented in this thesis, f is produced in hypoxic region (third term on the right-hand side), diffuses throughout the extracellular matrix (first term on the right-hand side), and is consumed by endothelial cells (last term). Now, additionally, the tumor angiogenic factor is convected by the fluid, as modeled by the second term on the right-hand side. Equation (6.7) is a phase-field equation whose first term drives c either to $c = 1$ or to $c = -1$, generating smooth but thin transitions between them, which we interpret here as the intravascular, extravascular, and transvascular regions, respectively (see figure 6.2). Moreover, equation (6.7) includes a source term that accounts for endothelial cell proliferation.

The discrete agents (TECs) and their coupling Tip endothelial cells are modeled as circular discrete agents with radius R_{TEC}, that can get activated at any point in the domain if the following conditions are meet: 1) $c > c_{\text{act}}$, 2) $f > f_{\text{act}}$, and 3) the distance to every other TEC is greater than δ_4. An active TEC initially moves with a constant velocity $\mathbf{v}_{\text{TEC}} = \chi \frac{\nabla f}{|\nabla f|}$, where χ is the chemotactic constant. Once the TEC is outside the parent capillary, it develops filopodia, which we model as a set of check points distributed in an annulus sector, centered in the direction of the TAF gradient, with angle $2\pi/3$, and with internal and external radius $2R_{\text{TEC}}$ and $4R_{\text{TEC}}$, respectively (see figure 5.3). A positive check in one of these points

($c > -0.9$) implies that filopodia have detected a nearby endothelial cell and the TEC alters its velocity direction towards it. Finally, TECs get deactivated if they fail to meet any of the above-mentioned conditions for activation or if they encounter another TEC or capillary in their migration path (anastomosis).

The discrete agents are fully coupled with the continuous variables. On the one hand, their activation, movement, and deactivation depend on point-wise evaluations of these continuous variables and their gradients. On the other hand, the value of the phase-field c is overwritten at the region occupied by each TEC (a circle with radius R_{TEC}). In particular, c takes the value one within this region and TECs form automatically part of the intravascular region defined in this theory.

6.2.3 Parameters

Table 6.1 details the dimensionless values of the parameter of the model[2]. There, following the order of the above explanation, we categorize the parameters according to the different sub-models.

The fluid flow problem is completely defined by three parameters, namely, κ^e, κ^i, and κ^t. As shown in the table, the extravascular hydraulic conductivity is $5.008 \times 10^{-10}\,\text{cm}^2/\text{s/mmHg}$, which is within the range of data from the literature (Cattaneo and Zunino, 2014; Welter and Rieger, 2013). Note that in the definition of the conductivity, we normalized the transvascular and intravascular hydraulic conductivity with respect to the extravascular conductivity. We followed this strategy motivated by the absence of available data for them, so that we can estimate their values now. On the one hand, in the intravascular region the fluid flows more easily than through the interstitium suggesting that $\kappa^i \gg \kappa^e$. However, inside the capillaries the fluid is blood which due to its composition suffers resistance when it flows through the micro-circulatory system (Pries *et al.*, 1994). Thus, we estimate a ten-fold ratio between the intravascular and the extravascular conductivity. On the other hand, fluid flow through the vascular wall is more difficult than in the interstitium pointing to $\kappa^t \ll \kappa^e$. In our case, as we are dealing with tumor-induced capillaries characterized by their high permeability, we estimate that the transvascular conductivity is one order of magnitude lower than the extravascular.

The remaining parameters shown in table 6.1 belong to the continuous and discrete angiogenesis model, whose values were already established in previous chapters.

[2]Recall that the length and time scales to retrieve the physical values of these parameters are $L_0 = 1.25\,\mu\text{m}$ and $T_0 = 1560\,\text{s}$, respectively.

Table 6.1. *Values of the parameters grouped by the different sub-models given in dimensionless units.*

Sub-model	**Parameter**	**Symbol**	**Value**
Fluid flow (p and $\mathbf{u}$)	Extravascular hydraulic conductivity	κ^e	50.0
	Normalized intravascular hydraulic conductivity	$\bar{\kappa}^i$	10.0
	Normalized transvascular hydraulic conductivity	$\bar{\kappa}^t$	0.1
Angiogenesis (c and f)	Diffusion	D	100.0
	Maximum TAF production	f_{HYC}	1.0
	Mobility	M	0.025
	Interface width	λ	1.0
	Production	P	100.0
	Endothelial cell uptake	B_u	6.25
	Natural decay	B_d	0.1
	Proliferative rate	B_p	1.401
	TAF condition for highest proliferation	f_p	0.3
Angiogenesis (TECs)	Chemotatic constant	χ	7.28
	Nutrient and oxygen diffusion length	δ_{nox}	20.0
	Conditions for TEC activation	c_{act}	0.9
		f_{act}	0.001
		δ_4	64.0
	TEC radius	R_{TEC}	4.0

6.3 Numerical method

Our mathematical model is composed by a continuous and a discrete part. Furthermore, the former involves both steady state and transient partial differential equations. This results in several difficulties for the numerical method. In this section we present how we deal with them and how we couple the different parts of the model.

6.3.1 The continuous equations

Equations (6.1), (6.2), (6.6), and (6.7) form the continuous formulation of our problem. Let $\Omega \subset \mathbb{R}^d$ be an open set, where $d = 2$ or 3, and let $\partial\Omega = \Gamma = \Gamma_s \cup \Gamma_g$ be the Lipschitz boundary of this domain, where $\overline{\Gamma_s \cap \Gamma_g} = \varnothing$. Let also $\mathbf{n}$ be the well-defined unit outward normal of Ω. Introducing equation (6.2) into equations (6.1) and (6.6) yields the following strong form of this problem: find p, f, c such that

$$0 = \nabla \cdot (-\mathcal{K}\nabla p) \tag{6.10}$$

$$\frac{\partial f}{\partial t} = \nabla \cdot (D\nabla f) - \nabla \cdot (-\mathcal{K}\nabla p f) + \mathcal{P}(x)(f_{\text{HYC}} - f) - B_u f c \mathcal{H}(c) \tag{6.11}$$

$$\frac{\partial c}{\partial t} = \nabla \cdot \left(M\nabla\left(\mu(c) - \lambda^2 \Delta c\right)\right) + \mathcal{B}_p(f)\, c\mathcal{H}(c) \tag{6.12}$$

in $\Omega \times (0, T)$ and satisfying the following boundary conditions

$$\mathcal{K}\nabla p \cdot \mathbf{n} = 0 \quad \text{on} \quad \Gamma_s \times (0,T) \tag{6.13}$$

$$p = p_g(\mathbf{x}) \quad \text{on} \quad \Gamma_g \times (0,T) \tag{6.14}$$

$$\nabla f \cdot \mathbf{n} = 0 \quad \text{on} \quad \Gamma \times (0,T) \tag{6.15}$$

$$M\nabla\left(\mu(c) - \lambda^2\Delta c\right) \cdot \mathbf{n} = 0 \quad \text{on} \quad \Gamma \times (0,T) \tag{6.16}$$

$$M\lambda^2 \Delta c = 0 \quad \text{on} \quad \Gamma \times (0,T), \tag{6.17}$$

where p_g is a given function. In order to solve the above problem we first derive an equivalent varational formulation and then an approximate the problem with a space and time discretization.

Variational formulation Let $\mathcal{V}$ denote the trial and weighting function spaces, which are assumed to be equal. After multiplying by test functions and integrating by parts, we obtain the following weak form: find $p, f, c \in \mathcal{V}$ such that $\forall r, w, q \in \mathcal{V}$:

$$0 = \left(\nabla r, \mathcal{K}(c, \|\nabla c\|)\nabla p\right)_\Omega \tag{6.18}$$

$$
\begin{aligned}
0 =& \left(w, \frac{\partial f}{\partial t} \right)_\Omega + \left(\nabla w, D \nabla f \right)_\Omega + \left(\nabla w, \mathcal{K}\left(c, \|\nabla c\|\right) \nabla p f \right)_\Omega \\
& - \left(w, \mathcal{P}\left(x\right) \left(f_{\text{HYC}} - f \right) \right)_\Omega + \left(w, B_u f c \mathcal{H}\left(c\right) \right)_\Omega \qquad (6.19) \\
0 =& \left(q, \frac{\partial c}{\partial t} \right)_\Omega + \left(\nabla q, M \nabla \mu\left(c\right) \right)_\Omega \\
& + \left(\Delta q, M \lambda^2 \Delta c \right)_\Omega - \left(q, \mathcal{B}_p\left(f\right) c \mathcal{H}\left(c\right) \right)_\Omega , \qquad (6.20)
\end{aligned}
$$

where $(\cdot, \cdot)_\Omega$ denotes the $\mathcal{L}^2$ inner product in Ω. The weak form is equivalent to the strong formulation of the problem under the assumption that functions living in the space $\mathcal{V}$ are sufficiently smooth. In particular, because of the second order derivatives present in the weak form, $\mathcal{V}$ is a subset of $\mathcal{H}^2$, the Sobolev space of square integrable functions with square integrable first and second derivatives.

Spatial discretization We obtain the spatial discretization of the weak form making use of the Galerkin method. The above system of equations can thus be approximated by the following variational problem: find $p^h, f^h, c^h \in \mathcal{V}^h \subset \mathcal{V}$ such that $\forall r^h, w^h, q^h \in \mathcal{V}^h \subset \mathcal{V}$:

$$
\begin{aligned}
0 =& \left(\nabla r^h, \mathcal{K}\left(c^h, \|\nabla c^h\|\right) \nabla p^h \right)_\Omega \qquad (6.21) \\
0 =& \left(w^h, \frac{\partial f^h}{\partial t} \right)_\Omega + \left(\nabla w^h, D \nabla f^h \right)_\Omega + \left(\nabla w^h, \mathcal{K}\left(c^h, \|\nabla c^h\|\right) \nabla p^h f^h \right)_\Omega \\
& - \left(w^h, \mathcal{P}\left(x\right) \left(f_{\text{HYC}} - f^h \right) \right)_\Omega + \left(w^h, B_u f^h c^h \mathcal{H}\left(c^h\right) \right)_\Omega \qquad (6.22) \\
0 =& \left(q^h, \frac{\partial c^h}{\partial t} \right)_\Omega + \left(\nabla q^h, M \nabla \mu\left(c^h\right) \right)_\Omega \\
& + \left(\Delta q^h, M \lambda^2 \Delta c^h \right)_\Omega - \left(q^h, \mathcal{B}_p\left(f^h\right) c^h \mathcal{H}\left(c^h\right) \right)_\Omega . \qquad (6.23)
\end{aligned}
$$

Here, everything is defined except for the particular finite element space $\mathcal{V}^h = \text{span}\{N_A\}$, $A = 1, \ldots, n_b$, being N_A the basis functions and n_b the number of basis functions. Note that because we are using a conforming discretization this subspace needs to fulfill the same smoothness properties as $\mathcal{V}$. The discrete space needs also to capture the smooth but steep phase-field interfaces as in previous chapters. What is more, as suggested by figure 6.2, the pressure will have even steeper transitions at the transvascular region than the phase-field, which also need to be reproduced. Thus, in this model the pressure field is the major restriction

for the numerical method. For these reasons we make use again of isogeometric analysis, specially due to its high smoothness, variation diminishing property, and proven accuracy. In particular we choose second-order B-splines as our basis functions N_A and we define p^h, f^h, and c^h as

$$p^h(\mathbf{x},t) = \sum_{A=1}^{n_b} p_A(t)\, N_A(\mathbf{x}), \tag{6.24}$$

$$f^h(\mathbf{x},t) = \sum_{A=1}^{n_b} f_A(t)\, N_A(\mathbf{x}), \tag{6.25}$$

$$c^h(\mathbf{x},t) = \sum_{A=1}^{n_b} c_A(t)\, N_A(\mathbf{x}), \tag{6.26}$$

where p_A, f_A, and c_A are the control points.

Temporal discretization We use the notation $p^h_n, \dot{f}^h_n, f^h_n, \dot{c}^h_n, c^h_n$ for the space and time discrete solutions of the variables of the problem and their corresponding time derivatives. Here we perform a finite-difference-type temporal discretization of the spatially discretized problem. This problem derives, however, from a steady state equation for the fluid flow and two transient equations for the continuous angiogenesis model. We detail them separately and show afterwards how we incorporate them in our numerical scheme.

The problem for the fluid flow is defined as: given $f^h_{n+\beta_f}, c^h_{n+\beta_f}$, and the temporal discretization $\Delta t_n = t_{n+1} - t_n$, find p^h_{n+1} such that:

$$0 = \left(\nabla r^h, \mathcal{K}\left(c^h_{n+\beta_f}, \|\nabla c^h_{n+\beta_f}\|\right)\nabla p^h_{n+1}\right)_\Omega, \tag{6.27}$$

where β_f can be either one or zero and, as shown below, defines two different staggering numerical schemes.

As in previous chapters, we integrate the continuous angiogenesis model in time using the generalized-α method. The discrete angiogenesis problem can thus be stated as: given $p^h_{n+\beta_f}, \dot{f}^h_n, f^h_n, \dot{c}^h_n, c^h_n$, and the temporal discretization $\Delta t_n = t_{n+1} - t_n$, find $\dot{f}^h_{n+1}, f^h_{n+1}, \dot{c}^h_{n+1}, c^h_{n+1}$ such that:

$$\begin{aligned} 0 =& \left(w^h, \dot{f}^h_{n+\alpha_m}\right)_\Omega + \left(\nabla w^h, D\nabla f^h_{n+\alpha_f}\right)_\Omega \\ &+ \left(\nabla w^h, \mathcal{K}\left(c^h_{n+\alpha_f}, \|\nabla c^h_{n+\alpha_f}\|\right)\nabla p^h_{n+\beta_f} f^h_{n+\alpha_f}\right)_\Omega \end{aligned}$$

$$
\begin{aligned}
&-\left(w^h, \mathcal{P}\left(x\right)\left(f_{\text{HYC}} - f^h_{n+\alpha_f}\right)\right)_\Omega \\
&+\left(w^h, B_u f^h_{n+\alpha_f} c^h_{n+\alpha_f} \mathcal{H}\left(c^h_{n+\alpha_f}\right)\right)_\Omega, \qquad (6.28)\\
0 =&\left(q^h, \dot{c}^h_{n+\alpha_m}\right)_\Omega + \left(\nabla q^h, M\nabla\mu\left(c^h_{n+\alpha_f}\right)\right)_\Omega \\
&+\left(\Delta q^h, M\lambda^2\Delta c^h_{n+\alpha_f}\right)_\Omega - \left(q^h, \mathcal{B}_p\left(f^h_{n+\alpha_f}\right) c^h_{n+\alpha_f} \mathcal{H}\left(c^h_{n+\alpha_f}\right)\right)_\Omega, \qquad (6.29)
\end{aligned}
$$

where

$$\dot{f}^h_{n+\alpha_m} = \dot{f}^h_n + \alpha_m\left(\dot{f}^h_{n+1} - \dot{f}^h_n\right), \qquad (6.30)$$

$$f^h_{n+\alpha_f} = f^h_n + \alpha_f\left(f^h_{n+1} - f^h_n\right), \qquad (6.31)$$

$$f^h_{n+1} = f^h_n + \Delta t_n \dot{f}^h_n + \gamma\Delta t_n\left(\dot{f}^h_{n+1} - \dot{f}^h_n\right), \qquad (6.32)$$

$$\dot{c}^h_{n+\alpha_m} = \dot{c}^h_n + \alpha_m\left(\dot{c}^h_{n+1} - \dot{c}^h_n\right), \qquad (6.33)$$

$$c^h_{n+\alpha_f} = c^h_n + \alpha_f\left(c^h_{n+1} - c^h_n\right), \qquad (6.34)$$

$$c^h_{n+1} = c^h_n + \Delta t_n \dot{c}^h_n + \gamma\Delta t_n\left(\dot{c}^h_{n+1} - \dot{c}^h_n\right), \qquad (6.35)$$

$$\gamma = \frac{1}{2} + \alpha_m - \alpha_f, \qquad (6.36)$$

$$\alpha_m = \frac{1}{2}\left(\frac{3-\rho_\infty}{1+\rho_\infty}\right), \qquad (6.37)$$

$$\alpha_f = \frac{1}{1+\rho_\infty}, \qquad (6.38)$$

and ρ_∞ is the spectral radius of the amplification of the matrix as $\Delta t \to \infty$.

Equation (6.11) is a convection-diffusion equation and, as such, the numerical method may introduce instabilities in the form of spurious oscillations under certain conditions. These conditions are well represented by the element Peclet number, Pe, defined as

$$\text{Pe} = \frac{\|\mathbf{u}\|h}{2D}, \qquad (6.39)$$

where h is the element side. This dimensionless number is a measure of convective over the diffusion effects. When $\text{Pe} > 1$ the problem is said to be convection-dominated and may produce boundary layers that the numerical method may be unable to capture. Otherwise the problem is said to be diffusion-dominated.

A high element Peclet number indicates that an instability may arise during a simulation. However, other factors such as reaction terms or boundary conditions also

influence whether the instability appears or not, even for a convection-dominated problem. Consequently, we have to study our specific problem through simulations and, in the eventuality of spurious oscillations in the solution, address the issue. There are several alternatives to correctly solve boundary layers. The first and more direct is to reduce the element size enough to be able to capture smaller scales. This method is effective, but implies a higher computational cost. Another alternative is to implement one of the existent stabilization techniques, such as, streamline upwind/Petrov–Galerkin (SUPG, Brooks and Hughes, 1982) or variational multiscale (VMS, Hughes *et al.*, 1998). Both of them involve the incorporation of an extra term in equation (6.28). We advance here that we tested our model under several h-refined meshes and with and without SUPG and found no need to implement stabilization techniques in our problem.

6.3.2 The discrete component and the discrete–continuum coupling

The algorithms of the discrete components for the activation, movement, deactivation, and filopodia probing, as well as the coupling with the continuous variables are already explained in previous chapters of this thesis (see for example subsection 2.3.1 and section 5.3). For the sake of brevity, we avoid its repetition here. We want to highlight, however, the role of the seamless coupling between TECs and the continuous variables in this theory. The definition of the hydraulic conductivity relies heavily on the smoothness of the vascular wall, which is *a priori* guaranteed by the phase-field equation. However, in the coupling process, TECs modify the phase field by overwriting c with a constant value. If not properly handled, this could create sharp interfaces in the phase field in the transvascular region surrounding TECs. This would result in high gradients, which, in turn, would produce a non-smooth hydraulic conductivity. Our implementation of the coupling with template functions circumvents this potential problem, as they are based on the multidimensional generalization of an exact one-dimensional solution to the Cahn-Hilliard equation. The templates guarantee the required smoothness in the TECs transvascular region and, thus, a smooth hydraulic conductivity function.

6.3.3 Numerical scheme

In previous chapters we developed a numerical scheme (see figure 6.3a) which we restructure now to incorporate the equations for fluid flow (figures 6.3b and 6.3c). The first thing to note is that we removed from our formulation the discrete agents

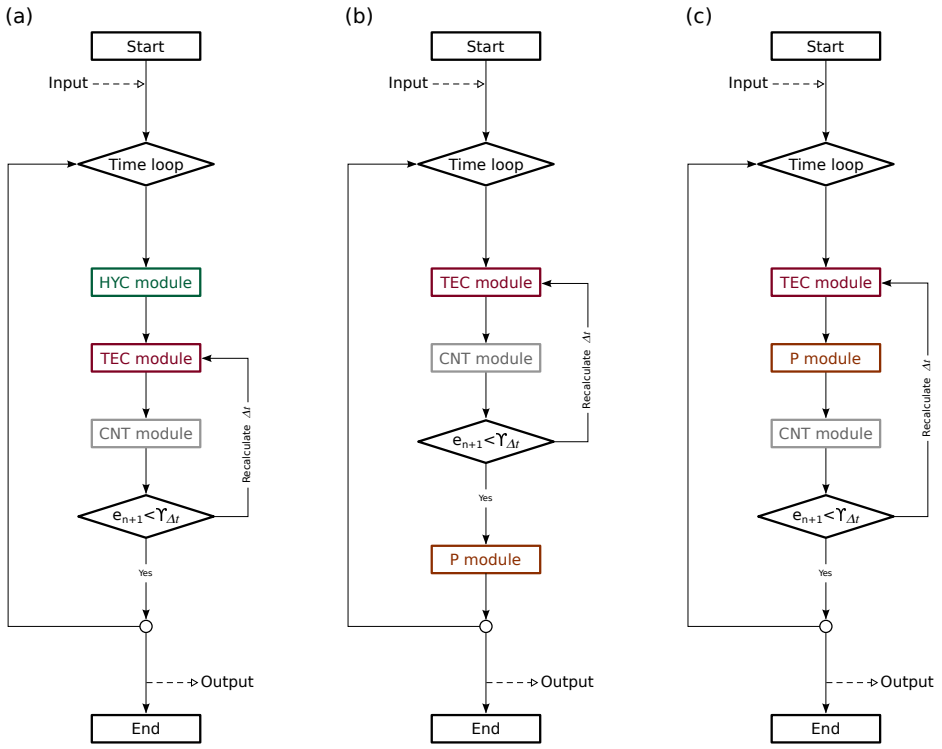

Figure 6.3. Staggering numerical schemes. *We modified the numerical scheme used in other section (a) to incorporate the fluid flow sub-model (P module in the figure). The proposed staggering numerical schemes (b) and (c) differ in the location of the P module.*

for HYCs, as they are now incorporated as a source term in equation (6.11). TEC and CNT modules for the discrete TEC agents and continuous angiogenesis sub-model continue unaltered in the numerical scheme. The only exception is their position within the scheme.

We have chosen to implement a staggering numerical scheme, rather than a monolithic one, to reduce the computational cost. We present in figures 6.3b and 6.3c two possibilities for these schemes, which we call scheme (b) and scheme (c), respectively. Each scheme is related with one value of β_f, so that $\beta_f = 1$ yields the former, and $\beta_f = 0$ the latter. In scheme (b), for each time step we solve first the same problem as in the scheme of figure 6.3a and then, with the updated values of the TAF and the phase-field f^h_{n+1}, c^h_{n+1}, we solve equation (6.27) (P module). In scheme (c), on the contrary, equation (6.27) is solved before CNT module, but

after TEC module, using the previous variable updates f_n^h, c_n^h.

We analyzed both schemes and draw the following conclusions. Scheme (b) is faster than scheme (c), as P module is outside of the time-step correction algorithm. It is however more inaccurate for this reason. In addition, scheme (b) presents problems because the pressure field used to update the convection term, p_n^h, is the solution from a previous time step, while the phase field c_n^h may have changed due to the discrete–continuum coupling. Finally, we decided to use scheme (c) in our computations.

6.4 Results

In this section we present several simulations of the mathematical model. First, we analyze the influence of tumor angiogenic factor convection in vascular patterning by means of a comparison with a model that lacks this phenomenon. Then, we study whether convection enhances tumor-induced angiogenesis in certain configurations, such as, different parent capillaries or hypoxic tumor sizes. Finally, we address the role of intratumoral pressure in tumor vascularization and malignancy.

6.4.1 Vascular patterning with TAF convection

In this first example we study angiogenesis with and without tumor angiogenic factor convection. As shown in figure 6.4 and video S6.1, we simulate our model in a squared domain which represents a 375 µm × 375 µm piece of tissue. We place two 6.25 µm-thick capillaries along the left and right sides of the square and a hypoxic region at its center, mimicking a 62.5 µm-radius, fully-hypoxic tumor. Furthermore, we arbitrarily define the left-hand side capillary to be the arterial side of the vascular bed and the right-hand side capillary to be the venous side. We impose accordingly, and as other models in the literature (Baxter and Jain, 1989; Cai *et al.*, 2011; Welter and Rieger, 2013), $p = 10\,\text{mmHg}$ and $p = 0\,\text{mmHg}$, respectively, for the pressure boundary conditions inside the capillaries. The remaining boundary conditions are free-flux conditions. We choose this configuration, because it is simple enough to study the model and the numerical method without added complexities, but also reproduces a common setting: A small growing tumor placed far enough from the capillaries to be hypoxic that triggers angiogenesis.

The first thing to asses in this model with respect to the numerical method is whether we need to implement a stabilization technique or not. As said above this decision is mainly based on the element Peclet number, defined here as $\text{Pe} = \frac{\mathcal{K}\|\nabla p\|h}{2D}$. Because of the highly nonlinear definition of the hydraulic conductivity, its

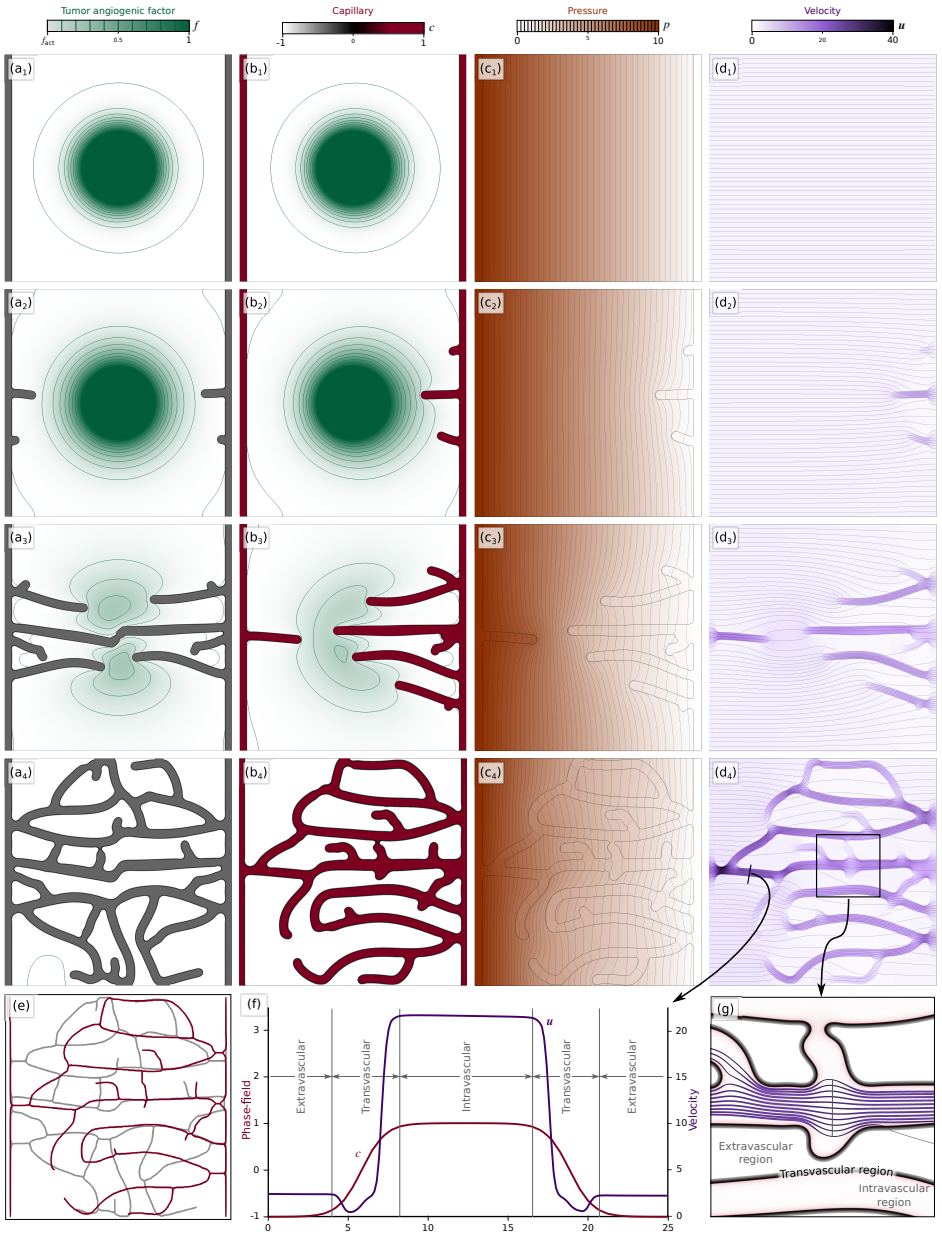

Figure 6.4. Non-convective versus convective vascular patterns. *Vascular patterns without TAF convection (a) and with TAF convection (b-d) create different vascular networks (e). The numerical method captures the fluid velocity (f,g).*

value is difficult to estimate. In the intravascular region, we can assume that there will be not enough TAF to form boundary layers because of the tumor angiogenic consumption by endothelial cells. In the extravascular region we can approximate $\mathcal{K}$ by κ^e and further assume a constant pressure drop, which using a 512×512 mesh, yields an estimated $\mathrm{Pe} = 1.42 \times 10^{-2}$, suggesting no spurious oscillations in that region. We conclude then that the potential location of instabilities is within the transvascular region, which we studied through computations. We simulated the model with and without the SUPG stabilization technique (results not shown) for the above mentioned initial and boundary conditions with a 512×512 mesh and found that there is no need to use SUPG[3].

Figure 6.4 shows two numerical simulations: One in which we removed tumor angiogenic factor convection (figure 6.4a) and one with the full model (figures 6.4b to 6.4d). There, one can observe snapshots of the evolution of the four variables of the model at $t = 2.43, 10.22, 18.16, 39.67$. Initially, there is a constant pressure drop from the higher pressures on the left-hand side capillary to the lower one in the right-hand side capillary (figure 6.4c$_1$). The fluid flows accordingly from left to right following straight trajectories as shown by the streamlines (black lines) in figure 6.4d$_1$. As it flows, the fluid convects tumor angiogenic factor to the right (figure 6.4b$_1$) altering its otherwise symmetric distribution when only diffusive mechanisms are in action (figure 6.4a$_1$). The difference in TAF distributions increases with time, and, by $t = 10.22$, it already promotes dissimilar TEC activation: While convection promotes the early activation of three TECs from the right-hand side parent capillary, the pure diffusive TAF distributions activates two TECs from each capillary. This incipient vascular network has already altered the pressure and velocity fields (figures 6.4c$_2$ and 6.4d$_2$) highlighting how deeply the variables of the model are coupled. At $t = 18.16$ the capillaries are inside the tumor and the TAF production has stopped. Figure 6.4a$_3$ shows at the center of the domain the first of many anastomosis events that will occur in these simulations. In particular, this anastomosis event is the result of a TEC-TEC detection by the filopodia of both cells which adjust their migration towards each other. In the simulation of the full model, the connection between parent capillaries occurs later because convection delays the activation of TECs from the right-hand side capillary.

The last snapshots of figures 6.4a to 6.4d, taken at $t = 39.67$, show the final results of these simulations. At this point, the vascular networks are fully developed and they completely pervade the tumor and its surroundings. Their shape is, however, completely different. We show in figure 6.4e and in figure S6.2 in the supporting information the superimposed skeletons of these networks which are

[3]We also checked the appearance of spurious oscillations in all simulations performed in this chapter and found none.

obtained using the same method as in chapter 3. Through the figure, one can easily appreciate that both networks differ in almost every feature. The only neovessels that match in both simulations are those created by the first activated TECs from the right-hand side, when the TAF distributions were more similar. After that moment, convection altered the distributions leading to non-matching patterns. The network generated only by TAF diffusion is more symmetric than its counterpart generated also by convection: While the former is connected with both parent capillaries by four vessels each, the latter has four connections to the left-hand side capillary, but only one to the right-hand side capillary. As shown in figure 6.4d$_4$, the asymmetry leads to high velocities (dark colors) in the only vessel that grew from the arterial side of the capillary bed. The majority of the fluid that flows through the new vascular network goes through this vessel, whose reduced caliber increases the velocity.

In figure 6.4f we show the velocity magnitude and phase-field profiles in a cut marked with a black line in figure 6.4d$_4$. The cut is perpendicular to the main capillary that connects the parent vessels and includes part of the extravascular region. The high continuity of the profiles shows that the numerical methods are able to capture not only the phase-field interface as in previous chapter, but also the steep interfaces of the velocity field. In the intra- and extravascular regions, the velocity curve forms plateaus, being the former almost seven-fold higher than the latter. The plateaus are connected with the lower velocity value in transvascular region through smooth transitions. The hydraulic conductivity in the transvascular region hinders the extravassation of the fluid. We show an example of this phenomenon in figure 6.4g, were we draw fluid streamlines that cross the black line at the center of the figure. The streamlines color and radius are plotted according to the velocity of the fluid: The darker and greater the radius, the higher velocity, and vice versa. Note that all stream lines but one remain within the intravascular region. The only one that transverses the vascular wall is thin, picturing a small velocity. Furthermore, note that, even under the assumptions explained above, the model captures how the velocity is reduced and how the streamlines separate from each at the center of the figure as they go through a capillary intersection.

6.4.2 Study on capillary types and tumor sizes

In the previous example we analyzed the influence of tumor angiogenic factor convection under the most basic configuration. Now we address how different configurations may alter the effect of convection in vascular patterning and whether it can favor the malignancy of a tumor.

Our first approach is to change the behavior of the parent capillaries, that is, their artery/venous conditions, by modifying the boundary conditions for the pressure field in the initial capillaries. We present in figure 6.5 four numerical simulations. Each one has different initial and boundary conditions, as shown in figure 6.5a. We use again the same mesh (512×512 knot spans), as it has proved to capture the steep variable transitions without showing spurious oscillations. For simulation (I) we choose the same configuration of the previous example, to allow an easy comparison. For the other three we choose the following configurations:

(II) Two symmetric parent vessels that connect the arterial side (top) with the venous side (bottom). The pressure varies linearly top to bottom from $p = 10$ to $p = 0\,\text{mmHg}$.

(III) Two antisymmetric parent vessels that connect the arterial side with the venous side. The arterial side is located at the top for the left-hand side capillary and at the bottom for the right-hand side counterpart. The pressure varies linearly from $p = 10$ to $p = 0\,\text{mmHg}$ top to bottom for the right capillary, and vice versa.

(IV) Two parent vessels, one representing the arterial side of the capillary bed and one representing the venous side (left and right, respectively) with pressure drops along their longitudinal direction. The pressure also varies linearly, but from $p = 10$ to $p = 6.6\,\text{mmHg}$ in the left-hand side capillary and from $p = 0$ to $p = 3.3\,\text{mmHg}$ in the right-hand side one (top to bottom).

Among these configurations, (IV) may be considered as the more general and realistic one. We show in figure 6.5b an intermediate time step ($t =\approx 15$) of the simulations. There we represent the capillaries, streamlines in black lines, and TAF equidistant contour lines. In addition, to measure the influence of convection we plot vector glyphs whose length, color, and direction show the convective term $\mathbf{u}f$. Figure 6.5c presents the final (skeletonized) vascular patterns after the simulation has finished.

In simulation (I) the fluid flows from the left parent capillary to the right one. The streamlines are the straighter and shorter among the four simulations. During a long time span of the simulation, the fluid is forced to travel through the extravascular region to reach the venous side. As a result, TAF is convected rightwards for a prolonged time and promotes the most asymmetric final vascular pattern. As shown by the glyphs, the convection term reaches the highest values in (I). In simulation (II), on the contrary, the fluid goes from the top corners of the domain to the bottom ones. However, most part of it flows through the parent capillaries. The vascular network initiates towards the bottom half of the domain. In simulation (III), the right-hand side parent vessel is flipped with respect to simulation (II). Consequently, the location of the first TECs that get activated in

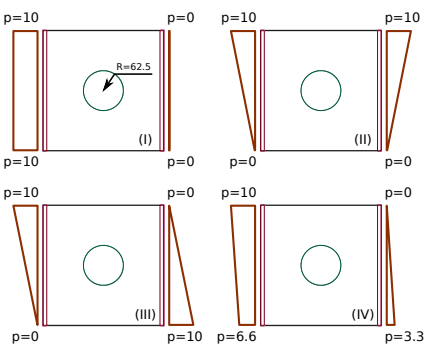

(a) *Initial conditions.*

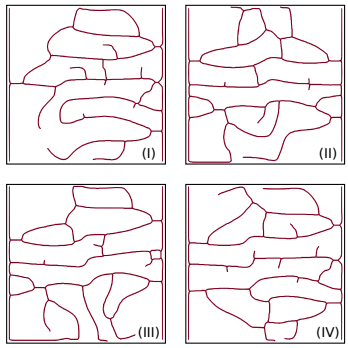

(c) *Final networks.*

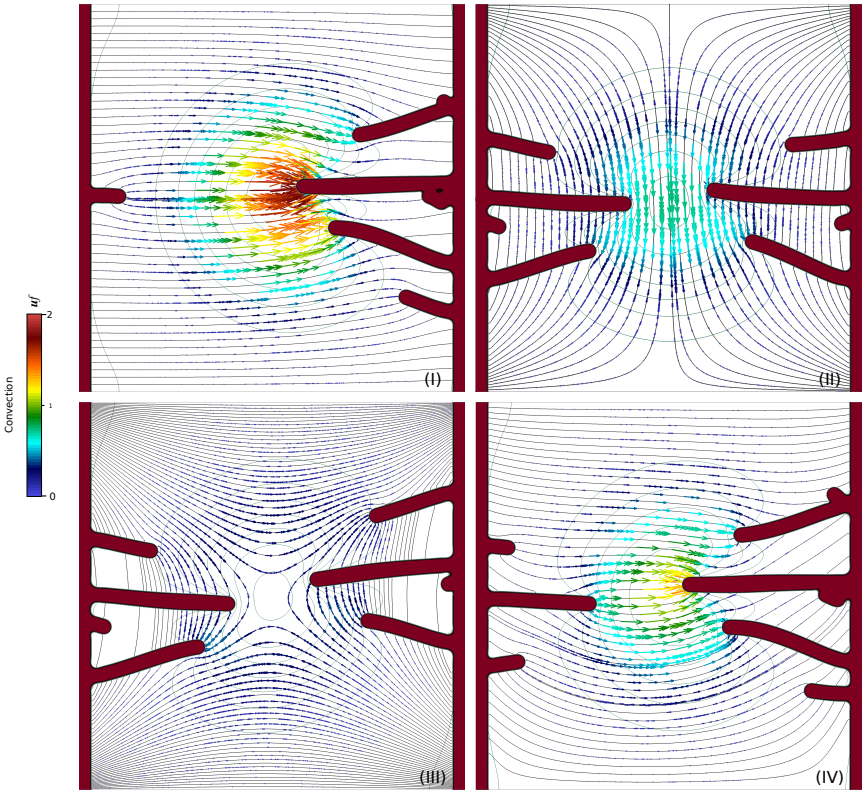

(b) *Snapshots of the simulations at an intermediate time step.*

Figure 6.5. Study of convection under common pressure setups. *Different pressure setups promote a wide pattern variability. Distance is given in µm and pressure in mmHg.*

the left-hand side matches. Those that get activated from the right-hand side, on the contrary, differ and tend to be at the upper half of the domain. This simulation presents the lowest value of the convective term. Finally, the boundary conditions of simulation (IV) may be viewed as a refined version of those in simulation (III), and, as such, the network is initiated in almost matching locations from both parent capillaries. Simulation (IV), however, presents a quite different velocity profile, as shown by the streamlines and the values of the convection term.

In summary, different configurations of the parent capillaries alter the vascular patterns, although in every one the tumor and its surroundings get pervaded by capillaries. The main difference is that the location of connections of the networks to the vascular patterns tends to be at the venous side of the capillary bed.

The second approach to study the effect of TAF convection is to alter the size of the tumor that is producing TAF. The proposed configurations may be thought of as increasingly small tumors that have the potential to induce angiogenesis, in which we study whether TAF convection enhances their ability to actually trigger angiogenesis. We show this study in figure 6.6, where we set the tumor radius in each simulation to $R = 50.00$, 31.25, and 18.75 µm, from left to right. The top and middle row of this figure correspond to intermediate time steps of simulations without TAF convection and with the full model, respectively, and the bottom row to the final vascular patterns. For these simulations we have used the same setup and mesh as simulation (I) in the previous example.

The patterns generated under these configurations differ from one another. For all the simulations with TAF convection, the vascular network only develops from the right-hand side capillary, while in the absence of convection, when angiogenesis occurs, new vessels grow from both parent capillaries. The model also predicts a slower development of the vascular networks for the TAF convection model. A comparison between the simulations with different tumor sizes reveals that the smaller the tumor, the sparser the vascular network. This is a consequence of the lower TAF concentration in the domain. Finally, the main conclusion from these simulations is that TAF convection plays a relevant role in enhancing the malignancy of small tumors. As shown in the simulations at the right-most column of the figure, small tumors, may not be able to trigger angiogenesis in the absence of convection. On the contrary, the model with convection predicts that the same tumor gets fully vascularized and becomes malignant.

6.4.3 Intratumoral pressure

In the above examples we have assumed the fluid pressure inside the tumor to be equal to that in the host tissue. This is, however, not necessarily true. Cancerous

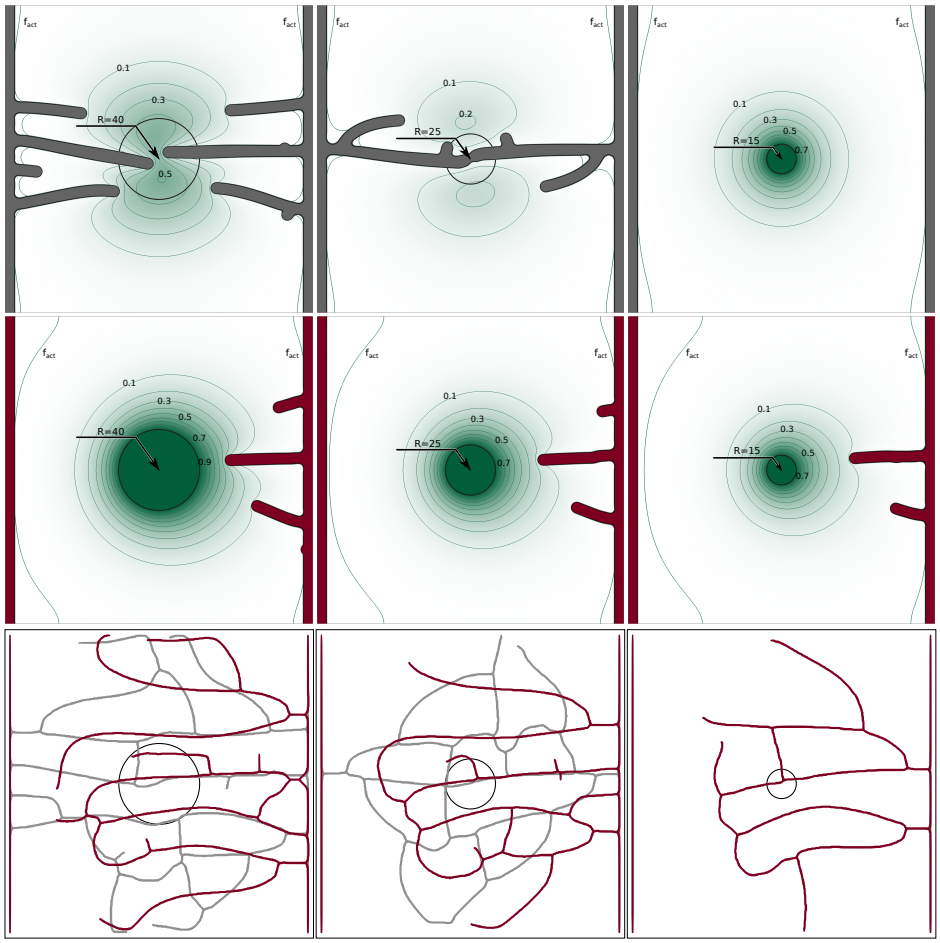

Figure 6.6. Convection-increased angiogenesis. *TAF reaches both or one of the initial capillaries at different times when the pellet radius is varied (40, 25, and 15 – left to right in dimensionless units). In the absence of convection the smaller tumor is not able to trigger angiogenesis.*

cells replicate rapidly and group forming densely packed tumors. The higher the density inside the tumor, the lower the interstitial space and, consequently, the pressure of the fluid flowing among cancerous cells increases. Furthermore, this high fluid pressure is not alleviated due to the absence of functional vessels, either lymph or blood vessels. In this example we study if a fluid intratumoral pressure higher than that of its micro-environment affects angiogenesis through

TAF convection and if the model predicts an increased tumor malignancy.

The proposed mathematical model does not explicitly consider a variable that represents cancerous cells; instead, the tumor is implicitly defined by one circular hypoxic region as big as the tumor. We make use of this definition to incorporate the intratumoral pressure in model. In particular, we impose $p = p_t$ in the hypoxic region by means of the penalty method. Figure 6.7 and video S6.3 show the result of a simulation in which $p_t = 7.4\,\text{mmHg}$. This simulation has the same setup as simulation (I) in the previous section: two initial capillaries at the left and right edges of a $375\,\mu\text{m} \times 375\,\mu\text{m}$ square tissue and one $62.6\,\mu\text{m}$-radius hypoxic region at its center. The left capillary is considered to be on the arterial side of the micro-circulatory system and consequently we impose there a Dirichlet boundary condition for the pressure $p = 10\,\text{mmHg}$. The homologous initial capillary represents the venous side and its associated boundary condition for the pressure is $p = 0\,\text{mmHg}$.

Figure 6.7 presents three snapshots of the simulation, each at a different time step and each highlighting different events and variables. Figure 6.7a displays the simulation just after the first TEC reaches the tumor, at $t = 13.09$. There, we plot contour lines of pressure (orange) and TAF (green), a black circle rendering the contour of the tumor, glyphs representing the convection term $\mathbf{u}f$, and the distribution of TAF and capillaries. The pressure contour lines are mostly parallel to the initial capillaries as in other simulations (see, e.g., figure 6.4c$_1$), showing the pressure drop between them. The imposed intratumoral pressure, however, disrupts the parallelism in the central region and reveals the presence of the tumor, even in the absence of the black circle. In particular, the contour line $p = 7$ bends towards the right surrounding the tumor and exposing its location. The tumor produces all the TAF in the domain that reaches the capillaries through diffusion and convection. Convection is, however, virtually nonexistent inside the tumor as shown by the absence of glyphs inside the tumor in the figure. After being produced, TAF escapes the tumor only by diffusion. Once in the extracellular matrix, convection starts to play a role in TAF distribution. This is specially noticeable at the right-hand side of the tumor, as shown by the color arrows representing the convection term. There, the higher difference between the intratumoral pressure and the extravascular pressure generates a high pressure gradient. In turn, convection is increased and drives TAF away from the tumor creating a region with low values of TAF. As a result and contrary to other simulations, the figure shows how the longest capillary turns upwards avoiding the tumor rather than going through it. This trend continues as the simulation evolves. By time $t = 20.07$ (figure 6.7b) two capillaries have almost fully encircled the tumor, one at the top and one at the bottom. Only when TAF has been consumed in the vicinity of the tumor, new capillaries penetrate this region. Figure 6.7b also displays the extravascular

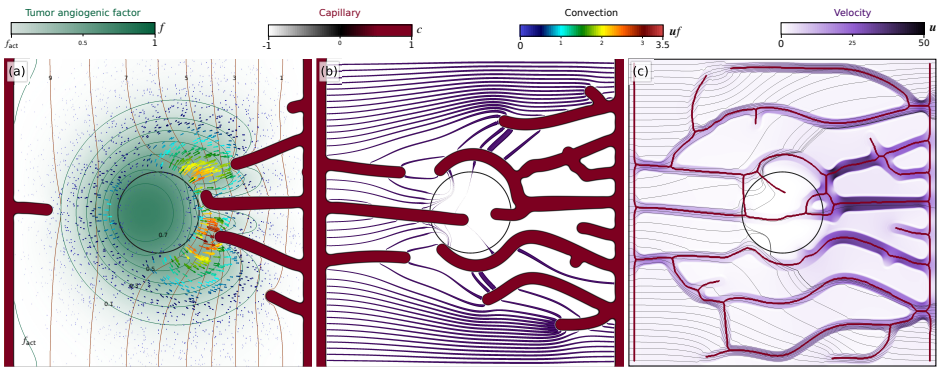

Figure 6.7. Influence of intratumoral pressure. *Intratumoral pressure alters the distribution of TAF which, in turn, drives capillaries around the tumor. The fluid velocity inside the tumor is low, even within the capillaries that transverse the tumor.*

fluid velocity by means of streamlines. Each streamline starts at the left-hand side capillary and its radius varies according to the magnitude of the fluid velocity. Interestingly, few streamlines transverse the tumor and those that do it present the smallest radius, that is the minimum velocities. In particular, $\|u\| < 1$ along these lines inside the tumor. The higher fluid velocity in the extravascular region occurs between the capillaries that encircle the tumor and those adjacent to them. The vascular network continues evolving until, by time $t = 32.07$, all the TAF in the domain has been consumed. We present a snapshot of this last step in figure 6.7c, where we show the final vascular network represented by its skeleton (red lines), streamlines of the velocity field (black lines), and the continuous velocity field (shades of purple). As in previous simulations with a similar setup, the final vascular network is asymmetric, being denser towards the venous side due to the effect of convection. The difference here is that the intratumoral pressure has forced capillaries to envelop the tumor. The velocity field highlights, first, that the fluid flows more rapidly within the capillaries and, second, that the velocity inside the tumor is very low. In fact, the only capillary that transverses the tumor presents velocities close to zero. The intratumoral pressure has rendered this capillary not functional. Finally, as in figure 6.7b, the streamlines barely penetrate the tumor.

The simulation predicts that even though the tumor is vascularized, nutrients, oxygen, or systemically administered drugs cannot easily reach the tumor, resulting in an increased tumor malignancy. The fluid flow both within the capillaries and in the extravascular region does not favor their penetration into the tumor.

6.5 Conclusions

In this chapter we investigated the role of TAF convection in angiogenesis which has been overlooked in mathematical models. We proposed a model for fluid flow based on Darcy's law which we coupled with a model for angiogenesis. The model required the development of an appropriate staggering time integration scheme to undertake the coupling. In addition, we studied the need to implement a stabilization technique to address the possible appearance of numerical instabilities due to the presence of a convection-diffusion equation.

We have shown through several simulations that TAF convection has a deep effect on the formation of vascular networks in tumor-induced angiogenesis. Fluid flow convects TAF from the arterial side of the micro-circulatory system to the venous side. As a result, TECs activate sooner in the latter side and generate an asymmetric final capillary network, which is denser towards the venous side. The fewer capillaries branching from the arterial parent vessel promote higher intravascular velocities at this side. The model predicts that TAF convection also plays a role in enhancing the malignancy of small tumors. Finally, by artificially including an intratumoral fluid pressure, the model predicts delayed capillary penetration and low fluid velocity within the tumor, hindering the delivery of treatments.

This model may be enhanced by the inclusion of convection-diffusion equations for nutrients, oxygen, or systemically-delivered drugs. A proposed line of further research is to change the definition of the hydraulic conductivity to capture the intratumoral pressure.

6.6 Supporting information

Supporting information includes the following videos and images that can be found online at `http://caminos.udc.es/gmni/gente/gvilanovac/thesis/`:

Video S6.1. Time evolution of vascular patterns without TAF convection and with TAF convection, as shown in figure 6.4.

Figure S6.2. Comparison of the final vascular networks of the simulations of figure 6.4.

Video S6.3. Development of a new vasculature influenced by intratumoral pressure. Related to figure 6.7.

Chapter 7

Summary, conclusions, and further work

This chapter presents a summary, the general conclusions, and a selection of lines for further research that continue the work developed in this thesis.

7.1 Summary

In chapter 1 the main objective of this thesis was divided into three goals, namely, modeling, simulation, and computational. Here we summarize the presented work from the point of view of these goals.

Modeling

The dynamics of tumor angiogenesis and its impact on cancer growth remain as fundamental open problems in cancer biology. Predictive medicine, and in particular mathematical oncology, are growing fields whose aim is to predict and give insight into these problems. To this end, in this thesis we have proposed three new mathematical models for tumor angiogenesis based on the phase-field method. The first one was developed in chapters 2 to 4. There, starting with a previous model that featured chemotaxis, we added a conceptual model for haptotaxis, which is one of the main mechanisms that governs tip endothelial

cell migration. The second one, presented in chapter 5, focuses on the long-term dynamics of tumor-induced angiogenesis, that is, on the regression and regrowth events occurring after the first growth of capillaries. The formulation of the model also incorporates filopodia as the tip endothelial cell apparatus to inspect their environment and basement membranes as the shortcut scaffold for vessel regrowth. Finally, in chapter 6, we developed a fully continuum theory for fluid flow at the tissue scale, which we coupled with our model for tumor angiogenesis. As a result, the model features how fluid flow alters tumor-induced vascular patterns.

Simulation

Throughout this thesis we have simulated the models under different settings that try to replicate relevant *in vitro* or *in vivo* experiments. In particular, the first model (chapters 2 to 4) was first studied under two-dimensional simplistic configurations to gain insight into the governing equations with the final objective of replicating an experiment in three-dimensions and using a real geometry. To this end, we evolved the settings first in two dimensions and then in three dimensions to represent larger domains, different and more realistic capillary configurations, and a variety of tumor arrangements. These simulations culminated in the development of a tumor-induced angiogenesis simulation of one of the most widely used *in vivo* assays, the mouse corneal micropocket angiogenesis assay, using a three-dimensional, subject-specific geometry with more than 28.9 million degrees of freedom. To the best knowledge of the author, this simulation allows for the first time the comparison between a computation and an experiment in a three-dimensional real geometry. Then, in chapter 5, the model for growth, regression, and regrowth was simulated both in a two-dimensional replication of the mouse corneal micropocket assay and in reproduction of an *in vivo* experimental setup. Finally, the simulations of the model for tumor angiogenic factor convection presented in chapter 6 were only done under theoretical setups.

Computational

The previous modeling and simulation goals could not have been achieved without the appropriate development of algorithms. Every model is hybrid and involves coupling cellular-scale discrete agents with averaged continuous theories. In addition, the models are grounded on the phase-field method which, in opposition to the classical description of sharp interfaces, describes the interface between phases as diffuse. This permits avoiding the resolution of moving boundary problems, but requires solving a higher-order partial differential equation with diffuse interfaces evolving dynamically over the computational domain. The simulations

in three-dimensional subject-specific geometries include a further hindrance, as they require three-dimensional, non-linear mappings and high precision to capture cellular-scale dynamics in tissue-scale domains.

Most numerical methods used in this thesis were introduced in chapters 2 and 3. There, our first step was to describe the original model in a coherent mathematical framework, so that we could afterwards define a seamless coupling between the discrete elements and the continuous variables to permit an efficient numerical treatment of the coupled problem. In addition, we devised a method to find the parametric coordinates of the known physical coordinates of the discrete agents in three-dimensional, non-linear mappings, which also works in parallel computations. For the resolution of the high-order partial differential equations involved in the formulation we used isogeometric analysis, which not only provides accuracy and robustness but also the geometric flexibility that we required to perform simulations in real geometries. We also used the generalized-α method and an adaptive time-stepping scheme that increased our solving efficiency. Finally, all these methods were adapted to run in parallel using a multi-patch technique.

7.2 General conclusions

The following conclusions are extracted from the work presented in this thesis:

- The model by Travasso *et al.* (2011b) presented in chapter 2 has shown significant potential predicting tumor-induced capillary growth in small-scale simulations. Using this model we have predicted different vascular patterns as a function of the proliferation and chemotactic rates.

- We developed a set of numerical methods and algorithms that have proven to be efficient, accurate, and robust. They allowed us to investigate the models presented in this thesis in a number of physically relevant simulations. In particular, for the above mentioned model, these methods provided us a way to study angiogenesis in medium-size domains (approximately 5 times larger than those used heretofore) under different hypoxic cell distributions and initial capillaries. We concluded that the predicted vascular patterns maintain their main characteristics at these scales.

- The model, which only featured chemotaxis, was extended with a conceptualization of haptotaxis. The results of the new model indicate that haptotaxis may have a significant impact in the final pattern achieved by capillary networks. In contrast with simulations of the model without haptotaxis, our results revealed increased vascular pattern complexity and connectivity,

more tortuous TEC trajectories, higher number of anastomosis events, and shorter capillaries.

- The mouse corneal micropocket angiogenesis assay is a widely used assay whose characteristics provide an outstanding arrangement to calibrate, quantify, and asses the predictability of tumor-induced angiogenesis mathematical models. It poses, however, a variety of numerical and computational hurdles to overcome and to date has only been reproduced in two-dimensional settings.

- The numerical methods and algorithms developed in this thesis provide a framework to perform simulations in three-dimensional, complex geometries as required for the mouse corneal micropocket angiogenesis assay. In particular, isogeometric analysis permitted to simulate the model in a computational domain which is the exact geometry of the cornea of a c57BL/6-strain mouse as defined in the literature.

- The three-dimensional *in silico* mouse corneal micropocket angiogenesis assay suggests that, for mathematical models to achieve the topological complexity observed in *in vivo* angiogenesis experiments, two-dimensional simulations may not be enough.

- The simulations on the cornea, even in the absence of the haptotaxis conceptualization, showed the well-known brush-border effect in three dimensions. In addition, they revealed that changes in the location of the pellet lead to different vascular patterns. These simulations also uncovered a new phenomenon not explicitly built into the model, which can be interpreted as capillary regression.

- The model for tumor-induced angiogenesis growth, regression, and regrowth predicts the plasticity and dynamic evolution of capillaries at long time spans. In particular, the simulations are in quantitative agreement with *in vivo* experiments and capture capillary regression induced by TAF inhibition and their subsequent regrowth after inhibition removal.

- Our conceptualization of filopodia has proven to increase the number of anastomosis events and number of loops, increasing thus the connectivity of the capillary network and favoring blood flow. Furthermore, our simulations revealed that filopodia play a major role in vessel regrowth in the model, as they enhance TEC exploration of the least resistant path for migration, which is formed by the left-behind basement membranes.

- Tumor angiogenic factor convection has been overlooked in mathematical modeling. We have shown, however, that it has a significant impact on

vascular patterning and that it should be incorporated in the models to enhance their predictive capabilities.

- Our numerical simulations predicted an increased malignancy of small solid tumors, as convection increased their ability to induce angiogenesis. They also showed that the combined effect of TAF convection and high intratumoral pressure hinders vascular spread through the tumor.

Finally, we conclude that mathematical modeling and numerical simulation of tumor-induced angiogenesis provide insights into the biological mechanisms that govern this complex phenomenon and may be used as a predictive tool.

7.3 Ongoing and further work

This thesis has opened new lines of research, some of them are the objective of our current research. We detail below a number of them which are in our opinion the most promising.

Mechanotaxis: Interaction among tip endothelial cells Tip endothelial cells migrate using three different mechanisms, namely, chemotaxis, haptotaxis, and mechanotaxis. In the first chapters of this thesis we augmented a model that already featured the first mechanism (see figures 2.1 and 3.1) by adding a conceptualization of haptotaxis. Mechanotaxis, the remaining mechanism, is defined as the migration of tip endothelial cells following cues delivered by mechanical forces. Tip endothelial cells detect an interact with one another through this mechanism as shown in figure 7.1. Thus, the next logical step is to incorporate mechanotaxis into the model.

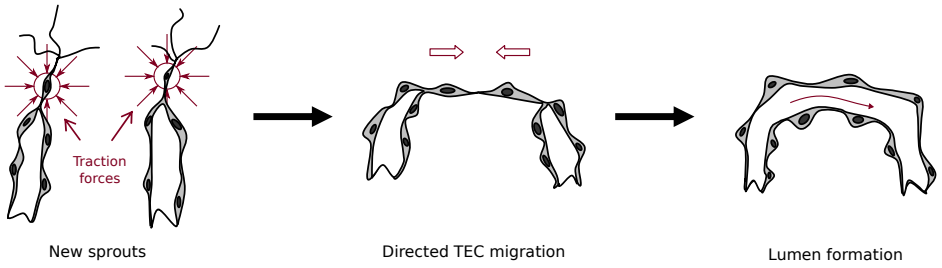

Figure 7.1. Mechanotaxis. *Tip endothelial cells exert traction forces that can be detected by other cells. (Based on Shiu* et al.*, 2005)*

Quantitative analysis During the development of this work, one of the major difficulties was to quantitatively compare the mathematical simulations with the real experiments. We could only achieve quantitative comparisons in a reduced number of two-dimensional cases. We have detected a lack of a well-founded quantitative method from which one can extract the main features of the vascular networks, specially in three dimensions. One of our ongoing lines of research tries to alleviate this deficiency by using skeletonization techniques and graph theory to characterize the new vasculature, as shown in figure 7.2. The major difficulty thus far has been to process the images from the experiments.

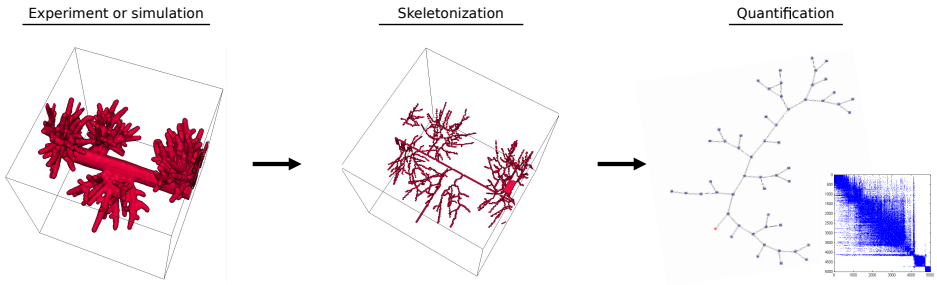

Figure 7.2. Quantification of a tumor induced vasculature. *Skeletonization and graph theory can be used as quantitative tool to characterize angiogenesis.*

Flow-based regression and remodeling In chapter 5 we proposed a model that incorporated TAF-dependent regression. There is also another kind of regression, more related to vascular remodeling, which depends on the functionality of a capillary. Briefly, this regression works as follows: if there is blood flowing through a capillary, the vessel is functional, recruits supporting cells, and maturates, while in the absence of blood flow, the vessel is non-functional and regresses. Thus, blood flow (and the forces that it exerts on the endothelial cells) mediates this kind of regression. And, although with other objective in mind, we have already posed in chapter 6 a model for fluid flow. We are currently working on a model that incorporates this type of regression by coupling the theories presented in chapters 5 and 6. With this model we expect to reproduce TAF and flow based vascular regression and remodeling.

Coupling angiogenesis and tumor growth models Throughout this thesis we have assumed the existence of a static, non-growing tumor whose only role was to release tumor angiogenic factor. This assumption permitted us to exclusively focus on the study of angiogenesis. However, for the model to be predictive, we

need to account also for the tumor growth dynamics and the nutrient release. We have been lately working on a two-dimensional theory that couples angiogenesis and tumor growth (figure 7.3) and we are now generalizing to three-dimensional, real geometries.

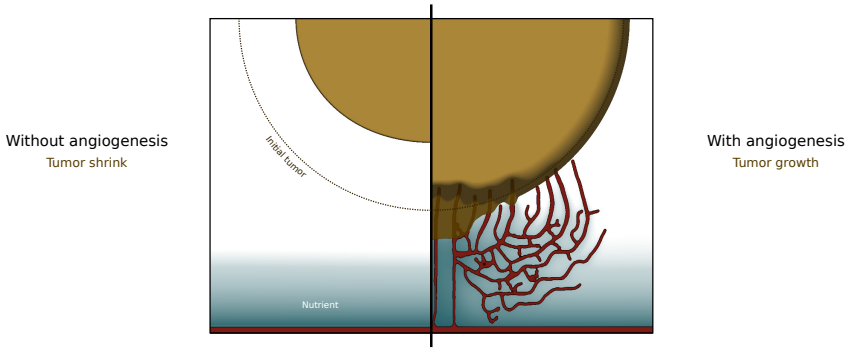

Figure 7.3. Coupling angiogenesis and tumor growth. *The mathematical model predicts how a tumor able to trigger angiogenesis becomes malignant.*

Other lines of research There are other research directions to advance the field of mathematical oncology based on this work. One of them is to study nutrient, oxygen, and drug delivery to tumors using the proposed continuous model for fluid flow. This same theory can also be enhanced by using a more complex model to incorporate other properties of blood. In addition, the numerical methods we used pave the way to study tumor-induced angiogenesis in patient-specific geometries, such as retinas or prostates.

Appendix A

List of publications

The elaboration of this doctoral thesis has resulted in peer-reviewed publications in international journals and contributions in national and international conferences which we detail in the following.

Articles in peer-reviewed international journals

The following journal articles, which are directly related to this thesis, are currently published:

- Vilanova, G., Colominas, I., and Gomez, H. 2001. A numerical study based on the finite element method of a multiscale continuum model of tumor angiogenesis, *Journal of Biomechanics*, vol. 45(S466), pp. S466. Associated with chapter 2.
- Vilanova, G., Colominas, I., and Gomez, H. 2013. Capillary networks in tumor angiogenesis: From discrete endothelial cells to averaged phase-field descriptions via isogeometric analysis, *International Journal for Numerical Methods in Biomedical Engineering*, vol. 29(10), pp. 1015–1037. Associated with chapter 2.
- Vilanova, G., Colominas, I., and Gomez, H. 2014. Coupling of discrete random walks and continuous modeling for three-dimensional tumor-induced angiogenesis, *Computational Mechanics*, vol. 53(3), pp. 449–464. Associated with chapters 3 and 4.

Three further works have been submitted for publication or are already in preparation:

- Vilanova, G., Colominas, I., and Gomez, H., Three-dimensional simulation of the mouse corneal micropocket angiogenesis assay, in preparation. Associated with chapter 4.
- Vilanova, G., Colominas, I., and Gomez, H., A mathematical model of tumor angiogenesis: Growth, regression, and regrowth, *Journal of the Royal Society Interface*, submitted. Associated with chapter 5.
- Vilanova, G., Colominas, I., and Gomez, H., Convection of tumor angiogenic factor modifies angiogenic vascular patterns, *Computer Methods in Applied Mechanics and Engineering*, in preparation. Associated with chapter 6.

Finally, the following articles have been co-authored by the author, being the first two closely related to this thesis:

- Xu, J., Vilanova, G., and Gomez, H. 2016. A mathematical model coupling tumor growth and angiogenesis, *PLoS ONE*, vol. 11(2), pp. e0149422.
- Xu, J., Vilanova, G., and Gomez, H., Three-dimensional vascular tumor growth in patient specific geometries, *Computer Methods in Applied Mechanics and Engineering*, in preparation.
- Lorenzo, G., Scott, M.A., Tew, K.B., Hughes, T.J.R., Zhang, J., Liu, L., Vilanova, G., and Gomez, H., Tissue-scale, patient-specific modeling of prostate cancer growth: a new perspective, *Proceedings of the National Academy of Sciences*, under review.

Selected contributions in international conferences

The work of this thesis was presented in several national or international conferences. A selection of these conferences includes:

- Kick-off Meeting – Mechanobiology Spanish Network of Excellence, Barcelona (Spain), February 24-25, 2015.
- 11th World Congress on Computational Mechanics (WCCM XI), Barcelona (Spain), July 20-25, 2015.
- Isogeometric Analysis: Integrating Design and Analysis (IGA 2014), Austin, Texas (USA) January 8-10, 2014. The contribution to this conference won the poster competition.

- Third International, African Conference on Computational Mechanics (AfriCOMP), Livingston (Zambia), July 30 to August 2, 2013.
- Congreso de Métodos Numéricos en Ingeniería, Bilbao (Spain), June 25-28, 2013.
- Mathways into Cancer II, Carmona (Spain), May 27-30, 2013.
- Advances in Computational Mechanics (ACM 2013) – A Conference Celebrating the 70th Birthday of Thomas J.R. Hughes, San Diego, California (USA), February 24-27, 2013.
- ESB2012 – the 18th Congress of the European Society of Biomechanics, Lisbon (Portugal), July 1-4, 2012.

Appendix B

The Hallmarks of Cancer

Normal cells may become malignant and enable tumor growth, but only by acquiring certain capabilities through mutations and/or changes in the transcriptional control. Although some of these capabilities may be different among cancer types, the basic ones are shared by the vast majority of them. In the last decades, they have been independently studied by many researches, but it was in Hanahan and Weinberg (2000, 2011) where Hanahan and Weinberg gathered them together and developed them further. Under the name of *Hallmarks of Cancer* they elaborated the following list (see Figure B.1): Sustaining proliferative signaling, evading growth suppressors, resisting cell death, enabling replicative immortality, inducing angiogenesis, activating invasion and metastasis, reprogramming of energy metabolism, and evading immune destruction. Furthermore, they included two *enabling characteristics* (tumor-promoting inflammation and genome instability and mutation) and the aid from the recruited cells of the tumor micro-environment, that favor the acquisition of the hallmarks.

All these hallmarks and enabling characteristics are not acquired at once, but as a progressive multi-step evolution. However, it is also known that a single mutation in a gene may influence one or more traits as, for example, the gene *TP53* which plays a role in programmed cell dead (apoptosis), genomic stability, and angiogenesis inhibition. Even more, the order and moment in which tumor suppressor genes and oncogenes are mutated is not the same among different types of cancer, not even among same-type tumors. This appendix is a brief description of the hallmarks of cancer and enabling characteristics.

Sustaining proliferative signaling

In adult tissue normal cells are in an homeostatic[1] state preserved by a complex signaling network. The only way a cell is able to escape homeostasis and to proliferate at a high rate, and thus acquire this hallmark, is to be self-sufficient in this signaling. Albeit the signaling network is barely understood in normal cells, it is considerably known how cancer cells achieve the necessary autonomy. One method is by autocrine stimulation, that is, cells produce growth factors (signals), release them to the exterior, and subsequently capture them by their own membrane receptors, thus controlling the signaling by themselves. Another way is to coerce non-cancerous and stromal cells to secrete growth factors. Proliferation can also be triggered by deregulating cell membrane receptors or altering signaling transduction, i.e., the modification of the pathway that follows a signal from the surface receptor to the nucleus, leading to changes in gene transcription.

Evading growth suppressors

During the cell cycle there are several mechanisms that prevent cell proliferation when the conditions of the environment are not suitable. Growth suppressors are an essential piece of these mechanisms that act at certain moments of the cell cycle, the so called checkpoints (Murray, 1994), and help to maintain tissue homeostasis. Growth suppressors rely on antigrowth signals that depend, for example, on the micro-environment level of glucose or oxygen. Hence, when these levels are low, proliferating cells are conducted out of the cell cycle to a quiescent state at the checkpoints. Through this hallmark, cells acquire the ability to downregulate the growth suppressors function, making themselves insensitive to antigrowth signals, and favoring uncontrolled proliferation.

Resisting cell death

Apoptosis is a complex process carried out in a multicellular organism by cells when they are not viable or not useful. Cells that enter the apoptotic program are divided in fragments which are suitable to be phagocytosed, thus preventing intracellular material to be released to the extracellular matrix with its consequent noxious effect. Apoptosis is tightly controlled by a wide variety of pro- and anti-apoptotic signals, many of which are still under investigation. Apoptosis is a

[1] Homeostasis: The ability or tendency of a living organism, cell or group to keep the conditions inside it the same, despite any changes in the conditions around it (from Cambridge dictionary).

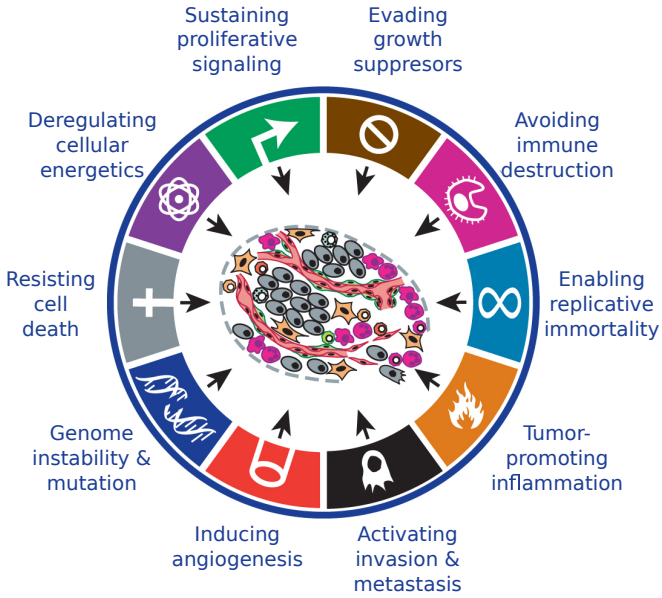

Figure B.1. The hallmarks of cancer and the enabling characteristics. *A normal cell must acquire all of them through mutations to become malignant. (Reproduced from Hanahan and Weinberg, 2011).*

natural barrier to tumor formation, as the body delivers pro-apoptotic signals to cancerous cells hindering the creation of unwanted, high-proliferative solid masses. However, cancer cells are able to circumvent the apoptotic program following different strategies, such as:

- Loosing *TP53* (DNA-damage suppressor gene) function.
- Increasing anti-apoptotic signaling.
- Downregulating pro-apoptotic factors.
- Short-circuiting the death pathway.

Enabling replicative immortality

Most cells are only able to replicate a limited number of times. This limit is imposed by a region of non-coding, repetitive DNA at the end of the chromosomes called *telomere*, whose role is to maintain the integrity of the chromosomes. Each

time a cell undergoes a replication, the telomere is shortened. Hence, after a certain number of replications, the telomere fails to perform its function, leading to end-to-end chromosome fusion. Before this critical point, cells have two options: either enter a rest state called *senescence*, in which the cell continues viable, but is no more replicative, or continue dividing until the telomere is completely lost, thus entering *crisis*, a state which leads to cell death due to chromosomic instability.

However, not all cells are restricted by this mechanism. Some cells, like stem cells[2], are able to divide as many times as required. They do not avoid telomere shortening, but reconstruct it to its previous length using an *ad hoc* enzyme called *telomerase*. For a cell to form a tumor, it must have the capacity to be immortal in the previous sense. In most tumors, cancerous cells upregulate the expression of telomerase, and less frequently use another methods to maintain telomere length.

Inducing angiogenesis

All cells in the body need sustenance, i.e. nutrients or oxygen, and a means of waste removal. During embryogenesis an intricate blood vessel network is created to perform these functions and, once the adult body is formed, only minimal vessel growth takes place, because different signaling types restrict cell proliferation to locations with appropriate sustenance, that is close enough to vessels. The episodes of vessel creation that occur during adulthood are transient and tightly controlled and only under certain circumstances such as wound healing.

However, cancer cells are aberrant and proliferate even without enough access to nutrients. Thus they usually create local hypoxic regions within the tumor where cells starve because nutrients and oxygen cannot arrive through diffusion mechanisms. If they are deprived of nourishment for a long time span they may become necrotic and die, creating a necrotic core of dead cells and debris inside the tumor. The access to nutrients becomes more difficult as the tumor grows, causing more and more cells to die from starvation. There is a point where the death and proliferation rate get balanced causing the halt on the global tumor growth. For tumors to grow beyond this threshold, cancerous cells must acquire the capability of inducing angiogenesis, that permits them to create their own vasculature from the preexisting one. This switch in tumor fate, usually called *angiogenesis switch*, is performed through different mechanisms (as upsetting directly the signal balance or indirectly by inflammatory cells) and in different gradations.

[2]Stem cells are biological cells found in all multicellular organisms, that can divide (through mitosis) and differentiate into diverse specialized cell types and can self-renew to produce more stem cells.

Activating invasion and metastasis

Cancer cells may acquire the capability to spread to other tissues or organs. When the colonized tissue is adjacent to the tissue where the tumor was originated, the process is called invasion, while when the tissue is not connected to it, it is called metastasis. Invasion is done at least in three different ways: mesenchymal, collective invasion, and ameboid. The first one corresponds with the so-called epithelial-to-mesenchymal transition (EMT). There are several genes thought to be involved in EMT and through it cells may be able to invade, resist apoptosis, and disseminate. In the second way of invasion, cancer cells advance *en masse* into the adjacent tissues. In the last way, a single cell with a plastic morphology that lacks its cell-cell and ECM-cell adhesions slips through the ECM interstices (Friedl and Wolf, 2008, 2010) and migrates to a neighbor organ.

Metastasis is a more complex process, although it shares some underlying mechanisms with invasion, such as EMT. Metastasis is usually divided into two major phases: the dissemination of cancer cells and the colonization of the new emplacement. The first one is thought to be achieved mainly through EMT. In it, cancerous cells have to migrate through the local tissue, intravasate into the blood or lymphatic vessels, survive in the cardiovascular or lymphatic system, extravasate from the vessels, and establish in the new tissue forming micro-metastasis. Once cells have arrived to their new emplacement they are no longer surrounded by the malignant micro-environment they had created in the primary location, but by a normal one which is not under their dominion. Thus, they need to colonize the tissue to form macro-metastasis, which usually passes through the reversion of their current migratory phenotype acquired via the EMT, undergoing the opposite process called mesenchymal-to-epithelial transition (MET). With the new phenotype they may have the chance to activate the stroma, grow, and form a new tumor (Hugo *et al.*, 2007).

Reprogramming of energy metabolism

Normal non-proliferative cells in a tissue obtain the energy from of adenosine 5-triphosphate or ATP [3] by transforming the received nutriment (glucose) through two different processes, depending on the external conditions:

[3] Adenosine 5'-triphosphate or ATP transports chemical energy within cells for metabolism. It is produced in cellular respiration and it is used as a source of energy in many vital processes during cell lifespan. Once an ATP molecule is used, it converts into adenosine diphosphate (ADP) or adenosine monophosphate (AMP) and can be phosphorylated again and reconverted into ATP.

- **Oxidative phosphorylation:** In presence of oxygen, glucose is first transformed into pyruvate acid via a metabolic pathway called *glycolysis*. Then, the major part of pyruvate is processed with the oxygen in the mitochondria, obtaining 36 mol ATP per mol of glucose. The rest of pyruvate is transformed into lactate.

- **Anaerobic glycolysis:** When there is not enough oxygen, all the pyruvate obtained by glucose glycolysis is transformed into lactate, therefore obtaining only 2 mol of ATP per mol of glucose.

The former produces a greater amount of ATP which may be thought as a greater amount of available energy. Surprisingly, proliferative cells do not metabolize the glucose via oxidative phosphorylation, even in presence of enough oxygen. This fact was first observed by Otto Warburg in cancer cells and this *aerobic glycolysis* is also called *Warburg effect* after him. Cancer cells, when proliferating, change their metabolism and produce essentially lactate (Vander Heiden *et al.*, 2009). Besides, in the last years, a deeper investigation in this subject brought to light that in the same tumor not all cells present the Warburg effect, but only subgroups. Consequently, a symbiosis is made between subgroups, since the one with altered metabolism produces lactate and the other uses it as the main source of energy (Feron, 2009; Kennedy and Dewhirst, 2010; Semenza, 2008). Through this emerging hallmark cancer cells change the energy metabolism and boost the uncontrolled proliferation.

Evade immune destruction

The role of the immune system is to detect external agents and defective cells and eliminate them to protect the organism. Consequently, it operates as a natural barrier to cancer –since it recognizes potential cancerous cells as faulty–, reducing tumor expansion in the vast majority of cancers, especially those which are virus-induced. To avoid their destruction, cancerous cells must gain the ability to eliminate the components dispatched by the immune system. What is more, cancerous cells may even include immune cells into their malignant stroma. One example is when the inflammatory cells are attracted with pro-inflammatory signals to remove the necrotic debris (Galluzzi and Kroemer, 2008; Grivennikov *et al.*, 2010; White *et al.*, 2010).

Enabling characteristics

Two characteristics also shared by almost every cancer could be added to these hallmarks. Both of them enable normal cells to acquire a malignant genotype. These characteristics are:

- **Genome instability and mutation:** Instability of genome is inherent to most cancer types (Loeb *et al.*, 2003), because it is a requirement to acquire the traits explained above. Every cell has a machinery whose mission is to prevent mutations, usually surveying the genome during cell division. Consequently, cancer cells need to breakdown and/or bypass one or several components of this machinery. Once a cell has acquired a viable mutation it proliferates and provides its offspring with the same genomic alteration. Thereafter, one of the descendants may suffer another mutation, generating thus clonal expansions (Loeb *et al.*, 2003), each one with increased number of acquired hallmarks.
- **Tumor-promoting inflammation:** For years, it has been known the presence of immune system cells in tumors and it has been thought that it was an attempt by the immune system to eradicate malignant cells from the tissues. Although this theory has been confirmed, another role has recently been associated to immune cells, but this time as tumor-promoting ones. Particularly, inflammatory cells contribute to the acquisition of many hallmarks of cancer and to furnish potentially cancer cells with different aids. Some examples extracted from DeNardo *et al.* (2010); Grivennikov *et al.* (2010); Karnoub and Weinberg (2006-2007); Qian and Pollard (2010) are:
  - Growth factors that sustain proliferative signals.
  - Survival factors that limit cell death.
  - Pro-angiogenic factors.
  - ECM-modifying enzymes that facilitate angiogenesis, invasion and metastasis.
  - Inductive signals that lead to activation of the EMT.
  - Other hallmarks-facilitating programs.

Appendix C

Molecular mechanisms of angiogenesis

Angiogenesis is a complex phenomenon governed by several molecular mechanism. Our understanding of these mechanisms is limited, but has exponentially increased over the last years. More knowledge on this topic has led to the improvement of antiangiogenic therapies, and not only in cancer, but also in other diseases. Nowadays, thousands of patients benefit from antiangiogenic therapies.The effect of these treatments is, however, limited: some patients are refractory to them, and many others develop resistance. Research continues in this field and strategies based on recently discovered molecular pathways have shown promising results.

In this appendix we show a compilation of the most known molecular mechanisms and a list of direct pharmacological inhibitors of angiogenesis, many of them approved for their use as antiangiogenic drugs.

Tumor angiogenic factors

Tumor-induced angiogenesis is known to be orchestrated by more than a dozen tumor angiogenic factors. This factors, their isoforms, and their receptors are produced by tumor cells and their malignant stroma, have a wide variety of functions, and can act in combination. Table C.1 summarizes the most well-known of this factors and roles in angiogenesis.

Table C.1. *Tumor angiogenic growth factors*

Tumor angiogenic factors		Secreted by	Receptors	Main function
Vascular endothelial growth factor	VEGF-A	A wide variety of cells and the majority of tumor cells.	VEGFR-1 VEGFR-2 NRP-1 NRP-2	It is mitogenic for endothelial cells and a potent inducer of vasodilatation. It depends on $\alpha_v\beta_5$ integrin.
	VEGF-B		VEGFR-1 NRP-1	Only restricted angiogenic activity in certain tissues. It is mitogenic for endothelial cells.
	VEGF-C		VEGFR-2 VEGFR-3 NRP-2	It is mitogenic and motogen for endothelial cells and enhances capillary hyperpermeability. It may have a specific role in lymphangiogenesis.
	VEGF-D		VEGFR-2 VEGFR-3	It is mitogenic (Stimulates EC proliferation following induction by the transcriptional regulator FOS).
	VEGF-E		VEGFR-2 NRP-1	
	PlGF		VEGFR-1 NRP-1	Main function remains to be investigated.

Endothelial cell mitogen and motogen *in vivo*.

Induces fenestration in endothelium of small venules and capillaries, increasing their permeability.

Acts sinergically with bFGF to stimulate tube formation *in vitro*.

Continued on next page

Tumor angiogenic factors		Secreted by	Receptors	Main function	
Fibroblast growth factor	aFGF	Tumor cells of central nervous system. Sarcomas Genitourinary tumors. Endothelial cells in the tumor vasculature.	FGFR-1 FGFR-2 FGFR-3 FGFR-4	FGF stimulates angiogenesis *in vitro* and *in vivo* by stimulating endothelial cell proliferation and enhancing endothelial cell migration. They stimulate endothelial cell mitosis and migration *in vitro* and are among the most potent angiogenic proteins *in vitro*. Stimulate the production of matrix proteases in endothelial cells. The action of FGF is not specific to ECs and they bind to the ECM.	This protein functions as a modifier of endothelial cell migration and proliferation, as well as an angiogenic factor.
	bFGF	Some tumor cells recruit macrophages and activate the to secrete bFGF. Others attract mast cells which could sequester bFGF.			bFGF is not an specific mitogen, but has several cell targets: Fibroblasts, smooth muscle cells, and neurons.
Angiopoietins	Ang-1	Endothelial cells. Mural and tumor cells.	Tie-2	Maintains endothelial cell quiescence. It is not a direct mitogen cell *in vivo*. It recruits pericytes and smooth muscle cells, mediated by PDGF-B when Tie-2 is activated by Ang-1.	Stabilizes nascent vessels by tightening the interaction between endothelial and periendothelial cells. Inhibits permeability.
	Ang-2	Tip cells. Also found at sites of vascular remodeling.	Tie-2	Functions as a competitive Ang-1 antagonist.	Enhances mural cell detachment, vascular permeability, and endothelial cell sprouting.
	Ang-4		Tie-2	It has not been as well studied, but it is thought to act like Ang-1.	

Continued on next page

Tumor angiogenic factors		Secreted by	Receptors	Main function
Platelet derived growth factor		Platelets, fibroblasts, macrophagues, and endothelial cells.	PDGFR-α PDGFR-β	Mitogen and chemoattractant for most mesenchymally derived cells. Stimulates pericyte proliferation. Increases capillary wall stability.
Transforming growth factor	TGF-α	Tumor cells.		May act as a autocrine signal for tumor cells.
	TGF-β	Expressed in a full spectrum of cell types, including ECs and pericytes in the microcirculation.	Serine/ threonine kinases receptor-type.	Members of the TGF-β family are multifunctional cytokines with effects on cell . Proliferation, migration, inflammation, and angiogenesis. Stimulates *in vivo* angiogenesis in presence of inflammatory response. Stimulates/inhibits *in vitro* angiogenesis. Produces net antiproteolytic activity via modulating the production of matrix proteases and protease inhibitors. Stabilizes nascent vessels by stimulating mural cell induction, differentiation, proliferation, and migration and stimulating matrix production.
Integrins	$\alpha_v\beta_3$	Upregulated in activated endothelial cells.	*They are receptors themself*	Mediates endothelial cell attachment, spreading, and migration. Inhibits endothelial cell apoptosis. Highly expressed on activated endothelial cells. Present on angiogenic capillary sprouts. Localizes MMP-2 to capillary sprouts. Required for FGF-stimulated angiogenesis *in vivo*.
	$\alpha_v\beta_5$			Required for VEGF-stimulated angiogenesis *in vivo*.

Continued on next page

Tumor angiogenic factors		Secreted by	Receptors	Main function
Matrix proteases	MMP-1	Produced by a variety of cell types, including: Endothelial cells Pericytes Smooth muscle cells in blood vessel walls.		They degrade the ECM. They are also important for the release of angiogenic stimuli from the ECM pool and the exposure of cryptic binding sites in the ECM to promote cell adhesion and migration. Most MMPs and PAs are secreted as inactive pro-proteins which are activated when cleaved by extracellular proteinases.
	MMP-2			
	MMP-9			
	MMP-13			
	PA (Plasminogen activator)			

VEGF and bFGF stimulate the shedding of vesicles containing MMPs.
Degrade ECM components.
Mediate cell migration and matrix remodeling.
EC-derived vesicles contain the latent forms of MMP-2 and -9 (proMMP-2,-9).
Most MMPs are also involved in the breakdown of extracellular matrix in normal physiological processes, such as embryonic development, reproduction, and tissue remodeling, as well as in disease processes, such as arthritis and metastasis.

Mediate cell migration and matrix remodeling.

Continued on next page

	Tumor angiogenic factors	Secreted by	Receptors	Main function
Chemokines	SDF-1α	Hypoxic cells Cancer associated fibroblasts	CXCR4	Promote revascularization under hypoxia.
	S1P	S1PRs		Regulates endothelial cell barrier function, vessel stability, and angiogenesis, in part by crosstalking to PDGF and VEGF receptors.
	Others		Endothelial G-protein-coupled chemokine receptors	Recruit pro-angiogenic immune cells and endothelial progenitor cells. Activate endothelial G-protein-coupled chemokine receptors.

Other tumor angiogenic factors with relevant roles in tumor angiogenesis include:

- The Notch and WNT signalling pathways.
- Junctional molecules.
- Chemokines and G-protein-coupled receptors.
- Roundabouts (ROBO) are guidance receptors.
- UNC5B is a receptor for Netrins whose expression is enriched in tip cells.
- Semaphorins are secreted or membrane-bound guidance cues, although most of them suppress angiogenesis.
- EPH receptors and their ephrin ligands are regulators of cell-contact-dependent signaling.

The reader is referred to Carmeliet and Jain (2011); Figg and Folkman (2011a); Potente *et al.* (2011); Tahtis and Bicknell (2005); Thurston and Kitajewski (2008); Weis and Cheresh (2011) for more information on this subject.

Direct pharmacological inhibitors of angiogenesis

The objective of antiangiogenic therapies is to block the molecular mechanisms that govern angiogenesis. They can be focused at different points of their molecular pathways, such as, the diffusion of tumor angiogenic factors or the dimerization of their receptors, and in many occasions they disrupt the pathways at several points. We show below a list of direct inhibitors of angiogenesis for VEGF, were we highlight those that have been approved for use in the clinic. Note that the majority of them are approved only in combination with chemotherapy. More angiogenic inhibitors that are at the present in clinical trials can be found at Cancer Research UK (2015).

- Anti-VEGF agents
  - Anti-human agents A4.6.1.
  - **Bevacizumav (Avastin):** Approved for metastatic colorectal cancer, metastatic non-squamous non-small-cell lung cancer (with chemotherapy), metastatic breast cancer (with chemotherapy, and only in Europe), recurrent glioblastoma multiforme (with interferon), and metastatic renal cell carcinoma.
  - Anti-murine VEGF-A antibodies.

  - **Aflibercept (Zaltrap):** Approved for metastatic colorectal cancer.
  - **Ramucirumab (Cyramza):** Approved for advanced gastric or gastro-esophageal junction adenocarcinoma and metastatic non-small-cell lung carcinoma (in combination with chemotherapy).

- Anti-VEGFR agents
  - DC101
  - Rat anti-mouse VEGFR2 monoclonal antibody
  - Antibody blocking dimerization of VEGFR2 and VEGFR3
  - VEGF receptor tyrosine kinase inhibitors (TKIs)
    * **Sunitinib (Sutent):** Approved for metastatic renal cell carcinoma, imatinib-resistant gastrointestinal stromal tumor, and some pancreatic cancers.
    * **Sorafenib (Nexavar):** Approved for metastatic renal cell carcinoma, unresectable hepatocellular carcinoma, and radioactive iodine resistant advanced thyroid carcinoma.
    * **Pazopanib (Votrient):** Approved for metastatic renal cell carcinoma, soft tissue sarcomas, and gastrointestinal stromal tumors.
    * **Vandetanib (Caprelsa):** Approved for late-stage (metastatic) medullary thyroid cancer.
    * **Nintedanib (Vergatef):** Approved for non-small-cell lung cancer (in combination with chemotherapy).
    * **Axitinib (Inlyta):** Approved for kidney cancer.
    * Cediranib
    * Semaxanib
    * TSU68
    * **Cabozantinib (Cometriq):** Approved for thyroid cancer.
    * **Regorafenib (Stivarga):** Colorectal cancer and gastrointestinal stromal tumors.

Appendix D

Angiogenesis assays

Angiogenesis assays are used to asses the validity and efficacy of antiangiogenic therapies and to identify potential targets for new drugs. In this appendix we detail the most used assays. They can be either *in vitro* or *in vivo* and most studies use both of them, usually in that order. *In vitro* angiogenesis assays are easier to perform than *in vivo* assays. In addition, they are usually faster, cheaper, and their results are far more easy to quantitate. However, these results must be interpreted with caution, as they may lack complex molecular mechanisms involved in angiogenesis. They are usually complemented with *in vivo* assays which, on the contrary, are more informative. The main disadvantage of the latter is they are time consuming and difficult to quantitate.

***In vitro* assays** Some of the more common *in vitro* assays include:

- Proliferation assays. They consist on monitoring endothelial cell proliferation and counting.
- Cell migration assays: Either for chemokinesis (random) and chemotaxis (directional).
- Tube formation *in vitro*.
- Coculture protocols: Their main components are endothelial cells, feeder layers and tumor fragments.

- Organ culture assays: They can more closely approximate *in vivo* assays. The most widely used organ culture system is the aortic ring assay.

***In vivo* assays** We detail in table D.1 the advantages and disadvantages of the major *in vivo* assays. Among them, the most frequently used in current practice are the CAM, the Matrigel plug, and the corneal micropocket assay (Figg and Folkman, 2011a; Norrby, 2006).

Table D.1. *Advantages and disadvantages of* in vivo *angiogenesis assays (Norrby, 2006)*

Assay	Advantages	Disadvantages
Corneal micropocket	New vessels are easily identified. Used in rabbits, rats, and mice. Permits non-invasive observation and long-term monitoring. Quantitative. Mammalian. Immunologically privileged site before vascularization. Angiogenesis by sprouting.	Atypical angiogenesis, as the normal cornea is avascular. Technically demanding, especially in mouse eye. Traumatic technique. Ethically questionable. The cornea is not a highly relevant site for tumor growth. Exposure to oxygen via surface can affect angiogenesis. Non-specific inflammatory response with some compounds. Expensive.
CAM	Technically simple. Inexpensive. Suitable for large-scale screening. Permits non-invasive observation. Suitable for mammalian xenografts.	Very sensitive to increase in oxygen tension. Visualization of new vessels can be difficult. Non-mammalian. Embryonic. Angiogenesis by sprouting and intussusceptive growth. Accelerates or suppresses organogenic angiogenesis (up to days 10-11). Non-specific inflammatory reactions common. Drugs that require metabolic activation cannot be assessed.
Disc assay	Technically simple. Assesses wound healing and angiogenesis. Quantitative analysis.	Encapsulated by granulation tissue. The subcutaneous tissue is not highly relevant for tumor growth.

Continued on next page

Assay	Advantages	Disadvantages
Mesentery	The adult tissue is vascularized and lacks significant. physiologic angiogenesis. Truly quantitative, allowing dose-response studies 3 in terms of microvessel spatial extension, density and number and length of microvessel segments and sprouts (in rat). Minimal trauma, if any, is inflicted in the test tissue. The test tissue is visceral; visceral organs are frequent sites of metastasis. Suitable for measurement of growth factor-induced signaling in intact microvessels. Suitable for intravital microscopy. Suitable for molecular-activity studies. Angiogenesis by sprouting.	Time consuming. Technically somewhat demanding. Mice are less suitable for quantitative angiogenesis analysis than rats. Rats demand approximately 10 times greater quantity of test agents than mice. Does not allow real-time observations.
Sponge/matrix implant	Technically simple. Inexpensive. Well tolerated. Time course of response can be recorded. Suitable for study of tumor angiogenesis.	Time consuming. Encapsulated by granulation tissue. Sponge composition varies, making inter-experimental comparisons difficult. Variable retention of test compound within implant. The subcutaneous tissue is not a highly relevant site for tumor growth. Animals have to be kept singly.
Matrigel plug	Technically simple. Suitable for large-scale screening. Rapid quantitative analysis in chambers.	The Matrigel is not chemically defined. Difficult to make plugs uniform in 3-dimensional shape (except in chambers). Analysis in plugs time consuming. The subcutaneous tissue is not highly relevant for tumor growth. Expensive. Not responsive to VEGF (in chambers).
Zebrafish	Intact whole animal. Technically simple. Allows gene analysis of vessel development. Truly quantitative. Large numbers of animals available for statistical analysis. Relatively fast assay. Suitable for large-scale screening.	Non-mammalian. Embryonic. Expensive to maintain in breeding condition.

Other assays usually performed in mice or rabbits include:

- The matrigel plug assay.
- The directed *in vivo* angiogenesis assay (DIVAA).
- Anterior-eye chamber and eat chamber in the rabbit.
- The mouse cranial window.
- The dorsal skinfold and other skin chambers in mice.
- The dorsal air-sack.
- The hollow-fiber solid tumor model.
- Intravital microscopy.
- The Angiomouse® system.

Research is also performed on other animals like hamsters, amphibians (as Rana and Xenopus), *Xenupus laevis* tadpole or monkeys. In humans, the prime methods employed in patients include the using imaging methods, such as, magnetic resonance imaging, positron emission tomography, or Doppler analysis. They allow to determine mean vessel density, assessing vascular patterns, or visualize blood flow.

Appendix E

Extended summary in Spanish

Introducción

En la actualidad, el cáncer es la segunda mayor causa de las muertes que ocurren en el mundo. El cáncer empieza con una única célula que ha acumulado una serie de mutaciones normalmente tras un largo período de tiempo. Una de las principales características de esta célula es su habilidad para crear copias de si misma sin límites, produciendo, en la mayoría de los casos, una densa masa de células hijas que forman un tumor sólido. La proliferación de las células cancerígenas y, por lo tanto, el crecimiento del tumor, depende de los nutrientes y el oxígeno que les suministran los capilares que existían previamente en el tejido. Este suministro no es suficiente para mantener la alta tasa de crecimiento potencial de un tumor, que, como consecuencia, mantiene un tamaño pequeño y entra en un estado de letargo; es decir, es un tumor benigno. En algunas ocasiones, sin embargo, las células cancerígenas adquieren la habilidad de estimular el crecimiento de nuevos vasos capilares hacia ellas. Este proceso se llama angiogénesis tumoral y a través de él los tumores adquieren un suministro constante de nutrientes y oxígeno. Por lo tanto, aquellos tumores capaces de estimular la angiogénesis se vuelven malignos al ser capaces de crecer sin límites. Los nuevos capilares les proporcionan además acceso a todo el cuerpo a través del sistema circulatorio, facilitando la formación de metástasis. Los tumores malignos pueden crecer tanto como para afectar el correcto funcionamiento del órgano en el que se encuentran y, finalmente, producir la muerte del individuo.

E · Extended summary in Spanish

La angiogénesis tumoral es un fenómeno complejo que describimos a continuación brevemente.

Las células cancerígenas que son capaces de inducir la angiogénesis liberan sustancias químicas solubles conocidas genéricamente como *factores angiogénicos tumorales*. Cuando llegan a las células endoteliales que forman los vasos capilares algunas de ellas adquieren un fenotipo migratorio y empiezan a moverse hacia la fuente de factor angiogénico. Estas células se denominan células endoteliales estrelladas debido a que desarrollan unas protuberancias (filopodios) que les dan forma de estrella. Las células endoteliales adyacentes adquieren por el contrario un fenotipo proliferativo y, a medida que se duplican, aumentan la longitud del capilar. Las células endoteliales estrelladas migran utilizando tres mecanismos diferentes: la quimiotaxis, la haptotaxis y la mecanotaxis. El primero está gobernado por sustancias químicas solubles, el segundo por sustancias químicas no solubles y por puntos de adhesión focal y el tercero por señales mecánicas. El proceso de crecimiento de nuevos vasos capilares continúa hasta que las células endoteliales estrelladas detectan otras células endoteliales próximas y se fusionan con ellas en un proceso denominado anastomosis. Así se van generando nuevas redes vasculares por los que puede circular la sangre y abastecer la demanda de nutrientes y oxígeno. Debido a que la demanda de los tumores aumenta con su tamaño y a que los nuevos capilares son defectuosos, la angiogénesis tumoral continúa produciéndose a medida que el tumor crece.

Hace unas décadas, algunos científicos propusieron que boquear la angiogénesis podría ser un tratamiento efectivo contra el cáncer. Esta terapia, denominada terapia antiangiogénica, ha mostrado resultados prometedores en ensayos preclínicos, pero no se han trasladado en los resultados esperados en la clínica. En la actualidad, está emergiendo un nuevo paradigma en la Medicina, la Medicina Predictiva, que se espera que cambie el campo de la Oncología y que puede proporcionar el enfoque adecuado para entender el problema de las terapias antiangiogénicas. La Medicina Predictiva está basada en modelos matemáticos y en la computación y ha sido aplicada con éxito en varias áreas de la Medicina. En el campo de la Oncología no ha hecho más que empezar, pero ya ha producido resultados satisfactorios. Más concretamente, en la angiogénesis tumoral, numerosos investigadores han planteado modelos matemáticos para abordar el problema de las terapias antiangiogénicas, aunque todavía son necesarias mejoras para lograr este objetivo. La angiogénesis es un fenómeno complejo que involucra varias escalas y mecanismos, muchos de los cuales todavía no están contemplados en estos modelos. Además, la mayoría de los modelos se simulan en geometrías bidimensionales simples, mientras que la angiogénesis es un proceso tridimensional que ocurre en tejidos u órganos con geometrías no triviales.

Objetivos

En esta tesis desarrollamos modelos matemáticos de angiogénesis tumoral que incluyen mecanismos biológicos fundamentales y simulamos estos modelos en configuraciones experimentales relevantes y en geometrías tridimensionales específicas de un sujeto. Esta tesis continúa la investigación desarrollada en el Grupo de Métodos Numéricos en Ingeniería (GMNI) de la Universidade da Coruña en el campo de la Mecánica Computacional y, en particular, es la primera en explorar el subcampo de la Biomecánica Computacional. También es la primera tesis desarrollada dentro del proyecto *Modeling and Simulation of Cancer Growth* (MuSIC), cuyo objetivo es desarrollar modelos predictivos para el crecimiento de cáncer con el objetivo de cambiar el tradicional paradigma diagnóstico del tratamiento de cáncer hacia uno predictivo y específico para cada paciente. El trabajo de esta tesis también ha sido desarrollado en el *Institute for Computational Engineering and Sciences* (ICES) de la *University Of Texas At Austin* durante una estancia de investigación de cuatro meses de duración.

Los objetivos esta tesis se pueden dividir en las siguientes tres categorías:

- **Modelización**: La finalidad es desarrollar nuevos modelos matemáticos de angiogénesis tumoral que incluyan mecanismos biológicos fundamentales, en concreto, la migración de células endoteliales estrelladas por haptotaxis, la capacidad de regresión y recrecimiento de los capilares en función de los estímulos externos y la convección de los factores angiogénicos por el flujo intersticial. Todos estos modelos incluyen variables continuas gobernadas por ecuaciones diferenciales en derivadas parciales de alto orden, así como elementos discretos.

- **Simulación**: La mayoría de los modelos matemáticos que se encuentran en la literatura son simulados en geometrías bidimensionales simples. Estas configuraciones facilitan el estudio de dichos modelos. En esta tesis realizaremos simulaciones *in silico* de los modelos mencionados anteriormente utilizando geometrías bidimensionales que tratan de replicar configuraciones relevantes *in vivo*. Sin embargo, la angiogénesis es un proceso tridimensional que se desarrolla en tejidos con geometrías complejas. Por lo tanto, el segundo objetivo de esta tesis es ir paso más allá y realizar simulaciones tridimensionales utilizando geometrías reales que permitan comparar los resultados con los experimentales. En particular, nuestra meta es desarrollar simulaciones de angiogénesis tumoral de uno de los experimentos *in vivo* más usados: el experimento denominado *mouse corneal micropocket angiogenesis assay*. Estas simulaciones serán realizadas en tres dimensiones utilizando geometrías específicas de sujetos y, hasta donde saben los autores, permitirán por primera

vez la comparación entre una simulación y un experimento en geometrías reales.

- **Computacional**: El tercer objetivo es desarrollar algoritmos numéricos capaces de realizar de manera eficiente las simulaciones detalladas arriba. En primer lugar, necesitamos desarrollar un marco matemático en el que se puedan integrar perfectamente los elementos discretos y las variables continúas del modelo. También necesitamos utilizar un tecnología recientemente introducida, el análisis isogeométrico, capaz de manejar los términos de alto orden de las ecuaciones en derivadas parciales, tanto en dos como en tres dimensiones. Por último, los algoritmos tienen que ser robustos y ser capaces de ejecutarse de manera eficiente en paralelo.

Metodología

La dinámica de la angiogénesis tumoral y su impacto en el crecimiento del cáncer permanecen como problemas fundamentales abiertos en la biología del cáncer. La Medicina Predictiva y, en particular la Oncología Matemática, son campos que están en desarrollo y cuyo objetivo es predecir y proporcionar una mayor comprensión de estos problemas. Con este fin, en este documento se han propuesto tres nuevos modelos matemáticos para la angiogénesis tumoral que se han simulado en dos y tres dimensiones, tanto en geometrías simples como complejas.

Los tres modelos propuestos comparten una serie de características comunes desde el punto de vista numérico. Por lo tanto, para lograr nuestros objetivos de modelado y simulación, hemos desarrollado en primer lugar algoritmos numéricos adecuados. Los tres modelos son híbridos, es decir, involucran elementos discretos gobernados por una serie de reglas discretas y variables continuas gobernadas por ecuaciones en derivadas parciales. Ambos deben ser acoplados de manera robusta y eficiente. Además, la evaluación de las reglas discretas implica evaluar las variables continuas en determinados puntos. De estos puntos sólo se conocen sus coordenadas físicas, mientras que las paramétricas, que son las necesarias para evaluar las variables continuas, se desconocen. En geometrías simples con mapeos lineales las coordenadas paramétricas se pueden obtener de manera directa. Sin embargo, en geometrías complejas es necesario desarrollar un algoritmo adecuado para obtenerlas. Por último, los tres modelos basan su definición de los capilares en la teoría de campo de fase la cual involucra ecuaciones diferenciales en derivadas parciales de alto orden. El método numérico tiene que ser capaz de lidiar con estos términos para hallar una solución a las ecuaciones.

El primer paso para desarrollar el método numérico es describir los modelos en un

marco matemático coherente. De esta manera podemos formular el acoplamiento entre los elementos discretos y las variables continuas para permitir un tratamiento numérico eficiente del problema junto. Esta formulación está basada en unas plantillas predefinidas que utilizan la solución a la ecuación de campo de fase de Cahn-Hilliard en una dimensión en un dominio infinito. Además, hemos desarrollado un método para encontrar las coordenadas paramétricas a partir de las coordenadas físicas conocidas de los puntos en los que se evalúan las reglas discretas. Este método funciona en geometrías tridimensionales complejas, que incluyen mapeos no lineales. Está fundamentado en el método de Newton-Raphson y es capaz de trabajar con cálculos paralelos. Para la resolución de las ecuaciones en derivadas parciales de orden superior involucradas en la formulación de los modelos se utilizó el análisis isogeométrico, que no sólo ofrece precisión y solidez sino también la flexibilidad geométrica lo que necesitamos para llevar a cabo simulaciones en geometrías reales. También hemos utilizado el método α-generalizado y un esquema de tiempo adaptativo que aumenta de la eficiencia de nuestros cálculos. Por último, todos estos métodos han sido adaptados para funcionar en paralelo usando una técnica *multi-patch*.

El primero modelo matemático que proponemos en esta tesis parte de uno previo que consideraba la quimiotaxis como mecanismo de migración celular. A este modelo le hemos añadido una conceptualización para la *haptotaxis* utilizando caminos aleatorios circulares sesgados. Este modelo se estudió primero en configuraciones bidimensionales con geometrías simples para adquirir una mayor comprensión de las ecuaciones de gobierno y que nos permitieron evaluar el papel de haptotaxis en la angiogénesis tumoral. El objetivo final era sin embargo reproducir un experimento en tres dimensiones usando de una geometría real. Con este fin, hemos evolucionado la configuración inicial para representar primero geometrías bidimensionales más grandes y después geometrías tridimensionales. En ellas realizamos diferentes análisis variando la disposición de los capilares iniciales y de los tumores, imitando configuraciones fisiológicas y experimentales. Estas simulaciones culminaron en el desarrollo de simulaciones de la angiogénesis tumoral que reproducen el experimento *in vivo* conocido como *mouse corneal micropocket angiogenesis assay*. En estas simulaciones utilizamos la geometría tridimensional, específica de un sujeto (la córnea de un ratón c57BL/6) con más de $28,9$ millones de grados de libertad. Hasta donde saben los autores, esta simulación permite por primera vez la comparación entre un experimento *in silico* y uno *in vivo* en una geometría tridimensional real.

El segundo modelo se centra en la dinámica a largo plazo de la angiogénesis tumoral, es decir, sobre los fenómenos de regresión y recrecimiento que se producen después del primer crecimiento de los vasos sanguíneos. La formulación de este modelo incluye una ecuación no conservada de campo de fase (Allen-Cahn)

cuya energía depende del factor angiogénico tumoral. Además, hemos incorporado una conceptualización de los filopodios que favorece la detección de células endoteliales próximas y por lo tanto la anastomosis. El modelo se simuló tanto en una réplica bidimensional del ensayo *mouse corneal micropocket angiogenesis assay* como en una reproducción de un experimento *in vivo* con el que se comparó cuantitativamente.

Por último, hemos desarrollado una teoría para el flujo sanguíneo e intersticial en la escala de tejidos que acoplamos con el modelo para la angiogénesis tumoral. La característica principal del modelo de flujo es que es una teoría completamente continua que incluye el flujo en los capilares, a través de la pared vascular y en el intersticio. El modelo de flujo está acoplado al de angiogénesis a través de la convección de los factores angiogénicos. Los resultados de las simulaciones muestran cómo el flujo altera los patrones vasculares inducidos por el tumor a través de esta convección.

Conclusiones

Las siguientes conclusiones han sido extraídas del trabajo presentado en esta tesis:

- El modelo de Travasso *et al.* (2011b) presentado en el segundo capítulo ha mostrado un potencial significativo en la predicción del crecimiento de capilares inducidos por tumores en simulaciones a pequeña escala. Utilizando este modelo hemos predecido la formación de diferentes patrones vasculares en función de la proliferación y la quimiotaxis.
- Hemos desarrollado un conjunto de métodos numéricos y algoritmos que han demostrado ser eficientes, precisos y robustos y que nos han permitido investigar los modelos presentados en esta tesis en diferentes simulaciones fisiológicamente relevantes. Respecto al modelo mencionado arriba en particular, estos métodos ha permitido estudiar la angiogénesis en dominios de tamaño medio (aproximadamente cinco veces mayores que los utilizados hasta el momento) bajo diferentes distribuciones de células hipóxicas y capilares iniciales. La conclusión de estas simulaciones es que los patrones vasculares que predicen mantienen sus principales características a estas escalas.
- El modelo, que originalmente solo incluía quimiotaxis, fue extendido con una conceptualización de haptotaxis. Los resultados de este nuevo modelo indican que la haptotaxis puede tener un papel relevante en los patrones vasculares finales. A diferencia de las simulaciones que no incluyen haptotaxis, nuestros resultados revelan una complejidad y conectividad mayor

de los patrones vasculares, unas trayectorias más tortuosas de las células endoteliales estrelladas, un mayor número de eventos de anastomosis y unos capilares más cortos.

- El experimento *mouse corneal micropocket angiogenesis assay* es ampliamente utilizado y sus características proporcionan un entorno excepcional para calibrar, cuantificar y evaluar la capacidad de predicción de los modelos matemáticos de angiogénesis. Este experimento plantea, sin embargo, numerosos obstáculos numéricos y computacionales y, probablemente por esta razón, sólo se ha reproducido en dos dimensiones hasta la fecha.

- Los métodos numéricos y algoritmos desarrollados en esta tesis proporcionan un marco para llevar a cabo simulaciones en geometrías tridimensionales complejas, tal y como se requiere para la reproducción del experimento *mouse corneal micropocket angiogenesis assay*. En particular, el análisis isogeométrico ha permitido simular el modelo en un dominio computacional que es la geometría exacta de la córnea de un ratón c57BL/6 usando datos de la literatura.

- Las simulaciones tridimensionales del experimento *mouse corneal micropocket angiogenesis assay* sugieren que, para que los modelos matemáticos puedan replicar la complejidad topológica observada *in vivo*, las simulaciones bidimensionales pueden no ser suficientes.

- Las simulaciones en la córnea mostraron, incluso en ausencia de la conceptualización de la haptotaxis, el efecto conocido como *brush-border effect* en tres dimensiones. Además, revelaron que los cambios en la ubicación de la fuente de factor angiogénico conducen a diferentes patrones vasculares. Estas simulaciones también dieron a conocer un nuevo fenómeno que no estaba expresamente incorporado en el modelo, el cual se puede interpretar como regresión capilar.

- El modelo de angiogénesis que incluye crecimiento, regresión, y recrecimiento de capilares predice la plasticidad y la evolución dinámica de la angiogénesis en períodos de tiempo largos. En concreto, las simulaciones muestran similitudes cuantitativas con experimentos *in vivo* y capturan la regresión de los capilares inducida por la inhibición de los factores angiogénicos y su posterior recrecimiento tras la eliminación de la inhibición.

- La convección de los factores angiogénicos tumorales ha sido pasada por alto en el modelado matemático. Hemos demostrado, sin embargo, que tiene un impacto significativo en el desarrollo de patrones vasculares y que debe ser incorporada en los modelos para mejorar sus capacidades predictivas.

- Nuestras simulaciones numéricas predicen un aumento de la malignidad de

los tumores sólidos pequeños, ya que la convección aumenta su capacidad de inducir la angiogénesis. También demuestran que el efecto combinado de la convección de los factores angiogénicos y la alta presión intratumoral dificulta la infiltración de la vasculatura en el tumor.

Por último, concluimos que los modelos matemáticos y la simulación numérica de la angiogénesis inducida por tumores proporcionan una mayor comprensión de los mecanismos biológicos que rigen este complejo fenómeno y que pueden ser utilizados como una herramienta predictiva.

Futuras líneas de trabajo

Esta tesis ha abierto nuevas líneas de investigación, algunas de las cuales son el objetivo de nuestra trabajo actual. A continuación detallamos algunas de las que, en nuestra opinión, son más prometedoras.

Mecanotaxis: Interacción entre células endoteliales estrelladas En los primeros capítulos aumentamos un modelo que ya contaba con quimiotaxis con una conceptualización de la haptotaxis. El mecanismo restante, la mecanotaxis, se define como la migración de las células endoteliales estrelladas siguiendo señales inducidas por fuerzas mecánicas. Además, a través de la mecanotaxis las células endoteliales estrelladas se detectan e interactúan unas con otras. Por lo tanto, el siguiente paso lógico es incorporar la mecanotaxis en el modelo.

Análisis cuantitativo Durante el desarrollo de este trabajo, una de las mayores dificultades fue comparar cuantitativamente las simulaciones matemáticas con los experimentos reales. Sólo pudimos lograr comparaciones de este tipo en un número reducido de casos bidimensionales. Hemos detectado la falta de un método cuantitativo a partir del cual se puedan extraer las principales características de las redes vasculares, especialmente en tres dimensiones. Una de nuestras líneas de investigación en curso trata de paliar esta deficiencia mediante el uso de técnicas de *esqueletonización* y la teoría de grafos para caracterizar la nueva vasculatura. La mayor dificultad hasta ahora ha sido obtener y procesar las imágenes de los experimentos.

Regresión y remodelación vascular basada en flujo En el penúltimo capítulo de esta tesis hemos propuesto un modelo que incorpora regresión de vasos sanguíneos en función de los factores angiogénicos. Existe también otro tipo

de regresión, más relacionada con la remodelación vascular, que depende de la funcionalidad de un capilar entendida como su capacidad de transportar sangre. Actualmente estamos trabajando en un modelo que incorpora este tipo de regresión mediante el acoplamiento de las teorías presentadas en el penúltimo y en el último capítulo. Con este modelo se espera reproducir la regresión y la remodelación vascular basada tanto en el factor angiogénico como en el flujo sanguíneo.

Acoplamiento de la angiogénesis con un modelo de crecimiento tumoral
A lo largo de esta tesis se ha supuesto la existencia de un tumor estático que no crece, cuya única función consiste en liberar factor angiogénico tumoral. Esta suposición nos permitió centrarnos exclusivamente en el estudio de la angiogénesis. Sin embargo, para mejorar las capacidades predictivas del modelo, tenemos que tener en cuenta también la dinámica de crecimiento del tumor y la liberación de nutrientes por parte de los capilares. Hemos estado trabajando recientemente en una teoría de dos dimensiones que acopla angiogénesis y crecimiento tumoral a través de los nutrientes y ahora estamos generalizando a geometrías tridimensionales reales.

Appendix F

Extended summary in Galician

Introdución

Na actualidade, o cancro é a segunda maior causa das mortes que ocorren no mundo. O cancro empeza cunha única célula que acumulou unha serie de mutacións normalmente tras un longo período de tempo. Unha das principais características desta célula é a súa habilidade para crear copias de si mesma sen límites, producindo, na maioría dos casos, unha densa masa de células fillas que forman un tumor sólido. A proliferación das células cancerígenas e, por tanto, o crecemento do tumor, depende dos nutrientes e o osíxeno que lles fornecen os capilares que existían previamente no tecido. Esta subministración non é suficiente para manter a alta taxa de crecemento potencial dun tumor, que, como consecuencia, mantén un tamaño pequeno e entra nun estado de letargo; é dicir, é un tumor benigno. Nalgunhas ocasións, con todo, as células cancerígenas adquiren a habilidade de estimular o crecemento de novos vasos capilares cara elas. Este proceso chámase angiogénesis tumoral e a través del os tumores adquiren unha subministración constante de nutrientes e osíxeno. Por tanto, aqueles tumores capaces de estimular a angiogénesis vólvense malignos ao ser capaces de crecer sen límites. Os novos capilares proporciónanlles ademais acceso a todo o corpo a través do sistema circulatorio, facilitando a formación de metástases. Os tumores malignos poden crecer tanto como para afectar o correcto funcionamento do órgano no que se atopan e, finalmente, producir a morte do individuo.

A angiogénesis tumoral é un fenómeno complexo que describimos a continuación

brevemente.

As células cancerígenas que son capaces de inducir a angiogénesis liberan substancias químicas solubles coñecidas xenericamente como *factores angiogénicos tumorales*. Cando chegan ás células endoteliales que forman os vasos capilares algunhas delas adquiren un fenotipo migratorio e empezan a moverse cara á fonte de factor angiogénico. Estas células denomínanse células endoteliales estreladas debido a que desenvolven unhas protuberancias (filopodios) que lles dan forma de estrela. As células endoteliales adxacentes adquiren pola contra un fenotipo proliferativo e, a medida que se duplican, aumentan a lonxitude do capilar. As células endoteliales estreladas migran utilizando tres mecanismos diferentes: a quimiotaxis, a haptotaxis e a mecanotaxis. O primeiro está gobernado por substancias químicas solubles, o segundo por substancias químicas non solubles e puntos de adhesión focal e o terceiro por sinais mecánicos. O proceso de crecemento de novos vasos capilares continúa ata que as células endoteliales estreladas detectan outras células endoteliales próximas e fusiónanse con elas nun proceso denominado anastomose. Así se van xerando novas redes vasculares polos que pode circular o sangue e abastecer a demanda de nutrientes e osíxeno. Debido a que a demanda dos tumores aumenta co seu tamaño e a que os novos capilares son defectuosos, a angiogénesis tumoral continúa producíndose a medida que o tumor crece.

Hai unhas décadas, algúns científicos propuxeron que boquear a angiogénesis podería ser un tratamento efectivo contra o cancro. Esta terapia, denominada terapia antiangiogénica, mostrou resultados prometedores en ensaios preclínicos, pero non se trasladaron nos resultados esperados na clínica. Na actualidade, está a emerxer un novo paradigma na Medicina, o Medicina Preditiva, que se espera que cambie o campo da Oncoloxía e que pode proporcionar o enfoque adecuado para entender o problema das terapias antiangiogénicas. A Medicina Preditiva está baseada en modelos matemáticos e na computación e foi aplicada con éxito en varias áreas da Medicina. No campo da Oncoloxía non fixo máis que empezar, pero xa produciu resultados satisfactorios. Máis concretamente, na angiogénesis tumoral, numerosos investigadores expuxeron modelos matemáticos para abordar o problema das terapias antiangiogénicas, aínda que son necesarias melloras para lograr este obxectivo. A angiogénesis é un fenómeno complexo que involucra varias escalas e mecanismos, moitos dos cales aínda non están contemplados nestes modelos. Ademais, a maioría dos modelos simúlanse en xeometrías bidimensionais simples, mentres que a angiogénesis é un proceso tridimensional que ocorre en tecidos ou órganos con xeometrías non triviais.

Obxectivos

Nesta tese desenvolvemos modelos matemáticos de angiogénesis tumoral que inclúen mecanismos biolóxicos fundamentais e simulamos estes modelos en configuracións experimentais relevantes e en xeometrías tridimensionais específicas dun suxeito. Esta tese continúa a investigación desenvolvida no Grupo de Métodos Numéricos en Enxeñería (GMNI) da Universidade dá Coruña no campo da Mecánica Computacional e, en particular, é a primeira en explorar o subcampo da Biomecánica Computacional. Tamén é a primeira tese desenvolvida dentro do proxecto *Modeling and Simulation of Cancer Growth* (MuSIC), cuxo obxectivo é desenvolver modelos preditivos para o crecemento de cancro co obxectivo de cambiar a tradicional paradigma diagnóstico do tratamento de cancro cara a un preditivo e específico para cada paciente. O traballo desta tese tamén foi desenvolvido no *Institute for Computational Engineering and Sciences* (ICES) da *University Of Texas At Austin* durante unha estancia de investigación de catro meses de duración.

Os obxectivos desta tese pódense dividir nas seguintes tres categorías:

- **Modelización**: A finalidade é desenvolver novos modelos matemáticos de angiogénesis tumoral que inclúan mecanismos biolóxicos fundamentais, en concreto, a migración de células endoteliales estreladas por haptotaxis, a capacidade de regresión e recrecemiento dos capilares en función dos estímulos externos e a convección dos factores angiogénicos polo fluxo intersticial. Todos estes modelos inclúen variables continuas gobernadas por ecuacións diferenciais en derivadas parciais de alta orde, así como elementos discretos.

- **Simulación**: A maioría dos modelos matemáticos que se atopan na literatura son simulados en xeometrías bidimensionais simples. Estas configuracións facilitan o estudo dos devanditos modelos. Nesta tese realizaremos simulacións *in silico* dos modelos mencionados anteriormente utilizando xeometrías bidimensionais que tratan de replicar configuracións relevantes *in vivo*. Con todo, a angiogénesis é un proceso tridimensional que se desenvolve en tecidos con xeometrías complexas. Por tanto, o segundo obxectivo desta tese é ir un paso máis aló e realizar simulacións tridimensionais utilizando xeometrías reais que permitan comparar os resultados cos experimentais. En particular, a nosa meta é desenvolver simulacións de angiogénesis tumoral dun dos experimentos *in vivo* máis usados: o experimento denominado *mouse corneal micropocket angiogenesis assay*. Estas simulacións serán realizadas en tres dimensións utilizando xeometrías específicas de suxeitos e, ata onde saben os autores, permitirán por primeira vez a comparación entre unha simulación e un experimento en xeometrías reais.

- **Computacional**: O terceiro obxectivo é desenvolver algoritmos numéricos capaces de realizar de maneira eficiente as simulacións detalladas arriba. En primeiro lugar, necesitamos desenvolver un marco matemático no que se poidan integrar perfectamente os elementos discretos e as variables continúas do modelo. Tamén necesitamos utilizar unha tecnoloxía recentemente introducida, a análise isoxeométrica, capaz de manexar os termos de alta orde das ecuacións en derivadas parciais, tanto en dúas como en tres dimensións. Por último, os algoritmos teñen que ser robustos e ser capaces de executarse de maneira eficiente en paralelo.

Metodoloxía

A dinámica da angiogénesis tumoral e o seu impacto no crecemento do cancro permanecen como problemas fundamentais abertos na bioloxía do cancro. A Medicina Preditiva e, en particular a Oncoloxía Matemática, son campos que están en desenvolvemento e cuxo obxectivo é predicir e proporcionar unha maior comprensión destes problemas. Con este fin, neste documento propuxéronse tres novos modelos matemáticos para a angiogénesis tumoral que se simularon en dúas e tres dimensións, tanto en xeometrías simples como complexas.

Os tres modelos propostos comparten unha serie de características comúns desde o punto de vista numérico. Por tanto, para lograr os nosos obxectivos de modelado e simulación, desenvolvemos en primeiro lugar algoritmos numéricos adecuados. Os tres modelos son híbridos, é dicir, involucran elementos discretos gobernados por unha serie de regras discretas e variables continuas gobernadas por ecuacións en derivadas parciais. Ambos deben ser acoplados de maneira robusta e eficiente. Ademais, a avaliación das regras discretas implica avaliar as variables continuas en determinados puntos. Destes puntos só se coñecen as súas coordenadas físicas, mentres que as paramétricas, que son as necesarias para avaliar as variables continuas, descoñécense. En xeometrías simples con mapeos lineais as coordenadas paramétricas pódense obter de maneira directa. Con todo, en xeometrías complexas é necesario desenvolver un algoritmo adecuado para obtelas. Por último, os tres modelos basean a súa definición dos capilares na teoría de campo de fase a cal involucra ecuacións diferenciais en derivadas parciais de alta orde. O método numérico ten que ser capaz de lidar con estes termos para achar unha solución ás ecuacións.

O primeiro paso para desenvolver o método numérico é describir os modelos nun marco matemático coherente. Desta maneira podemos formular o acoplamento entre os elementos discretos e as variables continuas para permitir un tratamento numérico eficiente do problema xunto. Esta formulación está baseada nuns padróns

predefinidos que utilizan a solución á ecuación de campo de fase de Cahn-Hilliard nunha dimensión nun dominio infinito. Ademais, desenvolvemos un método para atopar as coordenadas paramétricas a partir das coordenadas físicas coñecidas dos puntos nos que se avalían as regras discretas. Este método funciona en xeometrías tridimensionais complexas, que inclúen mapeos non lineais. Está fundamentado no método de Newton-Raphson e é capaz de traballar con cálculos paralelos. Para a resolución das ecuacións en derivadas parciais de orde superior involucradas na formulación dos modelos utilizouse a análise isoxeométrico, que non só ofrece precisión e solidez senón tamén a flexibilidade xeométrica o que necesitamos para levar a cabo simulacións en xeometrías reais. Tamén utilizamos o método α-xeneralizado e un esquema de tempo adaptativo que aumenta da eficiencia dos nosos cálculos. Por último, todos estes métodos foron adaptados para funcionar en paralelo usando unha técnica *multi-patch*.

O primeiro modelo matemático que propoñemos nesta tese parte dun previo que consideraba a quimiotaxis como mecanismo de migración celular. A este modelo engadímoslle unha conceptualización para a *haptotaxis* utilizando camiños aleatorios circulares nesgados. Este modelo estudouse primeiro en configuracións bidimensionaies con xeometrías simples para adquirir unha maior comprensión das ecuacións de goberno e que nos permitiron avaliar o papel da haptotaxis na angiogénesis tumoral. O obxectivo final era con todo reproducir un experimento en tres dimensións usando dunha xeometría real. Con este fin, evolucionamos a configuración inicial para representar primeiro xeometrías bidimensionais máis grandes e despois xeometrías tridimensionais. Nelas realizamos diferentes análises variando a disposición dos capilares iniciais e dos tumores, imitando configuracións fisiológicas e experimentais. Estas simulacións culminaron no desenvolvemento de simulacións da angiogénesis tumoral que reproducen o experimento *in vivo* coñecido como *mouse corneal micropocket angiogenesis assay*. Nestas simulacións utilizamos a xeometría tridimensional, específica dun suxeito (a córnea dun rato c57BL/6) con máis de $28,9$ millóns de graos de liberdade. Ata onde saben os autores, esta simulación permite por primeira vez a comparación entre un experimento *in silico* dun *in vivo* nunha xeometría tridimensional real.

O segundo modelo céntrase na dinámica a longo prazo da angiogénesis tumoral, é dicir, sobre os fenómenos de regresión e recrecemiento que se producen despois do primeiro crecemento dos vasos sanguíneos. A formulación deste modelo inclúe unha ecuación non conservada de campo de fase (Allen-Cahn) cuxa enerxía depende do factor angiogénico tumoral. Ademais, incorporamos unha conceptualización dos filopodios que favorece a detección de células endoteliales próximas e por tanto a anastomose. O modelo simulouse tanto nunha réplica bidimensional do ensaio *mouse corneal micropocket angiogenesis assay* como nunha reprodución dun experimento *in vivo* co que se comparou cuantitativamente.

Por último, desenvolvemos unha teoría para o fluxo sanguíneo e intersticial na escala de tecidos que acoplamos co modelo para a angiogénesis tumoral. A característica principal do modelo de fluxo é que é unha teoría completamente continua que inclúe o fluxo nos capilares, a través da parede vascular e no intersticio. O modelo de fluxo está acoplado ao de angiogénesis a través da convección dos factores angiogénicos. Os resultados das simulacións mostran como o fluxo altera os patróns vasculares inducidos polo tumor a través desta convección.

Conclusións

As seguintes conclusións foron extraídas do traballo presentado nesta tese:

- O modelo de Travasso *et al.* (2011b) presentado no segundo capítulo mostrou un potencial significativo na predición do crecemento de capilares inducidos por tumores en simulacións a pequena escala. Utilizando este modelo predixemos a formación de diferentes patróns vasculares en función da proliferación e a quimiotaxis.
- Desenvolvemos un conxunto de métodos numéricos e algoritmos que demostraron ser eficientes, precisos e robustos e que nos permitiron investigar os modelos presentados nesta tese en diferentes simulacións fisiológicamente relevantes. Respecto ao modelo mencionado arriba en particular, estes métodos permitiu estudar a angiogénesis en dominios de tamaño medio (aproximadamente cinco veces maiores que os utilizados ata o momento) baixo diferentes distribucións de células hipóxicas e capilares iniciais. A conclusión destas simulacións é que os patróns vasculares que predín manteñen as súas principais características a estas escalas.
- O modelo, que orixinalmente só incluía quimiotaxis, foi estendido cunha conceptualización de haptotaxis. Os resultados deste novo modelo indican que a haptotaxis pode ter un papel relevante nos patróns vasculares finais. A diferenza das simulacións que non inclúen haptotaxis, os nosos resultados revelan unha complexidade e conectividade maior dos patróns vasculares, unhas traxectorias máis tortuosas das células endoteliales estreladas, un maior número de eventos de anastomoses e uns capilares máis curtos.
- O experimento *mouse corneal micropocket angiogenesis assay* é amplamente utilizado e as súas características proporcionan unha contorna excepcional para calibrar, cuantificar e avaliar a capacidade de predición dos modelos matemáticos de angiogénesis. Este experimento expón, con todo, numerosos obstáculos numéricos e computacionales e, probablemente por esta razón, só se reproduciu en dúas dimensións ata a data.

- Os métodos numéricos e algoritmos desenvolvidos nesta tese proporcionan un marco para levar a cabo simulacións en xeometrías tridimensionais complexas, tal e como se require para a reprodución do experimento *mouse corneal micropocket angiogenesis assay*. En particular, a análise isoxeométrico permitiu simular o modelo nun dominio computacional que é a xeometría exacta da córnea dun rato c57BL/6 usando datos da literatura.

- As simulacións tridimensionais do experimento *mouse corneal micropocket angiogenesis assay* suxiren que, para que os modelos matemáticos poidan replicar a complexidade topolóxica observada *in vivo*, as simulacións bidimensionais poden non ser suficientes.

- As simulacións na córnea mostraron, mesmo en ausencia da conceptualización da haptotaxis, o efecto coñecido como *brush-border effect* en tres dimensións. Ademais, revelaron que os cambios na localización da fonte de factor angiogénico conducen a diferentes patróns vasculares. Estas simulacións tamén deron a coñecer un novo fenómeno que non estaba expresamente incorporado no modelo, o cal se pode interpretar como regresión capilar.

- O modelo de angiogénesis que inclúe crecemento, regresión, e recrecemiento de capilares predín a plasticidade e a evolución dinámica da angiogénesis en períodos de tempo longos. En concreto, as simulacións mostran similitudes cuantitativas con experimentos *in vivo* e capturan a regresión dos capilares inducida pola inhibición dos factores angiogénicos e o seu posterior recrecemiento tras a eliminación da inhibición.

- A convección dos factores angiogénicos tumorales foi pasada por alto no modelado matemático. Demostramos, con todo, que ten un impacto significativo no desenvolvemento de patróns vasculares e que debe ser incorporada nos modelos para mellorar as súas capacidades preditivas.

- Nosas simulacións numéricas predín un aumento da malignidade dos tumores sólidos pequenos, xa que a convección aumenta a súa capacidade de inducir a angiogénesis. Tamén demostran que o efecto combinado da convección dos factores angiogénicos e a alta presión intratumoral dificulta a infiltración da vasculatura no tumor.

Por último, concluímos que os modelos matemáticos e a simulación numérica da angiogénesis inducida por tumores proporcionan unha maior comprensión dos mecanismos biolóxicos que rexen este complexo fenómeno e que poden ser utilizados como unha ferramenta preditiva.

Futuras liñas de traballo

Esta tese abriu novas liñas de investigación, algunhas das cales son o obxectivo de nosa traballo actual. A continuación detallamos algunhas das que, na nosa opinión, son máis prometedoras.

Mecanotaxis: Interacción entre células endoteliales estreladas Nos primeiros capítulos aumentamos un modelo que xa contaba con quimiotaxis cunha conceptualización da haptotaxis. O mecanismo restante, a mecanotaxis, defínese como a migración das células endoteliales estreladas seguindo sinais inducidos por forzas mecánicas. Ademais, a través da mecanotaxis as células endoteliales estreladas detéctanse e interactúan unhas con outras. Por tanto, o seguinte paso lóxico é incorporar a mecanotaxis no modelo.

Análise cuantitativa Durante o desenvolvemento deste traballo, unha das maiores dificultades foi comparar cuantitativamente as simulacións matemáticas cos experimentos reais. Só puidemos lograr comparacións deste tipo nun número reducido de casos bidimensionais. Detectamos a falta dun método cuantitativo a partir do cal se poidan extraer as principais características das redes vasculares, especialmente en tres dimensións. Unha das nosas liñas de investigación en curso trata de paliar esta deficiencia mediante o uso de técnicas de *esqueletonización* e a teoría de grafos para caracterizar a nova vasculatura. A maior dificultade ata agora foi obter e procesar as imaxes dos experimentos.

Regresión e remodelación vascular baseada en fluxo No penúltimo capítulo desta tese propuxemos un modelo que incorpora regresión de vasos sanguíneos en función dos factores angiogénicos. Existe tamén outro tipo de regresión, máis relacionada coa remodelación vascular, que depende da funcionalidade dun capilar entendida como a súa capacidade de transportar sangue. Actualmente estamos a traballar nun modelo que incorpora este tipo de regresión mediante o acoplamento das teorías presentadas no penúltimo e no último capítulo. Con este modelo espérase reproducir a regresión e a remodelación vascular baseada tanto no factor angiogénico como no fluxo sanguíneo.

Acoplamento da angiogénesis cun modelo de crecemento tumoral Ao longo desta tese supúxose a existencia dun tumor estático que non crece, cuxa única función consiste en liberar factor angiogénico tumoral. Esta suposición permitiunos centrarnos exclusivamente no estudo da angiogénesis. Con todo, para

mellorar as capacidades preditivas do modelo, temos que ter en conta tamén a dinámica de crecemento do tumor e a liberación de nutrientes por parte dos capilares. Traballamos recentemente nunha teoría de dúas dimensións que acopla angiogénesis e crecemento tumoral a través dos nutrientes e agora estamos a xeneralizar a xeometrías tridimensionais reais.

F · Extended summary in Galician

Bibliography

Adam, J.A. 1986. A simplified mathematical model of tumor growth. *Mathematical Biosciences*, vol. 81(2), pp. 229–244. ↑30

Adam, J.A. 1987a. A mathematical model of tumor growth. II. Effects of geometry and spatial uniformity on stability. *Mathematical Biosciences*, vol. 86(2), pp. 183–211. ↑30

Adam, J.A. 1987b. A mathematical model of tumor growth. III. Comparison with experiment. *Mathematical Biosciences*, vol. 86(2), pp. 213–227. ↑30

Adam, J.A. and Maggelakis, S.A. 1989. Mathematical models of tumor growth. IV. Effects of a necrotic core. *Mathematical Biosciences*, vol. 97(1), pp. 121–136. ↑30

Adam, J.A. and Maggelakis, S.A. 1990. Diffusion regulated characteristics of a spherical prevascular carcinoma. *Bulletin of Mathematical Biology*, vol. 52(4), pp. 549–582. ↑30

Addison-Smith, B., McElwain, D.L.S., and Maini, P.K. 2008. A simple mechanistic model of sprout spacing in tumour-associated angiogenesis. *Journal of Theoretical Biology*, vol. 250(1), pp. 1 – 15. ↑34

Ahrens, J., Geveci, B., and Law, C. 2005. *Visualization Handbook*, chapter ParaView: An End-User Tool for Large Data Visualization. Elsevier. ISBN 978-0123875822. ↑67

Akkerman, I., Bazilevs, Y., Kees, C.E., and Farthing, M.W. 2011. Isogeometric analysis of free-surface flow. *Journal of Computational Physics*, vol. 230(11), pp. 4137–4152. ↑40

Alarcón, T., Byrne, H.M., and Maini, P.K. 2003. A cellular automaton model for tumour growth in inhomogeneous environment. *Journal of Theoretical Biology*, vol. 225(2), pp. 257–274. ↑38

Alberts, B., Johnson, A., Lewis, J., Raff, M., Roberts, K., and Walter, P. 2007. *Molecular biology of the cell*. Garland Science. ISBN 0-8153-3218-1. ↑10 , ↑13 , ↑17 , ↑20

American Asociation for Cancer Research 2015. AACR Cancer Progress Report 2015. *Clinical Cancer Research*, vol. 21(Supplement I), pp. SI–S128. ↑5

Ames, B.N., Gold, L.S., and Willettt, W.C. 1995. The causes and prevention of cancer. *Proceedings of the National Academy of Sciences*, vol. 92(12), pp. 5258–5265. ↑5

Anderson, A.R.A. 2005. A hybrid mathematical model of solid tumour invasion: the importance of cell adhesion. *Mathematical Medicine and Biology*, vol. 22(2), pp. 163–186. ↑31 , ↑38

Anderson, A.R.A. and Chaplain, M.A.J. 1998a. Continuous and discrete mathematical models of tumor-induced angiogenesis. *Bulletin of Mathematical Biology*, vol. 60(5), pp. 857–899. ↑32 , ↑35 , ↑36 , ↑38

Anderson, A.R.A. and Chaplain, M.A.J. 1998b. A mathematical model for capillary network formation in the absence of endothelial cell proliferation. *Applied Mathematics Letters*, vol. 11(3), pp. 109–114. ↑32

Anderson, A.R.A., Chaplain, M.A.J., García-Reimbert, C., and Vargas, C.A. 2000. A gradient-driven mathematical model of antiangiogenesis. *Mathematical and Computer Modelling*, vol. 32(10), pp. 1141–1152. ↑32

Anijeet, D.R., Zheng, Y., Tey, A., Hodson, M., Sueke, H., and Kaye, S.B. 2012. Imaging and evaluation of corneal vascularization using fluorescein and indocyanine green angiography. *Investigative Ophthalmology & Visual Science*, vol. 53(2), p. 650. ↑105

Araujo, R.P. and McElwain, D.L.S. 2004. A history of the study of solid tumour growth: The contribution of mathematical modelling. *Bulletin of Mathematical Biology*, vol. 66(5), pp. 1039–1091. ↑28

Arroyo, M. and Ortiz, M. 2006. Local maximum-entropy approximation schemes: A seamless bridge between finite elements and meshfree methods. *International Journal for Numerical Methods in Engineering*, vol. 65(13), pp. 2167–2202. ↑39

Auricchio, F., Beirão da Veiga, L., Buffa, A., Lovadina, C., Reali, A., and Sangalli, G. 2007. A fully "locking-free" isogeometric approach for plane linear elasticity problems: A stream function formulation. *Computer Methods in Applied Mechanics and Engineering*, vol. 197(1-4), pp. 160–172. ↑44

Auricchio, F., Beirão da Veiga, L., Hughes, T.J.R., Reali, A., and Sangalli, G. 2010. Isogeometric collocation methods. *Mathematical Models and Methods in Applied Sciences*, vol. 20(11), pp. 2075–2107. ↑40

Auricchio, F., Beirão da Veiga, L., Hughes, T.J.R., Reali, A., and Sangalli, G. 2012. Isogeometric collocation for elastostatics and explicit dynamics. *Computer Methods in Applied Mechanics and Engineering*, vol. 249-252, pp. 2–14. ↑40

Auricchio, F., Conti, M., Ferraro, M., Morganti, S., Reali, A., and Taylor, R.L. 2015. Innovative and efficient stent flexibility simulations based on isogeometric analysis. *Computer Methods in Applied Mechanics and Engineering*, vol. 295, pp. 347–361. ↑40

Baffert, F., Le, T., Sennino, B., Thurston, G., Kuo, C.J., Hu-Lowe, D., and McDonald, D.M. 2006. Cellular changes in normal blood capillaries undergoing regression after inhibition of VEGF signaling. *American Journal of Physiology - Heart and Circulatory Physiology*, vol. 290(2), pp. H547–H559. ↑134

Balding, D. and McElwain, D.L.S. 1985. A mathematical model of tumour-induced capillary growth. *Journal of Theoretical Biology*, vol. 114(1), pp. 53–73. ↑31

Baluk, P., Hashizume, H., and McDonald, D.M. 2005. Cellular abnormalities of blood vessels as targets in cancer. *Current Opinion in Genetics & Development*, vol. 15(1), pp. 102–111. ↑25

Bartha, K. and Rieger, H. 2006. Vascular network remodeling via vessel cooption, regression and growth in tumors. *Journal of Theoretical Biology*, vol. 241(4), pp. 903–918. ↑38

Bauer, A.L., Jackson, T.L., and Jiang, Y. 2007. A cell-based model exhibiting branching and anastomosis during tumor-induced angiogenesis. *Biophysical Journal*, vol. 92(9), pp. 3105–3121. ↑36

Bauer, A.L., Jackson, T.L., and Jiang, Y. 2009. Topography of extracellular matrix mediates vascular morphogenesis and migration speeds in angiogenesis. *PLoS Computational Biology*, vol. 5(7), p. e1000445. ↑36

Baxter, L.T. and Jain, R.K. 1989. Transport of fluid and macromolecules in tumors I. Role of interstitial pressure and convection. *Microvascular Research*, vol. 37(1), pp. 77–104. ↑38 , ↑166

Baxter, L.T. and Jain, R.K. 1990. Transport of fluid and macromolecules in tumors II. Role of heterogeneous perfusion and lymphatics. *Microvascular Research*, vol. 4(2), pp. 246–263. ↑38

Baxter, L.T. and Jain, R.K. 1991a. Transport of fluid and macromolecules in tumors III. Role of binding and metabolism. *Microvascular Research*, vol. 41(1), pp. 5–23. ↑38

Baxter, L.T. and Jain, R.K. 1991b. Transport of fluid and macromolecules in tumors IV. A microscopic model of the perivascular distribution. *Microvascular Research*, vol. 41(2), pp. 252–272. ↑38

Bazilevs, Y., Calo, V.M., Cottrell, J.A., Hughes, T.J.R., Reali, A., and Scovazzi, G. 2007. Variational multiscale residual-based turbulence modeling for large eddy simulation of incompressible flows. *Computer Methods in Applied Mechanics and Engineering*, vol. 197(1-4), pp. 173–201. ↑40

Bazilevs, Y., Calo, V.M., Hughes, T.J.R., and Zhang, Y. 2008. Isogeometric fluid-

structure interaction: Theory, algorithms, and computations. *Computational Mechanics*, vol. 43(1), pp. 3–37. ↑40

Bazilevs, Y., Calo, V.M., Zhang, Y., and Hughes, T.J.R. 2006. Isogeometric fluid–structure interaction analysis with applications to arterial blood flow. *Computational Mechanics*, vol. 38(4-5), pp. 310–322. ↑40 , ↑62

Bazilevs, Y., Michler, C., Calo, V.M., and Hughes, T.J.R. 2010. Isogeometric variational multiscale modeling of wall-bounded turbulent flows with weakly enforced boundary conditions on unstretched meshes. *Computer Methods in Applied Mechanics and Engineering*, vol. 199(13-16), pp. 780–790. ↑39 , ↑62

Benson, D.J., Bazilevs, Y., Hsu, M.C., and Hughes, T.J.R. 2010. Isogeometric shell analysis: The Reissner–Mindlin shell. *Computer Methods in Applied Mechanics and Engineering*, vol. 199(5-8), pp. 276–289. ↑40

Bentley, K., Mariggi, G., Gerhardt, H., and Bates, P.A. 2009. Tipping the balance: Robustness of tip cell selection, migration and fusion in angiogenesis. *PLoS Computational Biology*, vol. 5(10), p. e1000549. ↑34 , ↑35

Bergers, G. and Benjamin, L.E. 2003. Tumorigenesis and the angiogenic switch. *Nature Reviews Cancer*, vol. 3(6), pp. 401–410. ↑7 , ↑12

Birsner, A.E., Benny, O., and D'Amato, R.J. 2014. The corneal micropocket assay: A model of angiogenesis in the mouse eye. *Journal of Visualized Experiments: JoVE*, (90), pp. e51375–e51375. ↑105 , ↑106

Bock, K.D., Georgiadou, M., and Carmeliet, P. 2013. Role of endothelial cell metabolism in vessel sprouting. *Cell Metabolism*, vol. 18(5), pp. 634 – 647. ↑27

Boon, R.A. and Dimmeler, S. 2015. MicroRNAs in myocardial infarction. *Nature Reviews Cardiology*, vol. 12(3), pp. 135–142. ↑27

Boondirek, A., Triampo, W., and Nuttavut, N. 2010. A review of cellular automata models of tumor growth. In *International Mathematical Forum*, vol. 5, pp. 3023–3029. ↑31

Breward, C.J.W., Byrne, H.M., and Lewis, C.E. 2004. A multiphase model describing vascular tumour growth. *Bulletin of Mathematical Biology*, vol. 65(4), pp. 609–640. ↑38

Brooks, A.N. and Hughes, T.J.R. 1982. Streamline upwind/Petrov-Galerkin formulations for convection dominated flows with particular emphasis on the incompressible Navier-Stokes equations. *Computer Methods in Applied Mechanics and Engineering*, vol. 32(1-3), pp. 199 – 259. ↑164

Bueno, J., Bona-Casas, C., Bazilevs, Y., and Gomez, H. 2015. Interaction of complex fluids and solids: theory, algorithms and application to phase-change-driven implosion. *Computational Mechanics*, vol. 55(6), pp. 1105–1118. ↑40

Bueno, J., Starodumov, I., Gomez, H., Galenko, P., and Alexandrov, D. 2016. Three dimensional structures predicted by the modified phase field crystal equation. *Computational Materials Science*, vol. 111, pp. 310 – 312. ↑40

Buffa, A., Sangalli, G., and Vázquez, R. 2010. Isogeometric analysis in electromagnetics: B-splines approximation. *Computer Methods in Applied Mechanics and Engineering*, vol. 199(17-20), pp. 1143–1152. ↑40

Burri, P.H., Hlushchuk, R., and Djonov, V. 2004. Intussusceptive angiogenesis: its emergence, its characteristics, and its significance. *Developmental Dynamics*, vol. 231(3), pp. 474–488. ↑20

Burton, A.C. 1966. Rate of growth of solid tumours as a problem of diffusion. *Growth*, vol. 30(2), pp. 157–176. ↑30

Byrne, H.M. 1999. A weakly nonlinear analysis of a model of avascular solid tumour growth. *Journal of Mathematical Biology*, vol. 39(1), pp. 59–89. ↑30

Byrne, H.M. and Chaplain, M.A.J. 1995. Mathematical models for tumour angiogenesis: Numerical simulations and nonlinear wave solutions. *Bulletin of Mathematical Biology*, vol. 57(3), pp. 461–486. ↑31 , ↑33

Byrne, H.M. and Chaplain, M.A.J. 1996. Explicit solutions of a simplified model of capillary sprout growth during tumor angiogenesis. *Applied Mathematics Letters*, vol. 9(1), pp. 69–74. ↑31

Byrne, H.M. and Chaplain, M.A.J. 1997. Free boundary value problems associated with the growth and development of multicellular spheroids. *European Journal of Applied Mathematics*, vol. 8(6), pp. 639–658. ↑30

Byrne, H.M., King, J.R., McElwain, D.L.S., and Preziosi, L. 2003. A two-phase model of solid tumour growth. *Applied Mathematics Letters*, vol. 16(4), pp. 567–573. ↑31

Byrne, H.M. and Preziosi, L. 2003. Modelling solid tumour growth using the theory of mixtures. *Mathematical Medicine and Biology*, vol. 20(4), pp. 341–366. ↑31

Cai, Y., Wu, J., Xu, S., Long, Q., and Yao, W. 2011. Numerical simulation of inhibiting effects on solid tumour cells in anti-angiogenic therapy: application of coupled mathematical model of angiogenesis with tumour growth. *Applied Mathematics and Mechanics - English Edition*, vol. 32(10), pp. 1287–1296. ↑38 , ↑166

Camidge, D.R. and Jodrell, D.I. 2005. *Introduction to the Cellular and Molecular Biology of Cancer*, chapter Chemotherapy, pp. 399–413. Oxford University Press Inc. ISBN 019852563X. ↑16

Campelo, F. and Hernández-Machado, A. 2006. Dynamic model and stationary shapes of fluid vesicles. *European Physical Journal E*, vol. 20(1), pp. 37–45. ↑49

Cancer Research UK 2015. URL `http://www.cancerresearchuk.org/`. ↑10 , ↑203

Cao, R., Brakenhielm, E., Pawliuk, R., Wariaro, D., Post, M.J., Wahlberg, E., Leboulch, P., and Cao, Y. 2003. Angiogenic synergism, vascular stability and improvement of hind-limb ischemia by a combination of PDGF-BB and FGF-2. *Nature Medicine*, vol. 9(5), pp. 604–613. ↑124 , ↑125

Cao, R., Lim, S., Ji, H., Zhang, Y., Yang, Y., Honek, J., Hedlund, E.M., and Cao, Y. 2011. Mouse corneal lymphangiogenesis model. *Nature Protocols*, vol. 6(6), pp. 817–826. ↑104

Capasso, V. and Morale, D. 2009. Stochastic modelling of tumour-induced angiogenesis. *Journal of Mathematical Biology*, vol. 58(1-2), pp. 219–233. ↑34

Carlier, A., Geris, L., Bentley, K., Carmeliet, G., Carmeliet, P., and Van Oosterwyck, H. 2012. MOSAIC: A multiscale model of osteogenesis and sprouting angiogenesis with lateral inhibition of endothelial cells. *PLoS Computational Biology*, vol. 8(10), p. e1002724. ↑37

Carmeliet, P. 2005. Angiogenesis in life, disease and medicine. *Nature*, vol. 438(7070), pp. 932–936. ↑19

Carmeliet, P. and Jain, R.K. 2000. Angiogenesis in cancer and other diseases. *Nature*, vol. 407(6801), pp. 249–257. ↑19 , ↑134

Carmeliet, P. and Jain, R.K. 2011. Molecular mechanisms and clinical applications of angiogenesis. *Nature*, vol. 473(7347), pp. 298–307. ↑21 , ↑22 , ↑203

Casquero, H., Bona-Casas, C., and Gomez, H. 2015a. A NURBS-based immersed methodology for fluid-structure interaction. *Computer Methods in Applied Mechanics and Engineering*, vol. 284, pp. 943–970. ↑40

Casquero, H., Lei, L., Bona-Casas, C., Zhang, J., and Gomez, H. 2015b. A hybrid variational-collocation immersed method for fluid-structure interaction using unstructured T-splines. *International Journal for Numerical Methods in Engineering*, vol. 105(11), pp. 855–880. ↑39

Casquero, H., Lei, L., Zhang, J., Reali, A., and Gomez, H. 2016. Isogeometric collocation using analysis-suitable T-splines of arbitrary degree. *Computer Methods in Applied Mechanics and Engineering*, vol. 301, pp. 164–186. ↑40

Cattaneo, L. and Zunino, P. 2014. Computational models for fluid exchange between microcirculation and tissue interstitium. *Networks and Heterogeneous Media*, vol. 9(1), pp. 135–159. ↑158

Chaplain, M.A.J. 1996. Avascular growth, angiogenesis and vascular growth in solid tumours: The mathematical modelling of the stages of tumour development. *Mathematical and Computer Modelling*, vol. 23(6), pp. 47–87. ↑28

Chaplain, M.A.J. 2000. Mathematical modelling of angiogenesis. *Journal of Neuro-Oncology*, vol. 50(1-2), pp. 37–51. ↑36

Chaplain, M.A.J. and Anderson, A.R.A. 1996. Mathematical modelling, simulation and prediction of tumour-induced angiogenesis. *Invasion Metastasis*, vol. 16(4-5), pp. 222–234. ↑36

Chaplain, M.A.J. and Anderson, A.R.A. 1999. *On Growth and Form: Spatio-Temporal Pattern Formation in Biology*, chapter Modeling the growth and form of capillary networks., pp. 225–249. Wiley. ↑32

Chaplain, M.A.J. and Anderson, A.R.A. 2006. Mathematical modeling of tumor-induced angiogenesis. *Annual Review of Biomedical Engineering*, vol. 8, pp. 233–257. ↑28

Chaplain, M.A.J. and Britton, N. 1993. On the concentration profile of a growth inhibitory factor in multicell spheroids. *Mathematical Biosciences*, vol. 115(2), pp. 233–243. ↑30

Chaplain, M.A.J., Giles, S.M., Sleeman, B.D., and Jarvis, R.J. 1995. A mathematical analysis of a model for tumour angiogenesis. *Journal of Mathematical Biology*, vol. 33(7), pp. 744–770. ↑32

Chaplain, M.A.J. and Orme, M.E. 1998. *Vascular Morphogenesis: In vivo, in vitro, in mente*, chapter Mathematical modeling of tumor-induced angiogenesis, pp. 205–240. Birkhauser Boston. ↑32

Chaplain, M.A.J. and Stuart, A.M. 1993. A model mechanism for the chemotactic response of endothelial cells to tumour angiogenesis factor. *IMA Journal of Mathematics Applied in Medicine and Biology*, vol. 10(3), pp. 149–168. ↑31

Chauviere, A.H., Hatzikirou, H., Lowengrub, J.S., Frieboes, H.B., Thompson, A.M., and Cristini, V. 2010. Mathematical oncology: How are the mathematical and physical sciences contributing to the war on breast cancer? *Current Breast Cancer Reports*, vol. 2(3), pp. 121–129. ↑7

Chen, L.Q. 2002. Phase-field models for microstructure evolution. *Annual Review of Materials Science*, vol. 32, pp. 113–140. ↑49

Chung, J. and Hulbert, G.M. 1993. A time integration algorithm for structural dynamics with improved numerical dissipation: The generalized-α method. *Journal of Applied Mechanics*, vol. 60, pp. 371–375. ↑61 , ↑91 , ↑141

Codling, E.A., Plank, M.J., and Benhamou, S. 2008. Random walk models in biology. *Journal of The Royal Society Interface*, vol. 5(25), pp. 813–834. ↑34

Collier, N., Dalcin, L., and Calo, V.M. 2013. PetIGA: High-performance isogeometric analysis. URL `https://bitbucket.org/dalcinl/petiga`. ↑40

Collin, A., Sangalli, G., and Takacs, T. 2015. Approximation properties of multi-patch C^1 isogeometric spaces. *ArXiv e-prints*. ↑115

Conrad, T.J., Chandler, D.B., Corless, J.M., and Klintworth, G.K. 1994. In vivo measurement of corneal angiogenesis with video data acquisition and computerized image analysis. *Laboratory investigation; a journal of technical methods and pathology*, vol. 70(3), pp. 426–434. ↑105

Cottrell, J.A., Hughes, T.J.R., and Bazilevs, Y. 2009. *Isogeometric analysis: Toward integration of CAD and FEA*. Wiley. ISBN 9786612259470. ↑141

Cottrell, J.A., Reali, A., Bazilevs, Y., and Hughes, T.J.R. 2006. Isogeometric analysis of structural vibrations. *Computer Methods in Applied Mechanics and Engineering*, vol. 195(41-43), pp. 5257–5296. ↑40

Criado, R., del Amo, A.G., Hernández-Bermejo, B., and Romance, M. 2006. New results on computable efficiency and its stability for complex networks. *Journal of Computational and Applied Mathematics*, vol. 192(1), pp. 59 – 74. ↑96

Cristini, V., Li, X., Lowengrub, J.S., and Wise, S.M. 2009. Nonlinear simulations of solid tumor growth using a mixture model: Invasion and branching. *Journal of Mathematical Biology*, vol. 58(4-5), pp. 723–763. ↑31 , ↑49

Cristini, V., Lowengrub, J.S., and Nie, Q. 2003. Nonlinear simulation of tumor growth. *Journal of Mathematical Biology*, vol. 46(3), pp. 191–224. ↑38

Cueto-Felgueroso, L. and Juanes, R. 2009. A phase field model of unsaturated flow. *Water Resources Research*, vol. 45(10), p. W10409. ↑49

Cyron, C.J., Arroyo, M., and Ortiz, M. 2009. Smooth, second order, non-negative meshfree approximants selected by maximum entropy. *International Journal for Numerical Methods in Engineering*, vol. 79(13), pp. 1605–1632. ↑39

Das, A., Lauffenburger, D., Asada, H., and Kamm, R.D. 2010. A hybrid continuum-discrete modelling approach to predict and control angiogenesis: Analysis of

combinatorial growth factor and matrix effects on vessel-sprouting morphology. *Philosophical Transactions of the Royal Society A: Mathematical, Physical and Engineering Sciences*, vol. 368(1921), pp. 2937–2960. ↑34

de Falco, C., Reali, A., and Vázquez, R. 2011. GeoPDEs: A research tool for isogeometric analysis of PDEs. *Advances in Engineering Software*, vol. 42(12), pp. 1020–1034. ↑40

De Lorenzis, L., Temizer, I., Wriggers, P., and Zavarise, G. 2011. A large deformation frictional contact formulation using NURBS-based isogeometric analysis. *International Journal for Numerical Methods in Engineering*, vol. 87(13), pp. 1278–1300. ↑40

De Smet, F., Segura, I., De Bock, K., Hohensinner, P.J., and Carmeliet, P. 2009. Mechanisms of vessel branching: Filopodia on endothelial tip cells lead the way. *Arteriosclerosis, Thrombosis, and Vascular Biology*, vol. 29(5), pp. 639–649. ↑138 , ↑140

Deakin, A. 1976. Model for initial vascular patterns in melanoma transplants. *Growth*, vol. 40(2), pp. 191–201. ↑31

DeNardo, D.G., Andreu, P., and Coussens, L.M. 2010. Interactions between lymphocytes and myeloid cells regulate pro- versus anti-tumor immunity. *Cancer and Metastasis Reviews*, vol. 29(2), pp. 309–316. ↑195

Dhote, R.P., Gomez, H., Melnik, R.N.V., and Zu, J. 2014. Isogeometric analysis of a dynamic thermo-mechanical phase-field model applied to shape memory alloys. *Computational Mechanics*, vol. 53(6), pp. 1235–1250. ↑40

Dhote, R.P., Gomez, H., Melnik, R.N.V., and Zu, J. 2015. 3D coupled thermo-mechanical phase-field modeling of shape memory alloy dynamics via isogeometric analysis. *Computers & Structures*, vol. 154, pp. 48 – 58. ↑40

Dias Soares Quinas Guerra, M.M. and Travasso, R.D.M. 2012. Novel approach to vascular network modeling in 3D. In *Bioengineering (ENBENG), 2012 IEEE 2nd Portuguese Meeting in*, pp. 1–6. ↑37

Dimitri, R., De Lorenzis, L., Wriggers, P., and Zavarise, G. 2014a. NURBS- and T-spline-based isogeometric cohesive zone modeling of interface debonding. *Computational Mechanics*, vol. 54(2), pp. 369–388. ↑40

Dimitri, R., Lorenzis, L.D., Scott, M.A., Wriggers, P., Taylor, R.L., and Zavarise, G. 2014b. Isogeometric large deformation frictionless contact using T-splines. *Computer Methods in Applied Mechanics and Engineering*, vol. 269, pp. 394 – 414. ↑40

Ellenberg, D., Azar, D.T., Hallak, J.A., Tobaigy, F., Han, K.Y., Jain, S., Zhou, Z., and Chang, J.H. 2010. Novel aspects of corneal angiogenic and lymphangiogenic privilege. *Progress in Retinal and Eye Research*, vol. 29(3), pp. 208 – 248. ↑102

Emmerich, H. 2003. *The diffuse interface approach in materials science*, vol. 73 of *Lecture Notes in Physics*. Springer Berlin Heidelberg. ISBN 978-3-540-36409-2. ↑49

Emmerich, H. 2008. Advances of and by phase-field modelling in condensed-matter physics. *Advances in Physics*, vol. 57(1), pp. 1–87. ↑56

Engel, G., Garikipati, K., Hughes, T.J.R., Larson, M.G., Mazzei, L., and Taylor, R.L. 2002. Continuous/discontinuous finite element approximations of fourth-order elliptic problems in structural and continuum mechanics with applications to thin beams and plates, and strain gradient elasticity. *Computer Methods in Applied Mechanics and Engineering*, vol. 191(34), pp. 3669–3750. ↑39

Evans, J.A. and Hughes, T.J.R. 2013. Isogeometric divergence-conforming B-splines for the unsteady Navier–Stokes equations. *Journal of Computational Physics*, vol. 241, pp. 141–167. ↑40

Falcon, B.L., Barr, S., Gokhale, P.C., Chou, J., Fogarty, J., Depeille, P., Miglarese, M., Epstein, D.M., and McDonald, D.M. 2011. Reduced VEGF production, angiogenesis, and vascular regrowth contribute to the antitumor properties of dual mTORC1/mTORC2 inhibitors. *Cancer Research*, vol. 71(5), pp. 1573–1583. ↑134

Fentiman, I.S. 2005. *Introduction to the Cellular and Molecular Biology of Cancer*, chapter Local treatment of cancer, pp. 390–398. Oxford University Press Inc. ISBN 019852563X. ↑16

Ferlay, J., Soerjomataram, I., Ervik, M., Dikshit, R., Eser, S., Mathers, C., Rebelo, M., Parkin, D., Forman, D., and Bray, F. 2012. GLOBOCAN 2012 v1.0, Cancer incidence and mortality worldwide: IARC CancerBase No. 11. URL `http://globocan.iarc.fr`. ↑1 , ↑2

Feron, O. 2009. Pyruvate into lactate and back: From the Warburg effect to symbiotic energy fuel exchange in cancer cells. *Radiotherapy and Oncology*, vol. 92(3), pp. 329–333. ↑194

Fidler, I.J. 2003. The pathogenesis of cancer metastasis: the "seed and soil" hypothesis revisited. *Nature Reviews Cancer*, vol. 3(6), pp. 453–458. ↑13

Fiedler, M. 1973. Algebraic connectivity of graphs. *Czechoslovak mathematical journal*, vol. 23(2), pp. 298–305. ↑96

Figg, W.D. and Folkman, J. 2011a. *Angiogenesis: An integrative approach from science to medicine*. Springer. ISBN 978-0-387-71518-6. ↑22 , ↑136 , ↑203 , ↑206

Figg, W.D. and Folkman, J. 2011b. *Angiogenesis: An integrative approach from science to medicine*, chapter Models for Angiogenesis, pp. 299–312. Springer. ISBN 978-0-387-71518-6. ↑102

Fischer, P., Klassen, M., Mergheim, J., Steinmann, P., and Müller, R. 2011. Isogeometric analysis of 2D gradient elasticity. *Computational Mechanics*, vol. 47(3), pp. 325–334. ↑44

Folkman, J. 1971. Tumor angiogenesis: Therapeutic implications. *New England Journal of Medicine*, vol. 285(21), pp. 1182–1186. ↑6 , ↑12 , ↑30

Folkman, J. and Kalluri, R. 1984. *Holland-Frei Cancer Medicine*, chapter Tumor angiogenesis, pp. 161–194. BC Decker Inc., 6 edition. ISBN 1-55009-213-8. ↑12

Frieboes, H.B., Jin, F., Chuang, Y.L., Wise, S.M., Lowengrub, J.S., and Cristini, V. 2010. Three-dimensional multispecies nonlinear tumor growth-II: Tumor invasion and angiogenesis. *Journal of Theoretical Biology*, vol. 264(4), pp. 1254–1278. ↑38

Frieboes, H.B., Lowengrub, J.S., Wise, S.M., Zheng, X., Macklin, P., Bearer, E.L., and Cristini, V. 2007. Computer simulation of glioma growth and morphology. *NeuroImage*, vol. 37(Suppl. 1), pp. S59–S70. ↑38 , ↑39

Friedl, P. and Weigelin, B. 2008. Interstitial leukocyte migration and immune function. *Nature Immunology*, vol. 9(9), pp. 960–969. ↑80

Friedl, P. and Wolf, K. 2008. Tube travel: the role of proteases in individual and collective cancer cell invasion. *Cancer Research*, vol. 68, pp. 7247–7249. ↑193

Friedl, P. and Wolf, K. 2010. Plasticity of cell migration: a multiscale tuning model. *Journal of Cell Biology*, vol. 188, pp. 11–19. ↑193

Galluzzi, L. and Kroemer, G. 2008. Necroptosis: a specialized pathway of programmed necrosis. *Cell*, vol. 135(7), pp. 1161–1163. ↑194

Gatenby, R.A. and Maini, P.K. 2003. Mathematical oncology: Cancer summed up. *Nature*, vol. 421(6921), pp. 321–321. ↑7

Gebb, S. and Stevens, T. 2004. On lung endothelial cell heterogeneity. *Microvascular Research*, vol. 68(1), pp. 1 – 12. ↑86

Gerhardt, H., Golding, M., Fruttiger, M., Ruhrberg, C., Lundkvist, A., Abramsson, A., Jeltsch, M., Mitchell, C., Alitalo, K., Shima, D., and Betsholtz, C. 2003.

VEGF guides angiogenic sprouting utilizing endothelial tip cell filopodia. *Journal of Cell Biology*, vol. 161(6), pp. 1163–1177. ↑24 , ↑138

Gerlee, P. and Anderson, A.R.A. 2007. Stability analysis of a hybrid cellular automaton model of cell colony growth. *Physical Review E*, vol. 75(5), p. 051911. ↑31

Gevertz, J.L. and Torquato, S. 2006. Modeling the effects of vasculature evolution on early brain tumor growth. *Journal of Theoretical Biology*, vol. 243(4), pp. 517–531. ↑38

Gimbrone Jr, M.A., Cotran, R.S., Leapman, S.B., and Folkman, J. 1974. Tumor growth and neovascularization: an experimental model using the rabbit cornea. *Journal of the National Cancer Institute*, vol. 52(2), pp. 699–705. ↑36

Goel, S., Duda, D.G., Xu, L., Munn, L.L., Boucher, Y., Fukumura, D., and Jain, R.K. 2011. Normalization of the vasculature for treatment of cancer and other diseases. *Physiological Reviews*, vol. 91(3), pp. 1071–1121. ↑26 , ↑134

Gomez, H., Calo, V.M., Bazilevs, Y., and Hughes, T.J.R. 2008. Isogeometric analysis of the Cahn-Hilliard phase-field model. *Computer Methods in Applied Mechanics and Engineering*, vol. 197(49-50), pp. 4333–4352. ↑40 , ↑44 , ↑49 , ↑62 , ↑142

Gomez, H., Cueto-Felgueroso, L., and Juanes, R. 2013. Three-dimensional simulation of unstable gravity-driven infiltration of water into a porous medium. *Journal of Computational Physics*, vol. 238, pp. 217–239. ↑62 , ↑142

Gomez, H. and Hughes, T.J.R. 2011. Provably unconditionally stable, second-order time-accurate, mixed variational methods for phase-field models. *Journal of Computational Physics*, vol. 230(13), pp. 5310–5327. ↑49 , ↑62 , ↑142

Gomez, H., Hughes, T.J.R., Nogueira, X., and Calo, V.M. 2010. Isogeometric analysis of the isothermal Navier-Stokes-Korteweg equations. *Computer Methods in Applied Mechanics and Engineering*, vol. 199(25-28), pp. 1828–1840. ↑44

Gomez, H. and Nogueira, X. 2012. An unconditionally energy-stable method for the phase field crystal equation. *Computer Methods in Applied Mechanics and Engineering*, vol. 249-252, pp. 52–61. ↑44

Gomez, H. and París, J. 2011. Numerical simulation of asymptotic states of the damped Kuramoto-Sivashinsky equation. *Physical Review E*, vol. 83, p. 046702. ↑44

Graner, F. and Glazier, J.A. 1992. Simulation of biological cell sorting using a two-dimensional extended Potts model. *Physical Review Letters*, vol. 69(13), pp. 2013–2016. ↑36

Greenspan, H.P. 1972. Models for the growth of a solid tumor by diffusion. *Studies in Applied Mathematics*, vol. 52(4), pp. 317–340. ↑30

Greenspan, H.P. 1974. On the self-inhibited growth of cell cultures. *Growth*, vol. 38(1), pp. 81–95. ↑30

Grivennikov, S.I., Greten, F.R., and Karin, M. 2010. Immunity, inflammation and cancer. *Cell*, vol. 140(6), pp. 883–899. ↑194 , ↑195

Grote, J. 1989. *Tissue respiration*, pp. 598–612. Springer Berlin Heidelberg. ISBN 978-3-642-73833-3. ↑87

Hanahan, D. and Weinberg, R.A. 2000. The hallmarks of cancer. *Cell*, vol. 100(1), pp. 57–70. ↑10 , ↑189

Hanahan, D. and Weinberg, R.A. 2011. Hallmarks of cancer: The next generation. *Cell*, vol. 144(5), pp. 646–674. ↑10 , ↑15 , ↑189 , ↑191

Harrington, H.A., Maier, M., Naidoo, L., Whitaker, N., and Kevrekidis, P.G. 2007. A hybrid model for tumor-induced angiogenesis in the cornea in the presence of inhibitors. *Mathematical and Computer Modelling*, vol. 46(3-4), pp. 513 – 524. ↑35 , ↑36 , ↑117 , ↑144

Hawkins-Daarud, A., Prudhomme, S., van der Zee, K.G., and Oden, J.T. 2013. Bayesian calibration, validation, and uncertainty quantification of diffuse interface models of tumor growth. *Journal of Mathematical Biology*, vol. 67(6-7), pp. 1457–1485. ↑31

Hawkins-Daarud, A., van der Zee, K.G., and Oden, J.T. 2012. Numerical simulation of a thermodynamically consistent four-species tumor growth model. *International Journal for Numerical Methods in Biomedical Engineering*, vol. 28(1), pp. 3–24. ↑31 , ↑39 , ↑56

Hellström, M., Phng, L.K., Hofmann, J.J., Wallgard, E., Coultas, L., Lindblom, P., Alva, J., Nilsson, A.K., Karlsson, L., Gaiano, N., Yoon, K., Rossant, J., Iruela-Arispe, M.L., Kalén, M., Gerhardt, H., and Betsholtz, C. 2007. Dll4 signalling through Notch1 regulates formation of tip cells during angiogenesis. *Nature*, vol. 445(7129), pp. 776–780. ↑22 , ↑138

Henriksson, J.T., McDermott, A.M., and Bergmanson, J.P.G. 2009. Dimensions and morphology of the cornea in three strains of mice. *Investigative Ophthalmology & Visual Science*, vol. 50(8), pp. 3648–3654. ↑114

Hill, N.A. and Häder, D.P. 1997. A biased random walk model for the trajectories of swimming micro-organisms. *Journal of Theoretical Biology*, vol. 186(4), pp. 503 – 526. ↑34

Hinow, P., Gerlee, P., McCawley, L.J., Quaranta, V., Ciobanu, M., Wang, S., Graham, J.M., Ayati, B.P., Claridge, J., Swanson, K.R., *et al.* 2009. A spatial model of tumor-host interaction: application of chemotherapy. *Mathematical Biosciences and Engineering: MBE*, vol. 6(3), p. 521. ↑30

Hogea, C.S., Murray, B.T., and Sethian, J.A. 2006. Simulating complex tumor dynamics from avascular to vascular growth using a general level-set method. *Journal of Mathematical Biology*, vol. 53(1), pp. 86–134. ↑38

Holmes, M.J. and Sleeman, B.D. 2000. A mathematical model of tumour angiogenesis incorporating cellular traction and viscoelastic effects. *Journal of Theoretical Biology*, vol. 202(2), pp. 95–112. ↑32

Hughes, T.J.R. 1987. *The Finite Element Method: Linear Static and Dynamic Finite Element Analysis*. Dover Civil and Mechanical Engineering. Dover Publications. ISBN 0486411818. ↑39

Hughes, T.J.R., Cottrell, J.A., and Bazilevs, Y. 2005. Isogeometric analysis: CAD, finite elements, NURBS, exact geometry and mesh refinement. *Computer Methods in Applied Mechanics and Engineering*, vol. 194(39-41), pp. 4135–4195. ↑39 , ↑141

Hughes, T.J.R., Feijóo, G.R., Mazzei, L., and Quincy, J.B. 1998. The variational multiscale method–a paradigm for computational mechanics. *Computer Methods in Applied Mechanics and Engineering*, vol. 166(1-2), pp. 3 – 24. ↑164

Hughes, T.J.R., Reali, A., and Sangalli, G. 2008. Duality and unified analysis of discrete approximations in structural dynamics and wave propagation: Comparison of ρ-method finite elements with k-method NURBS. *Computer Methods in Applied Mechanics and Engineering*, vol. 197(49-50), pp. 4104–4124. ↑40

Hughes, T.J.R., Reali, A., and Sangalli, G. 2010. Efficient quadrature for NURBS-based isogeometric analysis. *Computer Methods in Applied Mechanics and Engineering*, vol. 199(5-8), pp. 301–313. ↑40

Hugo, H., Ackland, M.L., Blick, T., Lawrence, M.G., Clements, J.A., Williams, E.D., and Thompson, E.W. 2007. Epithelial–mesenchymal and mesenchymal–epithelial transitions in carcinoma progression. *Journal of Cellular Physiology*, vol. 213, pp. 374–383. ↑193

Hystad, M.E. and Rofstad, E.K. 1994. Oxygen consumption rate and mitochondrial density in human melanoma monolayer cultures and multicellular spheroids. *International Journal of Cancer*, vol. 57(4), pp. 532–537. ↑30

Inai, T., Mancuso, M., Hashizume, H., Baffert, F., Haskell, A., Baluk, P., Hu-Lowe, D.D., Shalinsky, D.R., Thurston, G., Yancopoulos, G.D., and McDonald, D.M.

2004. Inhibition of vascular endothelial growth factor (VEGF) signaling in cancer causes loss of endothelial fenestrations, regression of tumor vessels, and appearance of basement membrane ghosts. *The American Journal of Pathology*, vol. 165(1), pp. 35 – 52. ↑134

Jackson, A.M. and Porte, J. 2005. *Introduction to the Cellular and Molecular Biology of Cancer*, chapter Immunotherapy of cancer, pp. 443–457. Oxford University Press Inc. ISBN 019852563X. ↑16

Jackson, T. and Zheng, X. 2010. A cell-based model of endothelial cell migration, proliferation and maturation during corneal angiogenesis. *Bulletin of Mathematical Biology*, vol. 72(4), pp. 830–868. ↑35 , ↑36 , ↑117

Jain, R.K. 2001. Normalizing tumor vasculature with anti-angiogenic therapy: A new paradigm for combination therapy. *Nature Medicine*, vol. 7(9), pp. 987–989. ↑26

Jain, R.K. 2005. Normalization of tumor vasculature: An emerging concept in antiangiogenic therapy. *Science*, vol. 307(5706), pp. 58–62. ↑26 , ↑27

Jain, R.K., Munn, L.L., and Fukumura, D. 2002. Dissecting tumour pathophysiology using intravital microscopy. *Nature Reviews Cancer*, vol. 2(4), pp. 266–276. ↑76

Jakobsson, L., Franco, C.A., Bentley, K., Collins, R.T., Ponsioen, B., Aspalter, I.M., Rosewell, I., Busse, M., Thurston, G., Medvinsky, A., Schulte-Merker, S., and Gerhardt, H. 2010. Endothelial cells dynamically compete for the tip cell position during angiogenic sprouting. *Nature Cell Biology*, vol. 12(10), pp. 943–953. ↑24

Jansen, K.E., Whiting, C.H., and Hulbert, G.M. 2000. A generalized-α method for integrating the filtered Navier-Stokes equations with a stabilized finite element method. *Computer Methods in Applied Mechanics and Engineering*, vol. 190(3-4), pp. 305 – 319. ↑61 , ↑91

Kaanders, J.H.A.M., Bussink, J., and van der Kogel, A.J. 2004. Clinical studies of hypoxia modification in radiotherapy. *Seminars in Radiation Oncology*, vol. 14(3), pp. 233–240. ↑110

Kadapa, C., Dettmer, W.G., and Perić, D. 2015. NURBS based least-squares finite element methods for fluid and solid mechanics. *International Journal for Numerical Methods in Engineering*, vol. 101(7), pp. 521–539. ↑40

Karma, A. and Rappel, W.J. 1998. Quantitative phase-field modeling of dendritic growth in two and three dimensions. *Physical Review E*, vol. 57, pp. 4323–4349. ↑138

Karnoub, A.E. and Weinberg, R.A. 2006-2007. Chemokine networks and breast cancer metastasis. *Breast Disease*, vol. 26(1), pp. 75–85. ↑195

Kennedy, K.M. and Dewhirst, M.W. 2010. Tumor metabolism of lactate: the influence and therapeutic potential for MCT and CD147 regulation. *Future Oncology*, vol. 6(1), pp. 127–148. ↑194

Kenyon, B.M., Voest, E.E., Chen, C.C., Flynn, E., Folkman, J., and D'Amato, R.J. 1996. A model of angiogenesis in the mouse cornea. *Investigative Ophthalmology & Visual Science*, vol. 37(8), pp. 1625–1632. ↑76 , ↑103 , ↑144 , ↑146

Kevrekidis, P.G. and Whitaker, N. 2005. Towards a reduced model for angiogenesis: A hybrid approach. *Mathematical and Computer Modelling*, vol. 41(8-9), pp. 987–996. ↑36

Kevrekidis, P.G., Whitaker, N., Good, D.J., and Herring, G.J. 2006. Minimal model for tumor angiogenesis. *Physical Review E*, vol. 73(6), p. 061926. ↑36

Kiendl, J., Bazilevs, Y., Hsu, M.C., Wüchner, R., and Bletzinger, K.U. 2010. The bending strip method for isogeometric analysis of Kirchhoff–Love shell structures comprised of multiple patches. *Computer Methods in Applied Mechanics and Engineering*, vol. 199(37-40), pp. 2403–2416. ↑40

Kilarski, W.W., Samolov, B., Petersson, L., Kvanta, A., and Gerwins, P. 2009. Biomechanical regulation of blood vessel growth during tissue vascularization. *Nature Medicine*, vol. 15(6), pp. 657–664. ↑19

Kiltie, A. 2005. *Introduction to the Cellular and Molecular Biology of Cancer*, chapter Radiotherapy and molecular radiotherapy, pp. 414–427. Oxford University Press Inc. ISBN 019852563X. ↑16

Kim, Y.T., Provatas, N., Goldenfeld, N., and Dantzig, J. 1999. Universal dynamics of phase-field models for dendritic growth. *Physical Review E*, vol. 59, pp. R2546–R2549. ↑138

Kirwan, R.P., Zheng, Y., Tey, A., Anijeet, D., Sueke, H., and Kaye, S.B. 2012. Quantifying changes in corneal neovascularization using fluorescein and indocyanine green angiography. *American Journal of Ophthalmology*, vol. 154(5), pp. 850–858.e2. ↑105

Kobayashi, R. 1993. Modeling and numerical simulations of dendritic crystal growth. *Physica D: Nonlinear Phenomena*, vol. 63(3-4), pp. 410–423. ↑138

Kobayashi, R. 1994. A numerical approach to three-dimensional dendritic solidification. *Experimental Mathematics*, vol. 3(1), pp. 59–81. ↑49 , ↑82

Kurz, H., Burri, P.H., and Djonov, V.G. 2003. Angiogenesis and vascular remodeling by intussusception: From form to function. *News in Physiological Sciences*, vol. 18(2), pp. 65–70. ↑19 , ↑20

Laird, A.K. 1964. Dynamics of tumour growth. *British Journal of Cancer*, vol. 18(3), pp. 490–502. ↑30

Lang, J. 1995. Two-dimensional fully adaptive solutions of reaction-diffusion equations. *Applied Numerical Mathematics*, vol. 18(1-3), pp. 223–240. ↑64

Lee, D.S., Rieger, H., and Bartha, K. 2006. Flow correlated percolation during vascular remodeling in growing tumors. *Physical Review Letters*, vol. 96(5), p. 058104. ↑38

Leenders, W.P.J., Küsters, B., and de Waal, R.M.W. 2002. Vessel co-option: How tumors obtain blood supply in the absence of sprouting angiogenesis. *Endothelium*, vol. 9(2), pp. 83–87. ↑19

Levine, H.A., Pamuk, S., Sleeman, B.D., and Nilsen-Hamilton, M. 2001a. Mathematical modeling of capillary formation and development in tumor angiogenesis: Penetration into the stroma. *Bulletin of Mathematical Biology*, vol. 63(5), pp. 801–863. ↑32

Levine, H.A., Sleeman, B.D., and Nilsen-Hamilton, M. 2000. A mathematical model for the roles of pericytes and macrophages in angiogenesis. I. The role of protease inhibitors in preventing angiogenesis. *Mathematical Biosciences*, vol. 168(1), pp. 77–115. ↑32 , ↑34

Levine, H.A., Sleeman, B.D., and Nilsen-Hamilton, M. 2001b. Mathematical modeling of the onset of capillary formation initiating angiogenesis. *Journal of Mathematical Biology*, vol. 42(3), pp. 195–238. ↑32

Levine, H.A., Tucker, A.L., and Nilsen-Hamilton, M. 2002. A mathematical model for the role of cell signal transduction in the initiation and inhibition of angiogenesis. *Growth Factors*, vol. 20(4), pp. 155–175. ↑32

Lima, E.A., Oden, J.T., and Almeida, R.C. 2014. A hybrid ten-species phase-field model of tumor growth. *Mathematical Models and Methods in Applied Sciences*, vol. 24(13), pp. 2569–2599. ↑38

Lima, E.A.B.F., Almeida, R.C., and Oden, J.T. 2015. Analysis and numerical solution of stochastic phase-field models of tumor growth. *Numerical Methods for Partial Differential Equations*, vol. 31(2), pp. 552–574. ↑31

Liu, G., Qutub, A.A., Vempati, P., Mac Gabhann, F., and Popel, A.S. 2011. Module-based multiscale simulation of angiogenesis in skeletal muscle. *Theoretical Biology and Medical Modelling*, vol. 8(6), pp. 1–26. ↑37

Liu, J., Gomez, H., Evans, J.A., Hughes, T.J.R., and Landis, C.M. 2013. Functional entropy variables: A new methodology for deriving thermodynamically consistent algorithms for complex fluids, with particular reference to the isothermal Navier-Stokes-Korteweg equations. *Journal of Computational Physics*, vol. 248, pp. 47–86. ↑40 , ↑62

Liu, J., Landis, C.M., Gomez, H., and Hughes, T.J.R. 2015. Liquid–vapor phase transition: Thermomechanical theory, entropy stable numerical formulation, and boiling simulations. *Computer Methods in Applied Mechanics and Engineering*, vol. In press. ↑40

Liu, W., Schultz, K.M., Zhang, K., Sasman, A., Gao, F., Kume, T., and Zhang, H.F. 2014. In vivo corneal neovascularization imaging by optical-resolution photoacoustic microscopy. *Photoacoustics*, vol. 2(2), pp. 81 – 86. ↑105

Loeb, L.A., Loeb, K.R., and Anderson, J.P. 2003. Multiple mutations and cancer. *Proceedings of the National Academy of Sciences*, vol. 100(3), pp. 776–781. ↑10 , ↑195

Logsdon, E.A., Finley, S.D., Popel, A.S., and Mac Gabhann, F. 2014. A systems biology view of blood vessel growth and remodelling. *Journal of Cellular and Molecular Medicine*, vol. 18(8), pp. 1491–1508. ↑28 , ↑134

Lowengrub, J.S., Frieboes, H.B., Jin, F., Chuang, Y.L., Li, X., Macklin, P., Wise, S.M., and Cristini, V. 2010. Nonlinear modelling of cancer: Bridging the gap between cells and tumours. *Nonlinearity*, vol. 23(1), pp. R1–R9. ↑28

Mahoney, A.W., Smith, B.G., Flann, N.S., and Podgorski, G.J. 2008. Discovering novel cancer therapies: A computational modeling and search approach. In *Computational Intelligence in Bioinformatics and Computational Biology, 2008. CIBCB '08. IEEE Symposium on*, pp. 233–240. ↑36

Mancuso, M.R., Davis, R., Norberg, S.M., O'Brien, S., Sennino, B., Nakahara, T., Yao, V.J., Inai, T., Brooks, P., Freimark, B., Shalinsky, D.R., Hu-Lowe, D.D., and McDonald, D.M. 2006. Rapid vascular regrowth in tumors after reversal of VEGF inhibition. *Journal of Clinical Investigation*, vol. 116(10), pp. 2610–2621. ↑24 , ↑134 , ↑135

Mantzaris, N.V., Webb, S., and Othmer, H.G. 2004. Mathematical modeling of tumor-induced angiogenesis. *Journal of Mathematical Biology*, vol. 49(2), pp. 111–187. ↑28

Marieb, E.N. 2003. *Essentials of Human Anatomy & Physiology*. Benjamin Cummings. ISBN 0321695984. ↑18

Marin-Padilla, M. 1985. Early vascularization of the embryonic cerebral cortex:

Golgi and electron microscopic studies. *The Journal of Comparative Neurology*, vol. 241(2), pp. 237–249. ↑136

Maxwell, P.H. and Ashcroft, M. 2009. Antiangiogenic cancer therapy. *British Journal of Cancer*, vol. 100(9), p. 1515. ↑135

May, M. 2014. Statistics: Attacking an epidemic. *Nature*, vol. 509(7502), pp. S50–S51. ↑3

Mayneord, W.V. 1932. On a law of growth of Jensen's rat sarcoma. *American Journal of Cancer*, vol. 16, pp. 841–846. ↑30

McDonald, D.M. and Choyke, P.L. 2003. Imaging of angiogenesis: from microscope to clinic. *Nature Medicine*, vol. 9(6), pp. 713–725. ↑25

McDougall, S.R., Anderson, A.R.A., and Chaplain, M.A.J. 2006. Mathematical modelling of dynamic adaptive tumour-induced angiogenesis: Clinical implications and therapeutic targeting strategies. *Journal of Theoretical Biology*, vol. 241(3), pp. 564–589. ↑36

McDougall, S.R., Anderson, A.R.A., Chaplain, M.A.J., and Sherrat, J.A. 2002. Mathematical modelling of flow through vascular networks: Implications for tumour-induced angiogenesis and chemotherapy strategies. *Bulletin of Mathematical Biology*, vol. 64(4), pp. 673–702. ↑36

McDougall, S.R., Watson, M.G., Devlin, A.H., Mitchell, C.A., and Chaplain, M.A.J. 2012. A hybrid discrete-continuum mathematical model of pattern prediction in the developing retinal vasculature. *Bulletin of Mathematical Biology*, vol. 74(10), pp. 2272–2314. ↑36

Milde, F., Bergdorf, M., and Koumoutsakos, P. 2008. A hybrid model for three-dimensional simulations of sprouting angiogenesis. *Biophysical Journal*, vol. 95(7), pp. 3146–3160. ↑34 , ↑35

Moreira, J. and Deutsch, A. 2002. Cellular automaton models of tumor development: A critical review. *Advances in Complex Systems*, vol. 5(2-3), pp. 247–267. ↑28 , ↑31

Morganti, S., Auricchio, F., Benson, D.J., Gambarin, F.I., Hartmann, S., Hughes, T.J.R., and Reali, A. 2015. Patient-specific isogeometric structural analysis of aortic valve closure. *Computer Methods in Applied Mechanics and Engineering*, vol. 284, pp. 508–520. ↑40

Murakami, T., Suzuma, K., Takagi, H., Kita, M., Ohashi, H., Watanabe, D., Ojima, T., Kurimoto, M., Kimura, T., Sakamoto, A., Unoki, N., and Yoshimura, N. 2006. Time-lapse imaging of vitreoretinal angiogenesis originating from both quiescent

and mature vessels in a novel ex vivo system. *Investigative Ophthalmology & Visual Science*, vol. 47(12), pp. 5529–5536. ↑138

Murray, A. 1994. Cell cycle checkpoints. *Current Opinion in Cell Biology*, vol. 6(6), pp. 872–876. ↑190

Muthukkaruppan, V.R., Kubai, L., and Auerbach, R. 1982. Tumor-induced neovascularization in the mouse eye. *Journal of the National Cancer Institute*, vol. 69(3), pp. 699–708. ↑36 , ↑76

Nagy, J. and Dvorak, H. 2012. Heterogeneity of the tumor vasculature: the need for new tumor blood vessel type-specific targets. *Clinical & Experimental Metastasis*, vol. 29(7), pp. 657–662. ↑26 , ↑27

Nguyen-Thanh, N., Nguyen-Xuan, H., Bordas, S.P.A., and Rabczuk, T. 2011. Isogeometric analysis using polynomial splines over hierarchical T-meshes for two-dimensional elastic solids. *Computer Methods in Applied Mechanics and Engineering*, vol. 200(21-22), pp. 1892–1908. ↑39

Nonomura, M. 2012. Study on multicellular systems using a phase field model. *PLoS ONE*, vol. 7(4), p. e33501. ↑49

Norrby, K. 2006. In vivo models of angiogenesis. *Journal of Cellular and Molecular Medicine*, vol. 10(3), pp. 588–612. ↑102 , ↑206

Oden, J.T., Hawkins-Daarud, A., and Prudhomme, S. 2010. General diffuse-interface theories and an approach to predictive tumor growth modeling. *Mathematical Models and Methods in Applied Sciences*, vol. 20(3), pp. 477–517. ↑31 , ↑49

Oden, J.T., Lima, E.A.B.F., Almeida, R.C., Feng, Y., Rylander, M.N., Fuentes, D., Faghihi, D., Rahman, M.M., DeWitt, M., Gadde, M., and Zhou, J.C. 2015. Toward predictive multiscale modeling of vascular tumor growth. *Archives of Computational Methods in Engineering*, pp. 1–45. ↑28

Oden, J.T., Prudencio, E.E., and Hawkins-Daarud, A. 2013. Selection and assessment of phenomenological models of tumor growth. *Mathematical Models and Methods in Applied Sciences*, vol. 23(7), pp. 1309–1338. ↑31

Olsen, L., Sherratt, J.A., Maini, P.K., and Arnold, F. 1997. A mathematical model for the capillary endothelial cell-extracellular matrix interactions in wound-healing angiogenesis. *Mathematical Medicine and Biology*, vol. 14(4), pp. 261–281. ↑37

Olszewski, M.M. 2010. From macroscopic to microscopic: A brief history of the origins and treatment of cancer in the western world. *University of Toronto Medical Journal*, vol. 87(3), pp. 181–186. ↑4

Orme, M.E. and Chaplain, M.A.J. 1996a. A mathematical model of the first steps of tumour-related angiogenesis: Capillary sprout formation and secondary branching. *IMA Journal of Mathematics Applied in Medicine and Biology*, vol. 13(2), pp. 73–98. ↑34

Orme, M.E. and Chaplain, M.A.J. 1996b. A mathematical model of vascular tumour growth and invasion. *Mathematical and Computer Modelling*, vol. 23(10), pp. 43 – 60. ↑38

Orme, M.E. and Chaplain, M.A.J. 1997. Two-dimensional models of tumour angiogenesis and anti-angiogenesis strategies. *Mathematical Medicine and Biology*, vol. 14(3), pp. 189–205. ↑32 , ↑33

Othmer, H.G. and Stevens, A. 1997. Aggregation, blowup, and collapse: The ABC's of taxis in reinforced random walks. *SIAM Journal on Applied Mathematics*, vol. 57(4), pp. 1044–1081. ↑84

Pauletti, M.S., Martinelli, M., Cavallini, N., and Antolin, P. 2015. Igatools: An isogeometric analysis library. *SIAM Journal on Scientific Computing*, vol. 37(4), pp. C465–C496. ↑40

Pérez-García, V.M., Calvo, G.F., Belmonte-Beitia, J., Diego, D., and Pérez-Romasanta, L. 2011. Bright solitary waves in malignant gliomas. *Physical Review E*, vol. 84(2), p. 021921. ↑31

Perfahl, H., Byrne, H.M., Chen, T., Estrella, V., Alarcón, T., Lapin, A., Gatenby, R.A., Gillies, R.J., Lloyd, M.C., Maini, P.K., Reuss, M., and Owen, M.R. 2011. Multiscale modelling of vascular tumour growth in 3D: The roles of domain size and boundary conditions. *PLoS ONE*, vol. 6(4), p. e14790. ↑38

Peterson, J.W., Carey, G.F., Knezevic, D.J., and Murray, B.T. 2007. Adaptive finite element methodology for tumour angiogenesis modelling. *International Journal for Numerical Methods in Engineering*, vol. 69(6), pp. 1212–1238. ↑32 , ↑33

Phipps, C. and Kohandel, M. 2011. Mathematical model of the effect of interstitial fluid pressure on angiogenic behavior in solid tumors. *Computational and Mathematical Methods in Medicine*, vol. 2011(Article ID 843765), pp. 1–9. ↑38

Piegl, L. 1986. The sphere as a rational Bézier surface. *Computer Aided Geometric Design*, vol. 3(1), pp. 45 – 52. ↑117

Piegl, L. and Tiller, W. 1997. *The NURBS Book*. Springer-Verlag Berlin Heidelberg. ISBN 978-3-642-97385-7. ↑39

Plank, M.J. and Sleeman, B.D. 2003. A reinforced random walk model of tumour

angiogenesis and anti-angiogenic strategies. *Mathematical Medicine and Biology*, vol. 20(2), pp. 135–181. ↑34

Plank, M.J. and Sleeman, B.D. 2004. Lattice and non-lattice models of tumour angiogenesis. *Bulletin of Mathematical Biology*, vol. 66(6), pp. 1785–1819. ↑34 , ↑80 , ↑87 , ↑88

Plank, M.J., Sleeman, B.D., and Jones, P.F. 2004. A mathematical model of tumour angiogenesis, regulated by vascular endothelial growth factor and the angiopoietins. *Journal of Theoretical Biology*, vol. 229(4), pp. 435 – 454. ↑32

Polverini, P.J., Bouck, N.P., and Rastinejad, F. 1991. Assay and purification of naturally occurring inhibitor of angiogenesis. In *Peptide Growth Factors Part C*, vol. 198 of *Methods in Enzymology*, pp. 440 – 450. Academic Press. ↑105

Potente, M., Gerhardt, H., and Carmeliet, P. 2011. Basic and therapeutic aspects of angiogenesis. *Cell*, vol. 146(6), pp. 873–887. ↑22 , ↑134 , ↑137 , ↑203

Preziosi, L. and Tosin, A. 2009. Multiphase modelling of tumour growth and extracellular matrix interaction: mathematical tools and applications. *Journal of Mathematical Biology*, vol. 58(4-5), pp. 625–656. ↑31

Pries, A.R., Reglin, B., and Secomb, T.W. 2001. Structural adaptation of microvascular networks: functional roles of adaptive responses. *American Journal of Physiology - Heart and Circulatory Physiology*, vol. 281(3), pp. H1015–H1025. ↑38 , ↑153

Pries, A.R., Secomb, T.W., and Gaehtgens, P. 1996. Biophysical aspects of blood flow in the microvasculature. *Cardiovascular Research*, vol. 32(4), pp. 654–667. ↑38

Pries, A.R., Secomb, T.W., and Gaehtgens, P. 1998. Structural adaptation and stability of microvascular networks: theory and simulations. *American Journal of Physiology - Heart and Circulatory Physiology*, vol. 275(2), pp. H349–H360. ↑38 , ↑153

Pries, A.R., Secomb, T.W., Gaehtgens, P., and Gross, J.F. 1990. Blood flow in microvascular networks: Experiments and simulation. *Circulation Research*, vol. 67(4), pp. 826–834. ↑38 , ↑153

Pries, A.R., Secomb, T.W., Geβner, T., Sperandio, M.B., Gross, J.F., and Gaehtgens, P. 1994. Resistance to blood and flow in microvessels and in vivo. *Circulation Research*, vol. 75(5), pp. 904–915. ↑38 , ↑158

Provatas, N., Goldenfeld, N., and Dantzig, J. 1998. Efficient computation of dendritic microstructures using adaptive mesh refinement. *Physical Review Letters*, vol. 80, pp. 3308–3311. ↑138

Qian, B.Z. and Pollard, J.W. 2010. Macrophage diversity enhances tumor progression and metastasis. *Cell*, vol. 141(1), pp. 39–51. ↑195

Qutub, A.A., Mac Gabhann, F., Karagiannis, E.D., Vempati, P., and Popel, A.S. 2009. Multiscale models of angiogenesis. *Engineering in Medicine and Biology Magazine, IEEE*, vol. 28(2), pp. 14 –31. ↑28

Reali, A. and Gomez, H. 2015. An isogeometric collocation approach for Bernoulli–Euler beams and Kirchhoff plates. *Computer Methods in Applied Mechanics and Engineering*, vol. 284, pp. 623 – 636. ↑40

Reali, A. and Hughes, T.J.R. 2015. An introduction to isogeometric collocation methods. In G. Beer and S. Bordas, editors, *Isogeometric Methods for Numerical Simulation*, vol. 561 of *CISM International Centre for Mechanical Sciences*, pp. 173–204. Springer Vienna. ISBN 978-3-7091-1842-9. ↑40

Reina-Romo, E., Valero, C., Borau, C., Rey, R., Javierre, E., Gómez-Benito, M.J., Domínguez, J., and García-Aznar, J.M. 2013. Mechanobiological modelling of angiogenesis: Impact on tissue engineering and bone regeneration. In L. Geris, editor, *Computational Modeling in Tissue Engineering*, vol. 10 of *Studies in Mechanobiology, Tissue Engineering and Biomaterials*, pp. 379–404. Springer Berlin Heidelberg. ISBN 978-3-642-32562-5. ↑37

Rogers, D.F. 2001. *An Introduction to NURBS: With Historical Perspective*. Morgan Kaufmann Publishers Inc., San Francisco, CA, USA. ISBN 1-55860-669-6. ↑39

Rogers, M.S., Birsner, A.E., and D'Amato, R.J. 2007. The mouse cornea micropocket angiogenesis assay. *Natature Protocols*, vol. 2(10), pp. 2545–2550. ↑103 , ↑105 , ↑144

Roose, T., Chapman, S.J., and Maini, P.K. 2007. Mathematical models of avascular tumor growth. *SIAM Reviews*, vol. 49(2), pp. 179–208. ↑28

Rosolen, A. and Arroyo, M. 2013. Blending isogeometric analysis and local maximum entropy meshfree approximants. *Computer Methods in Applied Mechanics and Engineering*, vol. 264, pp. 95–107. ↑40

Rosolen, A., Millán, D., and Arroyo, M. 2013. Second-order convex maximum entropy approximants with applications to high-order PDE. *International Journal for Numerical Methods in Engineering*, vol. 94(2), pp. 150–182. ↑39

Sanga, S., Frieboes, H.B., Zheng, X., Gatenby, R., Bearer, E.L., and Cristini, V. 2007. Predictive oncology: A review of multidisciplinary, multiscale in silico modeling linking phenotype, morphology and growth. *NeuroImage*, vol. 37(Supplement 1), pp. S120 – S134. ↑7

Sanga, S., Sinek, J.P., Frieboes, H.B., Ferrari, M., Fruehauf, J.P., and Cristini, V. 2006. Mathematical modeling of cancer progression and response to chemotherapy. *Expert Review of Anticancer Therapy*, vol. 6(10), pp. 1361–1376. ↑28

Santos-Oliveira, P., Correia, A., Rodrigues, T., Ribeiro-Rodrigues, T.M., Matafome, P., Rodríguez-Manzaneque, J.C., Seiça, R., Girão, H., and Travasso, R.D.M. 2015. The force at the tip - Modelling tension and proliferation in sprouting angiogenesis. *PLoS Computational Biology*, vol. 11(8), p. e1004436. ↑32

Schillinger, D., Dedé, L., Scott, M.A., Evans, J.A., Borden, M.J., Rank, E., and Hughes, T.J.R. 2012. An isogeometric design-through-analysis methodology based on adaptive hierarchical refinement of NURBS, immersed boundary methods, and T-spline CAD surfaces. *Computer Methods in Applied Mechanics and Engineering*, vol. 249-252, pp. 116–150. ↑39

Schmidt, R., Wüchner, R., and Bletzinger, K.U. 2012. Isogeometric analysis of trimmed NURBS geometries. *Computer Methods in Applied Mechanics and Engineering*, vol. 241-244, pp. 93–111. ↑39

Schmucker, C. and Schaeffel, F. 2004. A paraxial schematic eye model for the growing C57BL/6 mouse. *Vision Research*, vol. 44(16), pp. 1857–1867. ↑114

Scianna, M., Bell, C.G., and Preziosi, L. 2013. A review of mathematical models for the formation of vascular networks. *Journal of Theoretical Biology*, vol. 333, pp. 174–209. ↑28

Sciumè, G., Gray, W., Ferrari, M., Decuzzi, P., and Schrefler, B. 2013a. On computational modeling in tumor growth. *Archives of Computational Methods in Engineering*, vol. 20(4), pp. 327–352. ↑31

Sciumè, G., Gray, W., Hussain, F., Ferrari, M., Decuzzi, P., and Schrefler, B. 2014. Three phase flow dynamics in tumor growth. *Computational Mechanics*, vol. 53(3), pp. 465–484. ↑31

Sciumè, G., Shelton, S., Gray, W.G., Miller, C.T., Hussain, F., Ferrari, M., Decuzzi, P., and Schrefler, B.A. 2013b. A multiphase model for three-dimensional tumor growth. *New Journal of Physics*, vol. 15(1), p. 015005. ↑31

Scott, M.A., Thomas, D.C., and Evans, E.J. 2014. Isogeometric spline forests. *Computer Methods in Applied Mechanics and Engineering*, vol. 269, pp. 222–264. ↑39

Secomb, T.W., Alberding, J.P., Hsu, R., Dewhirst, M.W., and Pries, A.R. 2013. Angiogenesis: An adaptive dynamic biological patterning problem. *PLoS Computational Biology*, vol. 9(3), p. e1002983. ↑38

Secomb, T.W. and Pries, A.R. 2011. The microcirculation: physiology at the mesoscale. *The Journal of Physiology*, vol. 589(5), pp. 1047–1052. ↑38

Semenza, G.L. 2008. Tumor metabolism: cancer cells give and take lactate. *Journal of Clinical Investigation*, vol. 118(12), pp. 3835–3837. ↑194

Sherratt, J.A. and Chaplain, M.A.J. 2001. A new mathematical model for avascular tumour growth. *Journal of Mathematical Biology*, vol. 43(4), pp. 291–312. ↑30

Shirinifard, A., Gens, J.S., Zaitlen, B.L., Popławski, N.J., Swat, M., and Glazier, J.A. 2009. 3D multi-cell simulation of tumor growth and angiogenesis. *PLoS ONE*, vol. 4(10), p. e7190. ↑38

Shiu, Y.T., Weiss, J.A., Hoying, J.B., Iwamoto, M.N., Joung, I.S., and Quam, C.T. 2005. The role of mechanical stresses in angiogenesis. *Critical Reviews in Biomedical Engineering*, vol. 33(5), pp. 431–510. ↑69 , ↑107 , ↑181

Sleeman, B. and Wallis, I.P. 2002. Tumour induced angiogenesis as a reinforced random walk: Modelling capillary network formation without endothelial cell proliferation. *Mathematical and Computer Modelling*, vol. 36(3), pp. 339–358. ↑34 , ↑88

Speleers, H., Manni, C., Pelosi, F., and Sampoli, M.L. 2012. Isogeometric analysis with Powell–Sabin splines for advection–diffusion–reaction problems. *Computer Methods in Applied Mechanics and Engineering*, vol. 221-222, pp. 132–148. ↑39

Stamper, I.J., Byrne, H.M., Owen, M.R., and Maini, P.K. 2007. Modelling the role of angiogenesis and vasculogenesis in solid tumour growth. *Bulletin of Mathematical Biology*, vol. 69(8), pp. 2737–2772. ↑32

Starling, E.H. 1896. On the absorption of fluids from the connective tissue spaces. *The Journal of Physiology*, vol. 19(4), pp. 312–326. ↑153

Staton, C.A., Lewis, C., and Bicknell, R., editors 2007a. *Angiogenesis Assays: A critical appraisal of current techniques*, chapter Corneal angiogenesis assay, p. Siqing Shan and Mark W. Dewhirst. John Wiley & Sons. ISBN 978-0-470-01600-8. ↑102

Staton, C.A., Lewis, C., and Bicknell, R., editors 2007b. *Angiogenesis Assays: A critical appraisal of current techniques*. John Wiley & Sons. ISBN 978-0-470-01600-8. ↑105

Stéphanou, A., McDougall, S.R., Anderson, A.R.A., and Chaplain, M.A.J. 2005. Mathematical modelling of flow in 2D and 3D vascular networks: Applications to anti-angiogenic and chemotherapeutic drug strategies. *Mathematical and Computer Modelling*, vol. 41(10), pp. 1137–1156. ↑36

Stéphanou, A., McDougall, S.R., Anderson, A.R.A., and Chaplain., M.A.J. 2006. Mathematical modelling of the influence of blood rheological properties upon adaptative tumour-induced angiogenesis. *Mathematical and Computer Modelling*, vol. 44(1-2), pp. 96–123. ↑36

Stogner, R.H. and Carey, G.F. 2007. c^1 macroelements in adaptive finite element methods. *International Journal for Numerical Methods in Engineering*, vol. 70(9), pp. 1076–1095. ↑39

Stokes, C.L. and Lauffenburger, D.A. 1991. Analysis of the roles of microvessel endothelial cell random motility and chemotaxis in angiogenesis. *Journal of Theoretical Biology*, vol. 152(3), pp. 377–403. ↑34

Sudhakar, A. 2009. History of cancer, ancient and modern treatment methods. *Journal of cancer science & therapy*, vol. 1(2), pp. 1–4. ↑4

Sun, S., Wheeler, M.F., Obeyesekere, M., and Patrick, C.W. 2005. A deterministic model of growth factor-induced angiogenesis. *Bulletin of Mathematical Biology*, vol. 67(2), pp. 313–337. ↑34

Szabó, A. and Czirók, A. 2010. The role of cell-cell adhesion in the formation of multicellular sprouts. *Mathematical Modelling of Natural Phenomena*, vol. 5(1), pp. 106–122. ↑36

Szabó, A., Mehes, E., Kosa, E., and Czirók, A. 2008. Multicellular sprouting in vitro. *Biophysical Journal*, vol. 95(6), pp. 2702 – 2710. ↑36

Tahtis, K. and Bicknell, R. 2005. *Introduction to the Cellular and Molecular Biology of Cancer*, chapter Tumour angiogenesis, pp. 289–304. Oxford University Press Inc. ISBN 019852563X. ↑203

Takacs, T. and Jüttler, B. 2011. Existence of stiffness matrix integrals for singularly parameterized domains in isogeometric analysis. *Computer Methods in Applied Mechanics and Engineering*, vol. 200(49-52), pp. 3568 – 3582. ↑115

Takacs, T. and Jüttler, B. 2012. H^2 regularity properties of singular parameterizations in isogeometric analysis. *Graphical Models*, vol. 74(6), pp. 361–372. ↑115 , ↑117

Talmadge, J.E. and Fidler, I.J. 2010. AACR centennial series: the biology of cancer metastasis: historical perspective. *Cancer Research*, vol. 79, pp. 5649–5669. ↑13

Tang, Z., Zhang, F., Li, Y., Arjunan, P., Kumar, A., Lee, C., and Li, X. 2011. A mouse model of the cornea pocket assay for angiogenesis study. *Journal of Visualized Experiments: JoVE*, (54), p. e3077. ↑105

Taylor, C.A. and Figueroa, C.A. 2009. Patient-specific modeling of cardiovascular mechanics. *Annual Review of Biomedical Engineering*, vol. 11(1), pp. 109–134. ↑7

Taylor, M. and Prendergast, P.J. 2015. Four decades of finite element analysis of orthopaedic devices: Where are we now and what are the opportunities? *Journal of Biomechanics*, vol. 48(5), pp. 767 – 778. ↑7

Thompson, K. and Byrne, H.M. 1999. Modelling the internalization of labelled cells in tumour spheroids. *Bulletin of Mathematical Biology*, vol. 61(4), pp. 601–623. ↑31

Thurston, G. and Kitajewski, J. 2008. VEGF and Delta-Notch: interacting signalling pathways in tumour angiogenesis. *British Journal of Cancer*, vol. 99(8), pp. 1204–1209. ↑138 , ↑203

Tong, S. and Yuan, F. 2001. Numerical simulations of angiogenesis in the cornea. *Microvascular Research*, vol. 61(1), pp. 14–27. ↑35 , ↑36 , ↑38 , ↑117 , ↑146

Tong, S. and Yuan, F. 2008a. Dose response of angiogenesis to basic fibroblast growth factor in rat corneal pocket assay: I. experimental characterizations. *Microvascular Research*, vol. 75(1), pp. 10–15. ↑144

Tong, S. and Yuan, F. 2008b. Dose response of angiogenesis to basic fibroblast growth factor in rat corneal pocket assay: II. numerical simulations. *Microvascular Research*, vol. 75(1), pp. 16 – 24. ↑36 , ↑117 , ↑146

Torre, L.A., Bray, F., Siegel, R.L., Ferlay, J., Lortet-Tieulent, J., and Jemal, A. 2015. Global cancer statistics, 2012. *CA: A Cancer Journal for Clinicians*, vol. 65(2), pp. 87–108. ↑5

Travasso, R.D.M., Castro, M., and Oliveira, J.C.R.E. 2011a. The phase-field model in tumor growth. *Philosophical Magazine*, vol. 91(1), pp. 183–206. ↑28

Travasso, R.D.M., Corvera Poiré, E., Castro, M., Rodríguez-Manzaneque, J.C., and Hernández-Machado, A. 2011b. Tumor angiogenesis and vascular patterning: A mathematical model. *PLoS ONE*, vol. 6(5), p. e19989. ↑37 , ↑39 , ↑47 , ↑48 , ↑56 , ↑58 , ↑85 , ↑86 , ↑139 , ↑142 , ↑179 , ↑214 , ↑224

UCDavis 2016. URL `http://www.vetmed.ucdavis.edu/courses/vet_eyes/eye_path/epath_overview_index.html`. ↑103

Valenciano, J. and Chaplain, M.A.J. 2004. An explicit subparametric spectral element method of lines applied to a tumour angiogenesis system of partial differential equations. *Mathematical Models and Methods in Applied Sciences*, vol. 14(2), pp. 165–187. ↑32

Valero, C., Javierre, E., García-Aznar, J.M., and Gómez-Benito, M.J. 2013. Numerical modelling of the angiogenesis process in wound contraction. *Biomechanics and Modeling in Mechanobiology*, vol. 12(2), pp. 349–360. ↑37

Valero, C., Javierre, E., García-Aznar, J.M., Gómez-Benito, M.J., and Menzel, A. 2015a. Modeling of anisotropic wound healing. *Journal of the Mechanics and Physics of Solids*, vol. 79, pp. 80 – 91. ↑37

Valero, C., Javierre, E., García-Aznar, J.M., Menzel, A., and Gómez-Benito, M.J. 2015b. Challenges in the modeling of wound healing mechanisms in soft biological tissues. *Annals of Biomedical Engineering*, vol. 43(7), pp. 1654–1665. ↑37

Valizadeh, N., Bazilevs, Y., Chen, J.S., and Rabczuk, T. 2015. A coupled IGA–Meshfree discretization of arbitrary order of accuracy and without global geometry parameterization. *Computer Methods in Applied Mechanics and Engineering*, vol. 293, pp. 20–37. ↑40

Vander Heiden, M.G., Cantley, L.C., and Thompson, C.B. 2009. Understanding the Warburg effect: the metabolic requirements of cell proliferation. *Science*, vol. 324, pp. 1029–1033. ↑194

Vermolen, F.J. and Javierre, E. 2012. A finite-element model for healing of cutaneous wounds combining contraction, angiogenesis and closure. *Journal of Mathematical Biology*, vol. 65(5), pp. 967–996. ↑37

Wall, W.A., Frenzel, M.A., and Cyron, C. 2008. Isogeometric structural shape optimization. *Computer Methods in Applied Mechanics and Engineering*, vol. 197(33-40), pp. 2976–2988. ↑40

Ward, J.P. and King, J.R. 1997. Mathematical modelling of avascular-tumour growth. *Mathematical Medicine and Biology*, vol. 14(1), pp. 39–69. ↑31

Ward, J.P. and King, J.R. 1999. Mathematical modelling of avascular-tumour growth II: modelling growth saturation. *Mathematical Medicine and Biology*, vol. 16(2), pp. 171–211. ↑31

Weinberg, R. 1998. *One renegade cell: How cancer begins*. Basic Books. ISBN 0786724013. ↑4 , ↑11

Weis, S.M. and Cheresh, D.A. 2011. Tumor angiogenesis: molecular pathways and therapeutic targets. *Nature Medicine*, vol. 17(11), pp. 1359–1370. ↑22 , ↑203

Welter, M., Bartha, K., and Rieger, H. 2008. Emergent vascular network inhomogeneities and resulting blood flow patterns in a growing tumor. *Journal of Theoretical Biology*, vol. 250(2), pp. 257–280. ↑38

Welter, M., Bartha, K., and Rieger, H. 2009. Vascular remodelling of an arteriovenous blood vessel network during solid tumour growth. *Journal of Theoretical Biology*, vol. 259(3), pp. 405–422. ↑38

Welter, M. and Rieger, H. 2010. Physical determinants of vascular network remodeling during tumor growth. *The European Physical Journal E*, vol. 33(2), pp. 149–163. ↑38

Welter, M. and Rieger, H. 2013. Interstitial fluid flow and drug delivery in vascularized tumors: A computational model. *PLoS ONE*, vol. 8(8), p. e70395. ↑38 , ↑158 , ↑166

White, E., Karp, C., Strohecker, A.M., Guo, Y., and Mathew, R. 2010. Role of autophagy in suppression of inflammation and cancer. *Current Opinion in Cell Biology*, vol. 22(2), pp. 212–217. ↑194

Wise, S.M., Lowengrub, J.S., Frieboes, H.B., and Cristini, V. 2008. Three-dimensional multispecies nonlinear tumor growth-I: Model and numerical method. *Journal of Theoretical Biology*, vol. 253(3), pp. 524–543. ↑31 , ↑39

World Bank 2014. World development indicators. URL `http://dx.doi.org/10.1596/978-1-4648-0163-1`. ↑1

Wu, J., Long, Q., Xu, S., and Padhani, A.R. 2009. Study of tumor blood perfusion and its variation due to vascular normalization by anti-angiogenic therapy based on 3D angiogenic microvasculature. *Journal of Biomechanics*, vol. 42(6), pp. 712–721. ↑38

Wu, J., Xu, S., Long, Q., Collins, M.W., König, C.S., Zhao, G., Jiang, Y., and Padhani, A.R. 2008. Coupled modeling of blood perfusion in intravascular, interstitial spaces in tumor microvasculature. *Journal of Biomechanics*, vol. 41(5), pp. 996–1004. ↑38

Wu, M., Frieboes, H.B., McDougall, S.R., Chaplain, M.A.J., Cristini, V., and Lowengrub, J. 2013. The effect of interstitial pressure on tumor growth: Coupling with the blood and lymphatic vascular systems. *Journal of Theoretical Biology*, vol. 320, pp. 131–151. ↑38

Xia, S., Wang, X., and Qian, X. 2015. Continuity and convergence in rational triangular Bézier spline based isogeometric analysis. *Computer Methods in Applied Mechanics and Engineering*, vol. In press. ↑39

Xia, Y., Xu, Y., and Shu, C.W. 2007. Local discontinuous Galerkin methods for the Cahn-Hilliard type equations. *Journal of Computational Physics*, vol. 227(1), pp. 472–491. ↑39

Ye, X. and Cheng, X. 2005. The Fourier spectral method for the Cahn-Hilliard equation. *Applied Mathematics and Computation*, vol. 171(1), pp. 345–357. ↑39

Yu, P., Mustata, M., Peng, L., Turek, J.J., Melloch, M.R., French, P.M.W., and Nolte, D.D. 2004. Holographic optical coherence imaging of rat osteogenic sarcoma tumor spheroids. *Applied Optics*, vol. 43(25), pp. 4862–4873. ↑11

Zhang, T.Y. and Suen, C.Y. 1984. A fast parallel algorithm for thinning digital patterns. *Communications of the ACM*, vol. 27(3), pp. 236–239. ↑94

Zheng, X., Wise, S.M., and Cristini, V. 2005. Nonlinear simulation of tumor necrosis, neo-vascularization and tissue invasion via an adaptive finite-element/level-set method. *Bulletin of Mathematical Biology*, vol. 67(2), pp. 211–259. ↑38

Ziebert, F., Swaminathan, S., and Aranson, I.S. 2012. Model for self-polarization and motility of keratocyte fragments. *Journal of The Royal Society Interface*, vol. 9(70), pp. 1084–1092. ↑138